Universidade de Aveiro Departamento de Química
2016

Sónia Oliveira Pereira

Novas estratégias de polimerização na construção de nanoestruturas plasmónicas

New polymerization routes for plasmonic nanostructured assemblies

Universidade de Aveiro Departamento de Química
2016

Sónia Oliveira Pereira

Novas estratégias de polimerização na construção de nanoestruturas plasmónicas

New polymerization routes for plasmonic nanostructured assemblies

Tese apresentada à Universidade de Aveiro para cumprimento dos requisitos necessários à obtenção do grau de Doutor em Nanociências e Nanotecnologia, realizada sob a orientação científica da Doutora Ana Margarida Madeira Viegas de Barros Timmons, Professora Auxiliar do Departamento de Química da Universidade de Aveiro e do Doutor Tito da Silva Trindade, Professor Associado com Agregação do Departamento de Química da Universidade de Aveiro

Apoio financeiro da FCT e do FSE no âmbito do III Quadro Comunitário de Apoio (Bolsa de Doutoramento SFRH/BD/80156/2011).

Dedico este trabalho à minha família: mãe, irmãs e em especial ao meu marido pelo incansável apoio.

o júri

presidente	Prof. Doutor Paulo Jorge dos Santos Gonçalves Ferreira professor catedrático da Universidade de Aveiro
	Prof. Doutor José Paulo Sequeira Farinha professor auxiliar do Instituto Superior Técnico da Universidade de Lisboa
	Prof. Doutor Artur José Monteiro Valente professor auxiliar da Faculdade de Ciências e Tecnologias da Universidade de Coimbra
	Prof. Doutor Maria do Rosário Gomes Ribeiro professora auxiliar do Instituto Superior Técnico da Universidade de Lisboa
	Doutora Ana Luísa Daniel da Silva investigadora auxiliar da Universidade de Aveiro
	Prof. Doutora Ana Margarida Madeira Viegas de Barros Timmons professora auxiliar da Universidade de Aveiro

agradecimentos

Em primeiro lugar gostaria de agradecer aos meus orientadores, verdadeiros impulsionadores desta tese, por me terem guiado e ajudado a crescer no meio científico e pela excelente orientação ao longo destes anos. À Professora Ana Barro-Timmons um agradecimento especial pela sua permanente disponibilidade, incansável incentivo, valiosos conselhos e sugestões e pelo excelente apoio, confiança e amizade ao longo destes anos. Ao Professor Tito Trindade agradecer de igual forma por todas a discussões e sugestões oportunas que enriqueceram este trabalho, pelo seu entusiasmo, apoio e amizade.

Gostaria também de agradecer a tantas outras pessoas que contribuíram e colaboraram para o desenvolvimento do trabalho apresentado nesta tese. À Mestre Celeste Azevedo por todo o apoio nas técnicas espectroscópicas de UV-Visível e FTIR. À Professora Amparo Faustino pela disponibilização do fluorímetro para as medidas de fluorescência. Ao grupo de microscopia eletrónica da Universidade de Aveiro, em especial ao Bruno Almeida e à Marta Ferro. Agradecer ao projeto Encircle (IUPAC/0001/2009) em particular à Liliana Melro e à Paula Lacerda por todo o ensinamento na síntese dos agentes macroRAFT e respetivos copolímeros. Ao João Campos pelos ensinamentos e toda a ajuda disponibilizada da química de *click*. À Joana Barata pelo tempo disponibilizado na síntese do monómero fluorescente. Agradecer ao Professor Dmitry Evtyugin pelo tempo despendido nas análises de GPC-SEC. E agradecer a colaboração do Professor Osvaldo Oliveira Júnior, da Universidade de São Paulo em São Carlos, Brasil, na elaboração dos estudos na interface ar/água usando a técnica de LB.

Agradecer também ao CICECO e departamento de química da Universidade de Aveiro por proporcionarem condições trabalho para o desenvolvimento desta tese. À Fundação para a ciência e tecnologia (FCT) pela bolsa de doutoramento (SFRH/BD/80156/2011).

Agradeço também a todos os meus colegas de laboratório do NanoLab que sempre contribuíram para um bom ambiente, boa disposição, companheirismo, apoio e amizade ao longo deste percurso. Em particular à Joana Barata e ao Ricardo Pinto e deixar um obrigada especial à Ângela Pereira e Paula Pinheiro por tudo.

Agradeço ainda de forma especial a todos os meus amigos de percurso académico e pessoal que de forma indireta sempre contribuíram para o meu crescimento pessoal e académico ao longo destes anos. Sem querer nomear ninguém em particular porque eles são muitos, bons e sabem quem são.

Por último, mas não menos importante, quero expressar a minha gratidão à minha mãe e irmãs por todo o apoio, sem elas não era possível. E agradecer ao meu marido Mickael Santos por toda a força, apoio confiança, amizade e amor ao longo desta etapa. Todas as palavras são poucas para expressar o apoio deles.

palavras-chave

nanoestruturas plasmónicas, ouro, modificação e funcionalização de superfícies, polimerização RAFT, biodeteção.

resumo

Este trabalho descreve a preparação e caracterização de nanoestruturas funcionais de ouro do tipo coroa@núcleo para aplicações em biodeteção. O trabalho foi desenvolvido considerando duas abordagens principais na preparação de nanoestruturas polímero@Au (coroa@núcleo), nomeadamente utilizando: (i) polímeros disponíveis comercialmente e (ii) polímeros sintetizados por polimerização radicalar controlada, mais especificamente por polimerização de transferência de cadeia reversível por adição-fragmentação (RAFT). Foram também exploradas estratégias para a funcionalização destas nanoestruturas a fim de avaliar a sua potencialidade e especificidade em biodeteção. Neste sentido, o sistema modelo utilizado para estudar a resposta à biodeteção foi o de biotina-avidina (receptor –analito) e, como controlo, a albumina do soro de bovino (BSA).

No primeiro capítulo apresenta-se uma revisão bibliográfica dos tópicos abordados ao longo desta tese. Inicialmente é apresentada uma contextualização do trabalho onde é realçada a importância das propriedades óticas das nanopartículas (NPs) de ouro em aplicações biológicas. Seguidamente é dada ênfase à modificação e funcionalização de NPs de ouro tendo em vista precisamente este tipo de aplicações. Nesse sentido, foram analisadas criticamente as duas principais abordagens consideradas no âmbito desta tese. Uma primeira em que foram usados polímeros iónicos (polielectrólitos) disponíveis comercialmente para a modificação de NPs através de interações electrostáticas usando o método camada a camada (LbL). Numa segunda abordagem, com maior relevância neste trabalho, foram revistas estratégias para preparação de nanoestruturas de ouro utilizando o mecanismo de polimerização RAFT. Finalmente foi abordada a técnica Langmuir Blodgett (LB) no estudo de moléculas anfifílicas na interface ar/água e na preparação de filmes LB.

No segundo capítulo apresentam-se os resultados obtidos relativos à utilização do método LbL na preparação das nanoestruturas de ouro. Assim, foram preparadas nanoestruturas do tipo coroa@núcleo usando o policatião hidrocloreto de polialilamina (PAH) e o polianião sulfonato de poliestireno (PSS), funcionalizadas com biotina e um fluoróforo (isotiocianato de fluoresceína – FITC) e utilizando duas vias destintas. As nanoestruturas foram caracterizadas por espectroscopia no UV-Visível e de fluorescência, por medidas de potencial zeta e microscopia eletrónica. Por fim, a resposta ótica e a especificidade da resposta das nanoestruturas funcionalizadas à presença de avidina foi estudada por espectroscopia no UV-Visível e fluorescência.

No terceiro capítulo foram exploradas três estratégias para a preparação de nanoestruturas do tipo coroa@núcleo usando polímeros sintetizados por polimerização RAFT. Primeiramente foram polimerizados monómeros hidrofílicos (acrilato de poli(etileno glicol) metil éter (PEGA) e ácido acrílico (AA) em solução, usando o mecanismo de polimerização RAFT, obtendo-se

resumo (cont.)

polímeros que contêm o agente RAFT e por isso designados de agente macroRAFT (MR). Seguidamente, foi sintetizado um segundo bloco a partir do agente macroRAFT por polimerização RAFT em emulsão de monómeros hidrofóbicos (metacrilato de metilo (MMA) e acrilato de butilo (BA)), obtendo-se os respetivos copolímeros de bloco. Estes copolímeros foram depois utilizados nas duas primeiras estratégias: no caso da estratégia pós-modificação, as NPs de Au, também previamente preparadas, foram misturadas com o copolímero, enquanto que na estratégia in situ as NPs de ouro foram sintetizadas na presença do copolímero. Na terceira estratégia, o segundo bloco (bloco hidrofóbico) foi preparado a partir do agente macroRAFT previamente adsorvido à superfície das NPs de Au (MR@Au NPs). Nesta última estratégia foram identificados e otimizados alguns parâmetros que permitiram obter nanoestruturas do tipo copolímero@Au, como por exemplo a adição controlada dos monómeros hidrofóbicos, bem como a concentração de MR.

No quarto capítulo selecionou-se o tipo de nanoestrutura de copolímero@Au mais promissor obtido no capítulo anterior para ser funcionalizado e utilizado em ensaios de bioreconhecimento. As nanoestruturas de copolímero@Au foram funcionalizadas com biotina utilizando a química click e avaliou-se a resposta ótica e especificidade na presença de avidina. Visando compreender o modo de interação ao nível molecular entre o copolímero (funcionalizado, ou não, com biotina) e o bioanalito, foram realizados alguns estudos preliminares sobre o comportamento destes polímeros na interface ar/água utilizando a técnica Langmuir-Blodgett (LB). Adicionalmente, foram ainda preparadas nanoestruturas fluorescentes de copolímero@Au por polimerização RAFT de um monómero fluorescente (monómero modificado com FITC) a partir da superfície das MR@Au NPs e seguidamente de monómeros hidrofóbicos (MMA:BA), de modo a avaliar o efeito da distância entre o núcleo e o fluoróforo sobre a resposta ótica deste tipo de nanoestruturas.

As diferentes estratégias de preparação de nanoestruturas de ouro desenvolvidas ao longo desta tese permitiram estabelecer soluções para diversos aspetos críticos tais como a robustez, o controlo da morfologia e a estabilidade coloidal de nanoestruturas do tipo polímero@Au para aplicações em biodeteção, bem como estabelecer procedimentos com vista à sua funcionalização. A utilização do mecanismo RAFT utilizando a estratégia de polimerização a partir da superfície demonstrou ser particularmente útil para a encapsulação e (multi)funcionalização de NPs de ouro, e apresenta-se como estratégia promissora na aplicação a outros nanomateriais.

keywords Plasmonic nanostructures, gold, surface modification and functionalization, RAFT polymerization, biosensing.

abstract

This thesis describes the preparation and characterization of multifunctional gold shell@core nanostructures towards biosensing applications. The work was developed following two different approaches for the preparation of the polymer@Au (shell@core) nanostructures, using (i) commercially available polymers and (ii) polymers synthesized via reversible deactivation radical polymerization, specifically reversible addition fragmentation chain transfer (RAFT). Strategies aiming at the functionalization of these nanostructures were also explored in order to assess their potential use in biosensing using the biotin-avidin (bioreceptor-bioanalyte) system as model and bovine serum albumin (BSA) as control.

In the first chapter, a literature review concerning the main topics discussed in this thesis is presented. Initially, the work developed in this thesis is put in context highlighting the optical properties of gold nanoparticles (NPs) in biological applications and the strategies available for the modification and functionalization of Au NPs aiming at this type of applications. In that sense, two main approaches were reviewed considering the work developed in the thesis namely: the use of commercially available ionic polymers (polyelectrolytes) to modify NPs surface via electrostatic interactions using the Layer-by-Layer (LbL) method, and the preparation of gold nanostructures mediated by RAFT polymerization. Finally, the Langmuir Blodgett (LB) technique was a briefly presented for the study of amphiphilic molecules at air/water interface and in the preparation of LB films.

In the second chapter, the results obtained regarding the preparation of Au nanostructures using the LbL method are presented. The shell@core type nanostructures were prepared using the polycation poly(allylamine hydrochloride) (PAH) and the polyanion poly(sodium styrene sulfonate) (PSS) and were functionalized with biotin and a fluorophore (fluorescein isothiocyanate – FITC) following two distinct paths. The nanostructures were characterized by UV-Visible and fluorescence spectroscopy, zeta potential measurements and electron microscopy. Finally, the optical response and specificity of the functionalized NPs towards avidin was evaluated by optical measurements.

In the third chapter three strategies were explored for the preparation of the shell@core nanostructures using polymers synthesized via RAFT polymerization. First, hydrophilic monomers (poly(ethylene glycol) methyl ether acrylate (PEGA) and acrylic acid (AA)) were polymerized in solution via RAFT polymerization, yielding polymers containing the RAFT agent thus named macroRAFT (MR) agents. Then a second block was synthesized from the MR agent via RAFT emulsion polymerization of the hydrophobic monomers methyl methacrylate (MMA) and butyl acrylate (BA), yielding a block copolymer. This block copolymer was used in the two first strategies: for the preparation of the

abstract (cont.)

Au nanostructures. In the case of the *post-modification* strategy, previously prepared Au NPs were mixed with the copolymer, and in the case of *in situ* strategy Au NPs were generated in the presence of the block copolymer. In the third strategy, the second block (hydrophobic block) was grown from the MR agent previously adsorbed on the Au NPs surface (MR@Au NPs). In this last strategy, some parameters that allow obtaining copolymer@Au nanostructures were identified and optimized, such as the controlled addition of the hydrophobic monomers as well as the concentration of MR.

In the fourth chapter, the most promising type of copolymer@Au nanostructures obtained in the previous chapter was selected to be functionalized and used in biosensing tests. Copolymer@Au nanostrucures were functionalized with biotin using the *click chemistry* reaction and the optical response and specificity of the functionalized NPs towards avidin was evaluated by optical measurements. In order to get a better understanding of the interactions between the copolymer (functionalized, or not with biotin) and the bioanalyte at molecular level, preliminary studies have been carried out at the air-water interface using the Langmuir-Blodgett technique. Additionally, *fluorescent*-copolymer@Au nanostructures were also prepared via RAFT polymerization of a fluorescent monomer (monomer modified with FITC) from MR@Au NPs and subsequent polymerization of MMA:BA monomers in order to assess the effect of the distance between the core and the fluorophore on the optical response of this type of nanostructures.

The different strategies developed during this thesis to prepare gold nanostructures allowed to establish solutions for different critical aspects such as robustness, control of morphology and colloidal stability of polymer@Au nanostructures for applications in biodetection as well as procedures for functionalization. The use of the RAFT mechanism, in particular the *grafting from* strategy, proved very promising for the encapsulation and (multi)functionalization of AuNPs and can potentially be extended to other types of nanomaterials.

Publications resulted from this thesis

Publications in international journals

- **Pereira, S.O.**, Barros-Timmons, A., Trindade, T., **2014**. *Biofunctionalisation of colloidal gold nanoparticles via polyelectrolytes assemblies*. Colloid Polym Sci, 292: 33-50. doi: 10.1007/s00396-013-3037-3

- **Pereira, S.O.**, Trindade, T., Barros-Timmons, A., **2015** *Biotinylation of optically responsive gold/polyelectrolyte nanostructures*. Gold Bull, 48: 3-11. doi: 10.1007/s13404-014-0153-x

- **Pereira, S.O.**, Barros-Timmons, A., Trindade, T., *A comparative study of chemical routes for coating gold nanoparticles via controlled RAFT emulsion polymerization* ***(in preparation)***

- **Pereira, S.O.**, Trindade, T., Barros-Timmons, A., *RAFT assisted emulsion polymerization in the preparation of copolymer@Au nanostructures following a grafting from strategy* ***(in preparation)***

Communication in scientific meetings

Oral communications

- **Sónia Pereira.** *Strategies for the preparation of optically active nanostructured assemblies.* Workshop do Programa Doutoral de Nanociências e Nanotecnologia da Universidade de Aveiro. 19 de abril de 2013, Universidade de Aveiro.

- **Sónia Pereira.** *Strategies to prepare gold nanostructures for biosensing applications.* 2º Workshop do Programa Doutoral de Nanociências e Nanotecnologia da Universidade de Aveiro. 13 de março de 2015, Universidade de Aveiro.

- **Sónia O. Pereira,** Tito Trindade and Ana Barros-Timmons. *Biofunctional Au core@shell colloid prepared via RAFT assisted emulsion polymerization and click chemistry.* 6th Iberian Meeting on Colloids and Interfaces. 8 a 10 de julho de 2015, Guimarães, Portugal.

Poster communications

- **S.O. Pereira**, A.S. Pereira, A.V. Girão, T. Trindade, A. Barros-Timmons. *Optical responsive gold/polyelectrolyte nanostructures for bio-sensing*. Colloids and Nanomedicine 2012, 15-17 de julho de 2012, Amesterdão, Holanda. P1.72.

- **Sónia O. Pereira**, Tito Trindade, Ana Barros-Timmons. *Synthetic strategies towards optically active nanostructured assemblies.* Advanced Study Institute NATO "Nanomaterials and Nanoarchitectures", 30 de junho a 7 de julho de 2013 em Cork, Irlanda.

- Ana Barros-Timmons, Liliana Melro, **Sónia O. Pereira**, Paula S. S. Lacerda, Tito Trindade. *Exploring the use of macroRAFT agents and emulsion polymerisation in the preparation of functional nanocomposites.* 10th IUPAC International Conference of Advanced Polymers via Macromolecular Engineering. 18 a 22 de agosto de 2013. Universidade de Durham, Inglaterra. P16.

- **Sónia Oliveira Pereira**, Ana Barros-Timmons, Tito Trindade. *Synthetic strategies to prepare functional gold nanocomposites using macroRAFT agents and emulsion polymerization.* Inovação Pedagógica na Universidade de Aveiro – Teaching Day 2ª edição. 27 de novembro de 2013. Universidade de Aveiro.

- **Sónia Pereira**, Tito Trindade, Ana Barros-Timmons. *Synthetic strategies to prepare biofunctionalized gold nanocomposites using RAFT polymerization.* Research Day da Universidade de Aveiro. 3 de junho de 2014. Universidade de Aveiro.

- **Sónia Oliveira Pereira**, Liliana Melro, Paula Lacerda, Tito Trindade and Ana Barros-Timmons. *Well-controlled preparation of functional nanocomposites using macroRAFT agents.* ANM 2014 - 5th International Conference on Advanced Nano Materials, 2 a 4 de julho 2014, Universidade de Aveiro. P130.

- **Sónia Oliveira Pereira,** Tito Trindade and Ana Barros-Timmons. *Biotinylation of gold nanoparticles mediated by RAFT polymerization.* FPCOL´14- Frontiers of Polymer Colloids: From the Synthesis to Macro-Scale and Nano-Scale applications. 20 a 24 de julho de 2014, Institute of Macromolecular Chemistry, Academy of Sciences of the Czech Republic. Praga, República Checa. P-33.

- **Sónia O. Pereira**, Tito Trindade and Ana Barros-Timmons. *Biotinylation of gold nanoparticles mediated by RAFT polymerization.* Jornadas CICECO 2015: Nanotechnology… from the Lab to the Industry. 14 a 15 de abril 2015. Universidade de Aveiro. P116

CONTENTS

CONTENTS i

ABBREVIATIONS AND SYMBOLS v

LIST OF SCHEMES ix

LIST OF FIGURES ix

LIST OF TABLES xv

CHAPTER 1. General Introduction 1

- 1.1. Introduction 3
- 1.2. Gold nanoparticles 3
  - 1.2.1. Optical properties of gold nanoparticles 3
  - 1.2.2. Synthesis and stabilization of colloid gold nanoparticles 6
  - 1.2.3. Biosensing applications of gold nanoparticles 9
  - 1.2.4. Surface modification and functionalization of colloidal gold nanoparticles 11
- 1.3. Layer-by-Layer method to prepared colloidal gold nanostructures via electrostatic interactions 12
- 1.4. RAFT polymerization in the preparation of gold nanostructures 14
  - 1.4.1. Polymerization concepts 14
  - 1.4.2. RAFT polymerization concepts 18
  - 1.4.3. Preparation of polymer/gold nanostructures based on RAFT polymerization 25
  - 1.4.4. Click Chemistry 33
- 1.5. Langmuir-Blodgett technique 38
- 1.6. Motivation and aims of the work 42

CHAPTER 2. Functional gold nanostructures prepared via electrostatic self-assembly 43

- 2.1. Introduction 45
- 2.2. Preparation of gold nanostructures prepared via electrostatic self-assembly method 45

2.3. Functionalization gold nanostructures prepared via electrostatic self-assembly method...... 47

2.4. Response of the gold nanostructures towards avidin 50

2.5. Conclusions 53

CHAPTER 3. Gold nanostructures prepared via RAFT polymerization.................................... 55

3.1. Introduction 57

3.2. Preparation and characterization of macroRAFT agents.. 58

3.3. Preparation and characterization of copolymers derived from the macroRAFT agents 59

3.4. Preparation of gold nanocomposites via RAFT polymerization 61

3.4.1. Post-modification strategy.. 62

3.4.2. *In situ* generation of Au NPs in previously prepared copolymers................................. 64

3.4.3. *Grafting from* strategy 71

3.4. Conclusions 103

CHAPTER 4. Functionalization of gold nanostructures prepared via RAFT polymerization .. 105

4.1. Introduction 107

4.2. Preparation and characterization of functionalized macroRAFT agent 108

4.3. Preparation of functionalized gold nanocomposites via RAFT polymerization using the *grafting from* strategy 111

4.3.1. Study of RAFT emulsion polymerization using VA-044 as initiator........................... 112

4.3.2. Preparation and characterization of biofunctional copolymer@Au nanostructures..... 118

4.4. Response of the gold nanostructures towards avidin 121

4.5. Langmuir monolayers of copolymers at air/water interface.. 126

4.5.1. Langmuir monolayers of copolymers prepared via RAFT emulsion polymerization using VA-044 as initiator 127

4.5.2. Langmuir monolayers to study copolymer-biotin-avidin interactions 130

4.6. Preparation of fluorescence gold nanocomposites via RAFT polymerization using the *grafting from* strategy.. 132

4.7. Conclusions 146

CHAPTER 5. General Conclusions and future work 149

CHAPTER 6. Experimental procedures 155

6.1. Chemicals 157

Chemicals used in *Chapter 2* 157

Chemical used in *Chapter 3* and *Chapter 4* 157

6.2. Instrumentation 157

6.3. Experimental of chapter 2 158

6.3.1. Synthesis of Au NPs via citrate method 158

6.3.2. Modification of poly(allylamine hydrochloride) with fluorescein 159

6.3.3. Modification of PAH and PAHF with biotin 159

6.3.4. Preparation of Au/PE hybrid nanostructures 159

6.3.5. Optical response of Au/PE assemblies to avidin 160

6.4. Experimental of chapter 3 161

6.4.1. Synthesis of macroRAFT agents 161

6.4.2. Synthesis of copolymers via RAFT emulsion polymerization based on the MR agents 162

6.4.3. Synthesis of Au NPs via citrate method 162

6.4.4. Synthesis of Au nanocomposites via *post-modification* strategy 163

6.4.5. Synthesis of Au nanocomposites via *in situ* generation of Au NPs in previously prepared copolymers 163

6.4.6. Determination of CMC 164

6.4.7. Synthesis of Au nanocomposites following a *grafting from* strategy via *in situ* generation of Au NPs in previously prepared macroRAFT agents 164

6.4.8. Synthesis of Au nanocomposites following a *grafting from* strategy via macroRAFT adsorption onto previously prepared Au NPs 166

6.5. Experimental of chapter 4 169

6.5.1. Synthesis of the macroRAFT agent containing the azide function: P(azAA$_2$-*b*-PEGA$_{40}$)-TTC (*N3*-MR agent) 169

6.5.2. Synthesis of the copolymers via RAFT emulsion polymerization using VA-044 as initiator 170

6.5.3. Preparation of Au nanocomposites following a *grafting from* strategy via macroRAFT adsorption onto previously prepared Au NPs (at 44ºC) 171

6.5.4. Functionalization of biotin with an alkyne group 172

6.5.5. Azide alkyne 1,3-cycloaddition catalyzed by Cu(I) - Click chemistry reaction 173

6.5.6. Optical response of copolymer@Au nanostructures to Avidin 173

6.5.7. Preparation of Langmuir monolayers of copolymers 174

6.5.8. Preparation of Langmuir monolayers to study copolymer-biotin-avidin interactions.. 175

6.5.9. Preparation of fluorescent copolymer@Au NPs following a *grafting from* strategy via macroRAFT adsorption onto previously prepared Au NPs 175

REFERENCES 179

ANNEXES 195

ABBREVIATIONS AND SYMBOLS

General abbreviations

AR	Aspect ratio
ATR-FTIR	Fourier transform infrared with attenuated total reflection
ATRP	Atom-transfer radical polymerization
BSA	Bovine serum albumin
CMC	Critical micelle concentration
CRP	Controlled radical polymerization
CSIRO	Common-wealth Scientific and Industrial Research Organization
CTA	Chain transfer agent
CTAB	Hexadecyltrimethylammonium bromide
CuAAC	Cu(I) Azide-Alkyne Cycloaddition
d	Diameter
d_{average}	Hydrodynamic diameter, in average
$d_{\text{intensity}}$	Hydrodynamic diameter, in intensity distribution
d_{number}	Hydrodynamic diameter, in number distribution
DLS	Dynamic Light Scattering
DMAP	4-(Dimethylamino)pyridine
DMF	*N,N*-Dimethylformamide
DMSO	Dimethyl sulfoxide
DNA	Deoxyribonucleic acid
DP	Degree of Polymerization
EDC	(3-dimethylaminopropyl)-*N′*-ethylcarbodiimide hydrochloride
FITC	Fluorescein isothiocyanate
FRET	Förster resonance energy transfer
FTIR	Fourier transform infrared
GPC-SEC	Gel permeation chromatography – size exclusion chromatography
^{1}H-NMR	Proton nuclear magnetic resonance
LB	Langmuir-Blodgett
LbL	Layer-by-Layer
MADIX	Macromolecules design via the interchange xanthates
$\overline{M}_n$	Number average molecular weight

$\bar{M}_w$	Weight average molecular weight
MR	MacroRAFT
MW	Molecular weight
NMP	Nitroxide-mediated polymerization
NPs	Nanoparticles
NRs	Nanorods
NSs	Nanospheres
NSET	Nanoparticle surface energy transfer
LSPR	Localized Surface Plasmon Resonance
PBS	Phosphate buffer saline
PdI	Polydispersity index (from DLS measurements)
PE	Polyelectrolyte
PL	Photoluminescence
PM-IRRAS	Polarization modulation infrared reflection adsorption spectroscopy
QDs	Quantum dots
RAFT	Reversible addiction-fragmentation chain transfer
RDRP	Reversible-deactivation radical polymerization
SEM	Scanning electron microscopy
STEM	Scanning transmission electron microscopy
TEM	Transmission electron microscopy
THF	Tetrahydrofuran
UV	Ultraviolet
UV-Vis	Ultraviolet-Visible

Monomers

AA	Acrylic acid
AEM	2-Aminoethyl methacrylate hydrochloride
AM	Acrylamide
AN	Acrylonitrile
AzMA	2-azidoethyl methacrylate
BA	*n*-butyl acrylate
MA	Methyl acrylate
MMA	Methyl methacrylate

NiPAM	*N*-isopropylacrylamide
PEGA	Poly(ethylene glycol) methyl ether acrylate
PgA	Propargyl acrylate
PgMA	Propargyl methacrylate
PgOH	Propargyl alcohol
S	Styrene
VAc	Vinylacetate

RAFT agents

CBDN	α-Cyanobenzyl dithionaphthalate
CPDB	2- (2-Cyanopropyl) dithiobenzoate
TTC-A	2-(Dodecylthiocarbonothioylthio)-2-methylpropionic acid

Initiators

AIBN	2,2’-Azoisobutyronitrile
ACPA or ACVA	4,4′-Azobis(4-cyanopentanoic acid)
VA-044	2,2'-azobis[2-(2-imidazolin-2-yl)propane]dihydrochloride

Polymers

PAA	Poly(acrylic acid)
P(AA$_{40}$)-TTC or pAATTC	Poly(acrylic acid) synthesized from TTC
P(AA$_{40}$)-*b*-(MMA-*co*-BA)$_{160}$-TTC or copAATTC	Poly(acrylic acid)-*b*-poly(methyl methacrylate-*co*-butyl acrylate) synthesized from TTC
P(AA$_{2}$-*b*-PEGA$_{40}$)-TTC	Poly(acrylic acid)-*b*-poly[poly(ethylene glycol) methyl ether acrylate] synthesized from TTC
P(AA$_{2}$-*b*-PEGA$_{40}$)-*b*-(MMA-*co*-BA)-TTC	Poly(acrylic acid)-*b*-poly[poly(ethylene glycol) methyl ether acrylate]-*b*-poly(methyl methacrylate-*co*-butyl acrylate) synthesized from TTC
P(AA$_{20}$-*co*-PEGA$_{20}$)-*b*-(MMA-*co*-BA)-TTC	Poly(acrylic acid)-*co*-poly[poly(ethylene glycol) methyl ether acrylate]-*b*-poly(methyl methacrylate-*co*-butyl acrylate) synthesized
PAEA	Poly(2-aminoethylmethacrylamide)
PAH	Poly(allylamine hydrochloride)
PAMPS	Poly(sodium 2-acryl- amido-2-methyl propane sulfonate)
PAPTAC	Poly[(3-acryl- amidopropyl) trimethylammonium chloride]
PBA	Poly(*n*-butylacrylate)

PBA-*b*-PNiPAM	Poly(*n*-butylacrylate-*b*-*N*-isopropylacrylamide)
PDMAm	Poly(*N*,*N*-dimethyl-acrylamide)
PDMAEA	Poly(*N*,*N*-diemthylaminoethyl acrylate)
PDMAEMA	Poly(2-(dimethylamino)ethyl methacrylate)
PEG	Poly(ethylene glycol)
PEGMA	Poly(ethylene glycol)monomethylether)methacrylate
PEO	Poly(ethylene oxide)
PMAEDAPS-*b*-PDMAm	Poly(3-[2-*N*-methylacrylamido)-ethyl dimethyl ammonio propane sulfonate-*b*-*N*,*N*-dimethylacrylamide)
PMMA	Poly(methyl methacrylate)
PNiPAM	Poly(*N*-isopropyl acrylamide)
POEG-A-*co*-DEG-A	Poly(oligoethylene oxide acrylate-*co*-diethylene oxide acrylate)
P(PEGA$_{40}$)-TTC or pPEGATTC	Poly[poly(ethylene glycol) methyl ether acrylate] synthesized from TTC
P(PEGA$_{40}$)-*b*-(MMA-*co*-BA)$_{140}$-TTC or copPEGATTC	Poly[poly(ethylene glycol) methyl ether acrylate]-*b*-poly(methyl methacrylate-*co*-butyl acrylate) synthesized from TTC
PS	Poly(styrene)
PSS	Poly(sodium styrene sulfonate)
PVBTAC	Poly((*ar*-vinylbenzyl) trimethylammonium chloride)

Symbols

$\Delta\lambda$	Shift of the wavelength
Đ	Dispersity (from GPC-SEC analysis)
λ	Wavelength
λ_{exc}	Wavelength of excitation
λ_{LSPR}	Wavelength of LSPR
ζ	Zeta potential

LIST OF SCHEMES

Scheme 2.1. Preparation of Au/PE hybrid nanostructures: (A) Synthesis of Au NPs; (B) Functionalization of Au/Citrate NPs with poly(allylamine hydrochloride) (PAH) and poly(styrenesulfonic acid sodium salt) (PSS); (C) Functionalization of Au_n with the outermost layer. 45

Scheme 3.1. Strategies to prepare gold nanocomposites via RAFT assisted emulsion polymerization 57

Scheme 3.2. Schematic representation of the influence of pH on the generation of Au NPs in the presence of $P(AA_{40})$-TTC. 78

Scheme 3.3. Schematic representation of the influence of MR agent concentration on the size and size distribution of Au NPs obtained in the presence of MR agent and using $NaBH_4$ as reducing agent. 89

Scheme 4.1 Schematic representation of the reaction between the carboxylate ion at the surface of copolymer@Au nanostructure and the hydroxyl group from the 3-azido-1-propanol using EDC as intermediate. 108

Scheme 6.1. Washing steps of copolymer@Au NPs mixed with alkylated biotin by centrifugation aiming non-linked biotin removal. 174

LIST OF FIGURES

Figure 1.1. Schematic illustration of the interaction of polarized light and gold nanospheres (A) and nanorods (B) to form the electronic coherent localized surface plasmon resonance (LSPR) oscillation [10]. 4

Figure 1.2. Absorbance spectra, photographs and TEM micrographs of gold nanospheres with different sizes (A) and gold nanorods with different aspect ratios (B). Adapted from Zhong *et al.* 2007 [11] and Pérez-Juste *et al.* 2005 [12], respectively. 5

Figure 1.3. UV-Vis spectra of $HAuCl_4$ at various pH. Adapted from [43]. 7

Figure 1.4. Schematic illustration of two reaction pathways for synthesis of gold nanocrystals by citrate reduction. [44] 8

Figure 1.5. Schematic representation of Au NPs biosensor based on LSPR. Specific recognition of DNA (A) and of a specific ligand (B). 10

Figure 1.6. Schematic representation of Au NPs biosensor based on quenching fluorescence. Specific recognition of DNA (A) and of a specific ligand (B). 10

Figure 1.7. Schematic representation of surface stabilization and or functionalization of Au NPs, followed by surface (bio)functionalization. 12

Figure 1.8. Surface modification of nanoparticles using PE treatment (*n* represents the number of cycles). [76] 13

Figure 1.9. Schematic representation of the stages in a typical emulsion polymerization reaction. Adapted from [93]. 16

Figure 1.10. Polymer architectures available through RDRP [98]. 17

Figure 1.11. Structure of CTA/RAFT agent. 18

Figure 1.12. Structural features of thiocarbonylthio RAFT agent and intermediate formed on radical addition. Adapted from [96]. 19

Figure 1.13. Generic structures of RAFT chain-transfer agents. 19

Figure 1.14 Guidelines for selection of RAFT agents for various polymerizations. For Z, addition rates decrease and fragmentation rates increase from left to right. For R, fragmentation rates decrease from left to right. Dashed line indicates partial control (i.e. control of molecular weight but poor polydispersity or substantial retardation in the case of VAc) [96]. 20

Figure 1.15. Proposed mechanism of RAFT polymerization; (I and II) homopolymerization and (III) chain extension of a macroCTA. Adapted from [98]. 21

Figure 1.16. Structure of commonly used initiators in RAFT polymerization. 22

Figure 1.17. Schematic representation of surfactant-free emulsion RAFT polymerization. 24

Figure 1.18 Properties and functions of Au NP core and polymer shell on polymer/Au nanocomposite. 25

Figure 1.19. Common preparation methods of polymer/inorganic nanohybrids [99]. 26

Figure 1.20. Mechanism describing the immobilization of a RAFT-prepared copolymer onto gold surface [115]. 26

Figure 1.21. Proposed mechanisms describing synthesis, reduction, and immobilization onto a gold surface of RAFT-prepared PAA and PS [126]. 28

Figure 1.22 (left) Preparation of (co)polymer-stabilized transition metal nanoparticles, (right) UV-Vis spectra for $HAuCl_4$ sols and polymer-stabilized Au- NPs. P1 – PAMPS, P2 – PVBTAC, P3 – PDMA, and P4 - PMAEDAPS-*b*-PDMAm. Adapted from [130]. 29

Figure 1.23. Image of the final NPs solutions 5 min after reduction at 20 °C. The polymer concentration increases from left to right (0 to 0.15 wt.%). [106] 30

Figure 1.24. Scheme of the chemical structures of PNIPAMs used featuring the three types of end groups. [133] 30

Figure 1.25. (A) Schematic representation of the dispersion and encapsulation of pigment particles using RAFT mediated emulsion polymerization. (B) Encapsulated titanium dioxide pigment particles. Adapted from [136]. 32

Figure 1.26. Cryo-TEM picture of the CeO_2/poly(styrene-*co*-methyl acrylate) hybrid latex obtained in the presence of (A) poly($BA_{7.3}$-*co*-$AA_{9.8}$), (B) poly($BA_{7.2}$-*co*-$AMPS_{7.6}$) and (C) poly($BA_{5.0}$-*co*-$AA_{4.9}$-*co*-$AMPS_{3.6}$) macroRAFT agents. Adapted from [144]. 33

Figure 1.27. Representation of the azide-alkyne reaction catalyzed with Cu(I) and ruthenium complex. 34

Figure 1.28 Schematic representation of “click chemistry” combined with polymers. 35

Figure 1.29. Preparation of polyAzMA and polyAzMA derivatives by combining RAFT polymerization and “click chemistry”. [167] 38

Figure 1.30 Schematic representation of a typically Langmuir-Blodgett trough [184]. 39

Figure 1.31. Schematic representation of surface pressure vs area per molecule isotherm. 40

Figure 1.32. Schematic representation of LB deposition process on a hydrophilic substrate resulting in a three layer film. The hydrophilic molecular headgroups are represented by circles and the hydrophobic tails are represented by the attached “sticks”. Note that layers are deposited in alternating orientations on upstrokes (b and d) and downstroke (c) resulting in a multi-bilayer structure (e) [184]. 41

Figure 2.1. (A) UV-Vis spectra of Au_0PAH and Au_2PAH nanostructures and (B) zeta potential of Au/Citrate colloids and after their treatment with PAH and PSS (straight lines to guide the eye). 46

Figure 2.2. TEM images of (A) Au_0PAH nanostructures and (B) Au_2PAH nanostructures. 47

Figure 2.3. Visible spectra of (A) Au_0PAH and (B) Au_2PAH nanostrutures (the spectra were normalized at 450 nm) 47

Figure 2.4. (A and C) visible spectra and (B and D) fluorescence spectra (λ_{exc}=494nm) of Au0PAHF and Au2PAHF nanostructures. The visible spectra were normalized at 450nm. 49

Figure 2.5. $\Delta A(avidin/colloid)$ of (A) Au_0PAH and (B) Au_2PAH nanostructures in the presence of avidin. .. 51

Figure 2.6. (A and C) $\Delta A(avidin/colloid)$ and (B and D) $I_{517}(avidin)/I_{517}(colloid)$ of Au_0PAH and Au_2PAH nanostructures in the presence of avidin, respectively. 51

Figure 3.1. Chemical structures of TTC-A and ACPA.......... 58

Figure 3.2. Chemical structures of the hydrophilic monomers PEGA and AA and representation of the chemical structure of the macroRAFT agent. *R* depends on the monomer used. 58

Figure 3.3. Chemical structures of MMA and BA. 60

Figure 3.4. Chemical structures of block copolymers derived from (left) $P(PEGA_{40})$-TTC and (right) $P(AA_{40})$-TTC, and photographs of the corresponding latex. 60

Figure 3.5. UV-Vis spectra and (*insets*) photographs of polymer/Au nanocomposites prepared via *post-modification* strategy. Polymer/Au nanocomposite prepared with (A) copPEGATTC and (B) copAATTC. . 62

Figure 3.6. SEM images, in transmission mode, of polymer/Au nanocomposites prepared via *post-modification* strategy. Polymer/Au nanocomposites prepared using (A) copPEGATTC and (B) copAATTC. 63

Figure 3.7. UV-Vis spectra of *is*-copPEGATTC/Au nanostructures, varying (A, B and C) copPEGATTC and $HAuCl_4$ concentration and (C and D) pH. The *insets* show the corresponding photographs of the colloids... 66

Figure 3.8. SEM image, in transmission mode, of *is*-copPEGATTC/Au nanocomposites, after stirring, prepared using the ratio $[HAuCl_4]/[copPEGATTC]$=6 at pH=4. 66

Figure 3.9. (A) UV-Vis spectra and (B) the corresponding photographs of *is*-copAATTC/Au nanocomposites, after stirring, varying the copAATTC concentration. (C) UV-Vis spectra and (*inset*) the corresponding photographs of *is*-copAATTC/Au nanocomposites shown in A and B, after being precipitated by centrifugation and redispersed (*washed*) and the supernatant, respectively. 68

Figure 3.10. (A) UV-Vis spectra and (B) the corresponding photographs of *is*-copAATTC/Au nanocomposites, after stirring, varying pH. (C) UV-Vis spectra and (*inset*) the corresponding photographs of *is*-copAATTC/Au nanocomposites shown in A and B, after being precipitated by centrifugation and redispersed (*washed*) and the supernatant, respectively. 69

Figure 3.11. SEM images, in transmission mode, of *is*-copAATTC/Au nanostructures prepared at (A) pH 4 and (B) pH 8.......... 70

Figure 3.12. (A1, B1, C1) Conductivity and (A2, B2, C2) DLS measurements as a function of concentration of (A) $P(PEGA_{40})$-TTC, (B) $P(AA_{40})$-TTC and (C) $P(AA_{20}$-co-$PEGA_{20})$-TTC, prepared in ultra-pure water. In A1, B1 and C1 the intensity counts (kcps) from DLS measurements are also overlapped. 72

Figure 3.13. Zeta potential and pH measurements of (A) $P(PEGA_{40})$-TTC, (B) $P(AA_{40})$-TTC and (C) $P(AA_{20}$-co-$PEGA_{20})$-TTC, prepared in ultra-pure water. 73

Figure 3.14. Photographs of the resulting colloids after stirring overnight. The ratio $[HAuCl_4]:[MR]$ is 5.9 for pAATTC and 6.9 for pPEGATTC and pAAPEGATTC. 76

Figure 3.15. (A) UV-Vis spectra of colloids preparedusing $P(AA_{40})$-TTC at pH 7 after stirring overnight and (B) the corresponding photographs. (C) UV-Vis spectra of colloids prepared using $[HAuCl_4]$:[MR] ratios of 13.7 and 6.9, C1 and C2 respectively, after being centrifuged. 77

Figure 3.16. UV-Vis spectra and photographs of colloids prepared with (A) $P(PEGA_{40})$-TTC and (B) $P(AA_{20}$-*co*-$PEGA_{20})$-TTC after stirring overnight. (*dash lines*) UV-Vis spectra of the MR agents at the concentration used in the preparation of the Au NPs (0.022 mM and 0.043 mM).......... 79

Figure 3.17. UV-Vis spectra of colloids prepared using $P(AA_{20}$-*co*-$PEGA_{20})$-TTC, at pH 3. *Insets* show the photograph of the colloid after one night and 3 weeks. 80

Figure 3.18. SEM images, in transmission mode, of colloids after 4 weeks of synthesis. Colloids prepared at pH 3 using P(AA_{20}-*co*-$PEGA_{20}$)-TTC: (A*) [HAuCl$_4$]:[pAAPEGATTC]*=6.9 and (B) *[HAuCl$_4$]:[pAAPEGATTC]*=13.8. 81

Figure 3.19. (A) Photographs and (B, C) UV-Vis spectra of Au NPs generated in the presence of P($PEGA_{40}$)-TTC varying *[HAuCl$_4$]:[MR]* ratios over four weeks. UV-Vis spectra (B) after one night and (C) after 4 weeks. 82

Figure 3.20. UV-Vis spectra of Au NPs generated varying the ratio *[HAuCl$_4$]:[pPEGATTC]* over four weeks. (*solid line*) colloid before centrifugation; (*dash line*) precipitate redispersed; and (*dot line*) supernatant of centrifugation. 83

Figure 3.21. SEM images, in transmission mode, of Au NPs generated using the ratio *[HAuCl$_4$]:[pPEGATTC]*=18.5. (A) after one night and (B) after 4 weeks. 84

Figure 3.22. SEM images, in transmission mode, of Au NPs generated using the ratio *[HAuCl$_4$]:[pPEGATTC]*=9.2. (A) after one night and (B) after 4 weeks. 85

Figure 3.23. SEM images, in transmission mode, of Au NPs generated using the ratio *[HAuCl$_4$]:[pPEGATTC]=6.1*. (A) after one night and (B) after 4 weeks. 86

Figure 3.24. SEM images, in transmission mode, of Au NPs generated using the ratio *[HAuCl$_4$]:[pPEGATTC]=4.6*. (A) after one night and (B) after 4 weeks. 87

Figure 3.25. SEM images, in transmission mode, of Au NPs generated using the ratio *[HAuCl$_4$]:[pPEGATTC]=3.7*. (A) after one night and (B) after 4 weeks. 88

Figure 3.26. (A) UV-Vis spectra and (B) SEM image, in transmission mode, of copolymerized Au NPs generated using the ratio *[HAuCl$_4$]:[pPEGATTC]*=9.2........ 90

Figure 3.27. (A) UV-Vis spectra and (B) SEM image, in transmission mode, of copolymerized Au NPs generated using the ratio *[HAuCl$_4$]:[pPEGATTC]*=6.1........ 91

Figure 3.28. (A) UV-Vis spectra and (B) SEM image, in transmission mode, of copolymerized Au NPs generated using the ratio *[HAuCl$_4$]:[pPEGATTC]=3.7*........ 91

Figure 3.29. UV-Vis spectra of (A) *gf*-PEGATTC@Au, (B) *gf*-AATTC@Au and (C) *gf*-AAPEGATTC@Au nanocomposites prepared (A1, B1, C1) below the CMC and (A2, B2, C2) above the CMC. 95

Figure 3.30. SEM images, in transmission mode, of (A) *gf*-PEGATTC@Au, (B) *gf*-AATTC@Au and (C) *gf*-AAPEGATTC@Au nanocomposites prepared (A1, B1, C1) below the CMC and (A2, B2, C2) above the CMC. 96

Figure 3.31. UV-Vis spectra of *gf*-copPEGATTC@Au NPs prepared by adding the mixture of monomers (*M*) in one shot at the beginning and in a controlled way during the polymerization. 98

Figure 3.32. SEM images, in transmission mode, of *gf*-copPEGATTC@Au NPs prepared by adding the mixture of monomers (A) in one shot at the beginning and (B) in a controlled way during the polymerization. 98

Figure 3.33. UV-Vis spectra of (A) *gf*-copPEGATTC@Au, (B) *gf*-copAATTC@Au and (C) *gf*-copAAPEGATTC@Au nanocomposites prepared (A1, B1, C1) below the CMC and (A2, B2, C2) above the CMC........ 100

Figure 3.34. SEM images, in transmission mode, of (A) *gf*-copPEGATTC@Au, (B) *gf*-copAATTC@Au and (C) *gf*-copAAPEGATTC@Au nanocomposites prepared (A1, B1, C1) below the CMC and (A2, B2, C2) above the CMC. *Insets*: secondary electrons and/or transmission imaging showing in detail some core@shell nanoparticles. 102

Figure 4.1. *%Conversion* of AA and PEGA during the synthesis of the MR agent P(AA_2-b-$PEGA_{40}$)-TTC. 109

Figure 4.2. Preparation of *N3*-MR agent by esterification reaction between the carboxyl group from the MR agent and the hydroxyl from the 3-azido-1-propanol........ 110

Figure 4.3. ATR-FTIR spectra of MR agent P(AA_2-*b*-$PEGA_{40}$)-TTC before and after functionalization with the azide moiety. 110

Figure 4.4. ^{1}H-NMR spectra of MR agent P(AA_2-*b*-$PEGA_{40}$)-TTC before and after functionalization with the azide moiety. (*inset*) Chemical structure of the *N3*-MR agent. 111

Figure 4.5. *%Conversion* during the copolymerization of MMA:BA (10:1 w/w) in the presence of P($PEGA_{40}$)-TTC, using initiators ACPA and VA-044 at 70ºC. 112

Figure 4.6. GPC-SEC chromatograms of P($PEGA_{40}$)-*b*-(MMA-*co*-BA)$_n$-TTC copolymers prepared with ACPA or VA-044 at 70ºC. 114

Figure 4.7. *%Conversion* during the copolymerization of MMA:BA (10:1 w/w) in the presence of P($PEGA_{40}$)-TTC using the initiator VA-044 at 44ºC, varying the pH, [MR]/[initiator] ratio and polymerization time. *Inset* shows an amplification of the first 8h of polymerization. 115

Figure 4.8. GPC-SEC chromatograms of P($PEGA_{40}$)-*b*-(MMA-*co*-BA)$_n$-TTC copolymers prepared with the initiator VA-044 at 44ºC, varying the pH, [MR]/[initiator] ratio, and polymerization time. 116

Figure 4.9. (A*) %Conversion* and (B) GPC-SEC chromatograms of the copolymerization of MMA:BA (10:1 w/w) in the presence of P(AA_2-*b*-$PEGA_{40}$)-TTC using the initiator ACPA at 70ºC and VA-044 at 44ºC. At pH= 8 and *[MR]/[initiator]*=9. 117

Figure 4.10. UV-Vis spectra of Au nanostructures before and after emulsion copolymerization at 44ºC. Au nanostructure (A) without and (B) with azide function. 119

Figure 4.11. SEM images (transmission mode) of Au nanostructures prepared with (A) MR agent and with (B) the mixture 2MR:1 *N3*-MR agents. (A1 and B1) before and (A2 and B2) after emulsion copolymerization. (B2-*inset*) secondary electron imaging showing in detail the shell@core nanostructure. 120

Figure 4.12. Preparation of alkylated biotin. 121

Figure 4.13. Schematic representation of biotinylation of *N3*-copolymer@Au NPs via *click chemistry* reaction. 122

Figure 4.14. Visible spectra of copolymer@Au NPs and *biotin*-copolymer@Au NPs in the presence of Avidin and BSA. The spectra were normalized at 450nm. 123

Figure 4.15. Visible spectra of copolymer@Au NPs and *N3*-copolymer@Au NPs after "*click*" reaction with alkylated biotin, $CuSO_4$ and sodium ascorbate, in the presence of BSA and/or Avidin. The spectra were normalized at 450nm. 124

Figure 4.16. Visible spectra of copolymer@Au NPs submitted to the *click chemistry* reaction, and with several washing steps performed by centrifugation, in the presence of BSA or Avidin. 125

Figure 4.17. Chemical structure of the copolymer P($PEGA_{40}$)-*b*-(MMA-*co*-BA)$_n$-TTC. 126

Figure 4.18. Langmuir surface pressure-area isotherms of the copolymers after RAFT emulsion copolymerization of MMA:BA (10:1 w/w) in the presence of P($PEGA_{40}$)-TTC at 70ºC, using ACPA and VA-044. 128

Figure 4.19. Langmuir surface pressure-area isotherms of the copolymers after RAFT emulsion copolymerization of MMA:BA (10:1 w/w) in the presence of P($PEGA_{40}$)-TTC using VA-044 at 44ºC, during 22h and 53h, and at 70ºC during 4h. 129

Figure 4.20. Comparison of Langmuir surface pressure-area isotherms of the copolymer derived from the MR agent P(AA_2-b-$PEGA_{40}$)-TTC and P($PEGA_{40}$)-TTC prepared at 70ºC using ACPA. 129

Figure 4.21. Compression/expansion cycles of the copolymer P($PEGA_{40}$)-b-(MMA-co-BA)$_{168}$-TTC prepared using VA-044 at 70ºC during 4h. 130

Figure 4.22. Langmuir surface pressure-area isotherms of the copolymer P($PEGA_{40}$)-b-(MMA-co-BA)-TTC (VA-044 at 70ºC) mixed with biotin before spreading and using ultra-pure water as subphase or an avidin solution (0.5mg/L in ultra-pure water). 131

Figure 4.23. Langmuir surface pressure-area isotherm of P(PEGA$_{40}$)-b-(MMA-co-BA)-TTC (VA-044 at 70ºC, 4h) mixed with biotin, using avidin solution as subphase and varying the contact time before barriers compression starts. 132

Figure 4.24. Preparation of fluorescent monomer (AEM-FITC). 133

Figure 4.25. UV-Vis and PL spectra of AEM-FITC. 134

Figure 4.26. Visible and PL spectra (λ_{ex}=495 nm) of the aliquots withdrawn during the copolymerization of AEM-FITC after 2h (t_1) and of MMA:BA (10:1 w/w) (after 4h - t_2 and further 2h - t_3) from MR@Au NPs. t_0 corresponds to the mixture of MR@Au NPs with FITC-AEM before placing the reaction vessel at 70ºC. ... 136

Figure 4.27. Visible and PL spectra (λ_{ex}=495 nm) of the aliquots withdrawn during the copolymerization of AEM-FITC and MMA:BA (10:1 w/w) (t_0, t_1, t_2 and t_3) diluted 1:1 (v/v) with PBS (1M, pH=7.4). 136

Figure 4.28. SEM images, in transmission mode, of the aliquots withdrawn during the preparation of the fluorescent copolymer@Au NPs. A) t_0, B) t_1, C) t_2 and D) t_3. (*insets*) corresponding SEM images. 138

Figure 4.29. STEM images of aliquot t_3 of fluorescent copolymer@Au NPs (A) in transmission mode and *insets* in transmission and secondary electrons imaging; and (B) an amplification in transmission, Z contrast and secondary electrons imaging. 138

Figure 4.30. SEM images in Z contrast mode of (A) 1stCE-copolymer@Au NPs and (B) 2ndCE-copolymer@Au NPs, at different magnifications. 141

Figure 4.31. Visible spectra and PL spectra (λ_{ex}=495 nm) of Au NPs, MR@Au NPs and copolymer@Au NPs with one chain extension step (1stCE-copolymer@Au NPs). 142

Figure 4.32. Visible spectra and PL spectra (λ_{ex}=495 nm) of copolymer@Au NPs with one and two chain extension steps. (* after the second chain extension the precipitate colloid was redispersed in half of the volume). 143

Figure 4.33. PL spectra (λ_{ex}=495 nm) of copolymer@Au NPs with one and two chain extension steps diluted (1:1 v/v) with PBS (1M, pH 7.4). 143

Figure 4.34. Visible and PL spectra (λ_{ex}=495 nm) of *biotin*-copolymer@Au NPs in the presence of avidin and BSA. The visible spectra were normalized at 450nm. 145

Figure A.1. Example of ^{1}H-NMR spectra showing the assignments for the vinylic protons of the monomer and the assignment for 1,3,5-trioxane, used as internal standard. The spectra of the aliquot t_0 and the aliquot withdrawn after 4h of polymerization are presented. 197

Figure A.2. %Conversion profile of (A) P(PEGA$_{40}$)-TTC and (B) P(AA$_{40}$)-TTC determined by H^1-NMR. 198

Figure B.3. Evolution the copolymerization of P(PEGA$_{40}$)-TTC followed by determination of *%Conversion* by gravimetric analysis and DLS measurements. 200

Figure B.4. Evolution the copolymerization of P(AA$_{40}$)-TTC followed by determination of *%Conversion* by gravimetric analysis and DLS measurements. 200

Figure C.5. (A1, B1, C1) DLS and (A2, B2, C2) zeta potential and pH measurements in function of concentration of (A) P(PEGA$_{40}$)-TTC, (B) P(AA$_{40}$)-TTC and (C) P(AA$_{20}$-co-PEGA$_{20}$)-TTC, at pH between 7.5 and 8.0. 201

Figure D.6. UV-Vis spectra and (*inset*) photographs of colloids prepared at pH=7 using (A) P(PEGA$_{40}$)-TTC and (B) P(AA$_{20}$-*co*-PEGA$_{20}$)-TTC over 4 weeks. 202

Figure E.7. Adsorption studies of P(PEGA40)-TTC onto Au NPs. (square) samples prepared with the same concentration of Au NPs (1.2x10-9 mol NPs/L) increasing MR concentration and, (circle and triagle) two samples with the same MR concentration (0.16mM) varying Au NPs concentration: 2.1x10-10 mol NPs/L and 1.4x10-10 mol NPs/L, respectively. 203

Figure E.8. UV-Vis spectra of redispersed precipitates prepared for the adsorption studies of P(PEGA40)-TTC onto Au NPs. (A) samples prepared with the same concentration of Au NPs (1.2x10-9 mol NPs/L) increasing

MR concentration and, (B)) two samples with the same MR concentration (0.16mM) varying Au NPs concentration: 2.1x10-10 mol NPs/L and 1.4x10-10 mol NPs/L, respectively. 204

Figure E.9. Adsorption studies of P(AA_{40})-TTC onto Au NPs, dispersed in water (pH~4), at pH 7.7 and MR dispersed in citrate buffer (pH 7.4). 204

Figure E.10. UV-Vis spectra of redispersed precipitates prepared for the adsorption studies of P(AA_{40})-TTC onto Au NPs. (A) MR dispersed in water (pH~4), (B) at pH 7.7 and (C) MR dispersed in citrate buffer (pH 7.4). 205

Figure G.11. ^{1}H-NMR of alkylated biotin in DMSO-d_6. (* EDC residues). 207

Figure H.12. ^{1}H-NMR of AEM-FITC in D_2O. 208

Figure H.13. (A) Ionization equilibria of fluorescein and the pH-dependent spectra of fluorescein: B1) absorption spectra, B2) emission spectra. Adapted from [219]. 209

Figure I.14. STEM images of 2ndCE-copolymer@Au NPs in (A) transmission, (B) secondary electron and (C) Z contrast mode detection. 210

LIST OF TABLES

Table 1.1 Combination of “click chemistry” with RAFT polymerization using “clickable” RAFT agents 35

Table 1.2 Combination of “click chemistry” with RAFT polymerization using “clickable” monomers 37

Table 3.1. Theoretical and experimental data of *%Conversion*, molecular weight and degree of polymerization (DP) of MR agents, determined by H^1-NMR. 59

Table 3.2. Theoretical and experimental data of *%Conversion*, molecular weight and degree of polymerization (DP) of block copolymers, determined by gravimetric analysis and GPC-SEC. 60

Table 3.3. DLS and zeta potential measurements of the block copolymers* 61

Table 3.4. DLS measurements of polymer/Au nanocomposites. 64

Table 3.5. Results of critical micelle concentration (CMC) determination. 74

Table 3.6. DLS measurements of Au NPs generated using the ratio $[HAuCl_4]:[pPEGATTC]$=18.5. 84

Table 3.7. DLS measurements of Au NPs generated using the ratio $[HAuCl_4]:[pPEGATTC]$=9.2. 85

Table 3.8. DLS measurements of Au NPs generated using the ratio $[HAuCl_4]:[pPEGATTC]$=6.1. 86

Table 3.9. DLS measurements of Au NPs generated using the ratio $[HAuCl_4]:[pPEGATTC]$=4.6. 87

Table 3.10. DLS measurements of Au NPs generated using the ratio $[HAuCl_4]:[pPEGATTC]$=3.7. 88

Table 3.11. Summary of the average diameter determined by SEM images, before and after RAFT emulsion copolymerization from MR@Au NPs. 92

Table 3.12. Experimental conditions for the adsorption of MR onto Au NPs, below and above CMC. 94

Table 3.13. $d_{average}$ from DLS measurements of *gf*-copPEGATTC@Au NPs. 97

Table 3.14. $d_{average}$ from DLS measurements before and after emulsion copolymerization. 101

Table 4.1. Theoretical and experimental data of gravimetry and GPC-SEC analysis of block copolymers P($PEGA_{40}$)-*b*-(MMA-*co*-BA)$_n$-TTC prepared with ACPA or VA-044 at 70ºC. 113

Table 4.2. Theoretical and experimental data of gravimetry and GPC-SEC analysis of block copolymers P(PEGA$_{40}$)-*b*-(MMA-*co*-BA)$_n$-TTC prepared with VA-044 at 44ºC. 116

Table 4.3. Theoretical and experimental data of gravimetry and GPC-SEC analysis. Copolymers were prepared with P(AA$_2$-*b*-PEGA$_{40}$)-TTC using ACPA at 70ºC and VA-044 at 44ºC. 117

Table 4.4. λ_{LSPR} and $d_{average}$ Au nanostructures, without and with azide function, before and after emulsion copolymerization at 44ºC. 119

Table 4.5. λ_{LSPR} values of copolymer@Au NPs and *N3*-copolymer@Au NPs after "*click"* reaction in the presence of BSA and/or avidin. 124

Table 4.6. Mean molecular area at surface pressure = 0 mN/m (MMA$_0$) for the copolymer P(PEGA$_{40}$)-b-(MMA-co-BA)-TTC (VA-044 at 70ºC) mixed with biotin before spreading and using ultra-pure water as subphase or an avidin solution. 131

Table 4.7. DLS and zeta potential measurements of the aliquots withdrawn during the preparation of the fluorescent copolymer@Au NPs. 135

Table 4.8. DLS measurements of Au NPs after MR agent adsorption and emulsion copolymerization from MR@Au NPs. 140

Table 6.1. Experimental conditions for the synthesis of the macroRAFT agents. 161

Table 6.2. Experimental conditions for the synthesis of the block copolymers. 162

Table 6.3. Experimental conditions for the generation of Au NPs in the presence of P(PEGA$_{40}$)-*b*-(MMA-*co*-BA)$_{140}$-TTC. 163

Table 6.4. Experimental conditions for the generation of Au NPs in the presence of P(AA$_{40}$)-*b*-(MMA-*co*-BA)$_{160}$-TTC. 164

Table 6.5. Experimental conditions for the generation of Au NPs in the presence of P(AA$_{40}$)-TTC. 164

Table 6.6. Experimental conditions for the generation of Au NPs in the presence of P(PEGA$_{40}$)-TTC. 165

Table 6.7. Experimental conditions for the generation of Au NPs in the presence of P(AA$_{20}$-*co*-PEGA$_{20}$)-TTC. 165

Table 6.8. Experimental conditions for the generation of Au NPs in the presence of P(PEGA$_{40}$)-TTC. 165

Table 6.9. Experimental condition for the copolymerization of MMA:BA (10:1 w/w) from MR@Au NPs. 166

Table 6.10. Experimental conditions the preparation of *gf*-MR/Au NPs colloids, below and above CMC. 167

Table 6.11. Experimental conditions for the copolymerization of MMA:BA (10:1 w/w) from MR@Au NPs. 168

Table 6.12. Experimental conditions for the synthesis of the P(AA$_2$-b-PEGA$_{40}$)-TTC 169

Table 6.13. Experimental conditions for the copolymerization of MMA:BA (10:1 w/w) from P(PEGA$_{40}$)-TTC using VA-044 as initiator. 170

Table 6.14. Experimental conditions for the copolymerization of MMA:BA (10:1 w/w) from P(AA$_2$-*b*-PEGA$_{40}$)-TTC using ACPA or VA-044 as initiators. 171

Table 6.15. Experimental detail to prepare Langmuir monolayers of copolymers derived of P(PEGA$_{40}$)-TTC and P(AA$_2$-b-PEGA$_{40}$)-TTC. 174

Table B.1. Experimental formulation for the copolymerization of P(AA$_{40}$)-TTC. 199

Table B.2. Calculation of the dry latex in each aliquot. 199

Table B.3. Calculation of the *dry polymer* and *%conversion*. 200

CHAPTER 1. General Introduction

Part of this chapter was published in *Colloid and Polymer Science* (2014) Biofunctionalisation of colloidal gold nanoparticles via polyelectrolytes assemblies, 292: 33-50.

1.1. Introduction

Nanotechnology and Nanoscience are areas that have attracted a great deal of interest within the scientific community namely because nanomaterials (typically materials with at least one dimension from 1 to 100 nm) have distinct properties/characteristics from their bulk analogues. The great diversity of inorganic nanoparticles (e.g. quantum dots, carbon-based materials, metal oxides and noble metal nanoparticles) and the possibility to modify and functionalize their surface allows a wide range of applications, namely in (bio)applications. [1, 2]

In particular gold nanoparticles (Au NPs) have been exhaustively studied due to the Localized Surface Plasmon Resonance (LSPR) that is very sensitive to the size, shape and the surrounding environment (such as interparticle interaction and surface modification), which make these NPs of high interest in bioapplications, namely biosensing applications. However, the use of nanoparticles in such bioapplications requires their surface modification in order to confer colloidal stability and specific functionalities. There are already a large number of publications regarding the modification and functionalization of NPs, even so these topics continue to be a challenge namely regarding multifunctionality, specificity, stability in complex biological medium and biocompability. [3–6]

The main focus of this work was to explore different strategies of surface modification and functionalization of Au NPs with polymers towards biosensing applications. First, a revision regarding the optical properties, synthesis and stabilization of Au NPs will be presented which is followed by an overview of available routes to prepare Au nanostructures also comprising polymers.

1.2. Gold nanoparticles

1.2.1. Optical properties of gold nanoparticles

Gold nanoparticles (Au NPs) have been exhaustively studied for applications in biomedicine, biosensing, imaging and therapy due to their biocompatibility, dimensions, easy of characterization and surface modification mainly due to their optical properties associated with the Localized Surface Plasmon Resonance (LSPR) [3, 7–9].

The LSPR results from the interaction between the electromagnetic radiation and the Au nanoparticle which results in an oscillation frequency of the conduction electrons forming a dipole, as shown in Figure 1.1, resulting a strong absorption of light in the visible spectrum that explains the colour of the colloidal solutions. The LSPR of Au NPs is influenced by the size and shape of particles, by the refractive index of the surrounding medium and the distance between neighbouring nanoparticles [7, 10–12]. For instance, Au nanospheres (NSs), as represented in Figure 1.1-A, show one band in the visible spectrum, typically at 520 nm. However, Au nanorods (NRs) (Figure 1.1-B) show one band (transversal band) as similar to the NSs corresponding to the electron oscillation along the short axis (diameter) and one band (longitudinal band) in the visible/near-infrared region corresponding to the electron cloud oscillation along the long axis.

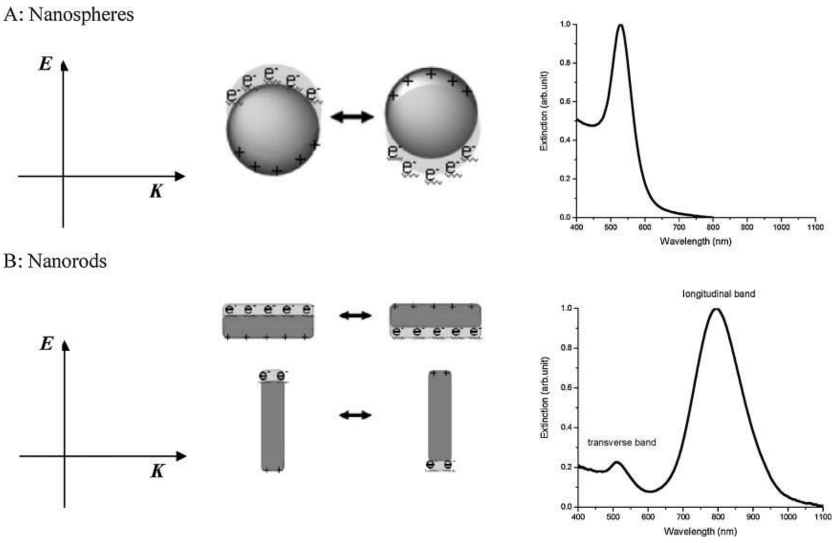
A: Nanospheres
E
K
e⁻
+
Extinction (arb.unit)
0.0
0.2
0.4
0.6
0.8
1.0
400
500
600
700
800
900
1000
1100
Wavelength (nm)
B: Nanorods
E
K
longitudinal band
transverse band
Extinction (arb.unit)
Wavelength (nm)

Figure 1.1. Schematic illustration of the interaction of polarized light and gold nanospheres (A) and nanorods (B) to form the electronic coherent localized surface plasmon resonance (LSPR) oscillation [10]**.**

Moreover, the size of the Au NSs and NRs also has influence on the location of the LSPR band. For Au NSs, by increasing the nanoparticles diameter shifts the LSPR to higher wavelengths as shown in Figure 1.2-A [11]. In the case of Au NRs, increasing the aspect ratio (AR = length/width) shifts the longitudinal band to higher wavelengths, in some cases reaching the near-infrared region (Figure 1.2-B) [12].

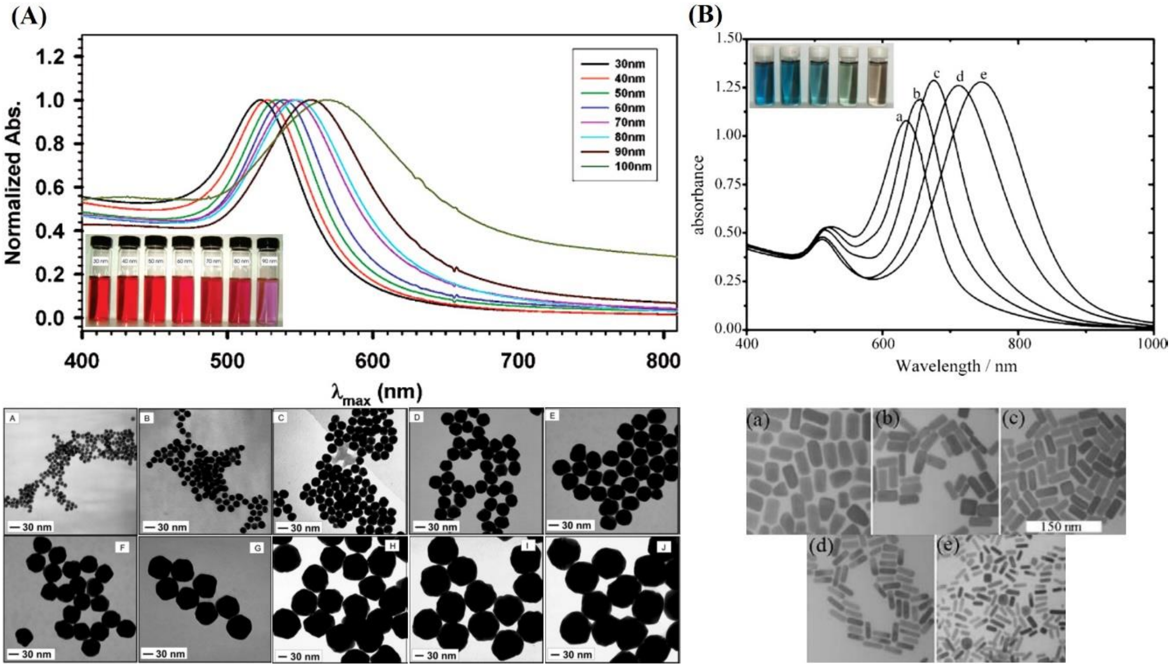

Figure 1.2. Absorbance spectra, photographs and TEM micrographs of gold nanospheres with different sizes (A) and gold nanorods with different aspect ratios (B). Adapted from Zhong *et al.* 2007 [11] **and Pérez-Juste *et al.* 2005** [12]**, respectively.**

As mentioned before, Au NPs due to their optical properties associated to the LSPR are very interesting and largely studied for bioapplications, namely biosensing application. The LSPR allows the use of Au NPs to monitor interactions between an analyte and the specific receptor, because Au NPs aggregation results in changes on the LSPR band. Indeed, this phenomenon can be observed by visual inspection: Au NSs dispersed in water present a red colour, but when aggregation is induced the colour changes to purple or blue depending on the aggregation state. Examples of the use of this property include the recognition of a specific DNA strand, as well as protein-ligand systems, for example avidin-biotin, which will be later revised (***1.2.3.***).

Additionally the presence of a fluorophore within the vicinity of Au NPs might experience fluorescence quenching which is a phenomenon attributed to FRET (Förster resonance energy transfer) as well as NSET (Nanoparticle Surface Energy Transfer), in which the latter results from distances nearly twice as far as FRET [13–17]. These phenomena further potentiate the use of Au NPs in biosensing. In FRET effect, the emission spectrum of the donor overlaps with the absorption spectrum of the acceptor resulting in several vibronic transitions in the donor that have practically the same energy as the corresponding transitions in the acceptor. In conventional FRET the critical distance between donor and acceptor (e.g. using organic dyes) is up to 10 nm. However, this phenomenon between a dye and a NP has been described to allow energy transfer within larger distances due to the so called NSET. For distances between 2-30 nm an efficient energy transfer occurs between the dye and the NP, while for longer distances (> 50 nm) the energy transfer can suffer oscillations [17–21]. As a result, this fluorescence quenching effect can be used to monitor receptor/ligand binding and release events through changes in fluorescence intensity or lifetime of the fluorophore, reflecting binding and unbinding states of analytes to sensors [19, 22–25], which will also be reviewed below (***1.2.3.***).

1.2.2. Synthesis and stabilization of colloid gold nanoparticles

There are several well-established methods to synthesize Au NPs, most of them are based on the reduction of a gold (III) salt using a reducing agent in the presence of a stabilizing agent which leads to different sizes and shapes in aqueous or organic medium. Well-known and established methods have been largely used but, with the increasing interest in Au NPs, several novel methods have been reported, using reducing agents that can also work as stabilizers to obtain different coatings and that are more environmentally friendly reagents [26–28]. The most relevant methods that have been reported regarding the synthesis of Au NSs will be presented, and some methods to prepare anisotropic nanoparticles will be briefly reviewed.

Gold nanospheres

The most popular method for synthesizing Au NSs is the citrate method introduced by Turkevich *et al.* [29], which involves Au NSs formation by the reduction of boiling tetrachloroauric acid ($HAuCl_4$) with sodium citrate ($Na_3[(COO)_3C_3H_5O]$) in aqueous medium. The citrate method allows control over the average particle diameter within a wide range (~10–50 nm) varying the concentration ratio between the gold salt and the sodium citrate. This method yields NSs stabilized by the citrate anion adsorbed at the surface of NPs conferring a negative charge to the Au NSs thus, providing colloidal stability in aqueous medium due to repulsive electrostatic forces of the particles surface double-layers [30, 31]. Monodisperse and quasi-spherical NPs with higher diameters, up to 300 nm, can also be synthesized via a seeded growth method using the citrate-Au NPs as seeds [32, 33].

Smaller NPs can be synthesized by the method discovered by Brust and Schiffrin in 1994 [34], also known as the two-phase synthesis. $HAuCl_4$ is transferred from aqueous solution to organic medium (e.g. toluene) via a phase-transfer reagent and reduced with aqueous sodium borohydride in the presence of a long chain thiol (e.g. dodecanethiol) yielding highly stable hydrophobic thiol capped Au NSs. In this case, the different sizes are obtained by varying the alkanethiol:$HAuCl_4$ molar ratio from 0:1 (8 nm) to 2:1 (2 nm), although the mechanism is not well understood, increasing the amount of alkanethiol the NPs size decreases independently of the amount of reducing agent. [35] For bioapplications aqueous stable Au NSs are required and therefore methods of phase exchange are particularly relevant. Noteworthy, hydrophobic Au NSs can be transferred from organic to aqueous medium using for example DMAP (4-(dimethylamino)pyridine) which acts as stabilizer and transfer agent [36, 37]. Methods using borohydride as a reducing agent in one-phase synthesis, namely aqueous medium, have also been reported but unlike the Turkevich method a stabilizing agent is required. Usually, ligands with a thiol group are used as stabilizer and the NSs size can be controlled by varying the ratio between the ligand, the Au(III) species and the reducing agent [38, 39]. Also, sodium citrate can be used in this case only as stabilizer since it does not reduce Au (III) extensively at room temperature [40]. However, others groups reported the synthesis of aqueous stable Au NSs using borohydride as a reducing agent without the addition of a stabilizing agent during the synthesis, in this case the reaction pH is 8 [41, 42].

In fact, $HAuCl_4$ can be hydrolyzed depending on the pH of the solution, as schematized in *equation 1*, forming other gold (III) complexes, in this case with OH^-, which has influence in the UV-Vis spectrum, as shown in Figure 1.3. [43]

$$[AuCl_4]^- \xrightarrow{increasing\ pH} [AuCl_x(OH)_{4-x}]^- \qquad (equation\ 1)$$

$$(pH\ between\ 2.9 -\ 5.0{:}\ x = 2 - 4; pH\ between\ 6.2\ and\ 10.3{:}\ x = 0 - 1)$$

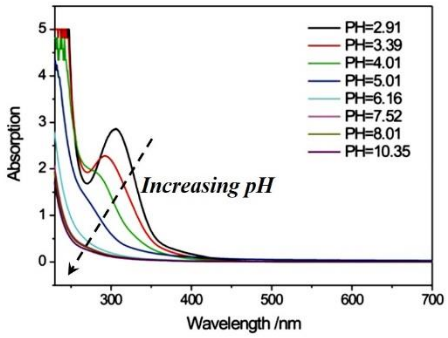

Figure 1.3. UV-Vis spectra of $HAuCl_4$ at various pH. Adapted from [43]**.**

The same authors [43] have reported that different Au(III) species have different chemical reactivity with direct impact on the nucleation and growth of Au NPs. For instance $[AuCl_4]^-$ and $[AuCl_3(OH)]^-$ are more easily reduced than $[AuCl(OH)_3]^-$ and $[Au(OH)_4]^-$. The authors reduced the $HAuCl_4$ at different pH values using ascorbic acid as a reducing agent and sodium benzenesulfonate as a protecting agent. At lower pH values, the nucleation was fast leading to smaller NPs with narrower size distributions. In contrast, at higher pH values, nucleation occurred slowly and growth of a less number of nuclei occurs, resulting in bigger NSs with larger size distributions. The influence of pH on the particle size distribution and evolution of Au NSs had already been studied by Peng *et al.* [44] by using sodium citrate as reducing agent. As summarized in Figure 1.4, the authors reported that at low pH values (pH < 6.5) the nucleation is fast, aggregation of the Au nuclei occurs forming wire-like NPs, which is followed by intraparticle ripening leading to spherical NPs. However, using high pH values (pH > 6.5) the nucleation occurs slowly as well as the growth, thus leading to NSs with narrower size distribution.

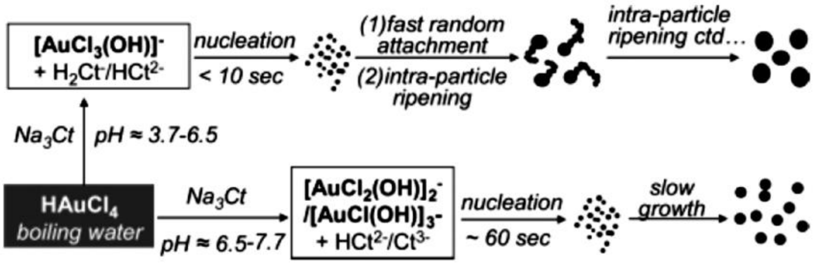
[AuCl3(OH)]-
+ H2Ct-/HCt2-
nucleation
< 10 sec
(1)fast random attachment
(2)intra-particle ripening
intra-particle ripening ctd…
Na3Ct
pH ≈ 3.7-6.5
HAuCl4
boiling water
Na3Ct
pH ≈ 6.5-7.7
[AuCl2(OH)]2-
/[AuCl(OH)]3-
+ HCt2-/Ct3-
nucleation
~ 60 sec
slow growth

Figure 1.4. Schematic illustration of two reaction pathways for synthesis of gold nanocrystals by citrate reduction. [44]

On the other hand, Yang *et al.* [45] using both citrate and borohydride anions as reducing agents have reported that the concentration of chloride ions also has a major influence on the Au NSs size. The authors argued that by increasing the Cl^-concentration aggregation of the primary NSs is promoted, due to the decrease of surface charge, leading to bigger NSs. Actually, controlling the pH and the Cl^-concentration, NSs with diameters in the range of 19 to 47 nm could be obtained using sodium citrate as reducing agent. Also, varying the Cl^-concentration NSs with diameters from 3 to 12 nm can be obtained using sodium borohydride as reducing agent.

In summary, the size of Au NSs can be controlled by varying not only the reducing agent but also several parameters such as the [stabilizer]:[Au(III)]:[reducing agent] ratio, Cl^-concentration, pH and temperature.

Anisotropic gold nanoparticles

Au NPs with morphologies, such as rods, prisms, wires and stars, have also been explored in order to get different optical properties. In the last years, several works were published reporting the controlled generation of Au NPs with the morphologies mentioned before, however the mechanism to promote the anisotropic growth is not fully understood. In general, the anisotropic growth occurs from Au(0) seeds usually prepared using the borohydride method ($d < 10$ nm), which are placed in a growth solution containing Au(III), a soft reducing agent (e.g. ascorbic acid) and shape-directing agent. The latter has been largely studied and it was found that halide counterions (Cl^-, Br^- and I^-) play an important role in shaping the different Au NPs morphologies. [46, 47]

For example, NPs with rod shape (NRs) have been prepared using the seed-mediated growth method introduced by Murphy *et al.* 2001 [48] which was later improved, in order to obtain a better control over the AR and thus allowing the synthesis of NRs with higher AR [49–51]. The first step of this method concerns the preparation of gold seeds (1.5 – 5 nm in diameter) using borohydride as reducing agent and then the seeds are mixed with a growth solution. The growth solution contains gold (III) salt, ascorbic acid, the surfactant CTAB (hexadecyltrimethylammonium bromide) and in some cases $AgNO_3$. The ascorbic acid is used as reducing agent but since it is a mild reducing agent it only promotes the growth, i.e. further nucleation events are not promoted. CTAB is used as stabilizing agent but most importantly it is used as a soft template for the rod shape. CTAB has preferential adsorption for the {110} or {100} faces that exist along the length of the NR, so in these faces deposition of gold is blocked and the growth is promoted in the {111} direction. Additionally the presence of silver ions helps the shape induction. According to Murphy *et al.* Ag^+ is adsorbed at the Au NPs surface in the form of AgBr restricting the growth in that specific facet (Br^- ions come from the CTAB). It is worth to note in this case Ag NPs are not generated [48–52]. A review about the parameters that influence the growth of Au NRs can be found in [53]. Although controversial, the presence of bromide ions seems to be essential to control the synthesis of Au NRs. Nevertheless, the synthesis of monodispersed Au NRs using bromide-free surfactants has also been described [54].

1.2.3. Biosensing applications of gold nanoparticles

As mentioned before, the leading interest of Au NPs in bioapplications is mainly due to the LSPR, which is very sensitive to variation of the surrounding environment, including the state of aggregation of the NPs and their behaviour in the presence of fluorophores. More specifically, these features allow the use of gold NPs in systems to identify specific (bio)analytes that induce the aggregation of NPs or, induce or cancel fluorescence (quenching fluoresce effect) in the presence of a fluorophore. These systems can be used in the identification of a specific strand of DNA, antibody-antigen or proteins-ligand [5, 8, 55–58].

For example, biosensors based on the LSPR allow the identification of biomolecules such DNA and proteins because when aggregation of Au NPs is induced due to specific recognition, the LSPR band shifts and the color changes from red to blue-purple (precipitation may also occur) [59–62]. Figure 1.5 shows a schematic representation of a biosensing based on the LSPR.

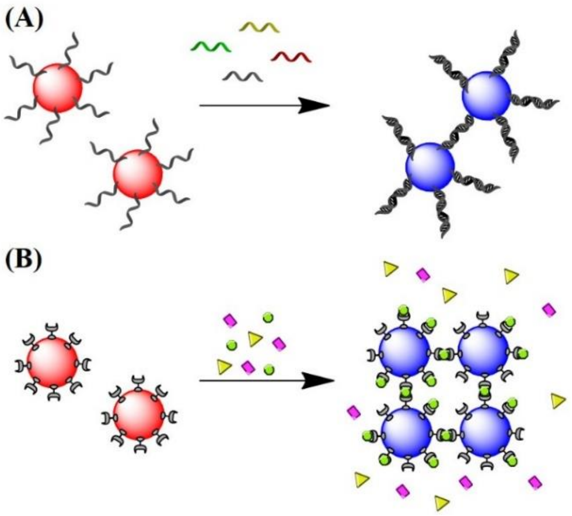

Figure 1.5. Schematic representation of Au NPs biosensor based on LSPR. Specific recognition of DNA (A) and of a specific ligand (B).

Regarding biosensing based on fluorescence quenching, the fluorescence intensity is dependent on the distance between the Au NP (quencher) and the fluorophore. Specific recognition of the biomolecules changes this distance allowing their identification [19, 22–25, 56, 63], as schematized in Figure 1.6.

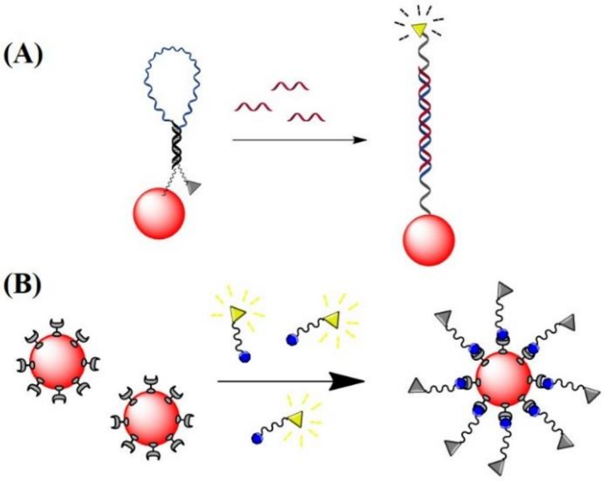

Figure 1.6. Schematic representation of Au NPs biosensor based on quenching fluorescence. Specific recognition of DNA (A) and of a specific ligand (B).

1.2.4. Surface modification and functionalization of colloidal gold nanoparticles

Typically, nanoparticles are synthesized in a medium containing a stabilizing agent however, additional surface modification is necessary to ensure adequate stabilization and functionalization of nanoparticles allowing their application in areas such as pharmaceutical, biomedical diagnosis, drug deliver and gene delivery [3, 64]. The functionalization of NPs is an area of major interest due to the possibility of controlling the chemical behaviour of the NPs, namely the surface charge and functional groups (e.g. carboxyl or amine groups) which in turn allows the labelling of the NPs with molecules, such as antibodies or DNA.

In the case of the citrate method, the reducing agent also acts as a stabilizer (citrate ions) but in other methods, a stabilizing agent is added during the Au NPs synthesis to avoid agglomeration and precipitation. For example, DMAP (4-(dimethylamino)pyridine) that confers positive charge [65] or thiol ligands (Figure 1.7-A). Thiol groups are well known to have high affinity to gold surfaces because gold is a soft Lewis acid and thiol containing molecules are soft bases. Therefore, thiol ligands such as sodium 10-mercaptodecanesulfonate [66] or polymers containing thiol groups can also be used as stabilizers. Others polymers namely polyelectrolytes can be used for surface modification via electrostatic interactions [66–71], see Figure 1.7-B. Regarding the functionalization of the NPs with biomolecules (Figure 1.7-C) two main strategies can be used. One involves electrostatic interactions between surface charged Au NP and charged biomolecule and the other one involves formation of covalent bonds between functional group at the surface of Au NP and functional groups of the biomolecules. Alternatively, a biomolecule modified with a thiol group is directly used for ligand exchange providing, in one step, stability and functionalization. This last strategy is commonly used for functionalization of DNA [59, 72].

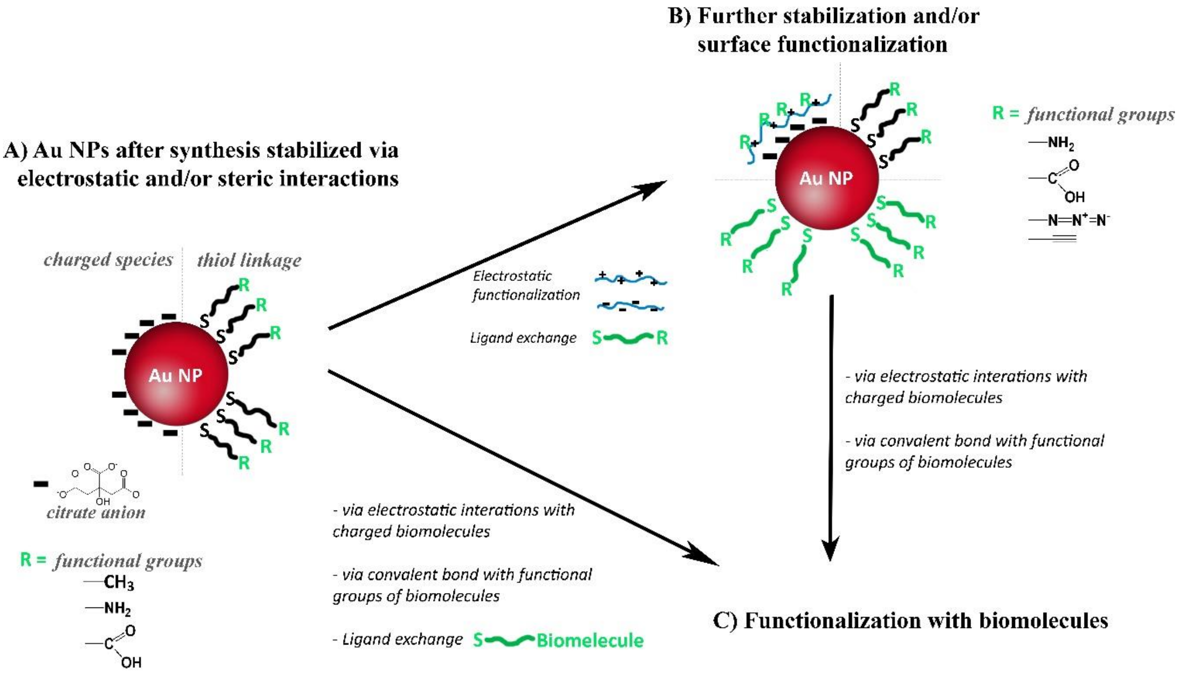
B) Further stabilization and/or surface functionalization
R = functional groups
—NH2
—C(=O)OH
—N=N+=N-
Au NP
A) Au NPs after synthesis stabilized via electrostatic and/or steric interactions
charged species
thiol linkage
Au NP
S
R
citrate anion
R = functional groups
—CH3
—NH2
—C(=O)OH
Electrostatic functionalization
Ligand exchange
S
R
- via electrostatic interations with charged biomolecules
- via convalent bond with functional groups of biomolecules
- via electrostatic interations with charged biomolecules
- via convalent bond with functional groups of biomolecules
- Ligand exchange
S
Biomelecule
C) Functionalization with biomolecules

Figure 1.7. Schematic representation of surface stabilization and or functionalization of Au NPs, followed by surface (bio)functionalization.

There is a large number of publications regarding the surface modification and functionalization of Au NPs. Amongst those the use of polymers has received considerable interest because this type of materials not only offer the possibility to prepare stable, robust and multifunctional polymeric shells keeping the optical properties of the Au core, but also the polymeric shell can be responsive to an external stimulus, such as pH or temperature. [73, 74] Having in mind the objective of this thesis two strategies will be reviewed here. The first strategy encompasses the use of polyelectrolytes combined with the Layer-by-Layer method (***1.3.***). The second strategy is based on the reversible-deactivation radical polymerization (RDRP), specifically reversible addition fragmentation chain transfer (RAFT) polymerization (***1.4.***).

1.3. Layer-by-Layer method to prepared colloidal gold nanostructures via electrostatic interactions

The *Layer-by-Layer* (LbL) method for the deposition of ionic polymers (polyelectrolyte, PE) through electrostatic self-assembly was first described for the surface modification of microparticles [75]. It is an easy and simple method that is based on the sequential deposition of PE layers via electrostatic interactions, so the deposition of a PE layer (e.g. positive charge) is followed by the deposition of a layer with opposite charge (negative charge). Washing steps are performed between each deposition step in order to remove excess of polyelectrolyte. The deposition cycles can be repeated until the required number of layers is obtained, as shown in the Figure 1.8. The final result is a multi-layered stratified shell which can be multifunctional, i.e. each layer can provide a specific function to the nanostructure.

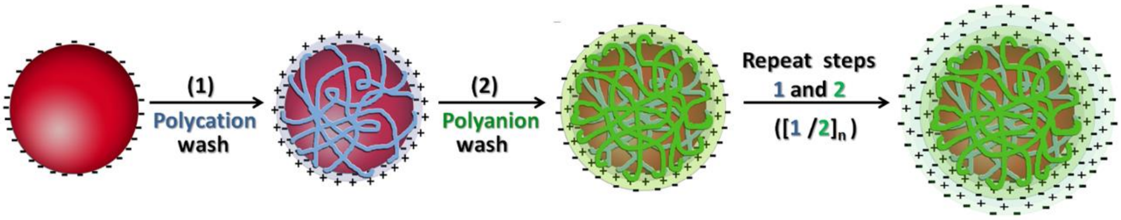

Figure 1.8. Surface modification of nanoparticles using PE treatment (*n* represents the number of cycles). [76]

This method was extended to Au NPs by Caruso *et al* [77], which because of their size led to several drawbacks due to their high surface curvature which can limit the adsorption of the PE layer. In fact, the LbL method and the parameters that influence the electrostatic assembly of the PE layers onto Au NPs was recently reviewed by us [76]. Accordingly, it was established that the final stability of the well-coated PE@Au (shell@core) nanostructures depends on several parameters: the particle size (surface curvature), concentration and surface charge density of Au NPs, the PE molecular weight and the nature of the repeating units (e.g. amine and its pKa), the molar ratio between the PE and the Au NPs and the pH and ionic strength of the medium. For instance, PE with low molecular weight should be used avoiding bridging between coated particles which in turn leads to agglomeration and aggregation. [76]

The easy implementation of this method and its versatility regarding the use of a wide range of polyelectrolytes makes this method a powerful technique to modify and functionalize Au NPs. Moreover, the thickness of the polymer shell as well as the chemical function and surface charge can be tailored, which are features of major relevance for bioapplications. In addition, another advantage of this technique is the possibility to (bio)functionalize each layer, with a (bio)receptor, drug, fluorophore or an antibody/protein, in order to provide a specific function to the multilayer shell envisaging a specific (bio)application of the Au nanostructure. [76]

The LbL method driven by electrostatic interactions has also been implemented for the preparation of films incorporating several charged materials. [78–80]. This method was firstly applied on the preparation of films by Decher *et al*. [81, 82]. Due to its simplicity and versatility a wide variability of materials have been explored for the preparation of well-ordered nanostructured functional films. Examples of those materials are polyelectrolytes, water-soluble proteins, enzymes, DNA, charged polysaccharides, charged inorganic nanoparticles thus, enabling the preparation of new and easier handling devices that can be used for example as biosensors. [69, 83–87]

1.4. RAFT polymerization in the preparation of gold nanostructures

Reversible addition fragmentation chain transfer (RAFT) polymerization is a reversible-deactivation radical polymerization (RDRP) that has proven to be a powerful and versatile mechanism in the preparation of polymers with well-controlled molecular weights and architectures and consequently it has been widely studied [88, 89]. Here, some general polymerization concepts (***1.4.1.***) and specifically the RAFT polymerization mechanism (***1.4.2.***) is first reviewed. Then the preparation of polymer/Au nanocomposites using RAFT polymerization is presented (***1.4.3.***). Finally, the use of "click chemistry" in connection with the functionalization of the polymer/Au nanostructures prepared via RAFT polymerization is surveyed (***1.4.4.***).

1.4.1. Polymerization concepts

Polymers are macromolecules formed by repeating units covalently bonded, named monomers. Polymers can be classified regarding their composition and structure. Homopolymers are composed by just one type of repeating unit whilst on the other hand, copolymers have at least two types of repeating units [88, 90, 91]. As the complexity of the polymer increases, more difficult or even impossible is its synthesis via conventional polymerization mechanisms. Fortunately, in the last decades new mechanisms, namely *reversible-deactivation radical polymerization* (RDRP), have been developed and improved in order to be possible the synthesis of new polymers with new composition and architectures and consequently new applications. [88, 89]

Polymerizations can be carried out using different techniques. In *bulk polymerization*, monomers are not diluted in solvents and the initiator should be soluble in the monomer. The advantage of this technique is that the resulting polymer is pure however, during the polymerization the viscosity increases hindering chain termination and dissipation of heat can lead to autoacceleration which can be dangerous namely for large scale production. In the case of *solution polymerization*, monomer and initiator are dissolved in a non-reactive solvent and the resulting polymer is also soluble in this solvent. This technique can solve the problem of bulk polymerization but at the same time has some drawbacks, such as the presence of impurities in solvents which can inhibit or retard the polymerization, chain transfer to solvent and also environmental problems since organic solvents are used. Furthermore, to obtain the pure polymer the solvent should be removed [90, 91].

Regarding multiphasic systems (e.g. two liquid phases), polymerization can be performed in *suspension*, *emulsion* or *miniemulsion*. Usually, one is the continuous phase – water and the other phase corresponds to the monomer or monomer dissolved in an organic medium. In *suspension polymerization* a stabilizer is used and the initiator is water insoluble. The stabilizer has the function to form a protective shell around the polymer particles (beads) during their formation, thus preventing their coagulation and fusion during the polymerization. In this technique polymer particles are produced with diameters ranging from 1 μm to 1 mm. In *emulsion polymerization* an initiator soluble in water and a surfactant are used. The surfactant, above the critical micelle concentration (CMC) allows the formation of nanoreactors suspended in the aqueous phase where the polymerization occurs and provides colloidal stability for the growing particles, yielding a colloidal dispersion of polymer particles known as latex. Water is a key aspect, although it does not participate in the polymerization, as it maintains the low viscosity, provides a good heat transfer and also acts as medium for the diffusion of the monomer. Thus, emulsion polymerization can be divided in three intervals: in interval I (Figure 1.19-I) the surfactant forms micelles with their hydrophobic cores being swollen with the monomer (monomer droplets) and particle nucleation occurs (oligomers formed in the aqueous phase are stabilized by the surfactant); in interval II (Figure 1.19-II) the nucleated particles in the interval I start to grow by diffusion of the monomer from monomer droplets to polymer particles; and in interval III (Figure 1.19-III) occurs exhaustion of the monomer droplets and the remaining monomers in the particle are polymerized. The size of the polymer particles can reach diameters up to 1 μm. *Miniemulsion polymerization* is similar to emulsion polymerization but smaller particles, in the nanometric scale, can be obtained. In this technique, a highly insoluble co-stabilizer is used to avoid Ostwald ripening and the dispersion is sonicated in order to get smaller droplets. Similarly to the suspension polymerization, the particle formation occurs in the droplets nucleation. [90–93]

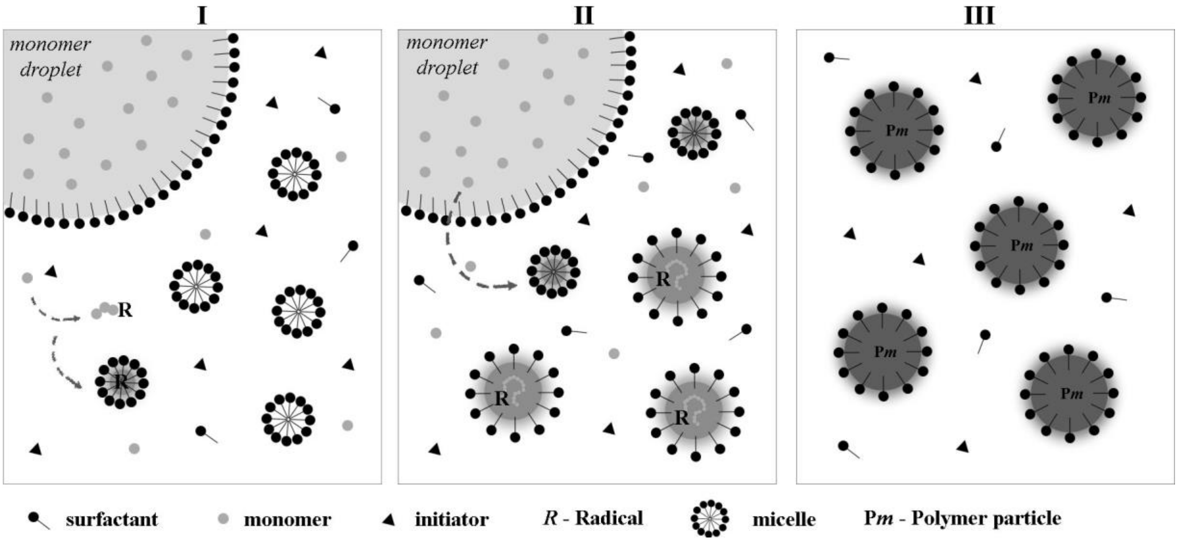

Figure 1.9. Schematic representation of the stages in a typical emulsion polymerization reaction. Adapted from [93]**.**

Concerning the polymerization mechanisms, the chain-growth polymerization, also known as addition polymerization, results from reactions between monomers (usually vinyl monomers) without losses of by-products. This polymerization mechanism occurs via three stages: (1) *chain initiation*, where a reactive species is formed and the polymerization is started; (2) *chain propagation*, once the polymerization is initiated the monomers are added one by one to the active chain and the polymer grows; and (3) *chain termination* is the final step where the polymerization is terminated and the polymer stops growing. The termination involves radical-radical termination which could be due to combination of two growing chains or by disproportion. [88, 90, 91]

Regarding the chain initiation stage, there are several initiators available which also characterize the polymerization: free radical and ionic (cationic and anionic). The choice of the initiator depends of the monomer and the reactions conditions, i.e. while the free radical polymerization can polymerize a large range of monomers in the presence of water and oxygen tolerating impurities, the ionic polymerization requires strict conditions, water and oxygen can not be present in the polymerization reaction for example. The range of monomers is limited and reaction temperature is critical. [88, 90, 91]

In the context of this work only the free-radical addition polymerization will be explored. In conventional free-radical polymerization irreversible termination occurs which prevents polymerization control. Furthermore, block copolymers and polymers with complex structures are difficult or impossible to prepare. Alternatively, polymerization methods that enable control over the molecular weight distribution, structure and architecture of a polymer have been developed. These methods known as RDRP, historically know as *living or controlled radical polymerization* (CRP) [94], have reversible termination. This means that the polymerization stops when all the monomer is consumed and it can be restarted anytime upon addition of more monomer, which allows the synthesis of block copolymers and complex polymer structures, as shown in Figure 1.10. [88, 95] Contrary to the conventional process where chains are continuously propagating and the termination occurs by radical-radical reaction, the RDRP uses reagents that act as polymerization mediators which help propagating radicals whilst the majority of the chains are maintained in a dormant form. Equilibrium between the active and dormant chains is achieved which is fundamental to obtain a linear chain growth, yielding narrower molecular weight distributions. Moreover, the initiation step should be rapid compared to the propagation step [88, 95–98].

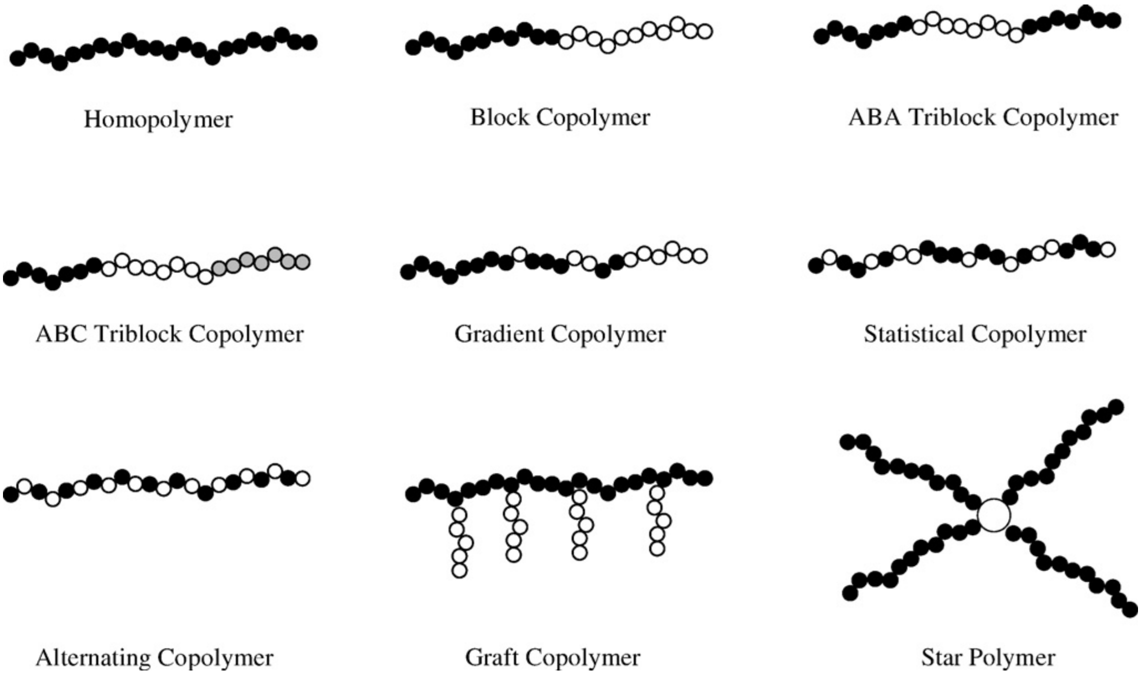

Figure 1.10. Polymer architectures available through RDRP [98]**.**

The most known and widely used RDRP technologies are: *nitroxide mediated polymerization* (NMP), *atom transfer radical polymerization* (ATRP) and *reversible addition fragmentation chain transfer* (RAFT) polymerization. All of these controlled polymerization mechanisms are mediated by a transfer agent which during the propagation step helps to control the equilibrium between the dormant and active species [88, 95]. Amongst these mechanisms, *reversible addition fragmentation chain transfer* (RAFT) polymerization has shown to be the most powerful mechanism due to its versatility associated with mild reaction conditions, no use of transition metals, the possibility of using several types of monomers, including monomers with functional groups (e.g. OH, NR_2, CO_2H, SO_3H, $CONR_2$) and allows well-controlled polymer architectures. Moreover, hydrophilic and amphiphilic polymers can be synthesized which is important for bioapplications [89, 95–98]. Moreover, RAFT polymerization has been successfully used for controlled functionalization of planar surfaces as well as micro- and nano- particles which is of major interest for a wide range of applications [89, 99], namely concerning the aims of this work.

1.4.2. RAFT polymerization concepts

Reversible addition fragmentation chain transfer (RAFT) polymerization was introduced in 1998 by two distinct research groups who described identical mechanisms but using different controlling agents. The Common-wealth Scientific and Industrial Research Organization (CSIRO) in Melbourne, Australia, which gave the name RAFT polymerization [100, 101], and the research group Rhodia Chim, from France, which patented a process that they named *macromolecules design via the interchange xanthates* (MADIX) which use xanthates as controlling agents [102].

The control over the composition and architecture of RAFT polymers depends on the kinetics of the reaction and the elimination/minimization of radical-radical terminations which is due to the use of a chain transfer agent (CTA), also known as RAFT agent. The CTA, with the structure shown in Figure 1.11, confers a “living” character to the polymerization since it mediates the polymerization via reversible chain-transfer process and its efficiency depends on the nature of the groups **X**, **Z** and **R** (Figure 1.11 – **1**). Although CTAs where **X**=CH_2 (Figure 1.11 – **3**) have been used, the most efficient CTA are thiocarbonylthio compounds (Figure 1.11 – **2**). [96, 97, 103]

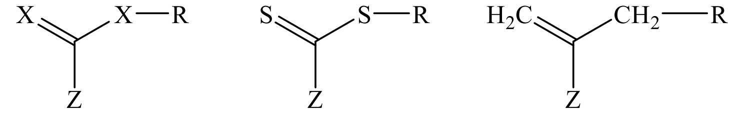

(**1**) (**2**) (**3**)

Figure 1.11. Structure of CTA/RAFT agent.

In turn, the **Z** and **R** groups are crucial for the efficiency of the addition-fragmentation reactions. The **Z** group controls the reactivity of the C=S double bond, influencing the rate of radical addition and fragmentation. The **R** group is the radical leaving group which also has to be able to reinitiate the polymerization for chain transfer. For an ideal RAFT agent, see Figure 1.12, the dormant species should have a reactive C=S double bond, the intermediate radical should fragment rapidly and give no side reaction and lastly radicals (**R**$^\bullet$) should efficiently re-initiate polymerization [89, 96, 97, 99, 103–105].

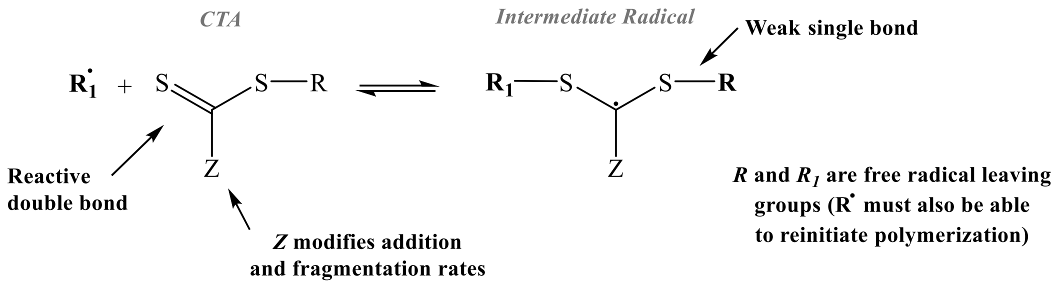
CTA
Intermediate Radical
Weak single bond
R₁• + S S—R
R₁—S S—R
Z
Z
Reactive double bond
Z modifies addition and fragmentation rates
R and R₁ are free radical leaving groups (R• must also be able to reinitiate polymerization)

Figure 1.12. Structural features of thiocarbonylthio RAFT agent and intermediate formed on radical addition. Adapted from [96]**.**

The most commonly used CTAs are the thiocarbonylthio compounds, with a general structure **Z-**(C=S)-S-**R** (e.g. dithioesters, xanthates, dithiocarbamates and trithiocarbonates **-** Figure 1.13), which have been used for the synthesis of different homopolymers and copolymers. Moad *et al.* 2005 and 2006 [96, 97] summarized a wide range of these CTAs that were used until then, and Lowe *et al.* 2007 [104] focus on CTAs used in the synthesis of water-soluble copolymers.

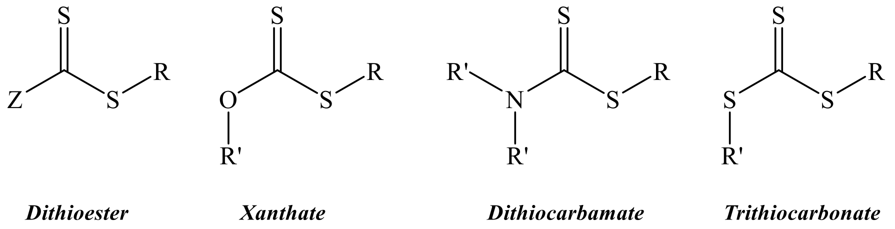
Dithioester
Xanthate
Dithiocarbamate
Trithiocarbonate

Figure 1.13. Generic structures of RAFT chain-transfer agents.

The choice of the CTA is a key aspect for a successful RAFT polymerization and it depends not only on the properties of the **R** and **Z** groups but also on the monomer that will be polymerized, as well as reactions conditions. Indeed, Moad *et al.*[96, 97] related the efficiency of the **Z** an **R** groups in the polymerization of some monomers such as methyl methacrylate (MMA), vinylacetate (Vac), styrene (S), methyl acrylate (MA), acrylamide (AM), and acrylonitrile (AN), see a resume in Figure 1.14.

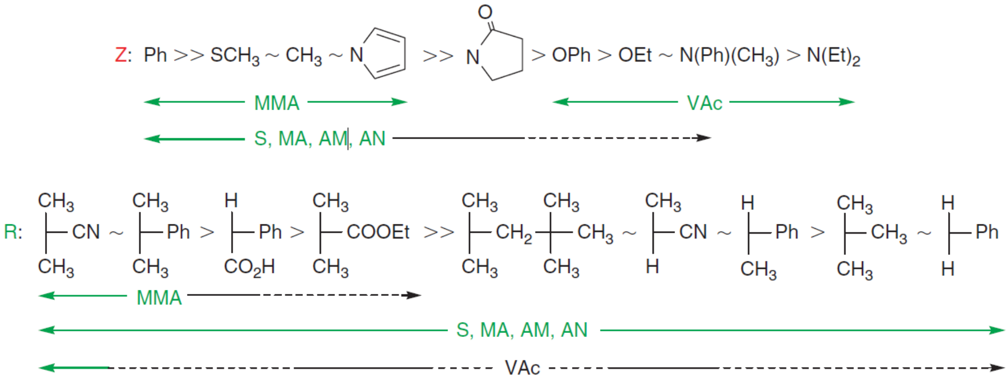
Z: Ph >> SCH3 ~ CH3 ~ N
>> N > OPh > OEt ~ N(Ph)(CH3) > N(Et)2
MMA
VAc
S, MA, AM, AN
R:
CN ~ Ph > Ph > COOEt >> CH2 CH3 ~ CN ~ Ph > CH3 ~ Ph
MMA
S, MA, AM, AN
VAc

Figure 1.14 Guidelines for selection of RAFT agents for various polymerizations. For Z, addition rates decrease and fragmentation rates increase from left to right. For R, fragmentation rates decrease from left to right. Dashed line indicates partial control (i.e. control of molecular weight but poor polydispersity or substantial retardation in the case of VAc) [96]**.**

The RAFT polymerization mechanism is based on a cycle of active and dormant chains, as can be observed in Figure 1.15- **I** and **II**. First occurs the initiation step where a polymeric active chain (**$P_n^{\bullet}$**) is formed. Then the primary radical formed reacts with the CTA forming an intermediate radical. In turn, this intermediate radical suffers fragmentation resulting in a dormant polymeric chain (which contains the –S-C(=S)-**Z** of the CTA) and a radical specie (**$R^{\bullet}$**). The radical species reacts with monomer (M) to form an active polymeric chain (**$P_m^{\bullet}$**). The rapid equilibrium between the propagating radical (active chain) and the macroCTA (dormant chain) is fundamental to control the molecular weight, as well as to ensure that the concentration of dormant chains is greater than the active chains. [89, 96–99, 104]

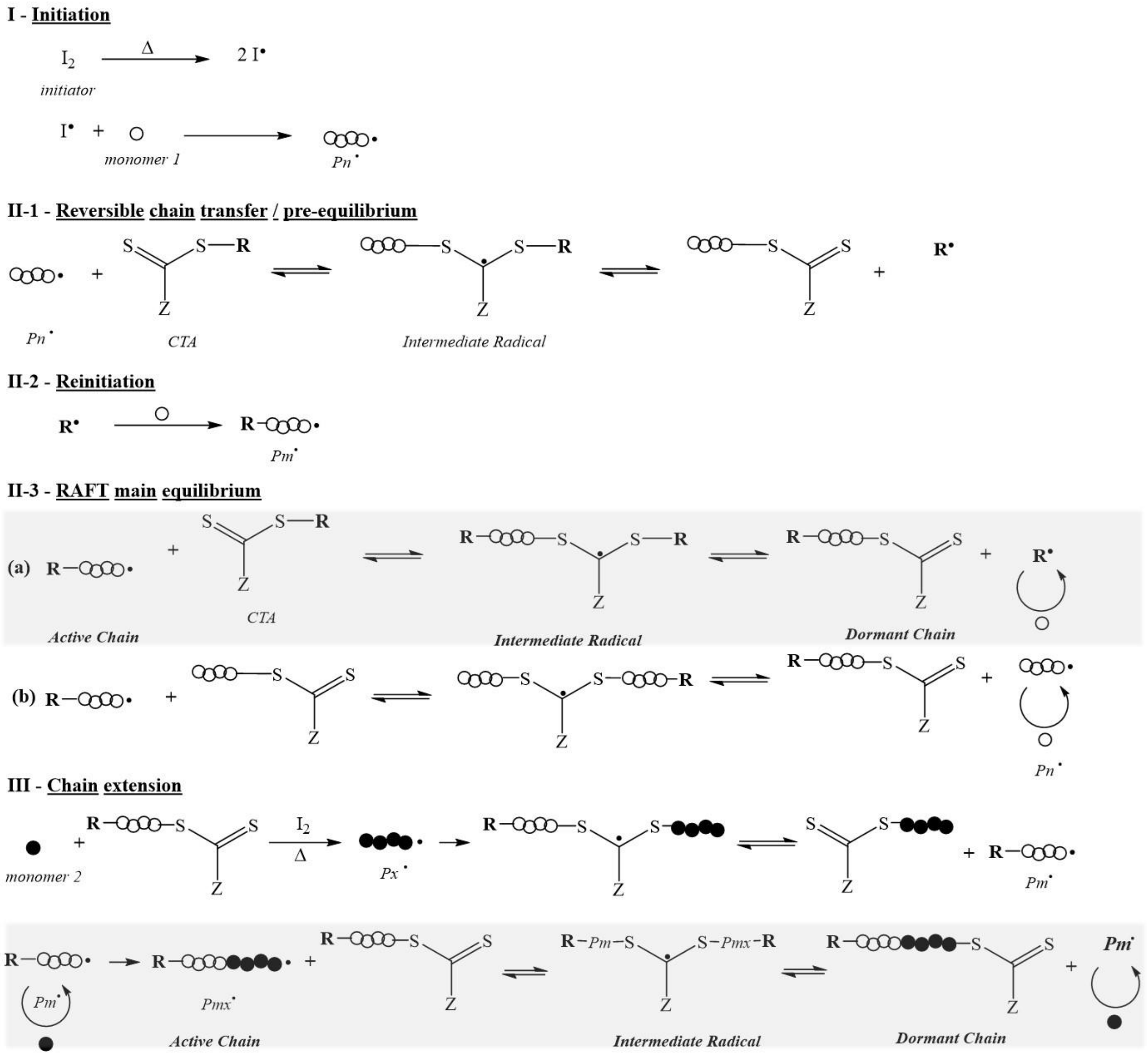
I - Initiation
I2
Δ
2 I•
initiator
I• + ○
monomer 1
Pn•
II-1 - Reversible chain transfer / pre-equilibrium
S
S—R
Z
CTA
Intermediate Radical
R•
II-2 - Reinitiation
R•
Pm•
II-3 - RAFT main equilibrium
(a)
Active Chain
CTA
Intermediate Radical
Dormant Chain
(b)
Pn•
III - Chain extension
monomer 2
I2
Δ
Px•
Pm•
Pmx•
R–Pm–S
S–Pmx–R
Active Chain
Intermediate Radical
Dormant Chain

Figure 1.15. Proposed mechanism of RAFT polymerization; (I and II) homopolymerization and (III) chain extension of a macroCTA. Adapted from [98]**.**

The molecular weight of chain and its distribution, the composition and the architecture of the resulting polymers can be controlled due to the fact that the termination step is minimized. Suppression, or at least significant reduction of termination is due to the equilibrium that is established between the propagating polymeric chains and a macroCTA, also named macroRAFT agent (i.e. a polymeric chain which contains the CTA). The CTA is preserved in the chain giving a “living” character to the macrochain which can be extended by adding a second monomer, as illustrated in Figure 1.15- **III**. In fact, the resulting macroCTA can be isolated and subsequently used in another batch under other reaction conditions, for instance aqueous medium. [89, 96–98] For example, Destarac *et al.* [106] synthesized the macroRAFT - poly(*n*-butylacrylate) (PBA) and then polymerized the NiPAM obtaining the amphiphilic diblock copolymer PBA-*b*-PNiPAM.

Beyond the high importance on the choice of the RAFT agent, experimental aspects should be also considered. For instance, RAFT polymerization started to be performed in organic medium being compatible with a wide range of organic solvents, but the solubility of the RAFT agent in the solvent should be a concern as well as the hydrolytic sensitivity of some RAFT agents to some solvents. Generally, RAFT polymerization in organic medium can be carried out in a range of temperature from room temperature to 140ºC, usually higher temperatures gives better results but can also promote conventional radical polymerization. Moreover, in RAFT polymerization any source of free radicals can be used as in the conventional radical polymerization. The most used initiators are thermal initiators such as AIBN (2,2'-azoisobutyronitrile), ACPA (4,4′-azobis(4-cyanopentanoic acid)) and $K_2S_2O_8$ (Figure 1.16), however other types of initiation can be used such as UV irradiation, γ-source, plasma field and thermal initiation in the case of styrene. There are additional aspects related to the initiator that need to be taken into consideration: one is the concentration of initiator which is important to achieve a balance between the polymerization rate and dead chains, usually the $[CTA]_0/[I]_0$ ratio is greater than one ensuring that there is a greater number of CTA molecules in solution than free radicals. The other aspect is related to the initiator-derived radical which should be a good leaving group regarding the propagating radical. [89, 96–98]

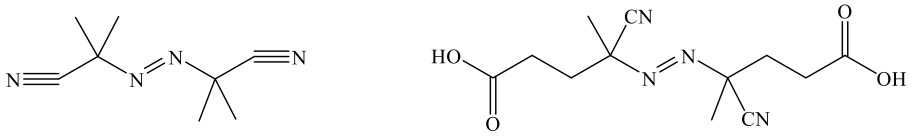

AIBN

ACPA

Figure 1.16. Structure of commonly used initiators in RAFT polymerization.

Another advantage of RAFT polymerization is the possibility to perform the polymerization in aqueous medium contrary to other RDRP mechanisms. Thus it enables polymerization of anionic, cationic, zwitterionic and neutral monomers leading to hydrophilic and functional polymers. In homogenous aqueous polymerization, the RAFT agents that have shown higher versatility are the dithioesters and trithiocarbonates. Concerning the initiators, the most used in aqueous medium are water soluble azo initiators. [89, 98, 104]

The first communication on RAFT polymerization in aqueous solution was reported by McCormick *et al.* 2001 [107] regarding the polymerization of sodium 4-styrenesulfonate using the CTA 4-cyanopentanoic acid dithiobenzoate and ACPA as initiator. Then this homopolymer was used as macroCTA to polymerize in aqueous conditions sodium 4-vinylbenzoate yielding the copolymer poly(sodium 4-styrenesulfonate-*block*-sodium 4-vinylbenzoate). Using a similar methodology, the authors have also prepared a block copolymer of (*ar*-vinylbenzyl)trimethylammonium chloride and

N,*N*-dimethylvinylbenzylamine. In the beginning, RAFT polymerization in aqueous solution showed some drawbacks concerning the hydrolysis of the RAFT agent, as well as the incompatibility of the RAFT agent with some functional groups such as primary and secondary amines, thiols and reducing agents. Later, in 2004, McCormick and Lowe [108] discussed the difficulties of RAFT polymerization in aqueous medium stating that choosing appropriate conditions (i.e. CTA, initiator, monomer, pH, temperature) a successfully water polymerization is possible and control over the molecular weight is achieved. Hence, the *theoretical number-average molecular weight* ($M_{n,\,th}$) and the *theoretical number fraction of living chains* (L) are given by the *equations 2* and *3, respectively* [109].

$$M_{n,th} = \frac{[M]_0 \times M_{monomer} \times \rho}{[CTA]_0 + 2f[I]_0\left(1-e^{-k_d t}\right)\left(1-\frac{f_c}{2}\right)} + M_{CTA} \qquad (\textit{equation } 2)$$

$$L = \frac{[CTA]_0}{[CTA]_0 + 2f[I]_0\left(1-e^{-k_d t}\right)\left(1-\frac{f_c}{2}\right)} \qquad (\textit{equation } 3)$$

Where the $[M]_0$, $[CTA]_0$ and $[I]_0$ are the initial concentration (mol/L) of the monomer, the CTA and the initiator, respectively; the $M_{monomer}$ and M_{CTA} are the molar masses of the monomer and the CTA (g/mol), and the ρ is the monomer conversion; *factor "2"* accounts for the fact that one molecule of azoinitiator yields two primary radicals with the efficiency f; k_d is the decomposition rate constant (s^{-1}) of the azoinitiator and t represents the polymerization time (in seconds); the term "$1 - (f_c/2)$" represents the number of chains produced in a radical– radical termination event with f_c representing the coupling factor (a f_c value of 1 means that all bimolecular terminations occur by combination, whereas a value of 0 indicates that 100% of bimolecular terminations result from disproportionation).

Although, a simplification of the *equation 2* is commonly used, *equation 4*:

$$M_{n,th} = \frac{[M]_0 \times M_{monomer} \times \rho}{[CTA]_0} + M_{CTA} \qquad (\textit{equation } 4)$$

Water soluble copolymers prepared via RAFT polymerization can be synthesized under homogenous conditions (aqueous and organic media) as well as in heterogeneous conditions, namely in emulsion [89, 104]. Despite of the fact that many works have been published using the conventional emulsion technique, RAFT polymerization gives the opportunity to perform RAFT emulsion polymerization without surfactant. This surfactant-free emulsion was firstly reported in 2002 by Hawkett *et al.* [110]. First, the authors polymerized a water soluble monomer (acrylic acid, AA) using the RAFT agent 2-

{[(butylsulfanyl)carbonothioyl]sulfanyl}propanoic acid and the initiator ACPA, in aqueous medium, obtaining $(AA)_x$-RAFT - macroRAFT agent. Then a hydrophobic monomer (butyl acrylate, BA) was polymerized yielding $(AA)_x$-$(BA)_y$-RAFT which forms micelles during the polymerization, where further polymerization can occur. Figure 1.17 shows a schematic representation of surfactant-free emulsion RAFT polymerization.

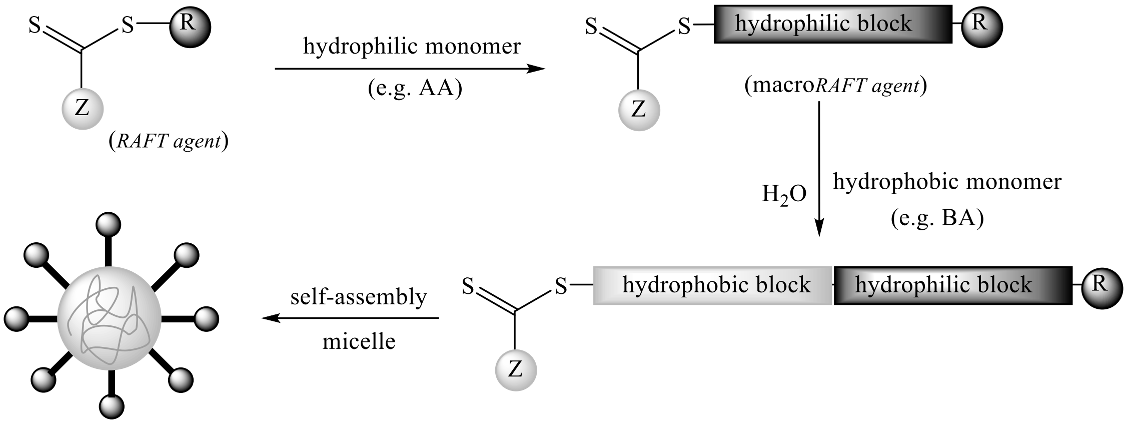

Figure 1.17. Schematic representation of surfactant-free emulsion RAFT polymerization.

This RAFT emulsion polymerization has been explored in the last years, since problems regarding colloidal stability and hydrophobicity/hydrophilicity of the RAFT agent usually were raised. One way to control this drawback was found by carrying the emulsion polymerization under starved conditions, i.e. the monomer is added in a controlled way and no monomer droplets are formed. Alternatively, adjusting the hydrophobicity of the RAFT agent or even the pH, in the case of macroRAFT agents based on acrylic acid, it is possible to control the micellar nucleation and therefore the molecular weight of the polymer particle. [111] For instance, Charleux *et al.* [112] modified the RAFT agent 2-(dodecylthiocarbonothioylthio)-2-methylpropanoic acid (TTC-A) with poly(ethylene oxide) (PEO) with different molecular weights. The authors found that the size of the PEO chain had influence in the polymer particle size independently of the length of the hydrophobic extended chain, in this case *n*-butyl acrylate was polymerized. In addition, RAFT emulsion polymerization allows the preparation of polymeric nano-objects (e.g. spheres, vesicles, fibers) through controlling the experimental conditions, such as pH and hydrophobic monomers, during the chain extension of macroRAFT agent. [113, 114]

1.4.3. Preparation of polymer/gold nanostructures based on RAFT polymerization

Composites are described as materials constituted by distinct components that retain their chemical identity combining their properties which can sometimes result in a synergistic effect. For nanocomposites one of the components should have at least one dimension in the nanometric scale (from 1 to 100 nm). Polymer/gold nanocomposites have been widely explored because of the optical properties of gold NPs (core) can be combined with polymeric shells that in turn can confer robustness, stability, functionality, responsiveness and biocompatibility to the nanocomposite. This leads to new materials for new applications or improving materials for existing applications (Figure 1.18). Additionally, RAFT polymerization allows control over molecular weight, molecular weight distribution, composition and architecture of these novel functional polymer shells.

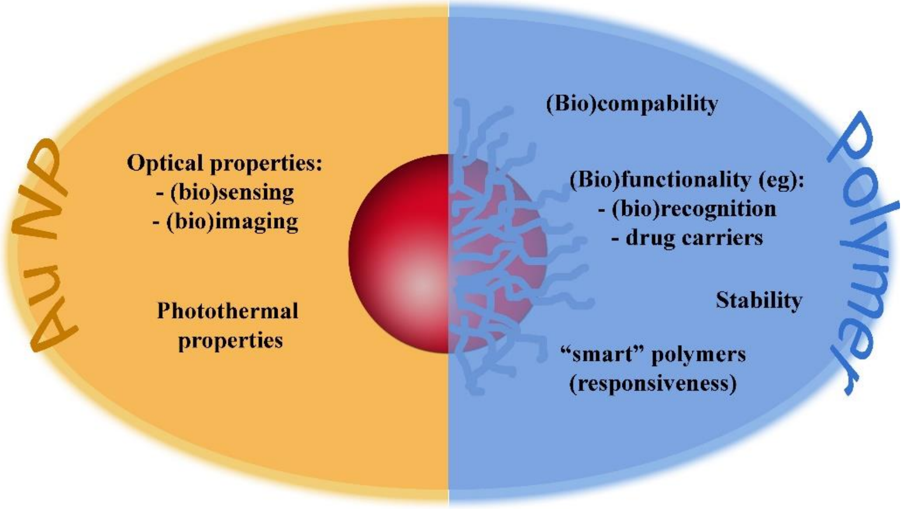

Figure 1.18 Properties and functions of Au NP core and polymer shell on polymer/Au nanocomposite.

The surface modification of inorganic nanoparticles using RAFT polymerization has been explored following four main approaches that are schematized in Figure 1.19. In "*in situ* preparation" and in the "post-modification" or "grafting to" a previously prepared polymer is used (Figure 1.19 top). In the former, NPs are synthesized using an inorganic precursor in the presence of the polymer, whilst in the second strategy the polymer and the NPs are mixed and the polymer chains adsorb or bind covalently onto the NPs surface, respectively. Regarding the other strategies (Figure 1.19 bottom), in "grafting from" the polymerization is carried out from the inorganic surface which is previously functionalized with the polymerization mediator (e.g. CTA) or the initiator. The "grafting through" is not so explored because it requires polymerizable moieties (e.g. vinylic moieties) on the NPs surface [89, 99].

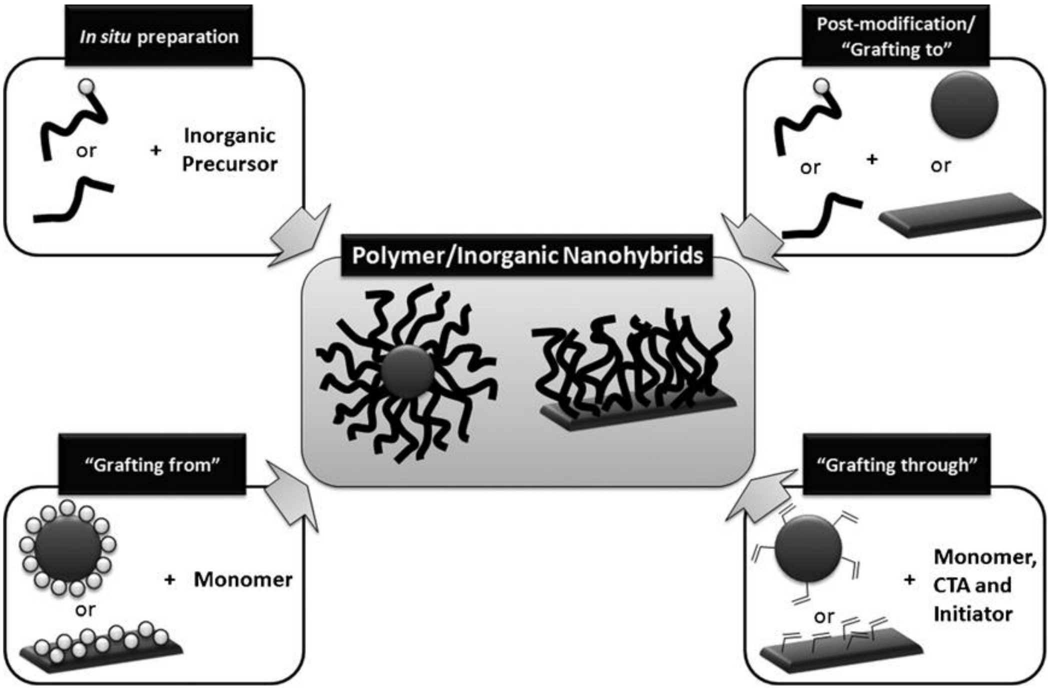
In situ preparation
or
+
Inorganic Precursor
Post-modification/ "Grafting to"
or
+
or
Polymer/Inorganic Nanohybrids
"Grafting from"
+ Monomer
or
"Grafting through"
+
Monomer, CTA and Initiator
or

Figure 1.19. Common preparation methods of polymer/inorganic nanohybrids [99]**.**

In the context of the preparation of polymer/Au nanocomposites, RAFT polymerization presents an advantage related with the use of CTA. CTA is usually a thiocarbonylthio compound, therefore has high affinity to gold surfaces due to the presence of sulfur atoms. Hence, polymers based on di-and tri-thio CTA agents have been used in the surface modification of gold nanoparticles due to the possibility of forming a strong linkage between the polymer and the NP surface [89, 99].

In fact, back in 2003 McCormick *et al.* [115] have reported the immobilization of polymers prepared by RAFT polymerization onto gold films. After the preparation of the polymers, poly(sodium 4-styrenesulfonate), poly((ar-vinylbenzyl)trimethylammoniumchloride), poly(N,N-dimethyl-acrylamide), and poly(3-[2-(N-methylacrylamido)-ethyldimethyl ammonio] propane sulfonate-b-N,N- dimethylacrylamide), the authors reduced the dithioester end group of the CTA to thiol using $NaBH_4$. Then the thiol containing polymers were immobilized onto gold surfaces due to the high affinity of thiol to gold, as depicted in Figure 1.20.

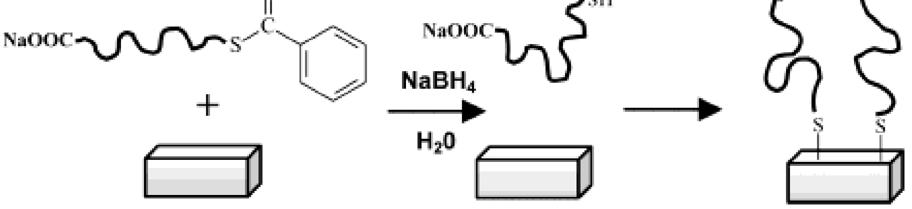
NaOOC
S
S
C
+
NaOOC
SH
NaBH4
H2O
NaOOC
NaOOC
S
S

Figure 1.20. Mechanism describing the immobilization of a RAFT-prepared copolymer onto gold surface [115]**.**

However, in 2006 Fustin *et al.*[116] demonstrated that CTA (dithioesters and trithiocarbonates) are also able to chemisorb onto gold surfaces, consequently their reduction into thiols is not mandatory. This demonstration was very helpful to increase the range of RAFT polymers that can be used for surface modification of gold, since some RAFT polymers are incompatible with $NaBH_4$.

Regarding the four strategies schematized in Figure 1.18, all of them present advantages and disadvantages in the preparation of polymer/Au nanocomposite, which are next presented. The ***post-modification*** or ***grafting to*** is the most easy and straightforward methodology since each component, the inorganic nanoparticle and the polymer, are previously prepared and then mixed together leading to the nanocomposite. So, in this methodology each component is synthesized individually allowing control over the size and shape of the inorganic particle as well as the molecular weight, structure and composition of the polymer [89, 99]. In addition, as mentioned before, chemisorption of the polymer onto Au NPs can be promoted through the thiol group, by removal of the of the RAFT [117–121] or can be carried out maintaining the RAFT agent (di- or tri-thio group), next some examples of the latter are shown. Hydrophilic polymers prepared by RAFT polymerization have been used to coat Au NPs. For example, Davis *et al.*[122] 2010, reported the stabilization of previously prepared Au NPs (*d* = 20 nm) using temperature and pH responsive polymers prepared via RAFT polymerization: poly(2-aminoethylmethacrylamide) (PAEA), poly(acrylic acid) (PAA), poly(N,N-diemthylaminoethyl acrylate) (PDMAEA), poly(oligoethylene oxide) acrylate (P(OEG-A)), poly(oligoethylene oxide acrylate-co-diethylene oxide acrylate) (P(OEG-A-*co*-DEG-A)) and poly(N-isopropyl acrylamide) (PNiPAM). Only the cationic polymers required special care during mixing with Au NPs to avoid aggregation due to the interactions with the citrate anions at the Au NPs surface. Destarac *et al.* coated Au NPs with 8 nm with three polymers synthesized by MADIX/ RAFT polymerization which in aqueous solutions have different behaviors: a cationic polymer, poly[(3-acryl- amidopropyl) trimethylammonium chloride] (PAPTAC), a thermoresponsive polymer PNiPAM, and a pH-responsive polymer PAA [123], and also reported the used of poly(N-vinyl caprolactam) [70]. Klok et al.[124] in 2010 prepared Au NPs with different sizes from 5 nm to 47 nm which then were coated, in aqueous solution, with the polymers poly(ethylene glycol)monomethylether)methacrylate (Mn= 16 800g/mol) and also poly(pentafluorophenyl methacrylate) (Mn= 12 400g/mol synthesized via RAFT polymerization using 4-cyanopentanoic acid dithiobenzoate as CTA [125].

Concerning anisotropic nanoparticles, in 2007 Boyes *et al.*[126] reported the surface modification of gold nanorods with polymers prepared via RAFT. Gold nanorods (*AR* = 10) were firstly synthesized and subsequently modified with hydrophilic polymers poly(2-(dimethylamino)ethyl methacrylate) (PDMAEMA) or poly(acrylic acid) (PAA), in aqueous solution, and with hydrophobic polymer PS in DMF. The authors demonstrated that the polymers were grafted to the Au nanorods surface by the di- or tri-thio group of the RAFT agent but also when these groups were reduced to a thiol, see Figure 1.21.

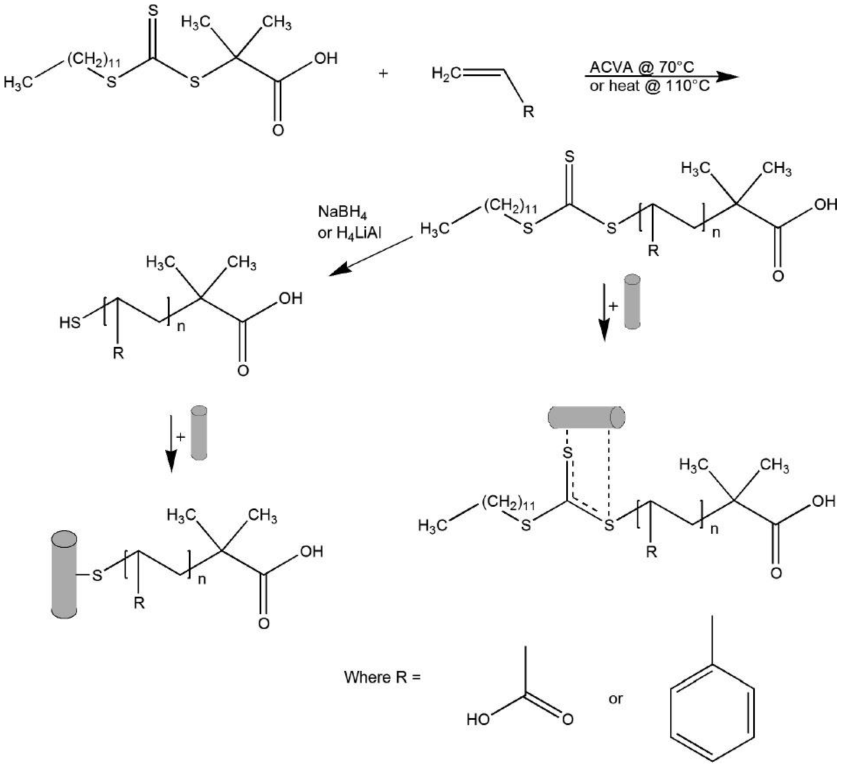

Figure 1.21. Proposed mechanisms describing synthesis, reduction, and immobilization onto a gold surface of RAFT-prepared PAA and PS [126]**.**

Destarac *et al.* [106] 2010 described the stabilization of previously prepared Au NPs (d = 8 nm) using not only hydrophilic polymer (poly(*N*-isopropyl-acrylamide), PNiPAM) but also amphiphilic diblock copolymer prepared by RAFT polymerization – poly(*n*-butyl acrylate-*b*-*N*-isopropyl-acrylamide) (PBA-*b*-PNiPAM). Interestingly, when PNiPAM was used to stabilize the NPs shell@core type NPs were obtained but when PBA_{2k}-*b*-PNiPAM_{8k} was used free polymer globules were also obtained. Actually, this last example demonstrate a disadvantage of the *post-modification* strategy in the preparation of polymer/Au nanocomposites. The amphiphilic block copolymers in aqueous solutions can form well-organized aggregates, such as micelles, depending on their concentration in solution which difficult the adsorption of the polymer onto the Au surface. In fact, what concerns the coating of Au NPs using the amphiphilic block copolymers, the methodology normally involves the use of organic solvents, such as THF or DMF, where this well-organized aggregates are not formed. [127–129]

In situ preparation of this type of nanocomposites seems to be a very simple approach since it occurs in one-pot procedure, i.e. the polymer with the desired molecular weight and structure is prepared and the metal nanoparticles are generated *in situ*, usually using sodium borohydride ($NaBH_4$) to reduce the inorganic precursor. However, this reducing agent can also reduce the dithioester- or trithiocarbonate-end groups of polymer chains leading to a thiol-ended polymer. This method involves several challenges such as the control over the size and shape of the nanoparticles [89, 99]. Nevertheless, in 2002 McCormick *et al*.[130], demonstrated a novel route for the preparation of copolymer stabilized gold nanoparticles via *in situ* preparation. The authors prepared four water soluble copolymers (anionic, cationic, neutral, and zwitterionic (betaine) species): poly(sodium 2-acrylamido-2-methyl propane sulfonate) (PAMPS), poly((*ar*-vinylbenzyl)-trimethylammonium chloride) (PVBTAC), poly(N,N-dimethyl- acrylamide) (PDMAm), and poly(3-[2-*N*-methylacrylamido]-ethyl dimethyl ammonio propane sulfonate-*block*-*N*,*N*-dimethylacrylamide) (PMAEDAPS-*b*-PDMAm). The metal salt ($HAuCl_4$) was mixed with the dithioester end-capped copolymer and after addition of the reducing agent ($NaBH_4$) copolymer-stabilized gold nanoparticles were obtained, as schematized in Figure 1.22. This procedure was also performed using the metal salts $AgNO_3$, $Na_2PtCl_6{\cdot}6H_2O$ and Na_3RhCl_6 resulting in the respective copolymer-stabilized nanoparticles. Here the authors proved that it is possible to synthesize stable metal nanoparticles in the presence of different RAFT polymers but concerning the particle size control studies have not been performed.

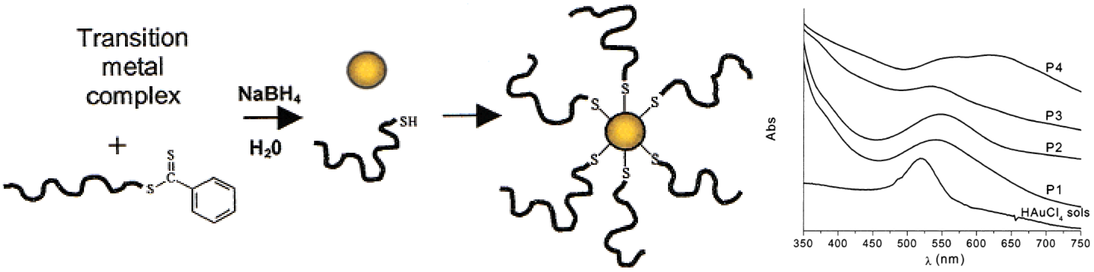

Figure 1.22 (left) Preparation of (co)polymer-stabilized transition metal nanoparticles, (right) UV-Vis spectra for $HAuCl_4$ sols and polymer-stabilized Au- NPs. P1 – PAMPS, P2 – PVBTAC, P3 – PDMA, and P4 - PMAEDAPS-*b*-PDMAm. Adapted from [130]**.**

Kim *et al.* [131] in 2008, prepared poly(ethylene oxide-*b*-N-isopropylacrylamide) by RAFT polymerization of NiPAM using PEO-based RAFT agent, varying the PNiPAM size block. The copolymer was mixed with $HAuCl_4$, in THF, and reduced using $NaBH_4$ dissolved in ethanol, yielding

Au NPs with 5 to 30 nm in diameter regardless the concentration and the length of PNiPAM block. Fan *et al*. [132] in 2011 reported the synthesis *in situ* of Au NPs in DMF using poly(styrene)-*b*-poly(ethylene oxide) (PS-*b*-PEO) block copolymer with a trithiocarbonate group located between the two blocks. The resulting Au NPs presented a diameter between 5 and 10 nm with λ_{LSPR} at 530 nm.

On the other hand, Destarac *et al.* [106] in 2010 reported the *in situ* synthesis of Au NPs, in water at pH= 8, using an amphiphilic diblock copolymer prepared by RAFT polymerization – poly(*n*-butyl acrylate-*b*-N-isopropyl-acrylamide) (PBA-*b*-PNIPAM). First, the authors observed that when a higher amount of polymer was used the reduction of the gold precursor was slower. Also the color of the colloidal solution varied from dark brown to light orange depending on the polymer concentration, as shown in Figure 1.23. This is directly correlated with the size of the Au NPs generated: without polymer d = 6 ± 3 nm; for lower concentration (2.5 x 10^{-3} wt %) d= 8 ± 6 nm, and for higher concentration 1.5 wt % d= 1.6 ± 0.4 nm. Note that the critical aggregation concentration of this copolymer is 3 x 10^{-4} wt %.

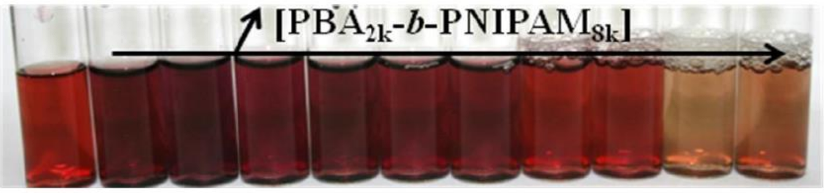

Figure 1.23. Image of the final NPs solutions 5 min after reduction at 20 °C. The polymer concentration increases from left to right (0 to 0.15 wt.%). [106]

In addition, in 2013 Marty *et al*. [133] demonstrated that the molecular weight of the polymer also influences the size of the Au NPs as well as the *end*-group of the polymer. Thereby, the authors prepared PNIPAM by RAFT polymerization with three different molecular weights and then the terminal xanthate group was reduced to a thiol or a hydrogen, as shown in Figure 1.24. An aqueous solution of $HAuCl_4$ was added to the polymer at pH = 8 and reduced with $NaBH_4$.

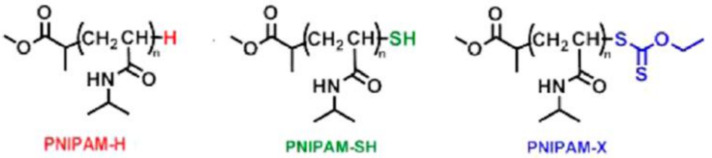

Figure 1.24. Scheme of the chemical structures of PNIPAMs used featuring the three types of end groups. [133]

Indeed, as others had reported before, increasing the concentration of the polymer leads to a decrease in NPs diameter. Additionally, small differences in the size were also found when different molecular weights were used. But significant differences in the size of the NPs, and consequently in the λ_{LSPR}, were observed as function of the type of end-group. For instance, using higher PNIPAM concentration (0.1 wt%) diameters obtained are: $d_{H\text{-}end} = 6.8 \pm 3.0$ nm, $d_{SH\text{-}end} = 3.2 \pm 0.4$ nm, and $d_{X\text{-}end} = 1.3 \pm 0.8$ nm; and the respective λ_{LSPR} are 545nm, 521 nm and no plasmon band. These results clearly show that the presence of sulphur atoms has an important role during the generation of the gold nuclei and in the growth of the NPs. The authors referred that the xanthate group strongly binds to gold blocking the growth of the NPs. It is important to remember that the reducing agent ($NaBH_4$) could also reduce the xanthate into thiol although the authors believe that in their case it did not happen.

Although the *in situ* synthesis seems to be a very simple strategy occurring in one-pot procedure, several parameters influence the generation of the NPs in the presence of the polymers. The molecular weight, the concentration and the functional groups of the polymer influence the size of the NPs. Besides, the chemical nature of the polymer (hydrophilic, hydrophobic or amphiphilic) and their configuration/organization in the solvent (aqueous or organic medium) has also influence. However, the parameter that has the major impact is the functional groups containing sulfur, which strongly binds to gold and can be block the growth of the NP. In general, for polymers containing sulfur, increasing the polymer concentration (consequently higher amount of sulfur atoms) the size of the NP decreases. Therefore, for each polymer, studies of the experimental conditions must be done in order to obtain the desired NP size in the nanocomposite.

Grafting from approach also known as *surface-initiated controlled radical polymerization* is an elegant method which allows the well-controlled synthesis of the polymer from the surface of a previously prepared nanoparticle. Here, the nanoparticle is previously prepared, so the size and the shape are controlled, being a methodology very attractive for coating anisotropic nanoparticles (e.g. nanorods). The g*rafting from* methodology, requires two steps: (i) anchoring of the CTA onto the NPs surface and, (ii) the polymerization from NPs surface. [89, 99]. The former can be a challenge since the CTA grafting density could influence the second step, the polymerization.

Surface-initiated RAFT polymerization has been more explored using silica NPs, as recently reviewed in [134], where the CTA is covalently bonded to the silica surface and then the monomer is polymerized, in organic medium (e.g. DMF or THF) from the surface of the silica particle. Also using organic medium, back in 2003, Tenhu *et al.* [135] reported the RAFT polymerization of PNiPAM from RAFT agent covalently grafted onto the Au NPs ($d = 3.2$ nm) surface containing 11-mercapto-1-undecanol in DMF. Surprisingly, in aqueous media there are no reports regarding the surface modification of Au NPs.

However, the *grafting from* strategy in aqueous media has been used to modify the surface of other NPs either via covalent bonding of a RAFT agent onto the surface of NPs and subsequent polymerization, or using a macroRAFT (MR) agent adsorbed onto NP surface. In the latter case chain extension by emulsion copolymerization is carried out from the MR agent on surface of the NP. This approach was first reported in 2008 by Hawkett *et al* [136] for the encapsulation of pigment NPs. A MR agent based on acrylic acid and butyl acrylate was used to stabilize the pigment and then a mixture of hydrophobic monomer (butyl acrylate and methyl methacrylate) was added in a control way, as illustrated in Figure 1.25. The MR agent acts as a surfactant during the RAFT emulsion polymerization thus allowing to emulsion polymerization without additional surfactants. Similar methodologies have been applied to several other particulates, such as clay platelets [137, 138], carbon nanotubes [139, 140], graphene oxide [141] and cerium oxide (CeO_2) NPs [142–144]. Nevertheless, in some methodologies additional surfactant was used, for example in the encapsulation of quantum dots (QDs) [145, 146] and cerium oxide (CeO_2) NPs [147].

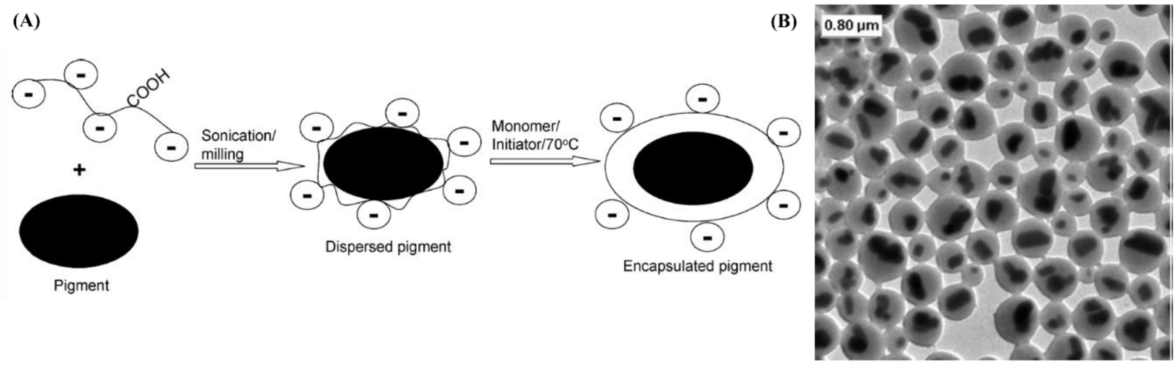

Figure 1.25. (A) Schematic representation of the dispersion and encapsulation of pigment particles using RAFT mediated emulsion polymerization. (B) Encapsulated titanium dioxide pigment particles. Adapted from [136]**.**

Concerning the RAFT mediated emulsion polymerization to encapsulate spherical NPs with diameters below 10 nm (e.g. cadmium sulfide (CdS) quantum dots (QDs) [145], lead sulphide (PbS) QDs [146] and cerium oxide (CeO_2) NPs [142–144, 147]), due to the small size of the NPs and the poor stability of macroRAFT/NP hybrid more than one inorganic NP was encapsulated per polymer particle. van Herk *et al* [144] were able to control the number of CeO_2 NPs per polymer particle by tailoring the chemical composition the MR agent. The MR agents were prepared using the RAFT agent dibenzyltrithiocarbonate, which has a symmetric structure, via RAFT polymerization of acrylic acid (AA), butyl acrylate (BA) and/or 2-acrylamido-2-methyl propane sulfonic acid (AMPS), yielding the MR agent poly(BA-*co*-AA), poly(BA-*co*-AMPS) and poly(BA-*co*-AA-*co*-AMPS). The authors demonstrated that the affinity of the repeating units in the MR agent influences its adsorption in the CeO_2 NPs surface and subsequently the encapsulation via RAFT emulsion polymerization. For instance, AA showed to have high affinity with CeO_2 NPs surface, contrary the AMPS has weak affinity. Therefore in the preparation of CeO_2/poly(styrene-*co*-methyl acrylate) hybrid latex in the presence of the MR agents poly(BA-*co*-AA) and poly(BA-*co*-AMPS), latex NPs with several or without CeO_2 NPs were found, respectively, see Figure 1.26-A and B. However, when the authors used the macroRAFT containing the three monomers, CeO_2/poly(styrene-*co*-methyl acrylate) hybrid latex with one or two CeO_2 NP per latex NP was obtained (Figure 1.26-C).

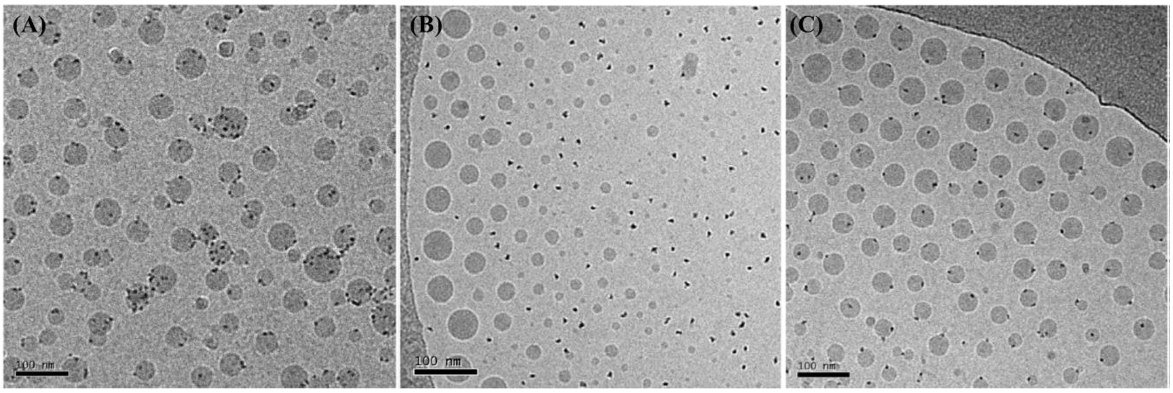

Figure 1.26. Cryo-TEM picture of the CeO_2/poly(styrene-*co*-methyl acrylate) hybrid latex obtained in the presence of (A) poly($BA_{7.3}$-*co*-$AA_{9.8}$), (B) poly($BA_{7.2}$-*co*-$AMPS_{7.6}$) and (C) poly($BA_{5.0}$-*co*-$AA_{4.9}$-*co*-$AMPS_{3.6}$) macroRAFT agents. Adapted from [144]**.**

However, to the best of our knowledge there are no publications regarding the encapsulation of Au NPs using RAFT mediated emulsion polymerization.

1.4.4. Click Chemistry

As mentioned previously, functionalization of polymer@Au NPs is required in order to provide a specific functionality towards a specific application. "Click chemistry", namely azide alkyne 1,3-cycloaddition catalyzed by Cu(I) - CuAAC reactions, has been successfully combined with polymerization, namely with RDRP, allowing the preparation of terminal- and pendant functional polymers, functional block copolymers and of complex architectures such as stars and hyperbranched polymers [148–150]. The first report combining CuAAC and polymers was published in 2005 using PS, PMMA and PEG, synthesized via ATRP and functionalized with azide- and alkyne- moieties, to prepare block copolymers [151]. One year later, the combination of RAFT polymerization and CuAAC to prepare block copolymers was reported. [152] Although early publications had more focus in the combination of "click chemistry" and ATRP, in the last years the number of publications combining "click chemistry" and RAFT polymerization has been increasing. This increase is mainly due to the advantages of RAFT polymerization, namely mild conditions, the wide range of monomers that can be polymerized and the fact that it does not require a catalyst. Further, in the scope of the present work only “click chemistry” combined with RAFT polymerization will be discussed.

The concept “Click Chemistry” was introduced by Sharpless *et al.* [153] in 2001, and it refers to high yielding reactions to bond two specific functional groups, an azide group and an alkyne by cycloaddition forming a triazole at elevated temperatures resulting in a mixture of two regioisomers. However, the use of catalysts, such as copper and ruthenium, allow the preparation of each isomer even at room temperatures: the 1,4-regioisomer and the 1,5-regioisomer, respectively, see Figure 1.27. [154, 155]

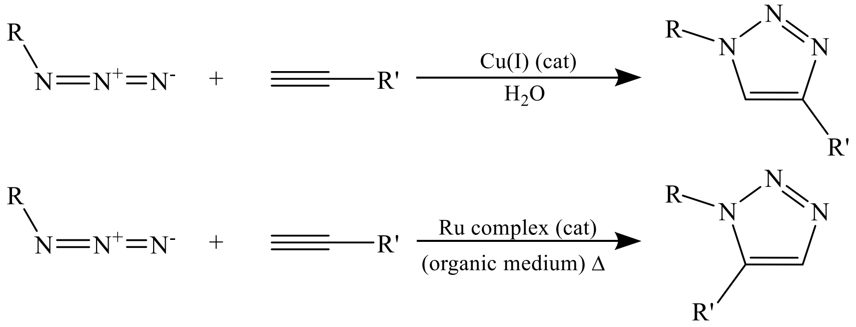

Figure 1.27. Representation of the azide-alkyne reaction catalyzed with Cu(I) and ruthenium complex.

The reaction catalyzed by Cu(I) is insensitive to solvents thus can be performed in aqueous media at room temperature, as well as physiological conditions, and is highly tolerant to functional groups. In fact, CuAAC has been proven to be a powerful tool in polymer science due to its efficiency, selectivity, versatility and simplicity. [148–150] Yet there are others such as copper-free azide–alkyne cycloadditions and thiol-ene ‘‘click’’ reactions, which do not use the copper catalyst. Indeed, in biological applications, copper is potentially toxic for living organism (*in vitro* and *in vivo)*, therefore these metal-free “click” reaction have been developed. [156] The copper-free azide–alkyne cycloadditions involve the chemical reaction between an azide and a strained cycloalkyne, more specifically derivatives of cyclooctyne, also leading to a triazole. This reaction without the catalyst is possible due to the geometric deformation of the alkyne, although the cycloaddition kinetics is slower in comparison with the CuAAC. The main disadvantage of this reaction is the demanding synthesis of the cyclooctyne. [157] Alternatively, thiol-ene ‘‘click’’ reactions, consists in the addition of a thiol to an ene bond, also without the need of a catalyst. Here the reaction can occur via the radical and base/nucleophilic forms of the thiol. In the former, the hydrothiolation is initiated forming the thiyl radical, RS•, using a photoinitiator, under irradiation, or by thermal lysis of the RS-H. In the second, a base such as trimethylamine can be use to promote the formation of the nucleophile thiolate ($R\text{-}S^-$). This reaction has been largely used in polymer chemistry due to the possibility of being performed at low temperatures (even at room temperature) in solvents such as water or DMF.

Moreover it tolerates the presence of oxygen and it is a specific and fast reaction (seconds). Several thiol as well as several ene bonds can be used although the reactivity depends on the substituents. [158]

Since CuAAC reactions are undoubtedly the most used, it is often referred as “click chemistry”. Its application in polymerization, namely RAFT polymerization, can be performed via two strategies: using “clickable” RAFT agents, or incorporating “clickable” monomers in the polymerization (Figure 1.28). This second strategy allows the preparation of polymers with high functional group densities. Polymers can be also post-modified with azide groups for subsequent “click” reaction. [150]

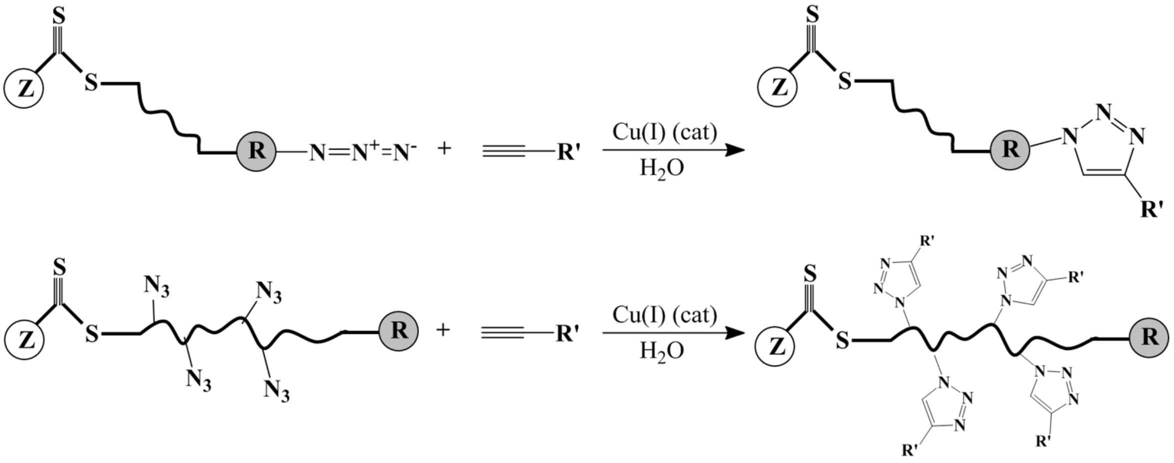

Figure 1.28 Schematic representation of “click chemistry” combined with polymers.

The first mentioned strategy can be used for post-functionalization of polymers (see some examples in Table 1.1) as well as for attaching the alkyne-RAFT agents in azide-surfaces (e.g. azide-silica NP [159]) and subsequently the polymerization occurs from the surface.

Table 1.1 Combination of “click chemistry” with RAFT polymerization using “clickable” RAFT agents

	Azide group	Alkyne group	Ref
1	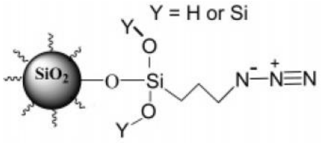	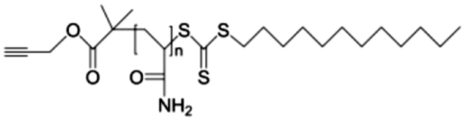	[160]

2	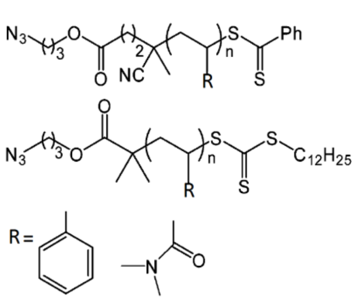 N_3 O 3 2 n S Ph NC R $C_{12}H_{25}$ R = N	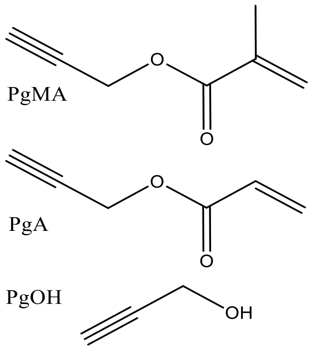 PgMA O PgA PgOH OH	[161]
3	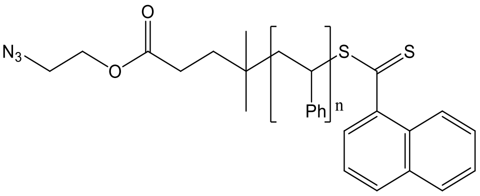	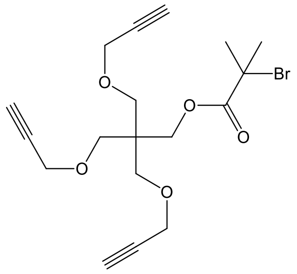	[162]
4	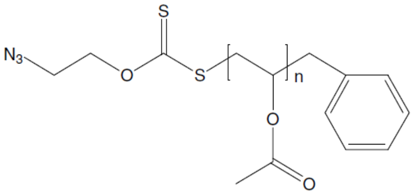	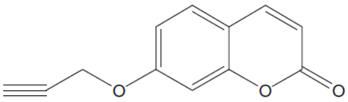	[163]
5	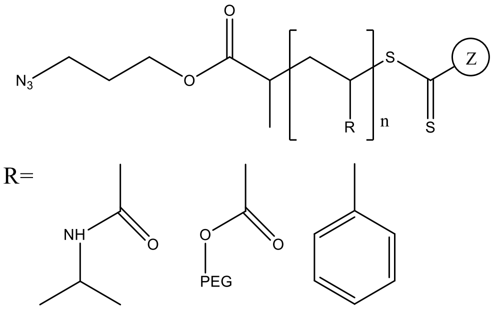 N_3 O S Z R n R= NH PEG	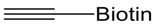	[164]
6	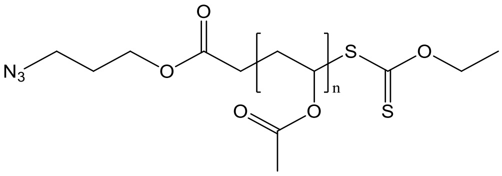	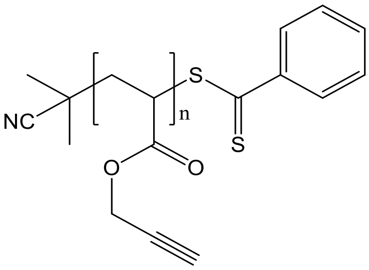	[165]

(PgMA- propargyl methacrylate; PgA - propargyl acrylate; PgOH- propargyl alcohol)

Regarding the second strategy mentioned before, i.e. using "clickable monomers" several works have also been published, Table 1.2 shows some examples of "clickable" monomers and the RAFT agents used for the polymerization.

Table 1.2 Combination of "click chemistry" with RAFT polymerization using "clickable" monomers

	"clickable" monomer	**RAFT agent**	**Ref**
1	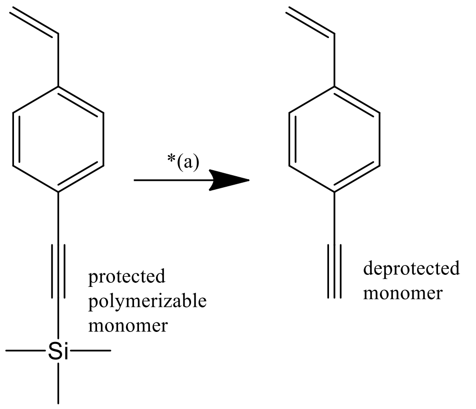 *(a) protected polymerizable monomer deprotected monomer	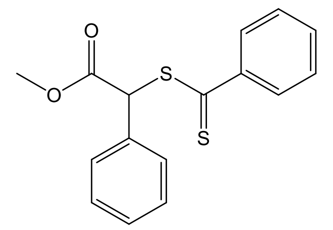(S)-methoxycarbonylphenylmethyldithiobenzoate	[166]
2	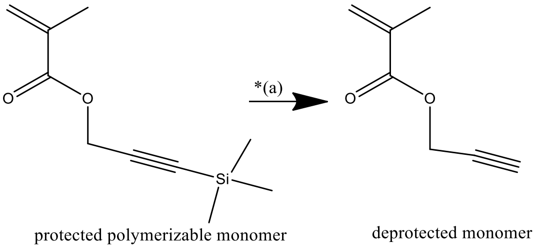 *(a) protected polymerizable monomer deprotected monomer	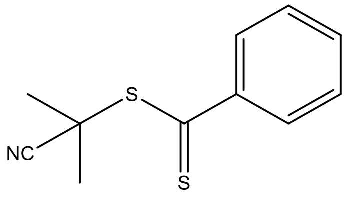CPDB	[165]
3	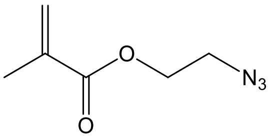	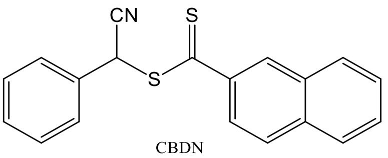CBDN	[167]

*(CBDN - α-Cyanobenzyl dithionaphthalate)

*(a) the alkyne monomers should be protected to avoid crosslinking reaction. After polymerization the alkyne is deprotected via acid catalyzed hydrolysis. [166]

An interesting feature of "click chemistry" is the fact that as demonstrated by Benicewicz *et al.*[167] there are no significance changes in the molecular weight distribution by performing the "click" functionalization either *pre*- or *post*- RAFT polymerization of 2-azidoethyl methacrylate (AzMA), as schematized in Figure 1.29.

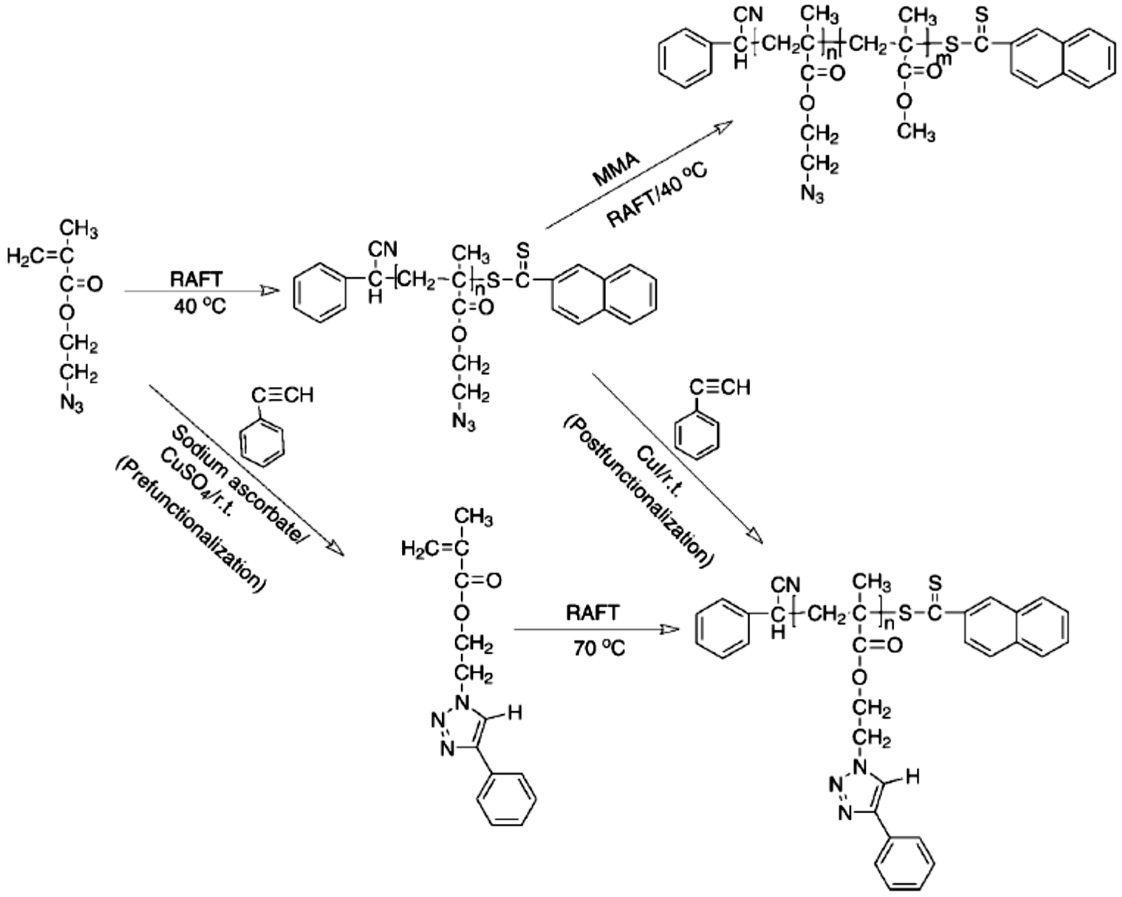

Figure 1.29. Preparation of polyAzMA and polyAzMA derivatives by combining RAFT polymerization and "click chemistry". [167]

"Click chemistry" has proven to be an interesting technique to prepare functional ligands, polymers, surfaces as well as nanoparticles. This "click" functionalization involves the linkage of organic dyes [163, 168–172], specific ligands of proteins (e.g. biotin [164, 173, 174]), proteins (e.g. lipases [175]), peptides [176], oligonucleotides [177, 178] and saccharides [179, 180].

1.5. Langmuir-Blodgett technique

The Langmuir-Blodgett (LB) technique has proven to be an interesting technique to study conformational alterations of amphiphilic block copolymers, obtained via RAFT polymerization, at air/water interface as well as to investigate molecular biorecognition processes which is an asset for the use of these nanostructures in biosensing applications. [181, 182]

The Langmuir-Blodgett technique is performed in a Langmuir-Blodgett trough as shown in Figure 1.30. This equipment consists of a Teflon trough, two movable barriers and a surface pressure sensor which measures the surface pressure as a function of the area of water surface available for each molecule, i.e. surface pressure vs. area per molecule isotherm. [183, 184]

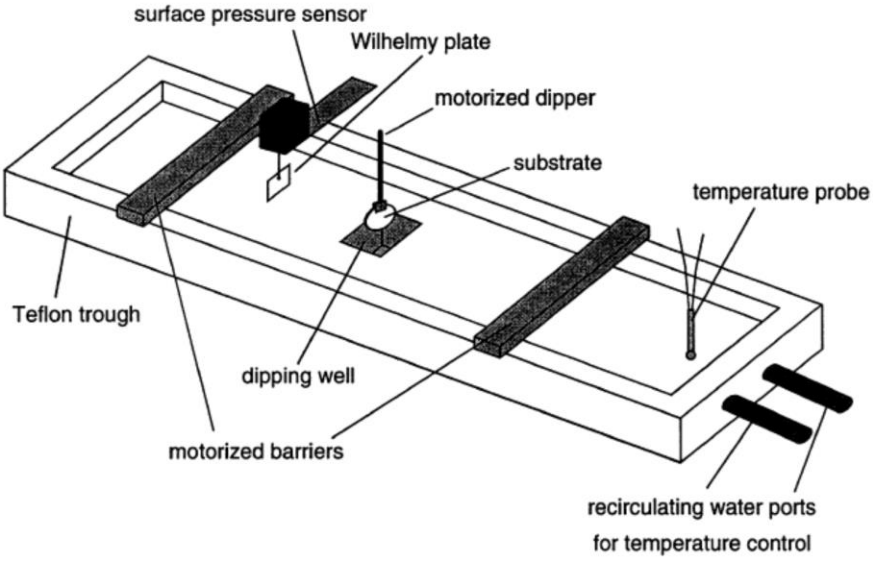
surface pressure sensor
Wilhelmy plate
motorized dipper
substrate
temperature probe
Teflon trough
dipping well
motorized barriers
recirculating water ports
for temperature control

Figure 1.30 Schematic representation of a typically Langmuir-Blodgett trough [184]**.**

The surface pressure-area isotherm gives information about the stability of the monolayer at the air/water interface, the orientation of the molecule, phase transitions and conformational transformations. After spreading a known amount of amphiphilic molecules on the water surface, experiments can be performed to study the isotherms of amphiphilic molecules. During compression three phases can be observed, as represented in Figure 1.31. When the barriers are open a *gaseous* phase is observed, where the molecules have a random motion at the water surface mimicking the behavior of a gas. Then, by closing the barriers, a *liquid-expanded* phase is observed where the molecules have a lower degree of freedom, due to the decrease of intermolecular distance, and start to have some organization. On further compression, the molecules achieve the *liquid-condensed* phase where the molecules are closely packed and well-oriented forming a monolayer. If this monolayer is further compressed it collapses and the surface pressure decreases rapidly, as observed in Figure 1.31. During the barriers compression, in some cases, transition phases are observed, such as liquid-condensed/liquid-expanded phase. [183, 185, 186]

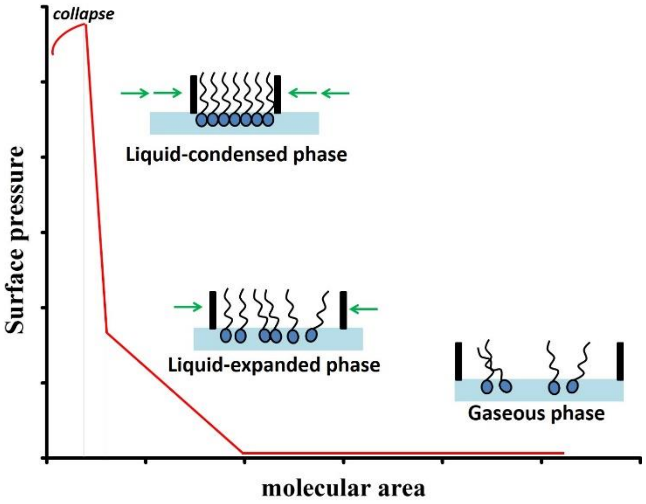

Figure 1.31. Schematic representation of surface pressure vs area per molecule isotherm.

The surface pressure-area isotherm is characteristic of each amphiphilic molecule, thus studies at the air/water interface can be performed in order to understand the interaction of the amphiphilic monolayer in the interface and (bio)molecules in the water subphase, namely towards biorecognition studies [181, 182]. Several works have already been published, using phospholipids monolayers as models of cell membranes in order to understand how biomolecules, such as proteins and polysaccharides, or nanoparticles dispersed in the subphase interact with the phospholipidic monolayer [187]. For instance, Oliveira Jr. *et al* studied the interaction of chitosan [188] and gold nanoparticles [189] with phospholipidic monolayers as models of cell membranes. Other amphiphilic molecules can also be used to study the specific recognition, i.e. using in the air/water interface functional amphiphilic molecules and adding to the subphase the specific target. [182, 190]

In addition to the surface pressure measurements, complementary surface characterization techniques can be used to help in a better understanding of the chemical interactions and/or organization of the molecules in the air/water interface, such as surface potential, fluorescence microscopy, Brewster angle microscopy and polarization modulation infrared reflection adsorption spectroscopy (PM-IRRAS). [187, 191]

Another interesting aspect of this technique is the possibility of preparing well-ordered thin-films. This technique, which was developed in the 30’s by Irving Langmuir and his assistant Katharina Blodgett [183], is being developed in Nanotechnology aiming the preparation of simple and easy handling biosensing devices.

LB films are prepared using the Langmuir-Blodgett trough by transferring vertically a compressed and highly dense monolayer at the air/water interface to a substrate. Each monolayer is transferred by dipping down and up the solid substrate. Repeating this procedure a well-ordered stratified multilayer film can be obtained, as depicted in Figure 1.32. If the substrate is hydrophilic, the first layer is transferred by dipping up the substrate. The opposite happens when hydrophobic substrates are used. [183, 184]

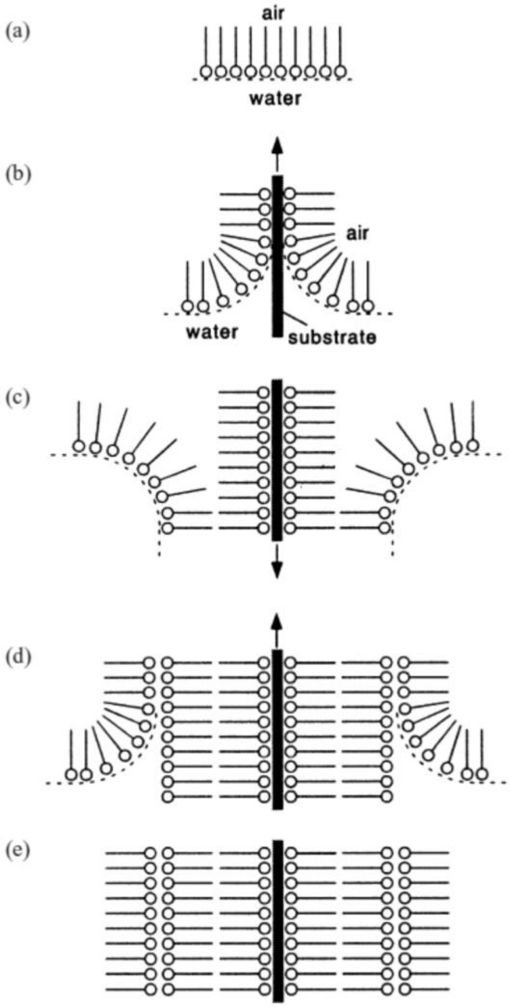

Figure 1.32. Schematic representation of LB deposition process on a hydrophilic substrate resulting in a three layer film. The hydrophilic molecular headgroups are represented by circles and the hydrophobic tails are represented by the attached "sticks". Note that layers are deposited in alternating orientations on upstrokes (b and d) and downstroke (c) resulting in a multi-bilayer structure (e) [184]**.**

Although very promising, the LB technique is limited in terms of scale up and the need of amphiphilic materials. On the contrary, the LbL technique has proven to be a scalable, easy and simple technique for the preparation of thin-film incorporating several charged nanomaterials and polymers.

1.6. Motivation and aims of the work

Despite the increasing number of contributions that have been reported in the past years concerning the preparation of Au nanostructured assemblies, some issues still need to be addressed in order to take full advantage of the unique and tunable properties of such materials. Among these challenges, the preparation of multifunctional and robust Au nanostructures stable in physiological medium appears has a very important topic for biosensing applications and their immobilization to design novel devices.

The general objective of this thesis was to develop new pathways towards functional Au nanostructured assemblies containing polymers in their composition. For that purpose two distinct approaches have been explored during this research. In the first approach, fluorescent biofunctional polymer@Au nanostructures were prepared via electrostatic assembly of polyelectrolytes onto Au nanostructures (***Chapter 2***), whilst in the second approach, biofunctional polymer@Au nanostructures were prepared using block copolymers synthesized via RAFT polymerization (***Chapter 3*** and ***Chapter 4***). The selection of the most efficient strategy and parameters optimization required a number of experimental procedures, which appear themselves as a new contribution to the field of Au nanocomposites formulations. Furthermore, in order to get a better understanding of the molecular interactions between the copolymer (functionalized, or not with biotin) and the bioanalyte, preliminary studies have been carried out at the air-water interface of such systems by using the Langmuir-Blodgett technique. Fluorescent copolymer@Au NPs were also prepared via RAFT polymerization of a fluorescent monomer (monomer modified with FITC) from MR@Au NPs and subsequent polymerization of MMA:BA monomers. In particular, the latter approach aimed to investigate the effect of the distance between the core and the fluorophore on the optical response of this type of Au nanostructures. The optical response of biofunctional shell@core nanostructures to the presence of a specific bioanalyte was evaluated using the biotin-avidin (bioreceptor-bioanalyte) system as model to evaluate the biosensing response, in which avidin is well known to have high affinity towards biotin. As a final remark, it should be noted that the research performed in two distinct assembly methods, either by using the layer-by-layer method (***Chapter 2***) and the Langmuir technique (***Chapter 4***), paved the way to the future fabrication of thin films comprising the above mentioned Au nanostructures.

CHAPTER 2. Functional gold nanostructures prepared via electrostatic self-assembly

The work reported in this chapter was published in *Gold Bulletin* (2015) Biotinylation of optically responsive gold/polyelectrolyte nanostructures, 48: 3-11.

2.1. Introduction

This chapter focuses on the surface modification and functionalization of Au NPs using polyelectrolytes (PE) and the electrostatic self-assembly method to confer fluorescence and biospecificity to the resulting colloids. As such, a variety of procedures has been investigated that combine the use of an organic dye (fluorescein isothiocyanate, FITC) and a specific bioanalyte (biotin). Scheme 2.1 shows the strategy followed in this work towards the biotinylation of Au/PE assemblies. The ensuing functionalized Au/PE assemblies were used in biosensing experiments to explore their optical properties as quencher when aggregation of Au NPs was induced.

Scheme 2.1. Preparation of Au/PE hybrid nanostructures: (A) Synthesis of Au NPs; (B) Functionalization of Au/Citrate NPs with poly(allylamine hydrochloride) (PAH) and poly(styrenesulfonic acid sodium salt) (PSS); (C) Functionalization of Au_n with the outermost layer.

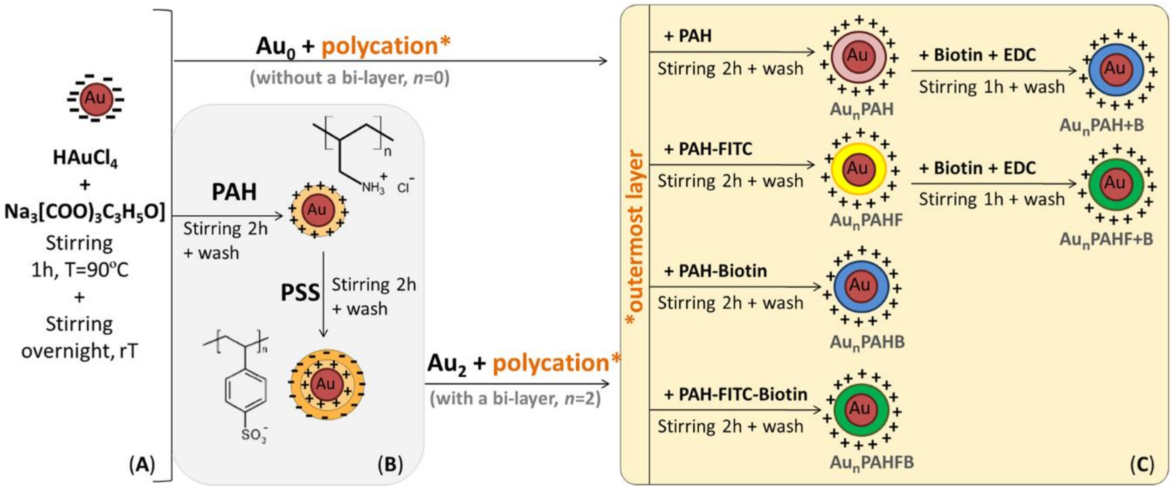
Au
HAuCl4
+
Na3[COO)3C3H5O]
Stirring
1h, T=90ºC
+
Stirring
overnight, rT
(A)
Au0 + polycation*
(without a bi-layer, n=0)
PAH
Stirring 2h
+ wash
NH3+ Cl-
n
PSS
Stirring 2h
+ wash
SO3-
(B)
Au2 + polycation*
(with a bi-layer, n=2)
*outermost layer
+ PAH
Stirring 2h + wash
AunPAH
+ Biotin + EDC
Stirring 1h + wash
AunPAH+B
+ PAH-FITC
Stirring 2h + wash
AunPAHF
+ Biotin + EDC
Stirring 1h + wash
AunPAHF+B
+ PAH-Biotin
Stirring 2h + wash
AunPAHB
+ PAH-FITC-Biotin
Stirring 2h + wash
AunPAHFB
(C)

2.2. Preparation of gold nanostructures prepared via electrostatic self-assembly method

Au/PE assemblies were prepared using the polycation poly(allylamine hydrochloride) (PAH) and the polyanion poly(styrenesulfonic acid sodium salt) (PSS), as depicted in Scheme 2.1. The colloidal stability of the Au/PE nanostructures was monitored by UV-Vis spectroscopy (Figure 2.1-A), and the spectra collected for all the samples have shown the typical LSPR band of colloidal Au, peaked at about 525 nm. The small shift of the LSPR maximum from 524.5 to 526.5 nm after PE treatment of the Au NPs is attributed to slight changes of the dielectric constant of the particles surrounding medium [67]. Also noticeable is the fact that the Au/PE nanostructures containing PSS exhibit a strong optical absorption in the UV region (peaked at 225 nm) which is due to π-π* electronic transitions of the benzene ring in the polyelectrolyte [67]. The zeta potential measurements (Figure 2.1-B) performed on colloidal Au treated with oppositely charged polyelectrolytes agree with the results obtained by UV-Vis spectroscopy. Whilst, the starting Au NPs show a negative ζ potential (−55mV) due to the citrate anions adsorbed at their surfaces, upon surface modification with the cationic polyelectrolyte PAH it changes to +62 mV, at the same pH value. Conversely, the treatment of the resulting colloids with the anionic polyelectrolyte PSS led to a negative value of zeta potential (−84mV), and finally, the deposition of the third layer of PAH confers the colloidal particles a highly positive surface charge (+73 mV), that renders colloidal stability to the Au/PE dispersed in water.

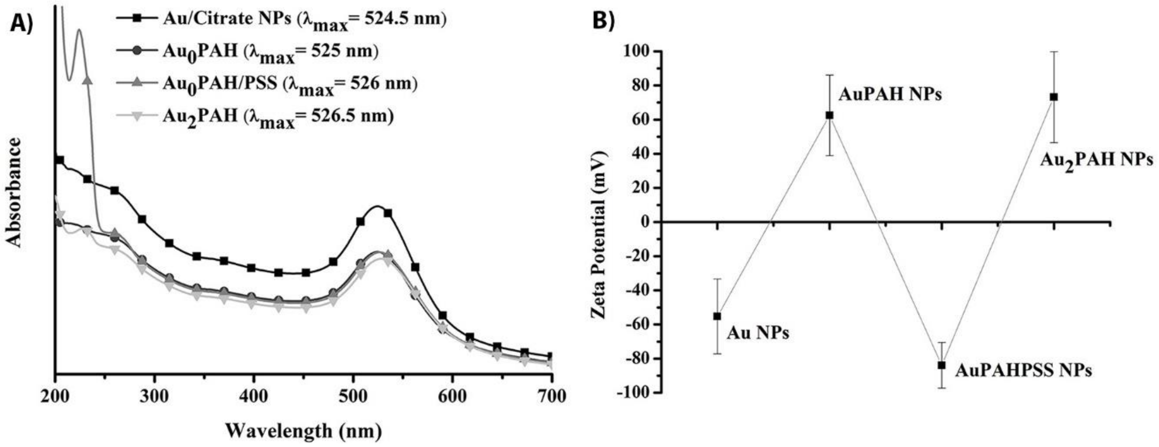

Figure 2.1. (A) UV-Vis spectra of Au$_0$PAH and Au$_2$PAH nanostructures and (B) zeta potential of Au/Citrate colloids and after their treatment with PAH and PSS (straight lines to guide the eye).

The morphologies of the Au/PE particles during the functionalization process were probed by TEM, and a systematic analysis of a number of TEM images has shown Au/PE core/shell structures whose cores have an average diameter of 17.7±2.7 nm that did not change significantly after PE treatment. On the other hand, as illustrated in Figure 2.2, the TEM images suggest an increase of the shell thickness from Au$_0$PAH to Au$_2$PAH in line with the increase in the number of PE layers deposited onto the Au cores. From these results, the PE shell thickness was estimated to be about 2‑4 nm, which is close to the value reported previously of 1.5 nm thickness for PAH/PSS bi-layers coating colloidal Au NPs [192]. Figure 2.2 also shows a set of three Au NPs wrapped by PAH layers, but it must be emphasized that this type of clustered structures was not predominant in the several samples analyzed. Instead, the surface-modified Au samples appeared mainly as discrete particles coated with PE.

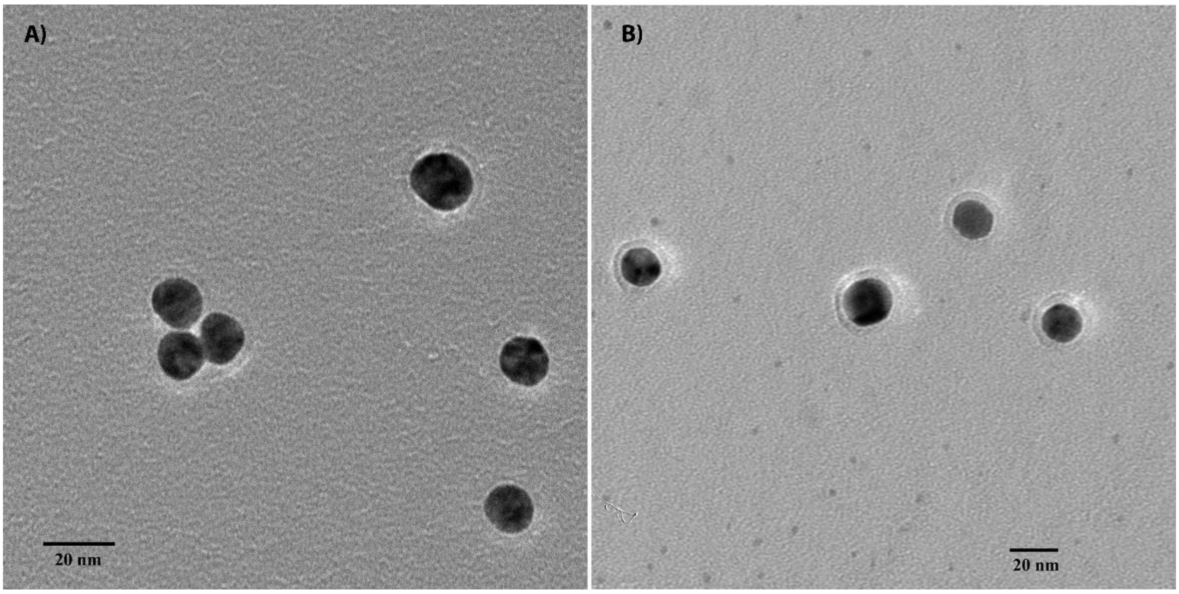

Figure 2.2. TEM images of (A) Au_0PAH nanostructures and (B) Au_2PAH nanostructures.

2.3. Functionalization gold nanostructures prepared via electrostatic self-assembly method

The biotinylation of the Au/PE nanostructures was monitored by optical absorption and fluorescence emission measurements for the diverse strategies employed. In general, the visible spectra have shown that biotinylation did not lead to significant changes of the LSPR band for the surface-modified samples, namely by comparison with the starting colloid shown in Figure 2.3.

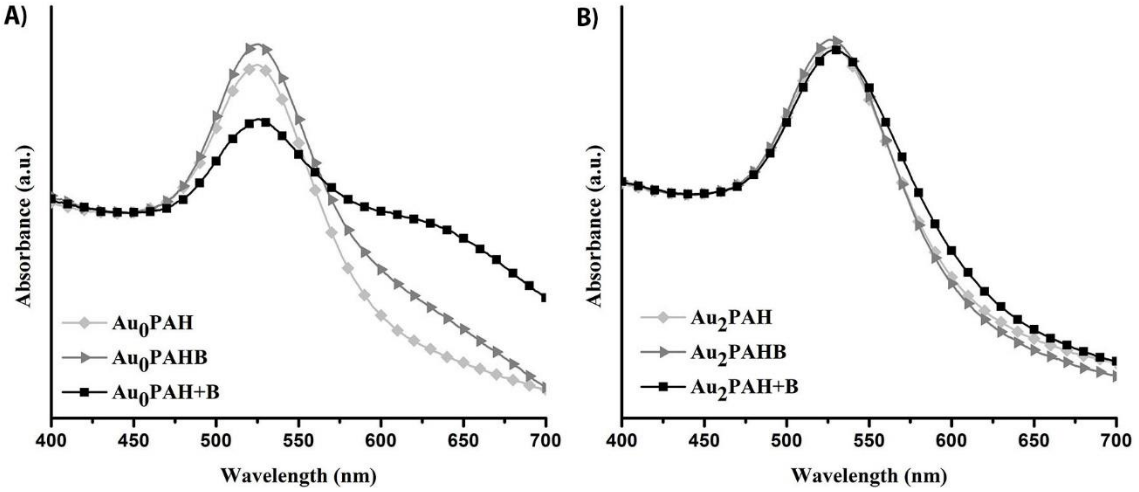

Figure 2.3. Visible spectra of (A) Au_0PAH and (B) Au_2PAH nanostrutures (the spectra were normalized at 450 nm)

However, an exception was observed for the Au_0PAH+B sample, in which the biotinylation of Au_0PAH resulted in a colloid whose visible spectrum also shows an absorption band peaked at 650 nm (Figure 2.3-A). Even though this effect is slightly detected for sample Au_0PAHB, it is hardly significant. This new band is probably associated with interparticle plasmon coupling resulting from the loss of colloidal stability during the biotinylation of Au_0PAH colloids. Interestingly, the nanostructures having an extra PE bilayer (Au_2PAH+B) did not show such optical behavior upon a similar biotinylation treatment, as illustrated in Figure 2.3-B. Although there is a slight red shift of the LSPR band ($\Delta\lambda$=2.5 nm) observed in the spectra of the Au_2PAH colloid and of the corresponding biotinylated sample (Au_2PAH+B), both visible spectra are similar. These results indicate that the intermediate PAH/PSS coating confers more robustness towards a posteriori treatment with biotin (or post-biotinylation), as opposed to what was observed for the biotinylation of the Au_0PAH sample, in which the PE monolayer was not capable of preventing the formation of aggregates.

Fluorescent Au/PE assemblies were prepared by labelling the outermost PE layers with a fluorescent organic dye. For that purpose, the PAH chains were first functionalized with FITC to afford PAHF which was then used in the coating of the Au NPs yielding FITC labelled Au_0PAHF and Au_2PAHF assemblies. Similarly to the FITC non-labelled systems described above, these fluorescent nanostructures were used as starting colloids in biotinylation procedures. As expected, the FITC labelled Au/PE nanostructures showed a broader absorption band that takes into account the contribution of both the LSPR band (λ_{max}=526.5 nm) of the Au NPs and the absorption due to FITC molecules (λ_{max}=497 nm). The visible spectra of biotinylated FITC labelled assemblies were similar regardless of the biotinylation procedure used (Figure 2.4).

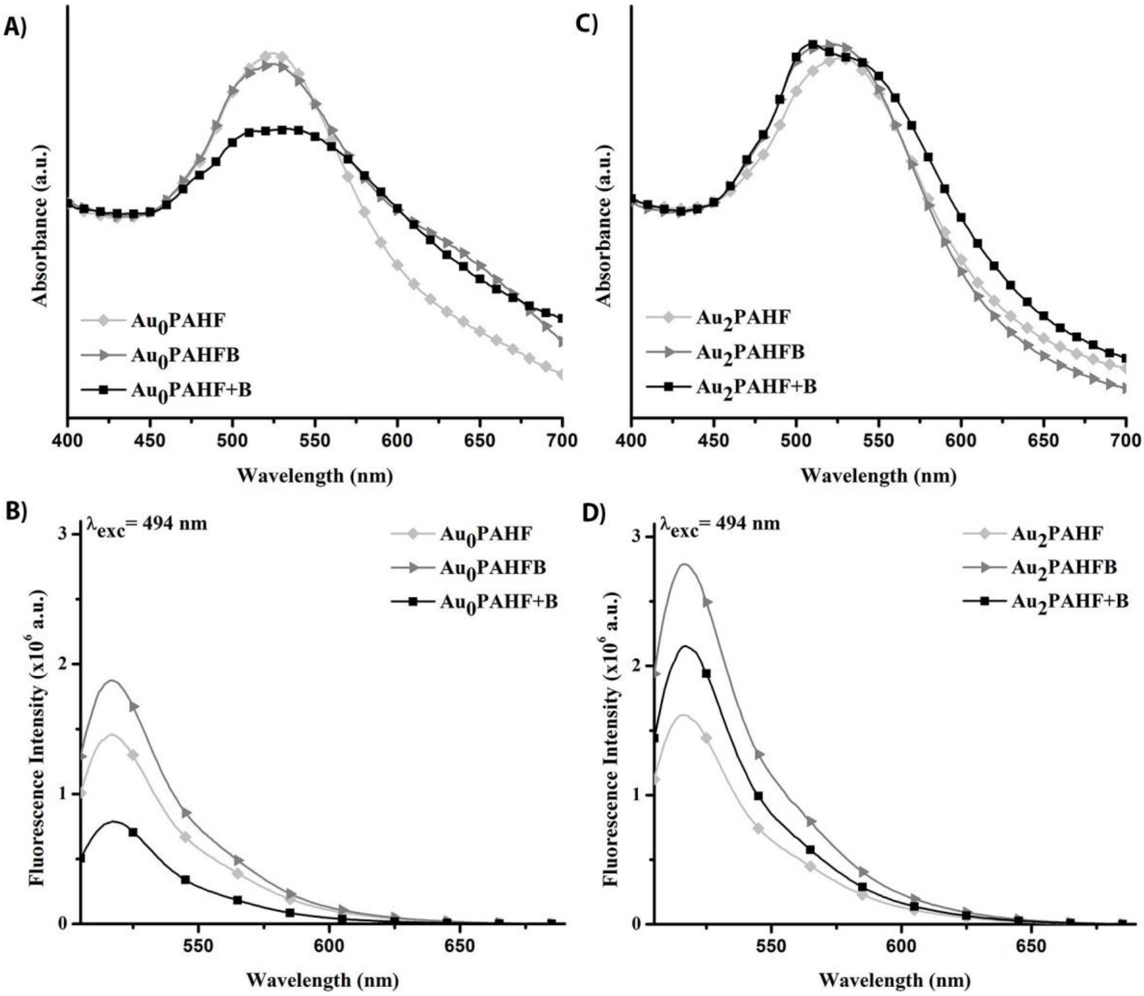

Figure 2.4. (A and C) visible spectra and (B and D) fluorescence spectra (λ_{exc}=494nm) of Au0PAHF and Au2PAHF nanostructures. The visible spectra were normalized at 450nm.

However, as previously observed for the FITC unlabelled analogues, *post-biotinylation* of the Au_0PAHF nanostructures caused significant changes on the respective visible spectrum, which is ascribed to the loss of colloidal stability during the biotinylation step. However, this was not observed for the Au_2PAHF+B assemblies. These results confirm that the presence of an extra PE bilayer leads to more robust colloids, thereby providing enhanced colloidal stability during *post-biotinylation* (Figure 2.4-A,C).

The fluorescence emission measurements (Figure 2.4-B,D) are in agreement with the results discussed above regarding the stability of each colloidal system. The fluorescence emission intensity depends on the biotinylation path followed and on the presence of the extra PE bilayer. Regarding the Au nanostructures with the extra PE bilayer, the presence of biotin has an incremental effect on the fluorescence emission intensity. For Au_2PAHFB, the increase of the fluorescence intensity is more pronounced when compared to the sample obtained via post-biotinylation (sample

$Au_2PAHF+B$). This is attributed to the fact that in sample Au_2PAHFB, the biotinylated polyelectrolyte may adopt a conformation around the Au NP that provides a longer distance between the fluorophore molecules and the metal surface, when compared to the non-biotinylated sample. In this situation, the fluorophore molecules being further away from the Au surfaces limit the FITC fluorescence quenching as a result of the fact that the process of energy transfer from FTIC (the donor) to Au (the acceptor) is dependent on the distance between them [192]. This explanation is in line with the observation that the Au_2PAHFB assemblies are more stable with subsequent increase of the FITC fluorescence emission (Figure 2.4-D). As regards the sample $Au_2PAHF+B$, the increment on the fluorescence intensity was not so pronounced after biotinylation. This may be associated with the reduction of the number of protonated aminic groups available for colloidal electrostatic stabilization. As a result, the colloidal stability of the nanostructures is compromised causing a detrimental effect on the FITC fluorescence emission due to the reduced distance between the fluorophore and the Au surfaces. Note that this explanation is consistent with the visible spectrum of Au NPs modified with a single PE layer shown in Figure 2.4-A for the same sample. Indeed, the fluorescent intensity for the $Au_0PAHF+B$ sample is even smaller than that recorded for the sample without biotin (Au_0PAHF) as shown in Figure 2.4-B. However, when an extra PE bilayer was used, the detrimental effect of the *post-biotinylation* process was less pronounced.

2.4. Response of the gold nanostructures towards avidin

In order to assess the optical response of the biotinylated Au/PE nanostructures for biosensing, avidin was added to all of the nanostructures prepared including the Au nanostructures without the extra PE bilayer. The nanostructures without biotin were used as blanks regarding the response to avidin under the same experimental conditions. Then the effect of time and analyte concentration was assessed by exposing the samples to solutions of avidin of two distinct concentrations and for different periods of time. All the results have been compiled and plotted in Figure 2.5 and Figure 2.6 as described in ***Experimental procedures*** chapter (**6.3.5.**)

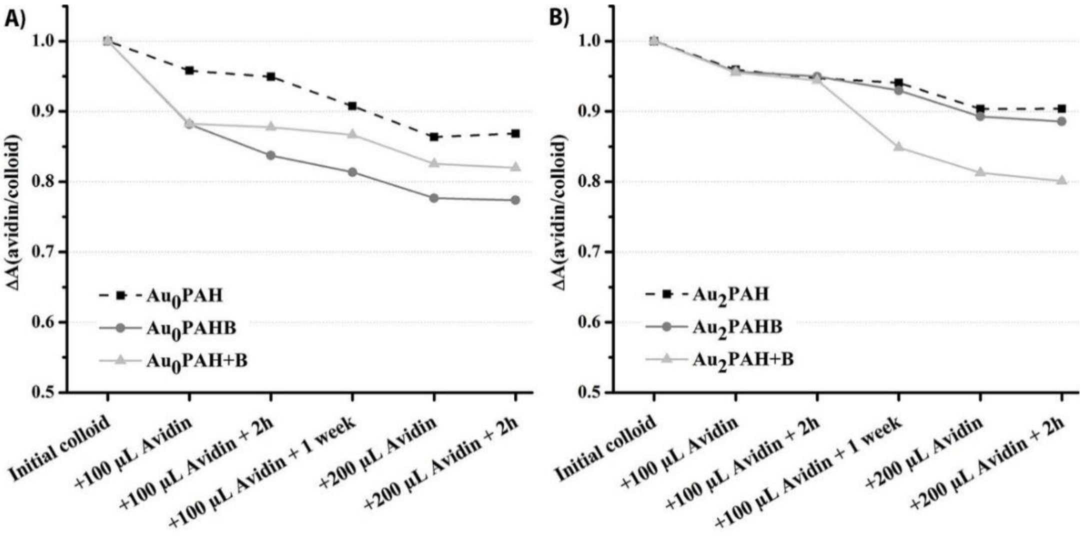

Figure 2.5. ***ΔA(avidin/colloid)*** **of (A) Au$_0$PAH and (B) Au$_2$PAH nanostructures in the presence of avidin.**

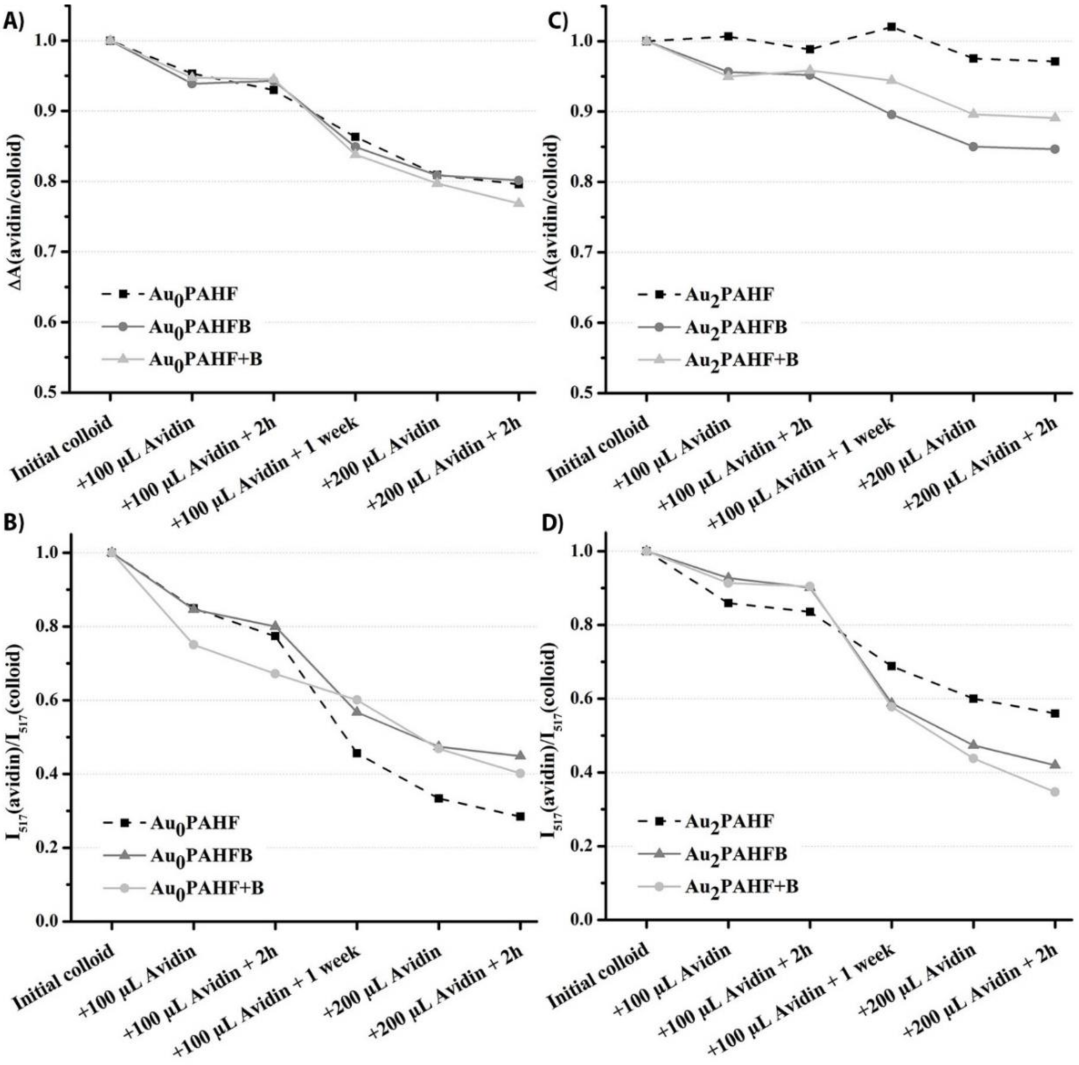

Figure 2.6. (A and C) ***ΔA(avidin/colloid)*** **and (B and D)** ***I_{517}(avidin)/I_{517}(colloid)*** **of Au$_0$PAH and Au$_2$PAH nanostructures in the presence of avidin, respectively.**

As regards the optical response of these assemblies towards the presence of avidin in terms of the absorbance of the LSPR band, a general trend towards its reduction is observed as illustrated in Figure 2.5 and Figure 2.6-A,C, which suggests that all the nanostructures respond to the presence of avidin, including those without biotin. This is an indication that both specific and non-specific interactions between avidin and the functionalized Au/PE assemblies took place. The reason for non-specific interactions seems to be associated with changes of the surrounding medium that affects colloidal stability which is particularly evident for the non-labelled assemblies submitted to the post-biotinylation method (namely those prepared with only one layer of PAH─see Figure 2.5-A). Indeed, He *et al.* have reported that non-specific interactions of streptavidin with uncoated Au NPs occurred via uncertain group binding [193]. Therefore, these nonspecific interactions may result from deficient surface protection associated with changes of composition of the surrounding medium. In view of the susceptibility of the Au assemblies prepared with only one PE layer (Au_0NPs), it is difficult to ascertain the formation of any specific interactions; thus, focus was given to the more robust assemblies prepared using the extra PE bilayer (Au_2NPs). As regards the biotinylated Au nanostructures, only the Au_2PAH+B seem to show a distinct response towards the presence of avidin (Figure 2.5-B), whilst the samples labelled with FITC, i.e., Au_2PAHFB and $Au_2PAHF+B$, have both shown specific response when compared to the control sample Au_2PAHF (Figure 2.6-C). In fact, when 100 μL of avidin were used, the reduction of $\Delta A(avidin/colloid)$ was only noticeable upon 1 week. Yet, when 200 μL of avidin were used, that reduction was almost immediate.

Whilst the optical spectra provide some information regarding the behavior of this type of Au assemblies towards the presence of avidin, more expressive results were obtained when fluorescence spectroscopy was used (Figure 2.6-D), which may indicate specific interaction between the biotin and the avidin. Although the observed decrease in the $I_{517}(avidin)/I_{517}(colloid)$ might be caused by particle aggregation following the addition of avidin, the optical response for the biotinylated samples was more pronounced which might be associated with their specific molecular recognition for avidin and associated quenching effects. Moreover, comparison with the results shown in Figure 2.6-B for the FITC labelled samples prepared with one single layer, it is clear that the effect of non-specific interactions leads to a distinct response associated with their poor colloidal stability but that cannot be discerned by optical spectroscopy.

2.5. Conclusions

Surface functionalization of gold nanoparticles was accomplished using functionalized polyelectrolytes and the electrostatic self-assembly method. The use of an extra PE bilayer between the Au core and the outermost functional layer proved to be crucial to provide robustness and stability to the ensuing nanostructures. Strategies to functionalize PAH led to the preparation of multifunctional Au nanostructures with fluorescence and biorecognition properties, which combine an organic fluorophore (FITC) and a biolinker (biotin). The functionalized Au nanostructures have shown potential for biosensing applications due to their optical response in forming biotin-avidin conjugates. Worth noting is the fact that in these tests, the analyte was not labelled with a fluorophore, as reported by others [22]. Moreover, whilst small changes due to particle aggregation during the bioassays caused a small reduction of $\Delta A(avidin/colloid)$, similar changes caused a pronounced decrease of the FITC emission band in the fluorescence emission spectra ($I_{517}(avidin)/I_{517}(colloid)$). Thus, fluorescence emission spectroscopy emerged here as an interesting tool to assess the ability of biotinylated Au assemblies to recognize avidin.

CHAPTER 3. Gold nanostructures prepared via RAFT polymerization

3.1. Introduction

In this chapter the preparation and characterization of MR agents **(3.2.)** and of the corresponding diblock copolymers **(3.3.)** is discussed. Next, three main strategies to prepare gold nanocomposites via RAFT assisted emulsion polymerization are discussed. Scheme 3.1 summarizes the work carried out in this context. First, the macroRAFT (MR) agents were synthesized in solution via RAFT polymerization and then a hydrophobic block was grown via RAFT emulsion polymerization. This block copolymer was used in the two first strategies: **(3.4.1.)** ***Post-modification* strategy** – which consisted in mixing previously prepared Au NPs with the block copolymer and **(3.4.2.)** ***In situ* strategy** – in which case Au NPs were generated in the presence of the block copolymer using sodium borohydride as reducing agent and $HAuCl_4$ as gold salt. In the third strategy, **(3.4.3.)** ***Grafting from* strategy**, the hydrophobic block was grown from Au NPs that were coated with the MR agent.

Scheme 3.1. Strategies to prepare gold nanocomposites via RAFT assisted emulsion polymerization

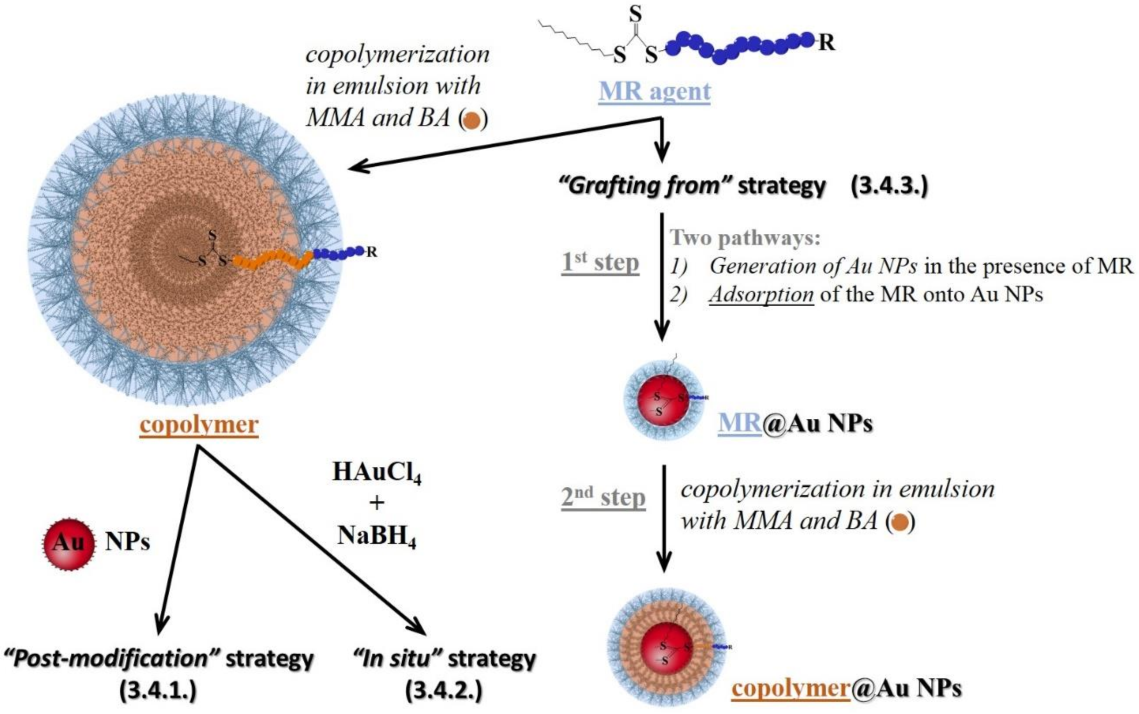
S
S S
R
MR agent
copolymerization in emulsion with MMA and BA (●)
S
S S
R
copolymer
"Grafting from" strategy (3.4.3.)
1st step
Two pathways:
1) Generation of Au NPs in the presence of MR
2) Adsorption of the MR onto Au NPs
MR@Au NPs
2nd step
copolymerization in emulsion with MMA and BA (●)
copolymer@Au NPs
Au NPs
HAuCl4 + NaBH4
"Post-modification" strategy (3.4.1.)
"In situ" strategy (3.4.2.)

3.2. Preparation and characterization of macroRAFT agents

MacroRAFT (MR) agents were synthesized in solution via RAFT polymerization using the RAFT agent 2-(dodecylthiocarbonothioylthio)-2-methylpropionic acid (TTC-A) and as initiator the 4,4′-azobis(4-cyanovaleric acid) (ACPA). The chemical structures are represented in Figure 3.1.

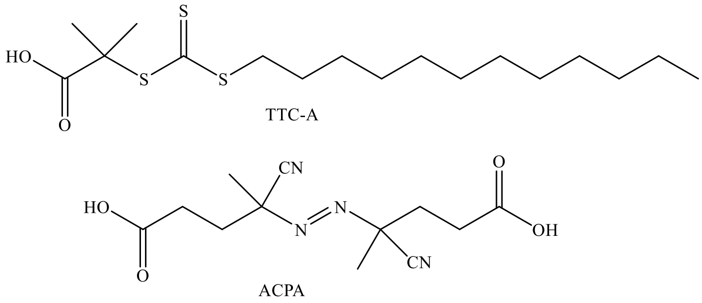

Figure 3.1. Chemical structures of TTC-A and ACPA

The MR agents studied in this work were prepared using two distinct hydrophilic monomers: poly(ethylene glycol) methyl ether acrylate (PEGA) and acrylic acid (AA). Figure 3.2 shows the chemical structures of the monomers and of the macroRAFT agent. The choice of these monomers is based on the fact that polymers such as poly(ethylene glycol) or poly(ethylene oxide) are known to have high biocompability and minimize interaction with proteins [194–196] which could be very important for the application of these nanocomposites as biosensors, thus eliminating possible nonspecific interactions with proteins. Furthermore this type of moiety is also associated with thermal responsiveness [121]. In turn, the acrylic acid monomer could confer to the nanocomposite pH responsiveness [123].

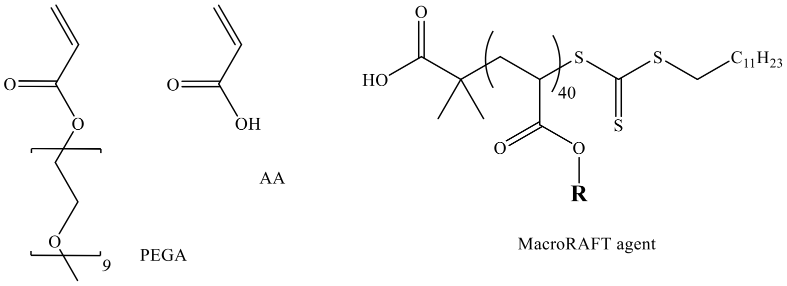

Figure 3.2. Chemical structures of the hydrophilic monomers PEGA and AA and representation of the chemical structure of the macroRAFT agent. *R* depends on the monomer used.

Theoretical and experimental molecular weight values of the MR agents are shown in Table 3.1. Conversion of monomer *(%Conversion*) was determined by H^1-NMR analysis of the withdrawn aliquots during the polymerization using 1,3,5-trioxane as internal standard. In ***Annex A*** a detailed explanation of the calculation and the *%Conversion* profile of the polymerization of each MR agent can be found.

Table 3.1. Theoretical and experimental data of *%Conversion*, molecular weight and degree of polymerization (DP) of MR agents, determined by H^1-NMR.

Sample name	***pPEGATTC***	***pAATTC***
macroRAFT agent	**P(PEGA$_{40}$)-TTC**	**P(AA$_{40}$)-TTC**
$\bar{M}_{n\ (theoretical)}$ g/mol	21387	3598
DP $_{(theoretical)}$	44	45
***%Conversion* (^{1}H-NMR)**	94%	95%
$\bar{M}_{n\ (exp\_NMR)}$ g/mol	20104	3436
DP $_{(exp\_NMR)}$	41	43

Table 3.1 shows that the monomer conversion (*%Conversion*) for both MR agents is high and the experimental $\bar{M}_n$ is very close to the theoretical $\bar{M}_n$. Although the $\bar{M}_n$ values of the MR agents are different, they were prepared with similar DP (~40) which is important to compare MR agents with different repeating units, i.e. with different chemical natures, but with the same degree of polymerization.

3.3. Preparation and characterization of copolymers derived from the macroRAFT agents

Block copolymers were synthesized via RAFT emulsion polymerization using the MR agents prepared in **3.2.**: P(PEGA$_{40}$)-TTC and P(AA$_{40}$)-TTC. As discussed in the introduction chapter, since the MR agent contains the RAFT agent in its structure, it is possible to use it as chain transfer agent for further polymerization. Moreover due to its amphiphilic character, emulsion polymerization can be carry out without the need of using additional surfactant. A mixture of two hydrophobic monomers was copolymerized: methyl methacrylate (MMA) and butyl acrylate (BA) in a ratio of 10:1 (w/w), and ACPA was used as initiator. The choice of these monomers for the hydrophobic chain is a commitment between the stiffness offered by MMA and also some flexibility afforded by BA, thus allowing to obtain a rigid structure capable of responsiveness to an external stimulus.

Figure 3.3 shows the chemical structures of MMA and BA and Figure 3.4 shows the chemical structures of the copolymers.

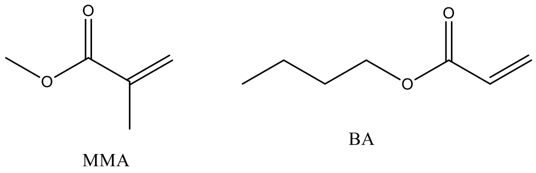

Figure 3.3. Chemical structures of MMA and BA.

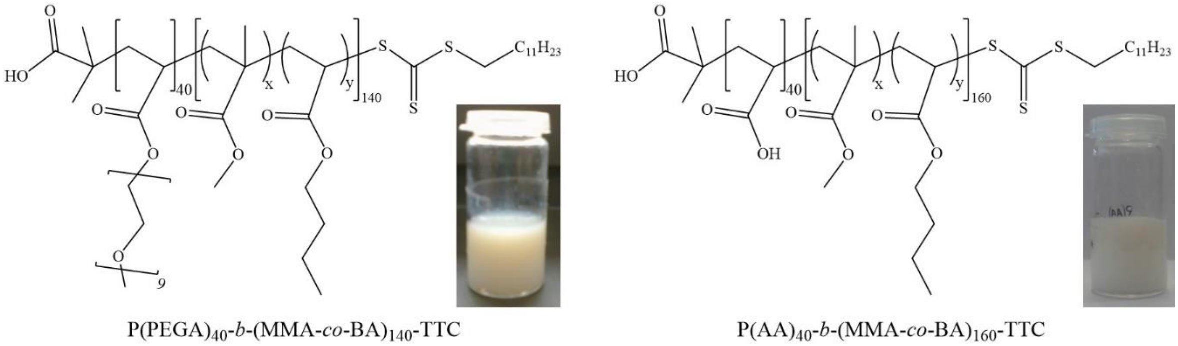

Figure 3.4. Chemical structures of block copolymers derived from (left) P(PEGA$_{40}$)-TTC and (right) P(AA$_{40}$)-TTC, and photographs of the corresponding latex.

Table 3.2 shows the theoretical and experimental molecular weight values of the block copolymers. Conversion of monomer was determined by gravimetric analysis of the withdrawn aliquots during the polymerization. In ***Annex B*** a detailed explanation of the calculation and the *%Conversion* profile of the polymerization can be found.

Table 3.2. Theoretical and experimental data of *%Conversion*, molecular weight and degree of polymerization (DP) of block copolymers, determined by gravimetric analysis and GPC-SEC.

Sample name	***copPEGATTC***	***copAATTC***
copolymer	**P(PEGA$_{40}$)-*b*-(MMA-*co*-BA)$_{140}$-TTC**	**P(AA$_{40}$)-*b*-(MMA-*co*-BA)$_{160}$-TTC**
$\bar{M}_{n\ (theoretical)}$ g/mol	35332	20726
DP $_{(theoretical)}$	173	168
%Conversion	81 %	95%
$\bar{M}_{n\ (exp\_grav)}$ g/mol*	31971	19862
DP $_{(exp\_grav)}$ *	140	160

* $\bar{M}$n and DP estimated using the *%Conversion* determined by gravimetric analyzes.

RAFT emulsion polymerization allowed to grow a hydrophobic chain from the previously prepared macroRAFT agents, yielding the diblock copolymers P(PEGA$_{40}$)-*b*-(MMA-*co*-BA)$_{140}$-TTC (named *copPEGATTC*) and P(AA$_{40}$)-*b*-(MMA-*co*-BA)$_{160}$-TTC (named *copAATTC*). Table 3.2 shows that good monomer conversion were obtained, yielding experimental $\bar{M}_n$ near the theoretical value.

These block copolymers have an amphiphilic character which self-assemble forming well-defined spherical micelles in water. Table 3.3 shows the results obtained from DLS measurements and in both cases, low values of PdI were achieved indicating that the samples are almost homogeneous, i.e. the spherical polymeric micelles have a narrow average size distribution. P(PEGA$_{40}$)-*b*-(MMA-*co*-BA)$_{140}$-TTC has an average hydrodynamic diameter (d_{average}) of 98.8 nm and a negative zeta potential. As expected, P(AA$_{40}$)-*b*-(MMA-*co*-BA)$_{160}$-TTC has a higher negative zeta potential and the d_{average} is also a little higher (125.1 nm). This could be due to the higher conversion of monomer which increases the hydrophobic chain and hence the diameter of the spherical micelle is bigger and/or due to the repulsive interactions inter- and intra- MR chains, thus making the hydrophilic chains more stretched and separated.

Table 3.3. DLS and zeta potential measurements of the block copolymers*.

	d_{average} (nm)	d_{number} (nm)	PDI	ζ (mV)	pH
copPEGATTC	98.8	74.7	0.057	- 30.5 ± 12.9	4.9
copAATTC	125.1	91.9	0.083	- 59.5 ± 11.1	7.5

Note: the measurements performed for the copolymers are from a dilution of the latex (~25µL of latex dispersed in 5 mL of ultra-pure water).

3.4. Preparation of gold nanocomposites via RAFT polymerization

As explained before, in this work three main strategies were explored in order to prepare gold nanocomposites using the block copolymers prepared via RAFT emulsion polymerization. The strategies is presented and discussed according to the following order: first (**3.4.1.**) the *post-modification* strategy, second (**3.4.2.**) the *in situ* generation of Au NPs in the presence of previously prepared copolymer, and third (**3.4.3.**) *grafting from* strategy. The last one is divided in two distinct pathways as discussed below.

3.4.1. Post-modification strategy

The *post-modification* strategy involves mixing of the diblock copolymer and Au NPs, prepared via the citrate method, at room temperature for 2 hours followed by centrifugation. The precipitate obtained was redispersed in ultra-pure water. This straightforward strategy was applied for the copolymers P(PEGA$_{40}$)-*b*-(MMA-*co*-BA)$_{140}$-TTC and P(AA$_{40}$)-*b*-(MMA-*co*-BA)$_{160}$-TTC, and the Au nanocomposites were named *pm*-copPEGATTC/Au and *pm*-copAATTC/Au, respectively. Note that for comparison, a diluted suspension of copolymer was also centrifuged and redispersed in the same conditions as the polymer/Au nanocomposites.

The resulting nanocomposites showed a pink color (Figure 3.5 - *insets*) due to the presence of the Au NPs.The optical properties of the nanocomposites were monitored by UV-Vis spectroscopy (Figure 3.5) and the characteristic LSPR band of Au NPs observed. As expected, a very small red-shift in the λ_{LSPR} ($\Delta\lambda$= 0.5 nm) is observed for the *pm*-copPEGATTC/Au, which can be due to the presence of the polymer that causes changes in the dielectric constant of the surrounding medium. However, in the case of *pm*-copAATTC/Au, a blue-shift ($\Delta\lambda$= - 4 nm) is observed.

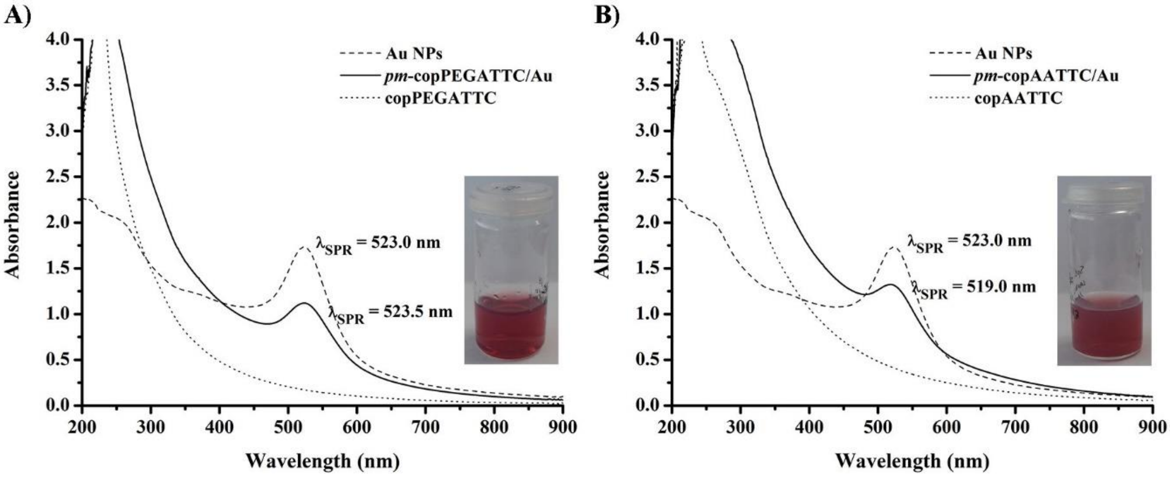

Figure 3.5. UV-Vis spectra and (*insets*) photographs of polymer/Au nanocomposites prepared via *post-modification* strategy. Polymer/Au nanocomposite prepared with (A) copPEGATTC and (B) copAATTC.

The morphology of the polymer/Au nanocomposites was probed by electron microscopy (Figure 3.6). In the case of *pm*-copPEGATTC/Au (Figure 3.6 - A), it is observed that the polymer spheres (indicated in the SEM images) are not well-defined which can be due to the soft character of the PEGA. Nevertheless, it is possible to conclude that the Au NPs are at the surface of the polymer, maybe interacting with the ether groups of the repeating unit PEGA. In fact, Au NPs are not observed isolated outside the polymer. Conversely, in the case of *pm*-copAATTC/Au (Figure 3.6 - B) most of Au NPs can be found in small aggregates outside of the polymer. This can be due to repulsive electrostatic interactions between the Au NPs (ζ= - 46 mV at pH 5.6) and the diblock copolymer, whose hydrophilic block consists in repeating units of acrylic acid, that confer a negative surface charge at pH above 4.25 (see Table 3.3). copAATTC also presents a spherical morphology, but here the polymeric spheres are more defined, which can be assigned to the rigid character of AA, in comparison to PEGA, so it is possible to measure the diameter using the SEM images: 68.7 ± 10.1 nm. This diameter value is in accordance with the d_{number} but much smaller than the d_{average} (Table 3.4), where aggregates and coalesced polymeric NPs contribute for the average diameter result.

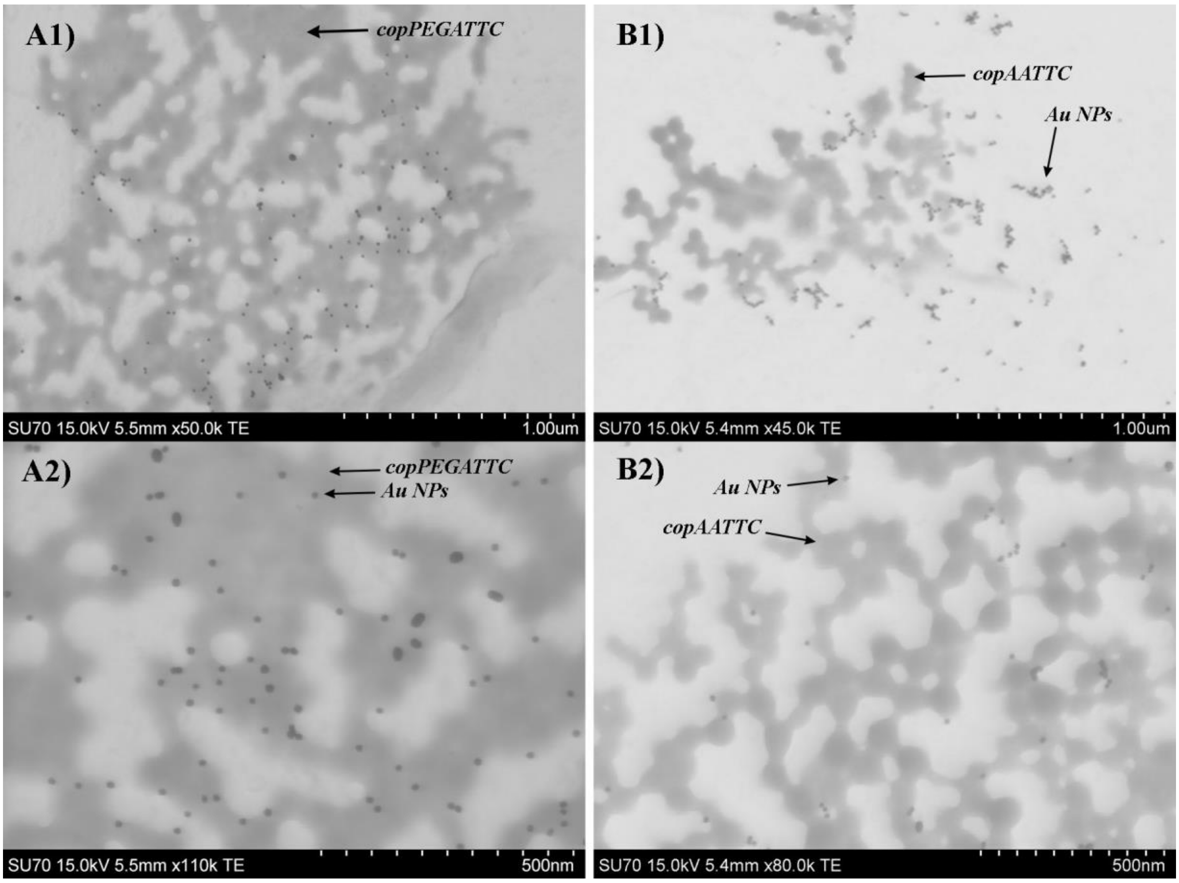
A1)
copPEGATTC
SU70 15.0kV 5.5mm x50.0k TE
1.00um
B1)
copAATTC
Au NPs
SU70 15.0kV 5.4mm x45.0k TE
1.00um
A2)
copPEGATTC
Au NPs
SU70 15.0kV 5.5mm x110k TE
500nm
B2)
Au NPs
copAATTC
SU70 15.0kV 5.4mm x80.0k TE
500nm

Figure 3.6. SEM images, in transmission mode, of polymer/Au nanocomposites prepared via *post-modification* strategy. Polymer/Au nanocomposites prepared using (A) copPEGATTC and (B) copAATTC.

Nevertheless, DLS measurements (Table 3.4) performed for both nanocomposites show only one peak in each case, for intensity and number distribution, suggesting that the Au NPs and the copolymer behave as one system during DLS measurements, but by SEM imaging in transmission mode, namely for *pm*-copAATTC/Au nanocomposites, phase separation seems to occur as a result of solvent evaporation. This suggests that in the colloidal dispersion it is thermodynamically favorable for the Au NPs to be interacting with the copolymer yet, upon water evaporation segregation is more favorable.

Table 3.4. DLS measurements of polymer/Au nanocomposites.

	$d_{average}$ (nm)	$d_{intensity}$ (nm)	d_{number} (nm)	PDI
***pm*-copPEGATTC/Au**	84.1	93.6	62.8	0.102
***pm*-copAATTC/Au**	106.9	119.9	75.51	0.105

The *Post-modification* strategy is a straightforward route because it basically involves mixing previously prepared Au NPs with the desired size and a copolymer that was prepared in a well-controlled manner via RAFT emulsion polymerization. The copolymers prepared here have the trithio moiety, which have high affinity to gold, but these copolymers form well-defined micelles in water and the trithio moiety stays in the hydrophobic core, thus it is not available to interact with the Au NPs. On the other hand, Au NPs can interact with the hydrophilic part of the copolymer (hydrophilic shell of the copolymer micelles). Here, the interaction of Au NPs with the copolymer containing PEGA is observed. In the case of the copolymer containing AA, repulsive electrostatic interactions seem to occur between the Au-Cit NPs (negative surface due to the citrate anions) and carboxylate groups from the repeating unit AA, yielding a colloid where the interactions between Au NPs and the copolymer result in phase separation upon solvent evaporation.

3.4.2. *In situ* generation of Au NPs in previously prepared copolymers

In this strategy, Au NPs were generated in the presence of the block copolymer. The gold precursor ($HAuCl_4$) was reduced using $NaBH_4$, and after stirring overnight, at room temperature, the mixture was centrifuged and the precipitate was redispersed in ultra-pure water; this sample was termed here as *washed* colloid. This strategy was explored using both copolymers P(PEGA$_{40}$)-*b*-(MMA-*co*-BA)$_{140}$-TTC and P(AA$_{40}$)-*b*-(MMA-*co*-BA)$_{160}$-TTC, and the polymer/Au nanocomposites were named *is*-copPEGATTC/Au and *is*-copAATTC/Au, respectively. Note that for comparison, a diluted suspension of copolymer was also centrifuged and redispersed in the same conditions as the polymer/Au nanocomposite. The reduction of $HAuCl_4$ was performed in variable conditions of concentration of copolymer/$HAuCl_4$ and pH, in order to understand how these parameters could influence the generation of the Au NPs in the presence of the copolymer.

Concerning, the nanocomposites prepared using P(PEGA$_{40}$)-*b*-(MMA-*co*-BA)$_{140}$-TTC (*is*-copPEGATTC/Au), the photographs and the corresponding UV-Vis spectra (Figure 3.7) clearly show that the *[HAuCl$_4$]/[copPEGATTC]* ratio influences the NP generation, indicating that there is interaction between the copolymer and the gold precursor. In fact, using a ratio of *[HAuCl$_4$]/[copPEGATTC]*=2.4 (Figure 3.7-A) a golden brown colloid is observed which is indicative of the presence of Au NPs smaller than 3 nm [38, 39]. Subsequent centrifugation of the colloid (*washed* colloid) led to a colorless solid composed of copolymer but not containing Au NPs. This indicates that the Au NPs are too small to be isolated by centrifugation at 15600g during for 30 minutes and have not been embedded in the copolymer. By decreasing the copPEGATTC concentration (*[HAuCl$_4$]/[copPEGATTC]*=4.8, Figure 3.7-B), the colloid exhibit a pink color (λ_{LSPR} 534.5 nm), however after centrifugation, the precipitate did not redisperse because it was irreversible aggregated. This could indicate that NPs were generated outside the copolymer and in the absence of surface stabilizers became prone to irreversible aggregation. Alternatively, in another experiment the $HAuCl_4$ concentration was increased (*[HAuCl$_4$]/[copPEGATTC]*=6.0, Figure 3.7-C) and a dark pink colored colloid (λ_{LSPR} 528.5 nm) was obtained. In this case, after centrifugation, the precipitate was redispersed in water but the supernatant still showed a pink color, which could indicate two situations. In the first situation, Au NPs with two average diameters were generated, i.e. Au NPs that did not precipitate by centrifugation at 15600g for 30 minutes, remained in the supernatant, and bigger Au NPs that precipitated by centrifugation. In the second situation, one can consider the generation of small NPs with and without copolymer, in which the NPs without copolymer are not isolated by centrifugation (at 15600g for 30 minutes) and the NPs with copolymer are. In fact, the size of the NPs in this colloid was confirmed by electron microscopy (Figure 3.8). Through SEM observation, it is concluded that Au NPs are dispersed outside the copolymer, and some NPs that seem to be at the surface of the polymeric sphere. These Au NPs have an average diameter of 8.1 ± 1.4 nm, which corroborates what was referred before in the second situation. Furthermore the observation of the Au NPs at the surface and outside the copolymer indicates that stabilizing interactions between gold species and the trithio group in the hydrophobic core of the polymer sphere were not present, instead interactions via the ether groups of the hydrophilic PEGA shell have probably occurred. One last experiment was performed using the ratio *[HAuCl$_4$]/[copPEGATTC]*=6.0, but in this case the pH of the mixture of $HAuCl_4$ with copPEGATTC was increased to 8 before adding the reducing agent ($NaBH_4$). Figure 3.7-C,D clearly show the pH influence on the Au NPs generation. When the pH was raised from 4 to 8 a slight brown color appeared and the characteristic LSPR band of Au NPs is not observed, even after 16h of reaction (Figure 3.7-D). In fact, as referred in the introduction, $[AuCl(OH)_3]^-$ and $[Au(OH)_4]^-$ are the species present in solution at pH 8, which have low reactivity and slow nucleation kinetics. [43, 44]

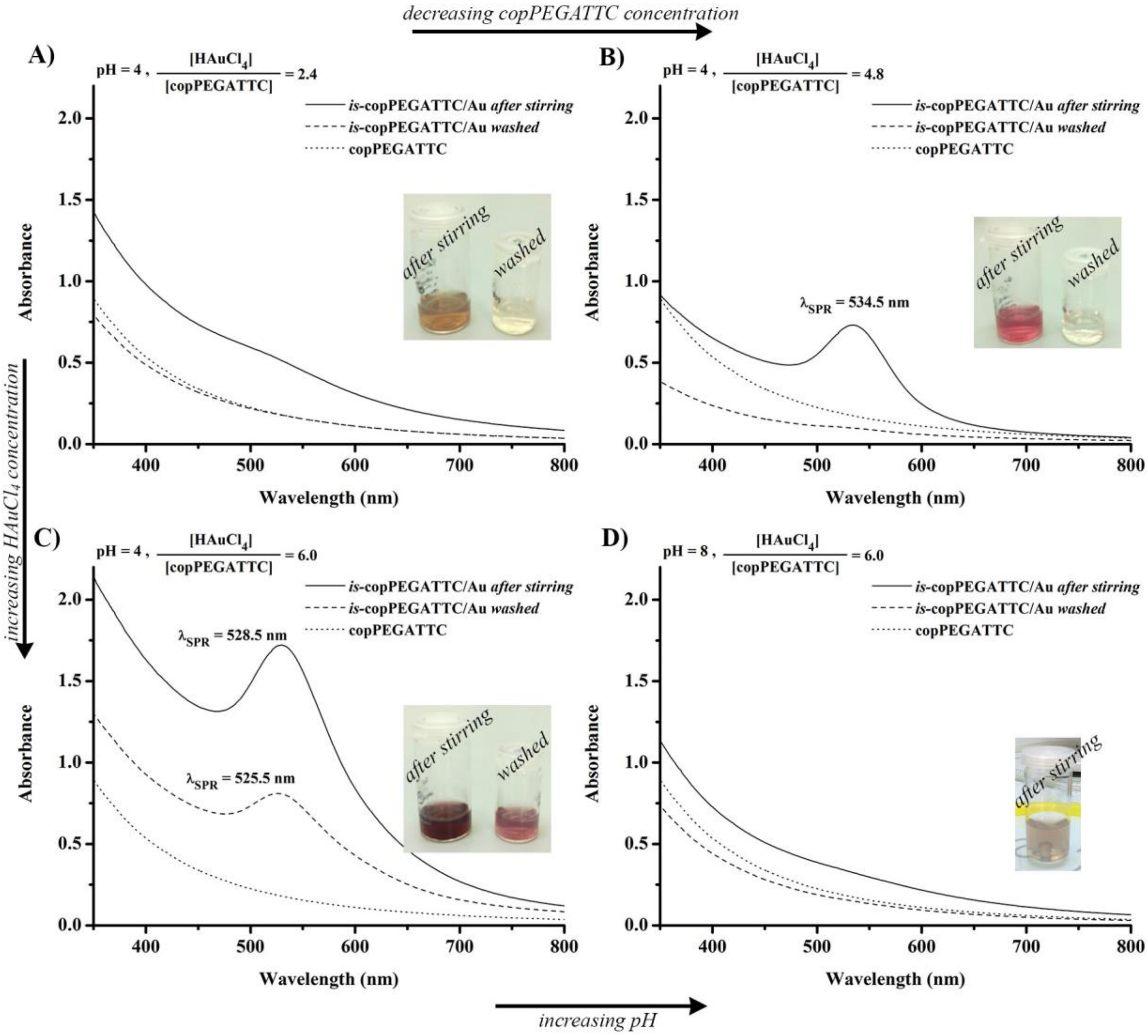

Figure 3.7. UV-Vis spectra of *is*-copPEGATTC/Au nanostructures, varying (A, B and C) copPEGATTC and $HAuCl_4$ concentration and (C and D) pH. The *insets* show the corresponding photographs of the colloids.

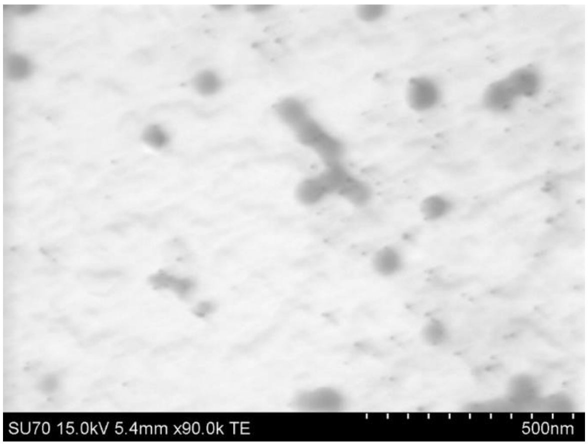

Figure 3.8. SEM image, in transmission mode, of *is*-copPEGATTC/Au nanocomposites, after stirring, prepared using the ratio *$[HAuCl_4]/[copPEGATTC]$*=6 at pH=4.

Similarly, nanocomposites of P(AA$_{40}$)-*b*-(MMA-*co*-BA)$_{160}$-TTC were prepared by varying the *[HAuCl$_4$]/[copAATTC]* ratio. As the best results using the previously discussed copolymer were obtained using the ratio *[HAuCl$_4$]/[copPEGATTC]=6, i*n this case a value below 6 was also considered as well as a couple of higher *[HAuCl$_4$]/[copAATTC]* ratios. Specifically, the values 4.0, 6.0, 12.0 and 30.0 have been tested in order to better understand the influence of the amount of copolymer on Au NPs generation. Actually, using the ratio *[HAuCl$_4$]/[copAATTC]*= 30 (Figure 3.9-A,B) a blue/purple colloid was obtained with a broad LSPR band, indicating that NPs with a large particle size distribution, anisotropic shapes and/or aggregates were generated. After centrifugation (Figure 3.9-C1), redispersion of this colloid was not possible since it aggregated irreversibly. Also the UV-Vis spectra of supernatant showed a peak at 225 nm assigned to $HAuCl_4$ suggesting that the gold salt was not completely reduced to Au^0. By increasing the copAATTC concentration (Figure 3.9-A,B) the color of the colloid turns from the purple/blue to a more purple-brownish color. Centrifugation of these colloids indicated that two populations of Au NPs were generated. Small Au NPs (< 10 nm) that did not precipitate by centrifugation at 15 600g, 30 min (as observed before when copPEGATTC was used) and Au NPs with bigger diameters or that are associated with the copolymer and were centrifuged together. Through visual and UV-Vis spectra observation of the washed colloids (Figure 3.9-C), it is possible to assert that using *[HAuCl$_4$]/[copAATTC]*= 12, the amount of copolymer still was not enough to obtain a stable colloid since the precipitate was not totally redispersed and it also presented a purple color thus indicating aggregation. Regarding *[HAuCl$_4$]/[copAATTC]*= 4 (Figure 3.9-C4), the supernatant presented a strong brown color and the UV-Vis spectrum does not show a LSPR band which could indicate that Au NPs have an average diameter below 3 nm. Using a ratio of *[HAuCl$_4$]/[copAATTC]*= 6, the supernatant also presented that brown color (Figure 3.9-C3), also indicating that NPs with diameter below 3 nm were generated. Yet, the redispersed precipitate had a pink color with a well-defined LSPR band at 523.5 nm, which indicates that bigger and stable NPs were generated, contrary to the ones prepared with *[HAuCl$_4$]/[copAATTC]*= 12 and 30.

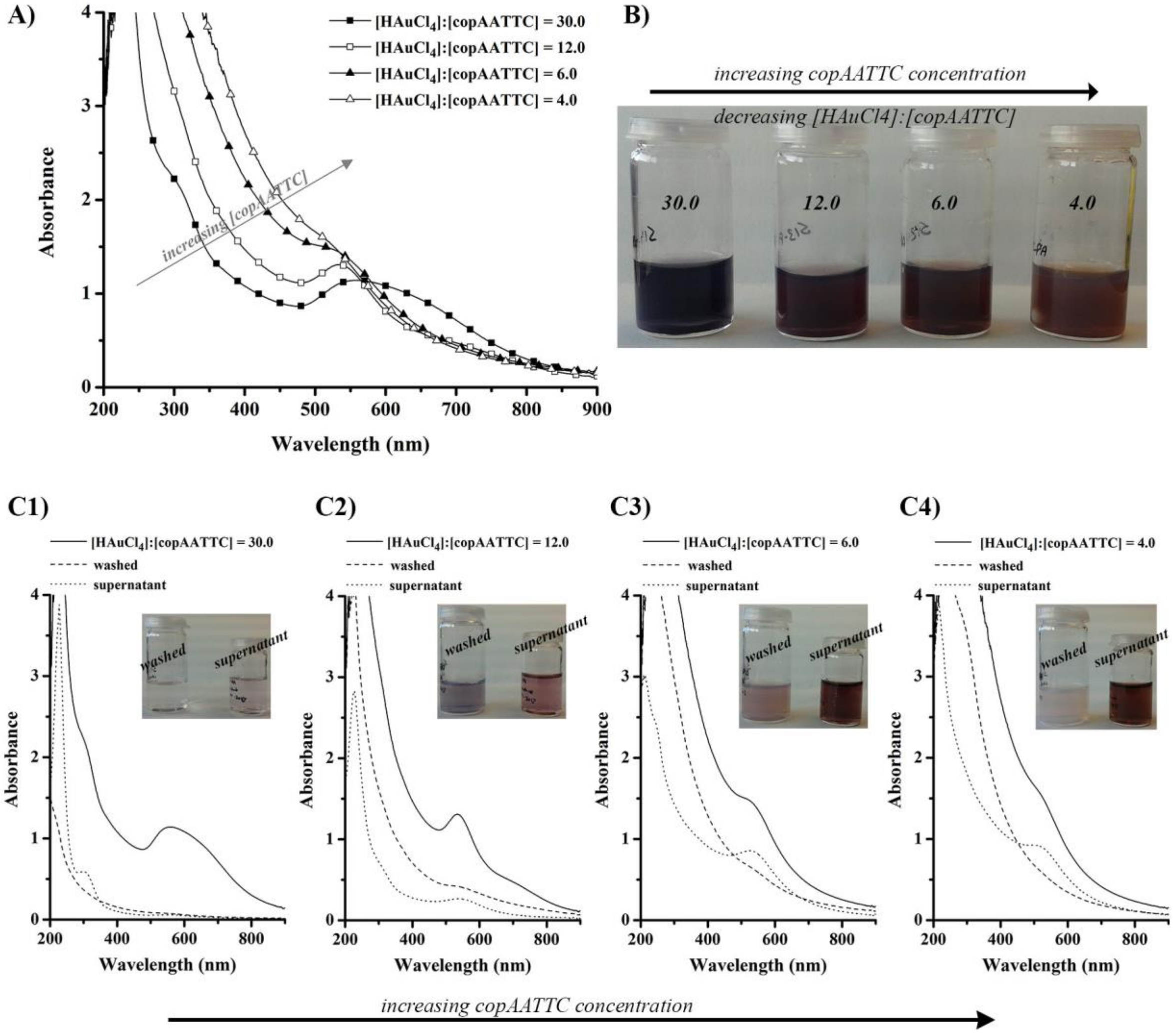

Figure 3.9. (A) UV-Vis spectra and (B) the corresponding photographs of *is*-copAATTC/Au nanocomposites, after stirring, varying the copAATTC concentration. (C) UV-Vis spectra and (*inset*) the corresponding photographs of *is*-copAATTC/Au nanocomposites shown in A and B, after being precipitated by centrifugation and redispersed (*washed*) and the supernatant, respectively.

The influence of pH in the generation of NPs was also studied. For that, the pH of a solution containing $HAuCl_4$ and copAATTC (*[$HAuCl_4$]/[copAATTC]* = 6, which have pH=4) was raised to pH 6 and 8 using NaOH. Figure 3.10-A,B show that with the increase of pH the absorbance of the LSPR band increases and the colloid is less brown, which could indicate that there is an increase of NP size with the increase of the pH. In fact, this was confirmed after centrifugation (Figure 3.10-C). By increasing the pH, the supernatant is less brown, indicating that less NPs below 3 nm were generated, and the precipitate redispersed is more purple/pink indicating that more NPs with bigger sizes were generated. In particularly, the washed nanocomposite prepared at pH 8 presented λ_{LSPR} at 522.5 nm.

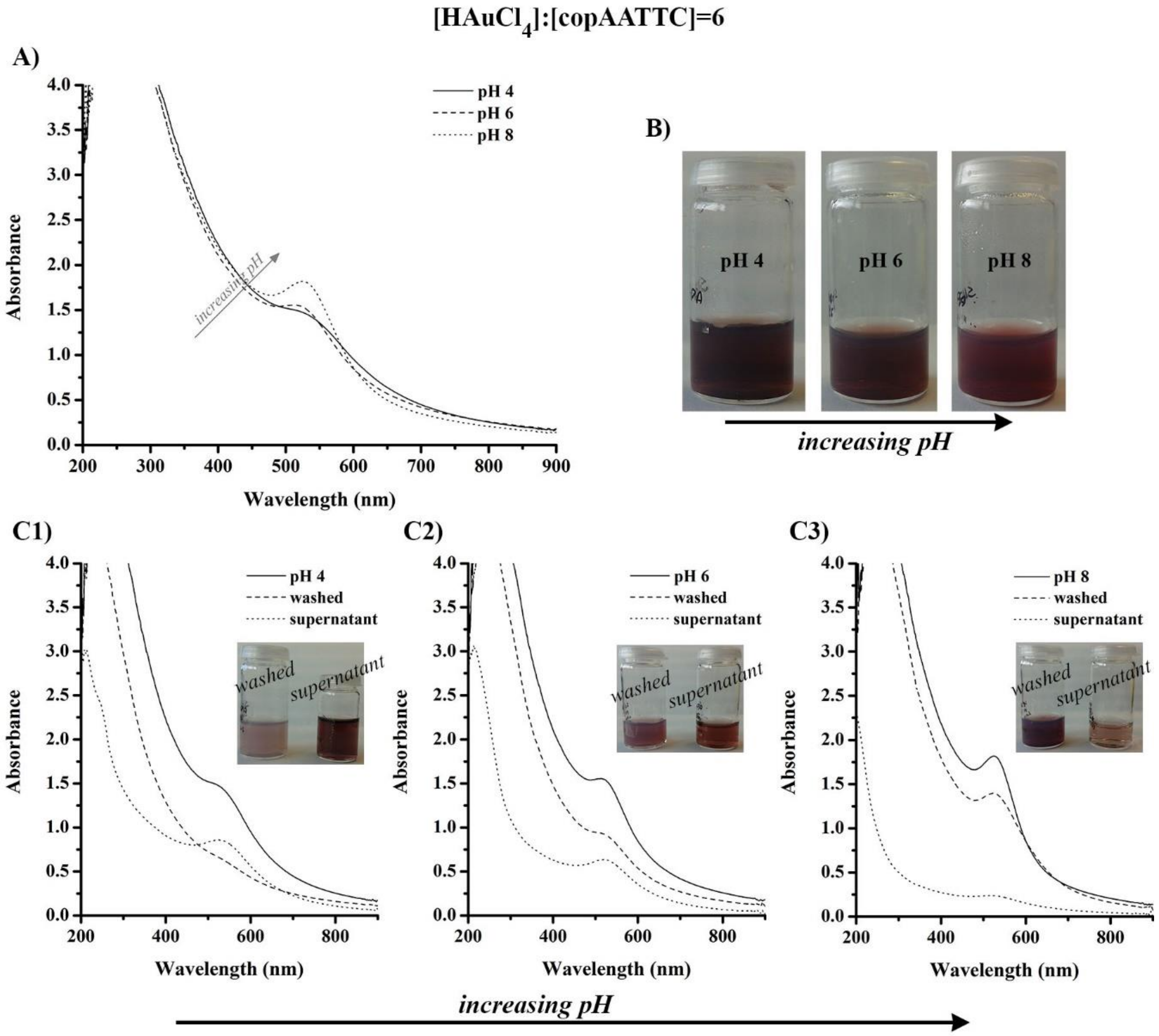

Figure 3.10. (A) UV-Vis spectra and (B) the corresponding photographs of *is*-copAATTC/Au nanocomposites, after stirring, varying pH. (C) UV-Vis spectra and (*inset*) the corresponding photographs of *is*-copAATTC/Au nanocomposites shown in A and B, after being precipitated by centrifugation and redispersed (*washed*) and the supernatant, respectively.

The morphology and the size of the Au NPs at pH 4 and 8 were probed by electron microscopy. Figure 3.11 shows that in both cases NPs seem to be at the surface of the polymeric spheres and have a spheroidal morphology. Although at pH 4 (Figure 3.11-A), some NPs seem to be inside the hydrophilic shell, namely in Figure 3.11-A1 where two Au NPs can be observed inside the copolymer, probably in the hydrophilic AA shell. The average diameter of the generated Au NPs is 4.5±1.1 nm and 5.9±1.6 nm for pH 4 and 8, respectively. In this case, the variation of pH influences not only the Au(III) species in solution but also the protonation of the carboxylic groups of hydrophilic AA shell. Thus on one hand, at pH 8, the $[AuCl(OH)_3]^-$ and $[Au(OH)_4]^-$ species have low reactivity contributing for a slower nucleation, and on the other hand Au^{3+} ion can form complexes with the deprotonated carboxylic groups from AA.

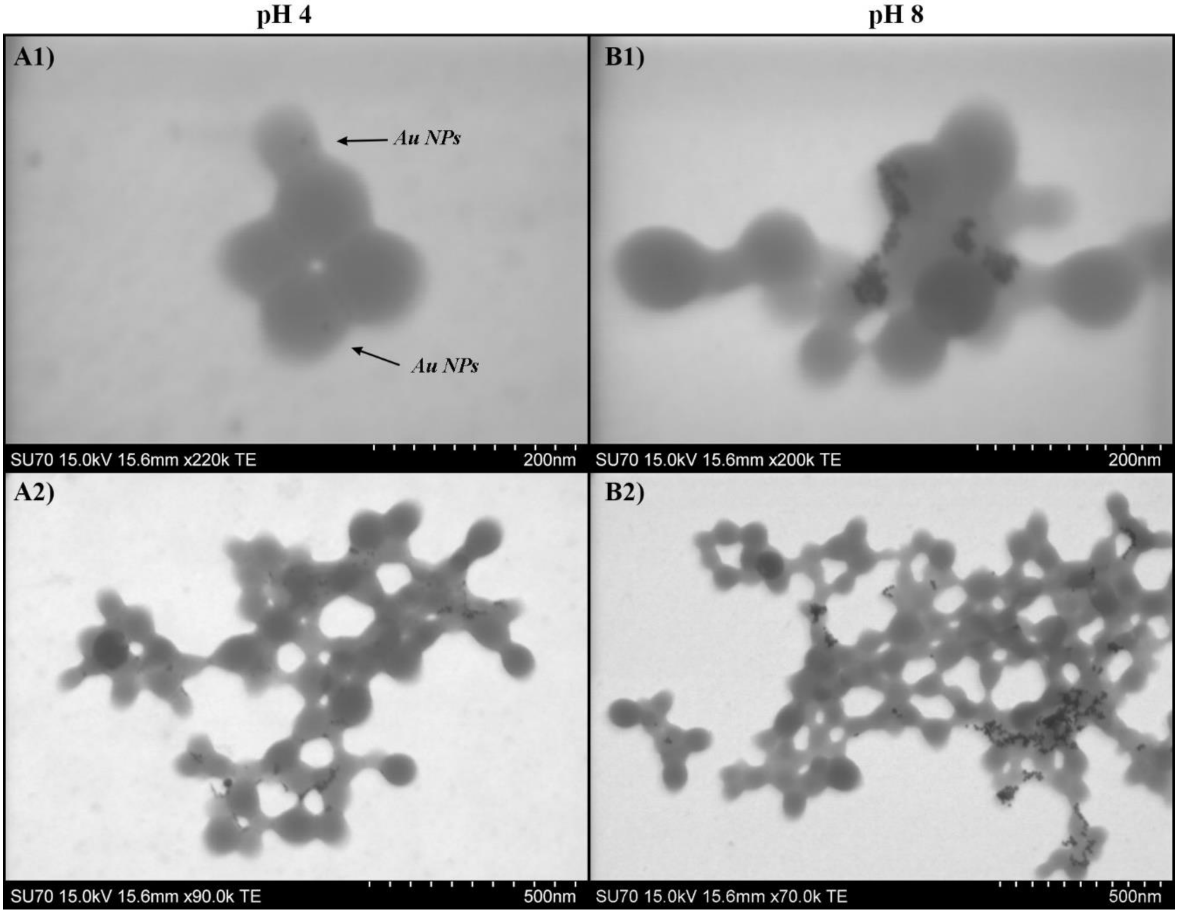
pH 4
pH 8
A1)
Au NPs
Au NPs
SU70 15.0kV 15.6mm x220k TE
200nm
B1)
SU70 15.0kV 15.6mm x200k TE
200nm
A2)
SU70 15.0kV 15.6mm x90.0k TE
500nm
B2)
SU70 15.0kV 15.6mm x70.0k TE
500nm

Figure 3.11. SEM images, in transmission mode, of *is*-copAATTC/Au nanostructures prepared at (A) pH 4 and (B) pH 8.

In situ generation of Au NPs in the presence of the diblock copolymers is very attractive since it occurs in a one-step synthesis. The block copolymer is previously well-tailored via RAFT emulsion polymerization and then the Au NPs are generated. In this sub-chapter the effect of several aspects, such as [$HAuCl_4$]/[copolymer] ratio, pH and the chemical nature of the copolymer, namely the hydrophilic part of the copolymer, on the size and size distribution of the NPs was demostrated. On one hand, using copPEGATTC the best results were found at pH = 4 using the ratio [$HAuCl_4$]/[copPEGATTC]=6, on the other hand, using copAATTC the best results were found using the same ratio ([$HAuCl_4$]/[copPEGATTC]=6) but at pH= 8. However, in both cases, Au NPs were generated on the surface of the copolymer and not in the hydrophobic core where the trithio moiety is located.

3.4.3. *Grafting from* strategy

The *grafting from* strategy involves the growth of a polymer from a surface. In this case the RAFT agents have the advantage to be able to form a strong interaction with gold due to the presence of the trithio group. Thus it is possible to immobilize the RAFT agent onto the surface of Au NPs and then grow the polymer chains in a controlled way via RAFT polymerization.

Here, the *grafting from* strategy requires two main distinct steps: 1st the preparation of well-coated Au NPs with MR; and 2nd the growth of a hydrophobic chain via RAFT emulsion polymerization from MR@AuNPs yielding stable and robust copolymer@AuNPs - shell@core type nanostructures. Actually, in the first step of the *grafting from* strategy, the preparation of MR@AuNPs was explored following two pathways which is discussed in the next *sub-chapters*: ***3.4.3.2.*** *in situ* generation of Au NPs in the presence of previously prepared macroRAFT agents, and ***3.4.3.3.*** adsorption of macroRAFT agents onto Au NPs.

Three macroRAFT agents were explored in this *grafting from* strategy: P(PEGA$_{40}$)-TTC, P(AA$_{40}$)-TTC and P(AA$_{20}$-*co*-PEGA$_{20}$)-TTC. The first two were already studied in the *post-modification* strategy and in the *in situ* generation of the Au NPs in the presence of the copolymer. The later was introduced here since it consists in a mixture of AA and PEGA (theoretical DP = 20 AA and 20 PEGA), $\overline{M}_n$ (experimental, ^{1}H-NMR) of 12869 g/mol which was available in the group. As these MR agents are amphiphilic their critical micelle concentration (CMC) was determined. The results are presented and discussed in the *sub-chapter* ***3.4.3.1.***

3.4.3.1. Determination of Critical Micelle Concentration (CMC) of MR agents

The MR agents studied in this work have an a amphiphilic character since they have two main moieties: a hydrophobic *C12* chain, which consists in the *Z*-group of the RAFT agent, and the *R*-group that consists in a hydrophilic chain containing repeating units of acrylic acid (AA) or/and poly(ethylene glycol) methyl ether acrylate (PEGA). Therefore, depending on their concentration in water, micelle structures can be formed, which may influence the generation of the Au NPs in the presence of the MR agent, as well as the MR agent adsorption onto Au NPs. In this *sub-chapter*, it is presented and discussed the results for the determination of the critical micelle concentration (CMC) of P(PEGA$_{40}$)-TTC, P(AA$_{40}$)-TTC and also of a third MR agent P(AA$_{20}$-*co*-PEGA$_{20}$)-TTC.

The determination of CMC was performed using conductivity measurements and also dynamic light scattering (DLS) measurements [197–199]. In the latter method, an increase in the intensity counts (kcps) indicates the formation of particles, additionally the hydrodynamic diameter of the formed particles is measured. For each MR agent (P(PEGA$_{40}$)-TTC, P(AA$_{40}$)-TTC and P(AA$_{20}$-*co*-PEGA$_{20}$)-TTC), a set of different concentrations in ultra-pure water was prepared and conductivity and DLS measurements were performed. In another experiment the same set of solutions was prepared but the pH was adjusted using NaOH solution (pH 7.5-8). In this case, the conductivity measurements were not performed because the ionic strength has a strong influence in the results. The results were compiled and are shown in Figure 3.12, Figure 3.13 and Figure C.5 (in ***Annex C***).

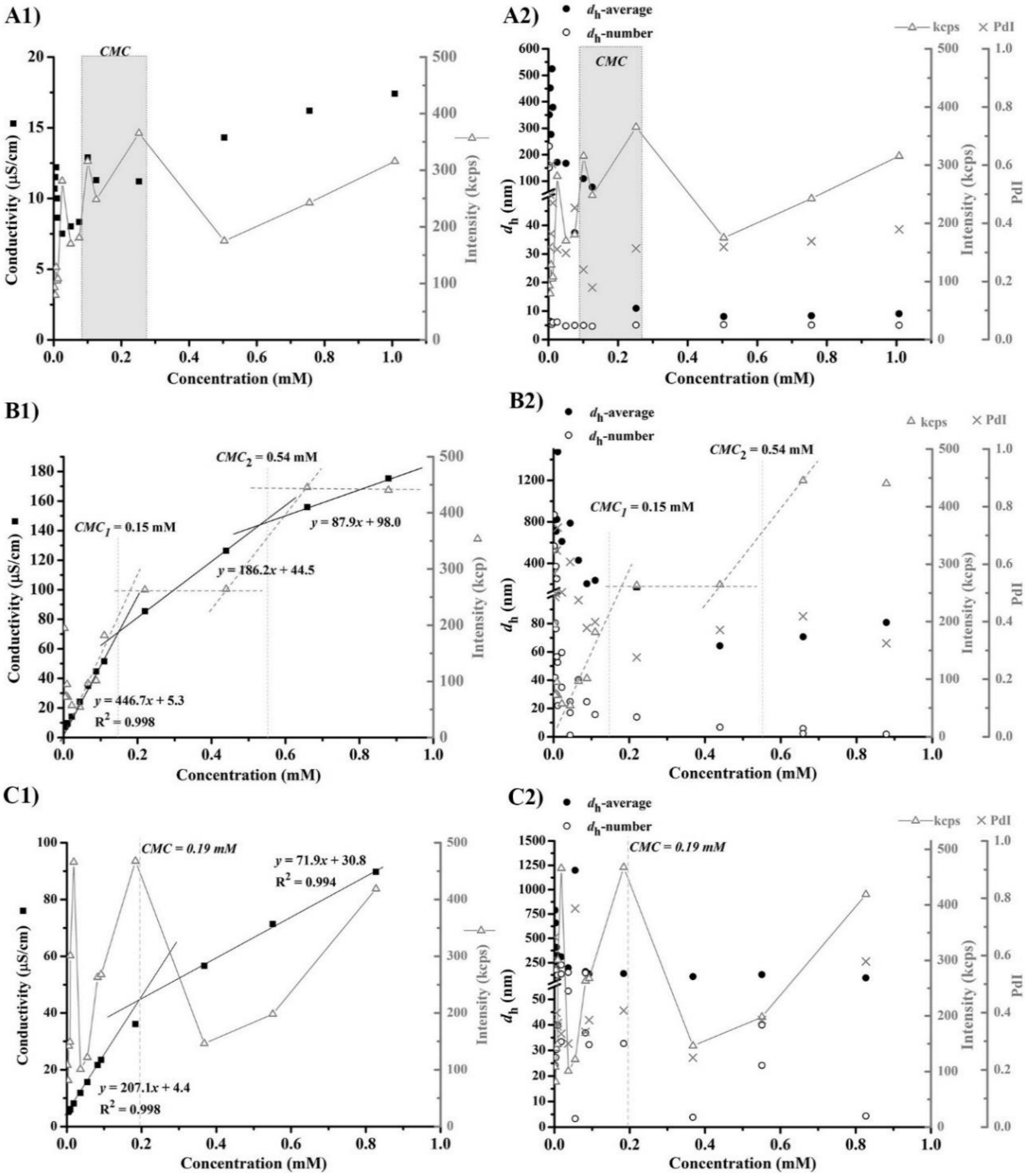

Figure 3.12. (A1, B1, C1) Conductivity and (A2, B2, C2) DLS measurements as a function of concentration of (A) P(PEGA$_{40}$)-TTC, (B) P(AA$_{40}$)-TTC and (C) P(AA$_{20}$-co-PEGA$_{20}$)-TTC, prepared in ultra-pure water. In A1, B1 and C1 the intensity counts (kcps) from DLS measurements are also overlapped.

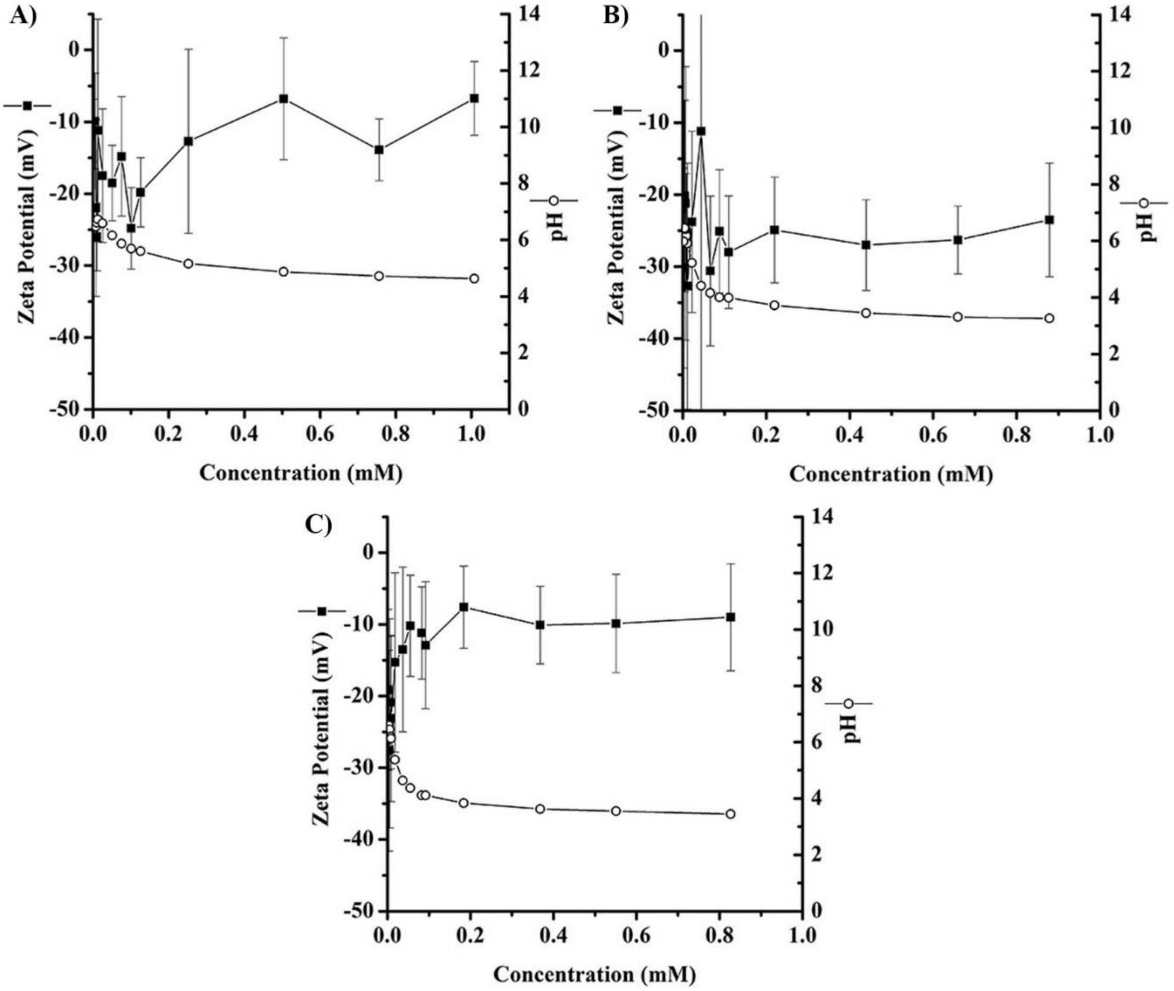

Figure 3.13. Zeta potential and pH measurements of (A) P(PEGA$_{40}$)-TTC, (B) P(AA$_{40}$)-TTC and (C) P(AA$_{20}$-co-PEGA$_{20}$)-TTC, prepared in ultra-pure water.

Regarding the samples prepared in ultra-pure water, the MR P(PEGA$_{40}$)-TTC presents low conductivity and therefore the conductivity profile is inconclusive for the determination of the CMC (Figure 3.12-A1). Still DLS measurements (Figure 3.12-A) seem to indicate the presence of three CMC values (at around 0.025, 0.1 and 0.25 mM). In fact, at concentration 0.1 mM the conductivity increases and PdI presented the lowest value which could indicate that this concentration corresponds to a CMC. DLS measurements also show that the hydrodynamic diameter, in average, stabilizes around 10 nm from the concentration 0.2 mM onwards whilst for all MR agent concentrations the hydrodynamic diameter, in number (d_{number}) is around 5 nm. Moreover, in Figure 3.13-A is observed that the pH decreased slightly with the increase of concentration and stabilizes around pH 4.5, and the zeta potential is negative for all concentrations with values around -10 to -20 mV.

Unlike the previously case, the MR agent P(AA$_{40}$)-TTC has in its structure repeating units containing carboxylic acid groups, so it was possible calculate a CMC at 0.15 mM by conductivity measurements, see Figure 3.12-B1. Furthermore, overlapping the intensity counts (kcps) (from DLS measurements) it seems that a second CMC may exist at 0.54 mM. Figure 3.13-B shows that the pH decreased slightly as the concentration increased and stabilized around pH 3, whilst the zeta potential is negative for all concentrations, around -25 mV.

Concerning P(AA_{20}-*co*-$PEGA_{20}$)-TTC, which also contains carboxylic acid groups in its structure, it was possible to calculate a CMC at 0.19 mM by conductivity measurements. Indeed, this value was confirmed by DLS measurements, see Figure 3.12-C1, where an increase of intensity counts is observed for the concentration 0.18 mM. pH measurements show that this MR agent behaves similarly to P(AA_{40})-TTC (pH ~3), but zeta potential measurements are more alike the P($PEGA_{40}$)-TTC (ζ around -10 mV).

In summary, by conductivity measurements it was possible to determine the CMC of P(AA_{43})-TTC and P(AA_{20}-*co*-$PEGA_{20}$)-TTC but for P($PEGA_{40}$)-TTC it was not possible due to its low conductivity. P(AA_{43})-TTC and P(AA_{20}-*co*-$PEGA_{20}$)-TTC have carboxylic acid groups on the repeating unit (acrylic acid) that confer some conductivity to the MR agent, but P($PEGA_{40}$)-TTC only has one carboxyl group per chain which belongs to the *R* terminal of the RAFT agent. These CMC values were confirmed using intensity counts of DLS measurements. Additionally, DLS measurements suggest that a second CMC value could exist for P(AA_{43})-TTC and P($PEGA_{40}$)-TTC but without certainties. Table 3.5 summarizes the CMC values determined for each MR agent.

Table 3.5. Results of critical micelle concentration (CMC) determination.

MR	**CMC by conductivity (mM)**	**CMC by DLS (mM)**	**ζ-potential (mV)**
P($PEGA_{40}$)-TTC	---	0.1 – 0.3	~ -10
P(AA_{40})-TTC	0.15	0.1 – 0.2	~ -25
P(AA_{20}-*co*-$PEGA_{20}$)-TTC	0.19	0.15 – 0.25	~ -10

As referred before, the CMC was also determined for MR agent solutions at pH between 7.5 and 8. The results are shown in ***Annex C***, Figure C.5, since it seems that the pH does not have a significant influence on the CMC. Nevertheless, for P($PEGA_{40}$)-TTC (Figure C.5-A) and P(AA_{20}-*co*-$PEGA_{20}$)-TTC (Figure C.5-C) the count rate intensity (kcps) as well as the hydrodynamic diameter are similar at both pH values. In the case of P(AA_{40})-TTC (Figure C.5-B), the count rate intensity (kcps) shows a different profile at pH 7.5 in comparison to that observed at pH 3. In this case, there is the indication of formation of micelles above concentration 0.1mM, which is in the same range of the CMC at pH 3. Although, DLS measurements suggest that the micelles at this pH have a higher hydrodynamic diameter, this can be explained by the increase of repulsive electrostatic interaction inter- and intra-MR chains since at this pH all the carboxylic acid groups are deprotonated. In addition, zeta potential decreases for higher negative values from the concentration 0.1 mM (at 0.1mM ζ~ - 30 mV; at 0.7 mM ζ~ -60 mV).

3.4.3.2. Grafting from strategy via in situ generation of Au NPs in previously prepared macroRAFT agents

Here, the MR@Au NPs were prepared by generation of Au NPs in the presence of the macroRAFT agents using sodium borohydride ($NaBH_4$) as reducing agent. In this *sub-chapter,* parameters such as the pH, the chemical nature of MR agent and the [$HAuCl_4$]:[MR] ratio is studied in order to understand their influence in the preparation of MR@Au NPs.

3.4.3.2.1. In situ generation of Au NPs in previously prepared macroRAFT agents

Gold salt ($HAuCl_4$) was reduced in the presence of P(AA_{40})-TTC, P($PEGA_{40}$)-TTC and P(AA_{20}-*co*-$PEGA_{20}$)-TTC using sodium borohydride ($NaBH_4$) and varying the $[HAuCl_4]:[MR]$ ratio and the pH. All the colloids were prepared using the same amount of $HAuCl_4$ and using a ratio of $[HAuCl_4]:[NaBH_4]$ =1. By naked eye, photographs in Figure 3.14 clearly show that pH, $[HAuCl_4]:[MR]$ ratio and also the chemical nature of the MR agent used influence the Au NPs generation. The different colors of the colloids indicate that different sizes and/or morphologies of Au NPs were generated.

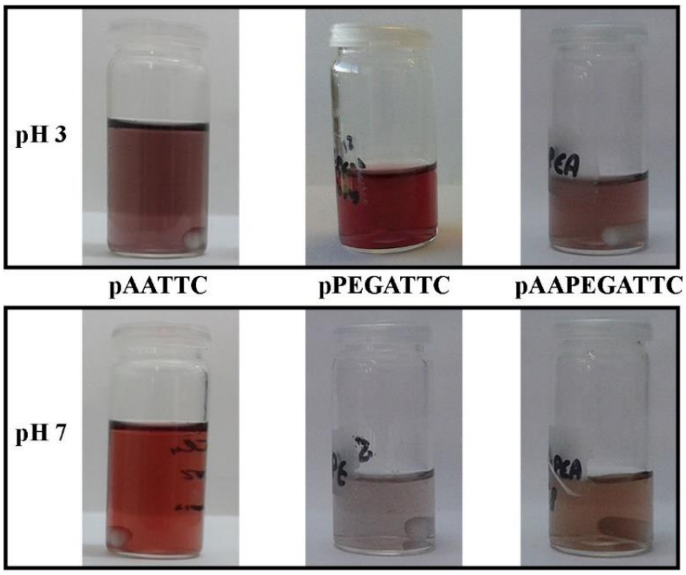

Figure 3.14. Photographs of the resulting colloids after stirring overnight. The ratio *[HAuCl$_4$]:[MR]* is 5.9 for pAATTC and 6.9 for pPEGATTC and pAAPEGATTC.

Focusing on P(AA$_{40}$)-TTC, Figure 3.14 shows that at pH 3 a purple-brownish color was observed and at pH 7 the colloid had a red-brownish color. This has already been observed before for the copolymer derived from the MR agent P(AA$_{40}$)-TTC, which at pH 8 originated a well-defined LSPR band and a more pinkish colloid than at pH 3. Therefore, for this MR agent we focused on the study of the variation of MR concentration, at pH 7, as shown in Figure 3.15. Increasing the MR concentration the colloidal solutions were browner indicating the formation of NPs with smaller diameters (Figure 3.15-B). In fact, observing the UV-Vis spectra in Figure 3.15-A, increasing MR concentration the LSPR band decreases and the maximum of LSPR appears at lower wavelengths ($\lambda_{LSPR,\ [HAuCl_4]:[MR]=\ 13.7}$ = 516.5 nm, $\lambda_{LSPR,\ [HAuCl_4]:[MR]=\ 6.9}$ = 515.0 nm, $\lambda_{LSPR,\ [HAuCl_4]:[MR]=\ 3.4}$ = 506.0 nm). After stirring overnight the colloids were washed by centrifugation and the resulting precipitate redispersed (*washed* colloid) as well as the supernatant were analyzed by UV-Vis spectroscopy, Figure 3.15-C. Using the higher concentration of MR agent, *[HAuCl$_4$]:[MR]* = 3.4, precipitation of the NPs was not possible which indicated that NPs have a diameter below 10 nm. Concerning the other colloids, after centrifugation the supernatant also showed a pink coloration indicating the generation of two sizes of Au NPs. Indeed, UV-Vis spectra show that the washed colloid prepared using the ratio *[HAuCl$_4$]:[MR]* = 6.9 (Figure 3.15-C2) has the λ_{LSPR} at 519.0 nm and the intensity of this peak is very weak whilst the absorbance of the *supernatant* peaked at 514.0 nm is much higher. The same is observed for the colloid prepared using *[HAuCl$_4$]:[MR]* = 13.7, whose the *supernatant* (λ_{LSPR} = 515.5 nm) has higher absorbance than the *washed* colloid (λ_{LSPR} = 519.0 nm). Moreover, it seems that more NPs with higher average diameter were generated in this last case, when compared with the colloid prepared using *[HAuCl$_4$]:[MR]* = 6.9.

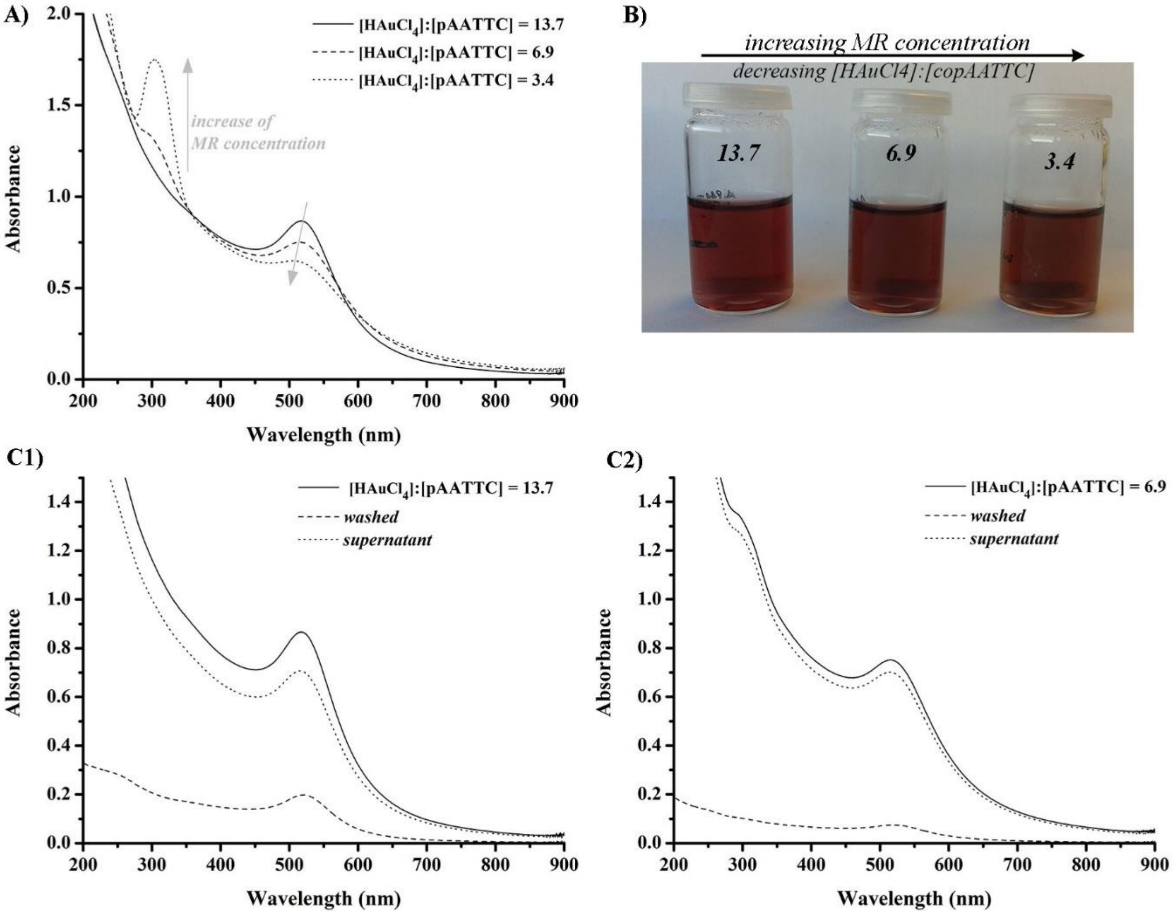

Figure 3.15. (A) UV-Vis spectra of colloids preparedusing P(AA$_{40}$)-TTC at pH 7 after stirring overnight and (B) the corresponding photographs. (C) UV-Vis spectra of colloids prepared using [*HAuCl$_4$*]:[MR] ratios of 13.7 and 6.9, C1 and C2 respectively, after being centrifuged.

The color of the colloids and the UV-Vis measurements indicate that increasing the concentration of MR agent reduces the diameter of the NP. In fact, the concentrations of MR agents used here are below to the CMC value, although using the *[HAuCl$_4$]:[MR]* = 3.4 ratio the MR agent concentration (0.1 mM) is very closed to the CMC (CMC_{pAATTC} = 0.1- 0.2 mM). Moreover, it is worth to remember that the triothio moiety is available to interact with the gold. Therefore, after reduction of the Au(III) species, Au^0 nuclei are generated but the growth depends on the amount of MR chains that will confine Au^0 nuclei. Hence, higher concentrations of MR agent prevents the growth therefore the NPs are smaller. Moreover, nucleation and growth of Au NPs are also affected by the pH of the medium, as illustrated in Scheme 3.2. In fact this scheme depicts the Au(III) species in solution as well as the protonation state of AA at each pH. Although the Au NPs generation was not fully studied under these conditions, it seems that the protonation state of the AA plays an important role in the Au NPs stabilization. At low pH values, the AA repeating units are protonated therefore the ability of the MR agent to stabilize the Au NPs is limited. In turn at higher pH values, the deprotonated carboxyl groups of the MR agent confer high stability to the Au NPs as a result of the repulsive electrostatic interactions.

Scheme 3.2. Schematic representation of the influence of pH on the generation of Au NPs in the presence of P(AA$_{40}$)-TTC.

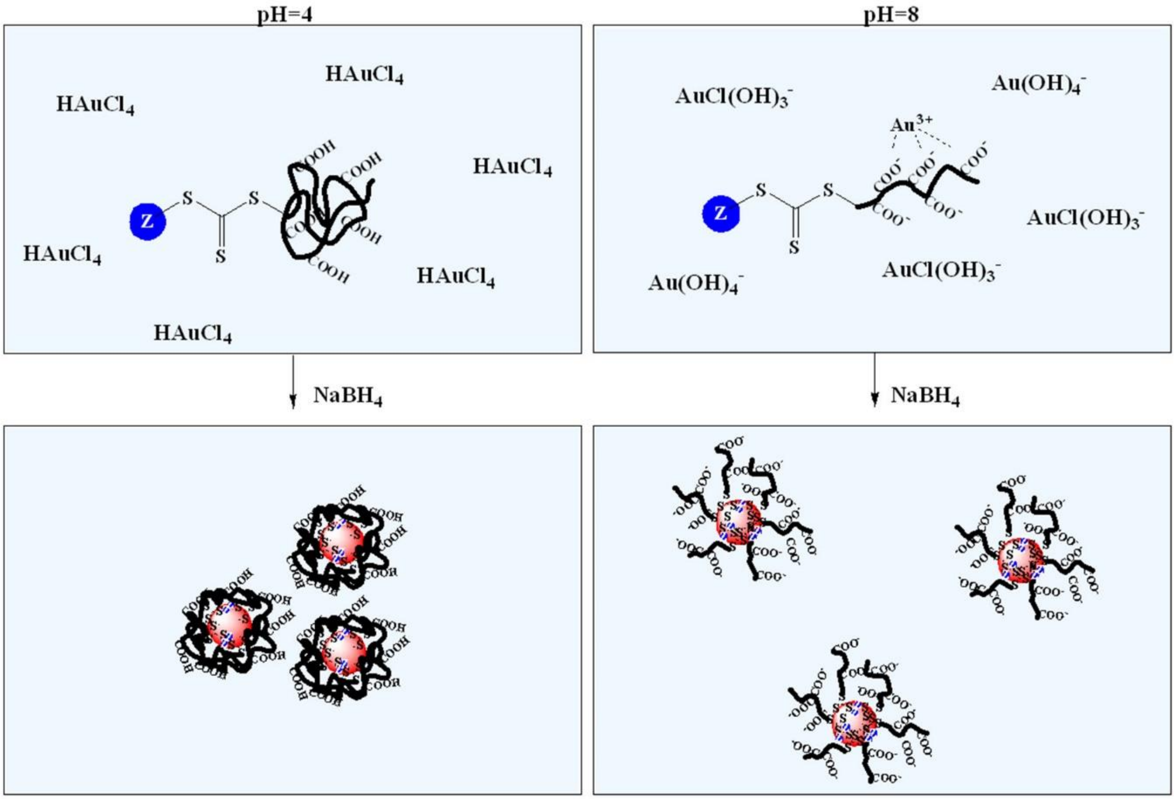

Likewise, the preparation of Au NPs in the presence of P(PEGA$_{40}$)-TTC and P(AA$_{20}$-*co*-PEGA$_{20}$)-TTC also indicates that not only the concentration of MR agent and pH influence the generation of Au NPs but also the chemical composition of the MR used, as shown in Figure 3.16. Contrary to P(AA$_{40}$)-TTC, the synthesis of Au NPs in the presence of P(PEGA$_{40}$)-TTC, at pH 3, leads to NPs with a pink color and a well-defined LSPR band ($\lambda_{LSPR,\ [HAuCl_4]:[MR]=\ 13.9}$ = 534.0 nm, $\lambda_{LSPR,\ [HAuCl_4]:[MR]=\ 6.9}$ = 530.0 nm), Figure 3.16-A. Also at pH=7 using *[HAuCl$_4$]:[MR]* = 13.9, a pink hue was observed but the LSPR band appears at lower wavelength (λ_{LSPR} = 514 nm) indicating that these NPs should be smaller. Yet, when the MR concentration was increased, *[HAuCl$_4$]:[MR]* = 6.9 at pH 7, the solution showed a purple hue and aggregates, indicating that this colloid is not stable. Alexandridis *et al* [200] described that $AuCl_4^-$ ion can form a complex with the ether groups from PEGA, which the authors referred as pseudocrown ether structures like cavities. Thus, these complexes may have an important role in the generation and stabilization of Au NPs as well as the trithio group. However, increasing the pH, $[AuCl(OH)_3]^-$ and $[Au(OH)_4]^-$ species present in solution which have low reactivity and in the presence of the ether groups could also form complexes with low reactivity. [43, 44]

In turn, the MR agent P(AA_{20}-*co*-$PEGA_{20}$)-TTC has in its chemical structure the repeating units of P($PEGA_{40}$)-TTC and P(AA_{40})-TTC. For all the cases shown in Figure 3.16-B, the colloid exhibited a brown color, although at pH 3 a slightly pink tone can be detected, namely for the one prepared using less MR - *[HAuCl₄]:[MR]*= 13.8. This colloid has a LSPR band peaked at 520.0 nm. These results show that the influence of the pH in the generation of Au NPs is associated with the chemical nature of the repeating units of the MR used. In the case of P(AA_{20}-*co*-$PEGA_{20}$)-TTC, the protonation or deprotonation of the carboxyl group of AA as well as the pseudocrown ether structure are influencing the generation of Au NPs.

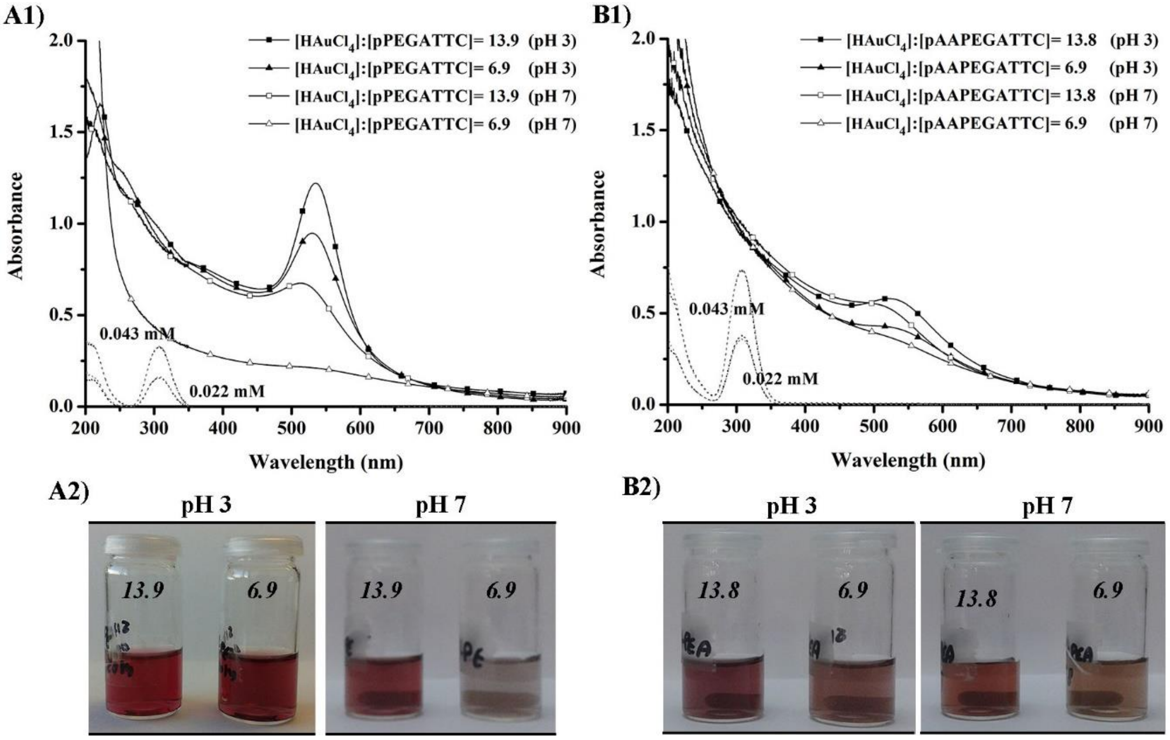

Figure 3.16. UV-Vis spectra and photographs of colloids prepared with (A) P($PEGA_{40}$)-TTC and (B) P(AA_{20}-*co*-$PEGA_{20}$)-TTC after stirring overnight. (*dash lines*) UV-Vis spectra of the MR agents at the concentration used in the preparation of the Au NPs (0.022 mM and 0.043 mM).

Additionally, it was also observed that the reduction of the gold precursor was not complete after one night (ca. 16h) and/or NPs are still evolving, namely for the colloids prepared at pH 3. In fact, in the spectrum of the colloid prepared using *[HAuCl₄]:[copPEGATTC]*= 13.9 (Figure 3.16-A1), it is possible to observe a peak at ~220 nm which is assigned to $HAuCl_4$. In view of this the colloids were characterized over 4 weeks. The colloids prepared at pH 7 did not show any significant change in the LSPR band as well as in the color over time, see the UV-Vis spectra in Figure D.6, ***Annex D***,

However for the colloids prepared using P(AA_{20}-*co*-$PEGA_{20}$)-TTC at pH 3 (Figure 3.17) the brownish-pink color observed after one night changed to a more intense pink color after 4 weeks and the UV-Vis spectra show that the LSPR band is better defined after this time. Using the ratio *[$HAuCl_4$]:[MR]*= 6.9, the increase of the LSPR band peaked at 550 nm after 4 weeks is clear. However, using the ratio *[$HAuCl_4$]:[MR]*= 13.8, which has less amount of MR agent, after the third week some aggregates started to form and so the absorbance is lower.

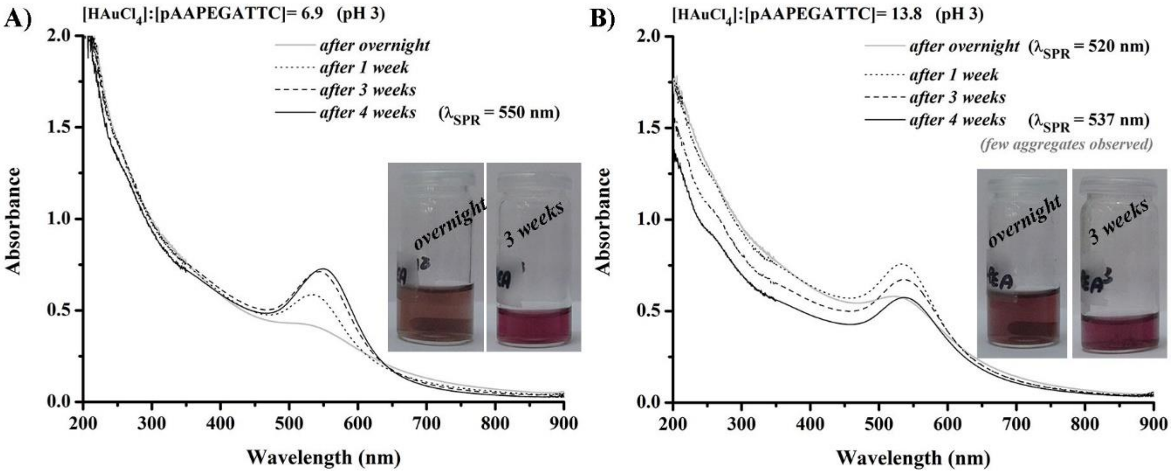

Figure 3.17. UV-Vis spectra of colloids prepared using P(AA_{20}-*co*-$PEGA_{20}$)-TTC, at pH 3. *Insets* show the photograph of the colloid after one night and 3 weeks.

Although the values of λ_{LSPR} (550 nm and 537 nm for *[$HAuCl_4$]:[MR]=6.9* and 13.8, respectively) indicate that the diameter of the NPs could be higher than 15 nm, SEM images (Figure 3.18) show NPs with diameters smaller than 10 nm. After 4 weeks the samples prepared using *[$HAuCl_4$]:[MR]=6.9* present two average sizes of Au NPs – 3.6 ± 0.1 nm and 8.6 ± 0.2 nm, and those prepared using *[$HAuCl_4$]:[MR]=13.8* present a larger size distribution - diameter of 5.0 ± 2.0 nm.

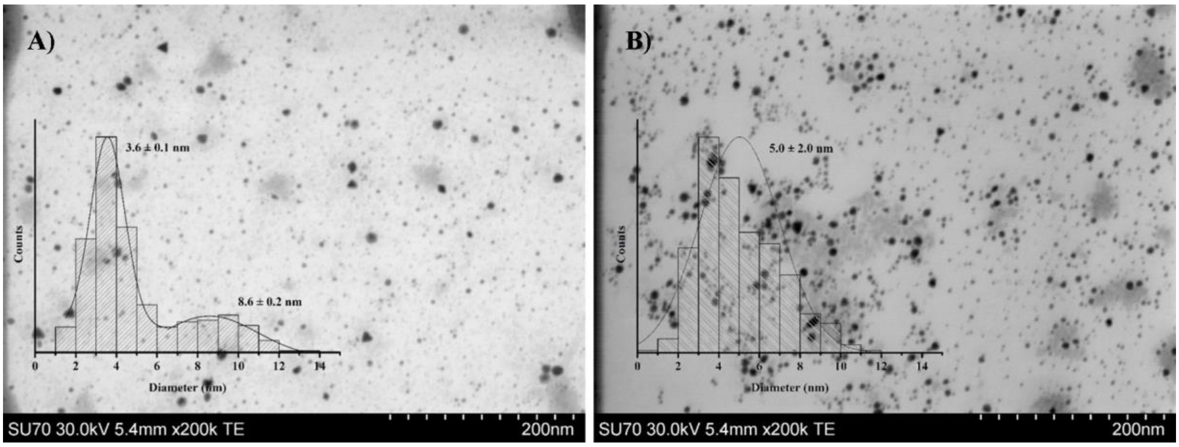

Figure 3.18. SEM images, in transmission mode, of colloids after 4 weeks of synthesis. Colloids prepared at pH 3 using P(AA_{20}-*co*-$PEGA_{20}$)-TTC: (A) *[$HAuCl_4$]:[pAAPEGATTC]*=6.9 and (B) *[$HAuCl_4$]:[pAAPEGATTC]*=13.8.

These results over time can indicate that the Au^0 nuclei generated (maybe ca. 3 nm due to the brown hue) after one night, started to aggregate leading to bigger NPs after some time. When the *[$HAuCl_4$]:[pAAPEGATTC]*=6.9 ratio was used it seems that some primary nuclei are stable and did not aggregate but other nuclei aggregated yielding NPs with an average diameter of 8.6 ± 0.2 nm. In contrast, decreasing the concentration of MR agent (*[$HAuCl_4$]:[pAAPEGATTC]*=13.8), less MR agent is available to stabilize the primary Au^0 nuclei so they grow during the first week. However, after this first week some aggregation starts to occur, as can be seen in the UV-Vis spectra (Figure 3.17-B) where the intensity of the LSPR band decreases.

Concerning the colloids prepared with P($PEGA_{40}$)-TTC at pH 3, a more detailed study was performed to better understand the evolution of the Au NPs over time in a larger range of *[$HAuCl_4$]:[MR] ratios*. For that, Au NPs were prepared using the ratios *[$HAuCl_4$]:[MR]*= 18.5, 9.2, 6.1, 4.6, 3.7, and 1.4, whilst the amount of $HAuCl_4$ was kept the same. The evolution of these colloids was followed by UV-Vis spectroscopy each week over four weeks, and DLS measurements and SEM were performed after one night and after the four weeks.

As already stated, the generation of the Au NPs is influenced by the *[$HAuCl_4$]:[MR]* ratio, as can be seen by the color of the colloids in Figure 3.19-A. Moreover, it can be observed that the intensity of the colloid color changes over the time, which is in agreement with the UV-Vis spectra shown in Figure 3.19-B and C, after one night and after 4 weeks, respectively.

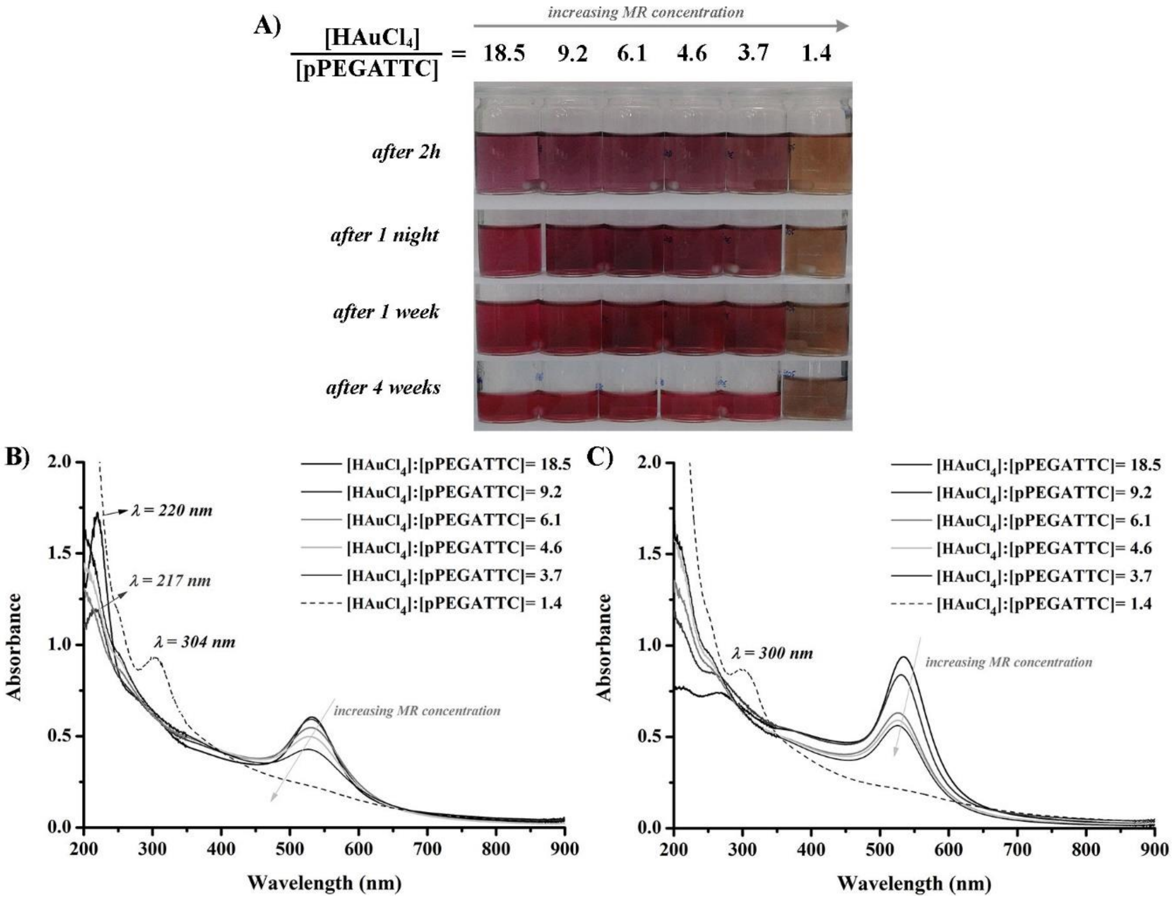

Figure 3.19. (A) Photographs and (B, C) UV-Vis spectra of Au NPs generated in the presence of P(PEGA$_{40}$)-TTC varying *[HAuCl$_4$]:[MR]* ratios over four weeks. UV-Vis spectra (B) after one night and (C) after 4 weeks.

After one night, 1 week and 4 weeks, each colloid was centrifuged, and both redispersed precipitate and the supernatant were characterized by UV-Vis spectroscopy. The results are compiled in Figure 3.20. In general, the absorbance of the LSPR band, of the redispersed precipitate, increases over time, indicating that Au NPs are growing. Next, these results will be discussed together with DLS measurements and SEM images, for each case.

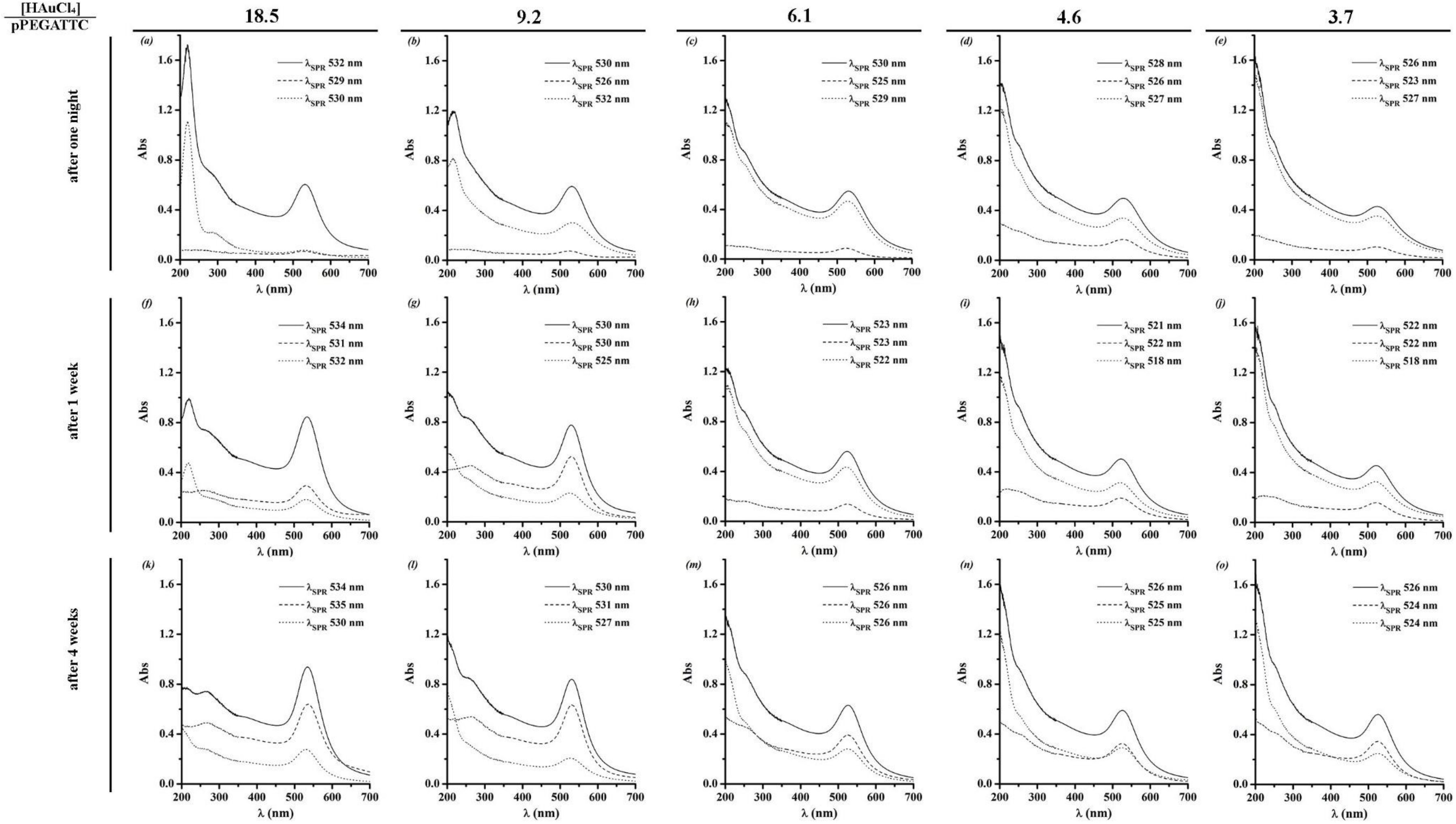

Figure 3.20. UV-Vis spectra of Au NPs generated varying the ratio *[HAuCl$_4$]:[pPEGATTC]* over four weeks. (*solid line*) colloid before centrifugation; (*dash line*) precipitate redispersed; and (*dot line*) supernatant of centrifugation.

Notes: colloids were centrifuged **(a, b)** 5 min at 15400g and **(f, k)** 2 min at 6000g, and a golden precipitate was formed; colloid was centrifuged **(c)** 5 min at 15400g **(g)** 5 min at 6000g, **(l)** 7min at 6000g **(m)** 7 min at 6000g, **(h)** 10 min at 15400g. The other colloids **(d, e, i, j, m, n, o)** were centrifuged 30 min at 15400g.

As regards the $[HAuCl_4]:[MR]=18.5$ ratio, the absorbance of the LSPR band increases overtime and the peak at 220 nm, assigned for $HAuCl_4$, decreases, indicating that the reduction reaction continues over the time, Figure 3.20-(*a,f,k*). Moreover, after one night the colloid was centrifuged (5min, 15400g) but a golden precipitate was formed in the eppendorf, so it was not possible to redisperse the Au NPs. This can be due to the size of the NPs and the lack of surface coverage and stability, yielding this irreversible golden aggregate. Indeed, SEM images in Figure 3.21 show a wide particle size distribution of Au NPs after one night, $d = 28.7 \pm 12.5$ nm, and also after 4 weeks, $d = 33.2 \pm 12.4$ nm. By DLS measurements, Table 3.6, an increase in the average hydrodynamic diameter (d_{average}) is observed that could be due to the increase of the NPs size associated with the consumption of gold precursor and/or coalescence of existing NPs. For this reason, the MR agent available to stabilize the resulting NPs is able to provide a better surface coverage thus leading to more stable NPs.

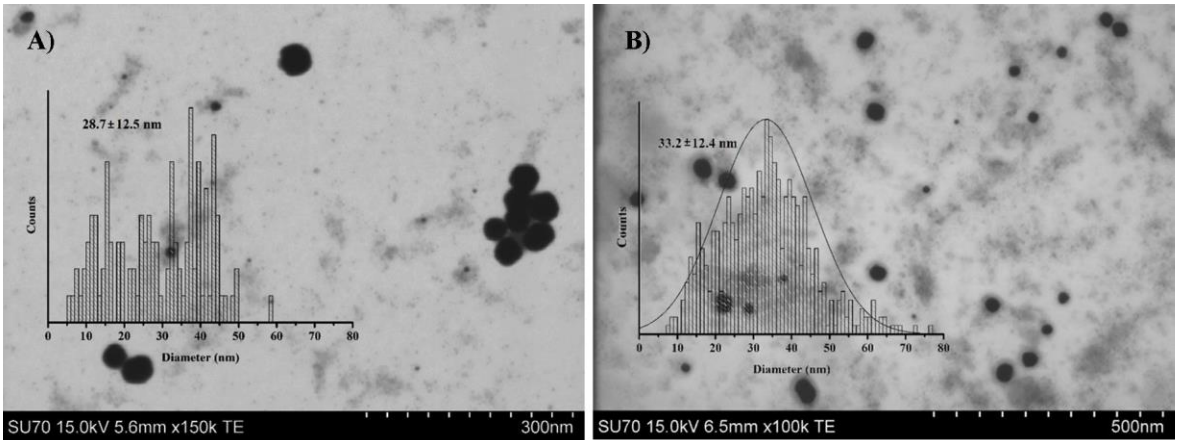

Figure 3.21. SEM images, in transmission mode, of Au NPs generated using the ratio $[HAuCl_4]:[pPEGATTC]=18.5$. (A) after one night and (B) after 4 weeks.

Table 3.6. DLS measurements of Au NPs generated using the ratio $[HAuCl_4]:[pPEGATTC]=18.5$.

	after one night			**after 4 weeks**		
	colloid[(a)]	***washed***[(b)]	***supernatant***	***colloid***[(a)]	***washed***[(b)]	**supernatant**
d_{average} (nm)	37.9	--	26.4	60.4	62.9	46.1
d_{number} (nm)	31.3 (50.2%) 3.2 (17.5%) 5.4 (17.3%)	--	1.5 (74.2%) 3.2 (25.8%)	19.3 (41.3%) 10.8 (38.0%) 50.1 (20.7%)	13.0 (59.6%) 49.0 (40.4%)	39.8 (80.0%) 5.3 (20.0%)
PDI	0.253	--	0.469	0.213	0.247	0.246

(a) colloid before centrifugation; (b) precipitate redispersed.

For the $[HAuCl_4]:[MR]=9.2$ ratio, Figure 3.20-(*b,g,l*) also shows a peak associated with the presence of $HAuCl_4$ (λ~220nm) that decreases over time. This colloid, also formed a golden precipitate after being centrifuged at 15400g during 5 min. However after 1 and 4 weeks, no golden precipitate was observed. SEM images in Figure 3.22 show that after one night the NPs have an average diameter of 9.8 ± 3.8 nm, and after 4 weeks 6.6 ± 2.1 nm although DLS measurements present higher d_{average}, Table 3.7. In fact, using this *[HAuCl4]:[pPEGATTC]* ratio, which corresponds to twice of MR agent concentration, in comparison to the *[HAuCl4]:[pPEGATTC]=18.5*, it can be observed that the increase of MR agent concentration is already confining the growth of the Au NPs. Even so, note that a few NPs with diameters between 20 and 30 nm are observed. In this case it seems that nucleation and growth occur leading to a large size distribution (below 10 nm) but after some time intraparticle digestive ripening takes place and probably the MR agent also re-organizes itself which leads to stable Au NPs with a lower average size. [35, 201] The higher d_{average}, from DLS measurements can be explained by the contribution of the larger NPs generated.

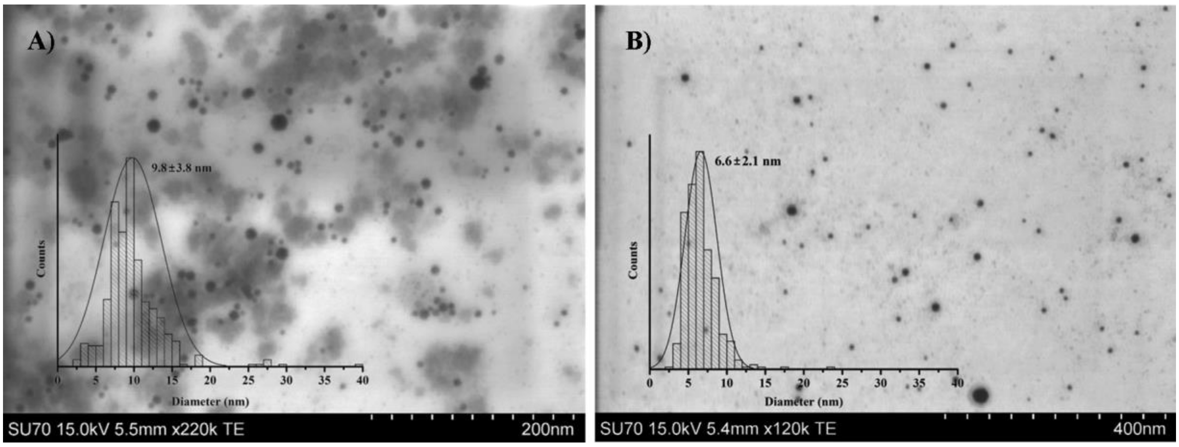

Figure 3.22. SEM images, in transmission mode, of Au NPs generated using the ratio *[HAuCl4]:[pPEGATTC]*=9.2. (A) after one night and (B) after 4 weeks.

Table 3.7. DLS measurements of Au NPs generated using the ratio *[HAuCl4]:[pPEGATTC]*=9.2.

	after one night			**after 4 weeks**		
	colloid$^{(a)}$	***washed***$^{(b)}$	***supernatant***	***colloid***$^{(a)}$	***washed***$^{(b)}$	**supernatant**
d_{average} (nm)	38.6	29.7	49.8	47.9	51.9	34.1
d_{number} (nm)	31.0 (81.0%) 10.5 (19.0%)	2.6 (100%)	10.6 (66.7%) 2.2 (33.3%)	39.6 (86.6%) 17.0 (13.4%)	43.0 (100%)	2.3 (100%)
PDI	0.249	0.513	0.101	0.233	0.241	0.407

(a) colloid before centrifugation; (b) precipitate of centrifugation redispersed.

When the *[HAuCl4]:[MR]*=6.1 ratio was used, spectra in Figure 3.20-(*c*,*h*,*m*) show that the absorbance of the LSPR band increases over time but the maximum shifts to lower wavelengths, indicating that smaller NPs were formed. SEM images show that the size distribution overtime is similar to those prepared using the ratio presented before (*[HAuCl$_4$]:[MR]*=9.2), as well as the d_{average} in DLS measurements (Table 3.8).

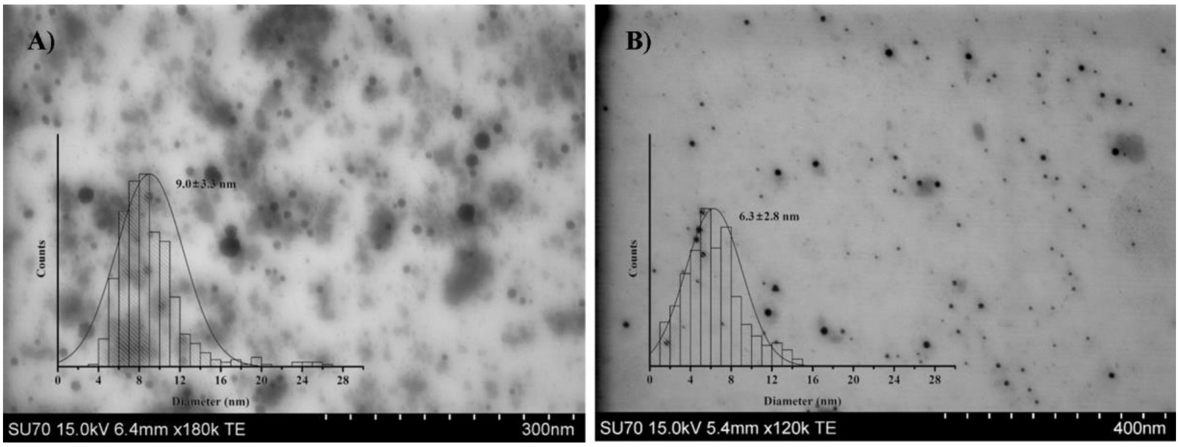

Figure 3.23. SEM images, in transmission mode, of Au NPs generated using the ratio *[HAuCl$_4$]:[pPEGATTC]=6.1*. (A) after one night and (B) after 4 weeks.

Table 3.8. DLS measurements of Au NPs generated using the ratio *[HAuCl$_4$]:[pPEGATTC]*=6.1.

	after one night			**after 4 weeks**		
	***colloid*$^{(a)}$**	***washed*$^{(b)}$**	***supernatant***	***colloid*$^{(a)}$**	***washed*$^{(b)}$**	**supernatant**
d_{average} (nm)	42.1	53.9	58.6	70.3	40.7	38.0
d_{number} (nm)	7.5 (100%)	29.2 (50.0%) 3.6 (50.0%)	17.6 (100%)	34.4 (66.7%) 8.7 (33.3%)	4.0 (57.2%) 13.8 (24.0%) 8.6 (18.8%)	13.7 (66.5%) 6.9 (33.5%)
PDI	0.253	0.316	0.232	0.529	0.337	0.218

(a) colloid before centrifugation; (b) precipitate of centrifugation redispersed.

By increasing the MR agent concentration, *[HAuCl$_4$]:[MR]*=4.6, UV-Vis spectra of the ensuing colloid in Figure 3.20-(*d,i,n*) seem to be similar to those obtained using the ratio discussed before. In particular the colloid after the 4 weeks also has λ_{LSPR} at 526nm. However, SEM images clearly show that two populations of Au NPs were generated: one in the same size range of those obtained using the ratio *[HAuCl$_4$]:[MR]*=6.1, which is 8.5 ± 1.6 nm that change to 7.5 ± 2.1 nm after 4weeks, and the other one which is even smaller: after one night 3.6 ± 0.9 nm and after 4 weeks 2.3 ± 0.5 nm. Yet, DLS measurements (Table 3.9) present high d_{average} values that do not correspond to the SEM images. This can be due to the fact that higher concentration of MR agent can form MR aggregates thus contributing to the hydrodynamic average diameter.

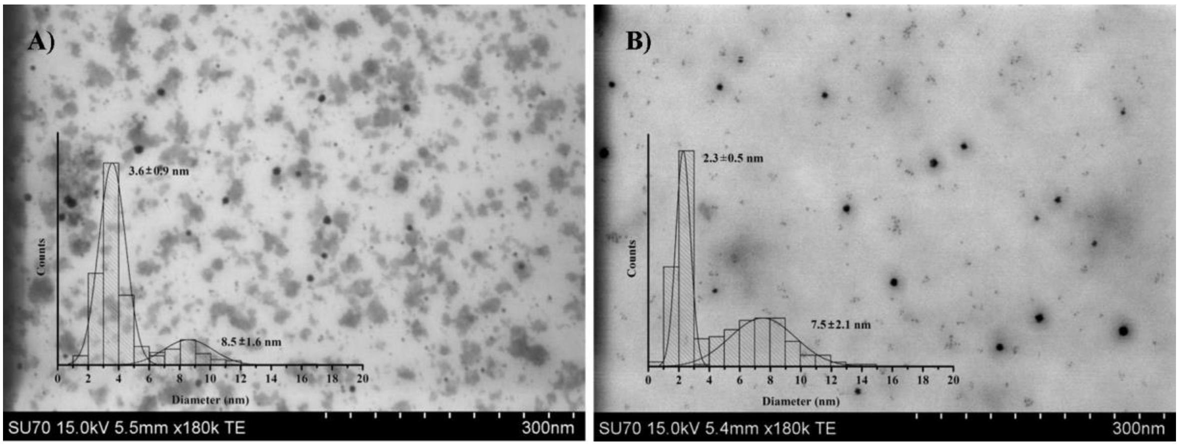
A)
3.6±0.9 nm
8.5±1.6 nm
Counts
0 2 4 6 8 10 12 14 16 18 20
Diameter (nm)
SU70 15.0kV 5.5mm x180k TE
300nm
B)
2.3±0.5 nm
7.5±2.1 nm
Counts
0 2 4 6 8 10 12 14 16 18 20
Diameter (nm)
SU70 15.0kV 5.4mm x180k TE
300nm

Figure 3.24. SEM images, in transmission mode, of Au NPs generated using the ratio *[HAuCl$_4$]:[pPEGATTC]=4.6*. (A) after one night and (B) after 4 weeks.

Table 3.9. DLS measurements of Au NPs generated using the ratio *[HAuCl$_4$]:[pPEGATTC]*=4.6.

	after one night			**after 4 weeks**		
	***colloid*$^{(a)}$**	***washed*$^{(b)}$**	***supernatant***	***colloid*$^{(a)}$**	***washed*$^{(b)}$**	**supernatant**
d_{average} (nm)	31.3	42.1	21.2	127.4	106.2	142.2
d_{number} (nm)	19.3 (100%)	1.5 (59.2%) 2.5 (26.6%) 0.9 (14.2%)	15.9 (100%)	16.5 (100%)	1.9 (100%)	14.3 (100%)
PDI	0.370	0.275	0.286	0.328	0.216	0.259

(a) colloid before centrifugation; (b) precipitate of centrifugation redispersed.

Concerning the *[HAuCl$_4$]:[MR]*=3.7 ratio, the λ_{LSPR} of the corresponding colloid after 4 weeks is also peaked at 526 nm (Figure 3.20-(*e,j,o*). SEM images, in Figure 3.25, show that the average diameter is even smaller, i.e. around 5 nm. Herein, the d_{number} of the supernatant after one night and 4 weeks corresponds to what is observed by SEM, see Table 3.10. However, it is necessary to remember that increasing P(PEGA$_{40}$)-TTC concentration, micelles/aggregates around 5 nm are formed, as observed during the determination of the CMC, which will contribute for the results obtained by DLS measurements of the colloid.

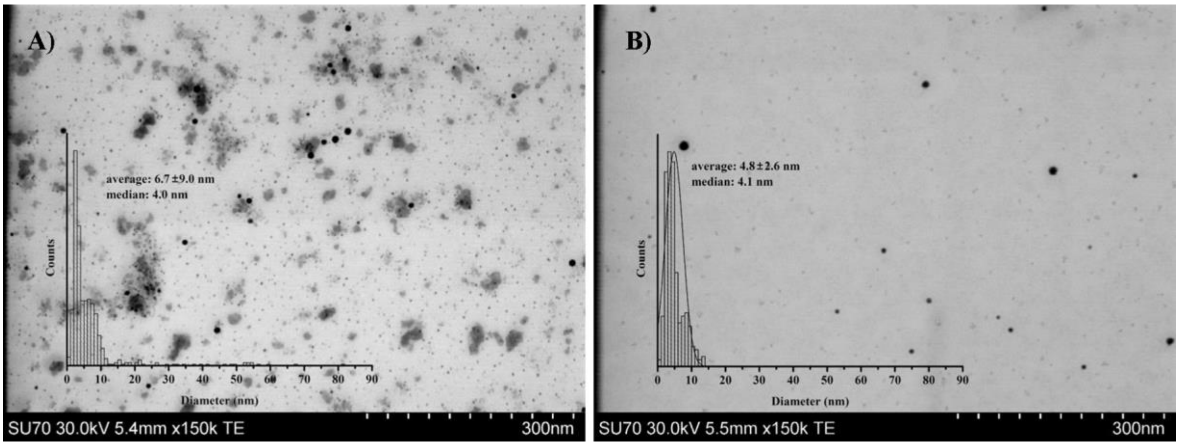
A)
average: 6.7±9.0 nm
median: 4.0 nm
Counts
0 10 20 30 40 50 60 70 80 90
Diameter (nm)
SU70 30.0kV 5.4mm x150k TE
300nm
B)
average: 4.8±2.6 nm
median: 4.1 nm
Counts
0 10 20 30 40 50 60 70 80 90
Diameter (nm)
SU70 30.0kV 5.5mm x150k TE
300nm

Figure 3.25. SEM images, in transmission mode, of Au NPs generated using the ratio *[HAuCl$_4$]:[pPEGATTC]=3.7.* (A) after one night and (B) after 4 weeks.

Table 3.10. DLS measurements of Au NPs generated using the ratio *[HAuCl$_4$]:[pPEGATTC]*=3.7.

	after one night			after 4 weeks		
	***colloid*[(a)]**	***washed*[(b)]**	***supernatant***	***colloid*[(a)]**	***washed*[(b)]**	**supernatant**
$d_{average}$ (nm)	45.3	73.3	21.7	60.2	60.8	23.7
d_{number} (nm)	9.5 (66.7%) 2.7 (33.3.%)	1.9 (100%)	6.8 (75.6%) 3.4 (24.4%)	19.0 (53.2%) 9.6 (26.1%) 6.1 (20.7%)	2.0 (100%)	6.5 (100%)
PDI	0.270	0.196	0.404	0.253	0.209	0.280

(a) colloid before centrifugation; (b) precipitate of centrifugation redispersed.

Finally, using the *[HAuCl$_4$]:[pPEGATTC]*=1.4 ratio, the LSPR band of the colloid is not detected and a brown color was observed instead (Figure 3.19). Indeed, at this ratio the concentration of MR (0.143 mM) agent is already in the CMC range (0.1-0.3 mM), which means that the MR agent is organized in micelles. This result suggest that, after the reduction the Au^0 nuclei (Au clusters) generated were confined in the MR agent micelles and the growth of the particles did not occur leading to NPs with a diameter below to 3 nm. [38, 39]

As a final remark, it was observed by UV-Vis spectroscopy, SEM and DLS measurements that the concentration of P(PEGA$_{40}$)-TTC has strong influence on the size and size distribution of the Au NPs, as can be seen in Scheme 3.3. In fact, lower concentrations of MR agent afford colloids with bigger dimensions and higher polydispersity ranging from 10 to 60 nm. Increasing the MR concentration, the average size of NPs decreases to around 10 nm, and for even higher MR concentrations the average size decreases to 4 nm. For the most concentrated colloid, which corresponds to a concentration above the CMC, the colloid does not show any LSPR band having a brown coloration which is typical for NPs smaller than 2 nm. At these concentration values, the Au nuclei are generated inside the MR agent micelles which confine their size and prevents their growth.

Scheme 3.3. Schematic representation of the influence of MR agent concentration on the size and size distribution of Au NPs obtained in the presence of MR agent and using NaBH$_4$ as reducing agent.

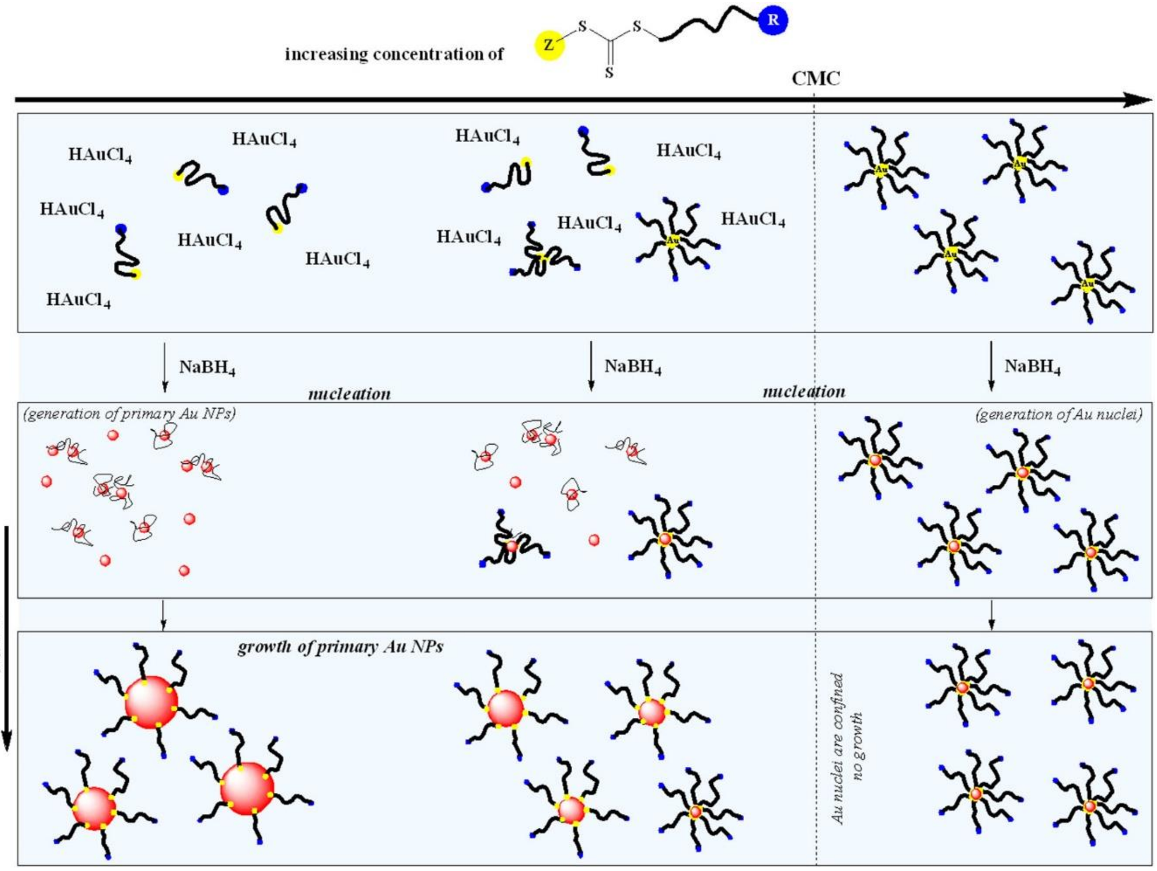
increasing concentration of
Z
S
S
S
R
CMC
HAuCl4
NaBH4
nucleation
(generation of primary Au NPs)
(generation of Au nuclei)
Au
over time
growth of primary Au NPs
Au nuclei are confined
no growth

3.4.3.2.2. Copolymerization from macroRAFT@Au nanostructures

Having selected the P(PEGA$_{40}$)-TTC MR agent for the systematic study of the influence of the *[HAuCl$_4$]* on the particle size of Au NPs, three of these ratios were considered to proceed with the second step of the *grafting from* strategy, during which the hydrophobic chain is grown from the surface of MR@Au NPs. The ratios considered (3.7, 6.1 and 9.2) correspond to concentrations below the MR agent CMC in order to minimize the formation of free polymer particles. In fact, at this stage to issues had to be kept in mind: (i) the location of the MR agent in the colloid solution as there is no evidence whether it covers the surface of the NPs or if it is in solution and (ii) the effect of NaBH$_4$

on the MR agent as this reducing agent has been frequently used to reduce the trithio- or dithio- group from the RAFT agent to thiol in order to eliminate the *Z*-group of RAFT agent and link the polymer prepared by RAFT polymerization to gold surface via thiol-Au interaction [133]. Nevertheless, the reduction of the gold precursor was clearly observed, so the extension of this second reaction should not have impact on the RAFT emulsion polymerization to grow the hydrophobic chain. Moreover, the colloids were used after four weeks of being prepared to ensure that the Au NPs were fully formed. Note that the optimization of the copolymerization will be discuss in the copolymerization from the MR@Au NPs prepared by adsorption of the MR onto Au NPs, in ***3.4.3.3.2.***.

For all the cases, stable colloids with pink coloration were obtained, after the RAFT emulsion copolymerization. UV-Vis spectra (Figure 3.26-A, Figure 3.27-A, Figure 3.28-A) reveal that polymerization occurred since it is possible to observe an increase in the absorbance near 200 nm. However, the expected shift of the λ_{LSPR} to higher wavelengths due to the copolymerization onto the NPs was not observed. However, SEM images of the colloids after copolymerization (Figure 3.26-B, Figure 3.27-B, Figure 3.28-B) showed that the copolymerization occur essentially in the free MR in solution and no evidence was found of growth of the polymeric shell around the Au NPs.

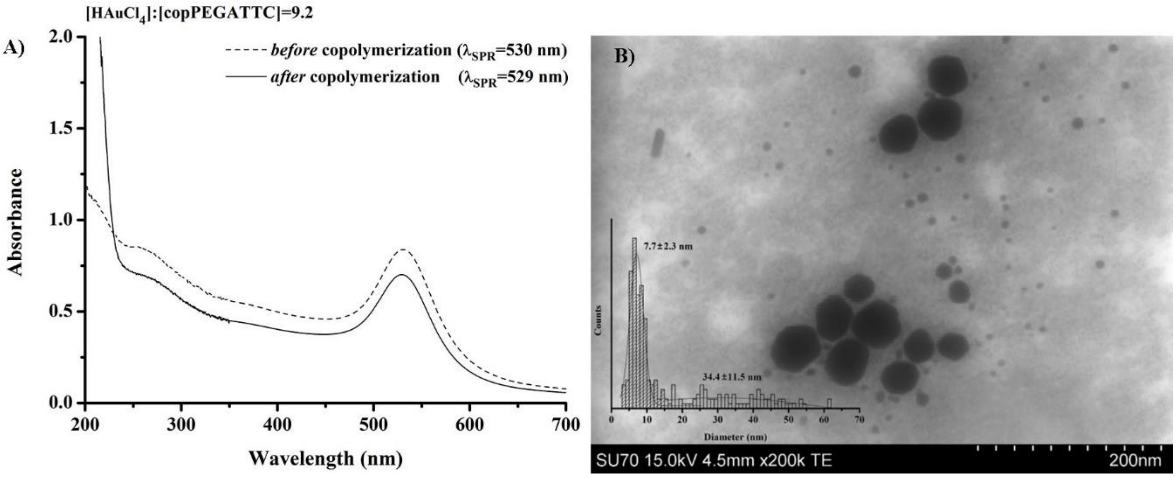

Figure 3.26. (A) UV-Vis spectra and (B) SEM image, in transmission mode, of copolymerized Au NPs generated using the ratio *[HAuCl$_4$]:[pPEGATTC]*=9.2.

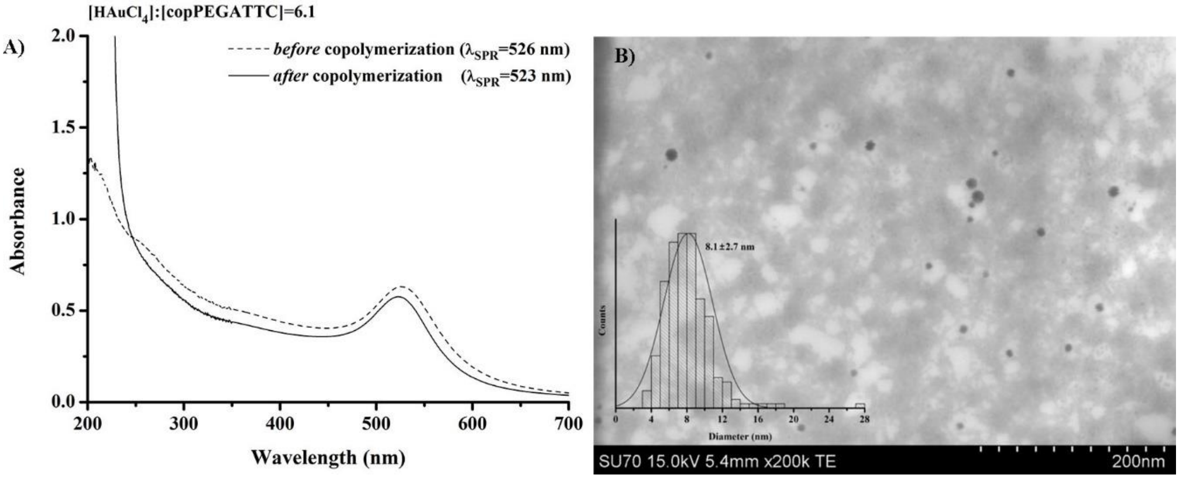

Figure 3.27. (A) UV-Vis spectra and (B) SEM image, in transmission mode, of copolymerized Au NPs generated using the ratio *[HAuCl$_4$]:[pPEGATTC]*=6.1.

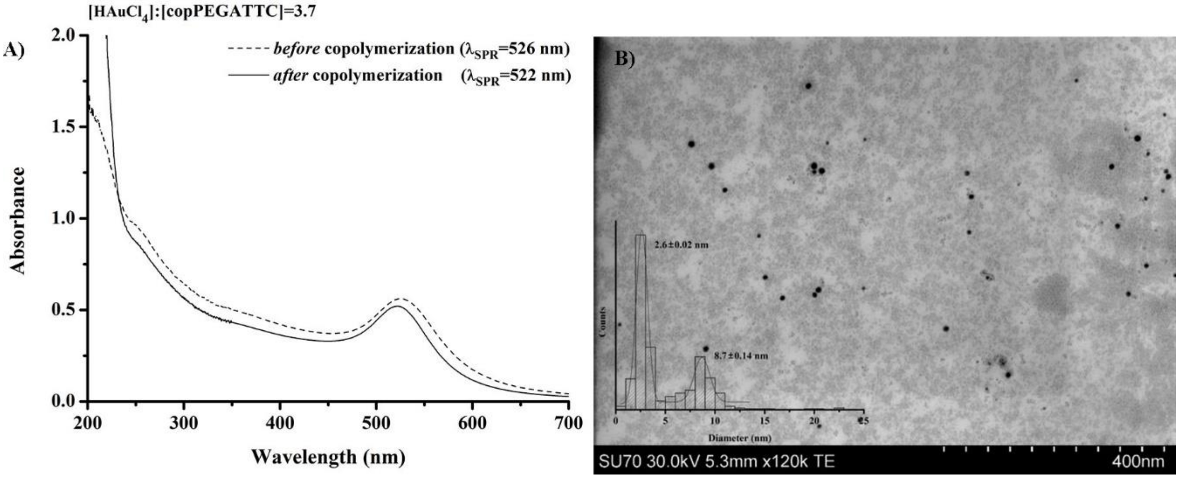

Figure 3.28. (A) UV-Vis spectra and (B) SEM image, in transmission mode, of copolymerized Au NPs generated using the ratio *[HAuCl$_4$]:[pPEGATTC]=3.7*.

Table 3.11 summarizes the size of the Au NPs before and after the RAFT emulsion copolymerization and highlights the changes upon polymerization.

Table 3.11. Summary of the average diameter determined by SEM images, before and after RAFT emulsion copolymerization from MR@Au NPs.

$\frac{[HAuCl_4]}{[MR]}$	Before copolymerization	After copolymerization
9.2	6.6 ± 2.1 nm	7.7 ± 2.5 nm 34.4 ± 11.5 nm
6.1	6.3 ± 2.8 nm	8.1 ± 2.7 nm
3.7	4.8 ± 2.1 nm	2.6 ± 0.02 nm 8.7 ± 0.14 nm

These changes can be attributed to the fact that the starting colloids were not centrifuged hence, the excess of free MR agent in solution was not removed. Moreover, the reaction temperature (70ºC) may also have contributed to changes of the Au NPs diameter. Aggregation and growing of primary and secondary Au NPs and also ripening effects are still taking place enhanced by the reaction temperature.

3.4.3.3. Grafting from strategy via macroRAFT adsorption onto previously prepared Au NPs

As already explained, an alternative path for the *grafting from* strategy explored before, is to adsorb the macroRAFT (MR) onto Au NPs surface that were previously prepared via the citrate method. The second step, is the same as in the previous strategy, during which a hydrophobic chain is grown from the surface of these MR coated NPs via RAFT emulsion polymerization. These two steps are discussed in two *sub-chapters*.

3.4.3.3.1. Adsorption of macroRAFT agents onto Au NPs

MR adsorption onto the surface of Au NPs is a critical step and optimal experimental conditions, namely the *[MR]/[AuNPs]* ratio, should be found in order to obtain well-coated NPs and few free chains of MR in solution. These aspects are important for the second step (copolymerization from MR@Au NPs) in order to obtain stable and well-coated copolymer@Au NPs and preventing the copolymerization from free MR agent in solution. In fact, one aspect that could influence the MR adsorption onto Au NPs is the critical micelle concentration (CMC). This is a very important aspect since the way the MR is organized in water, i.e. single chains, aggregates or micelles, will have an impact on how the MR interacts with the NP surface and if the trithio group is available to link to the gold surface.

Some preliminary adsorption studies onto Au NPs were performed for the MR agents P(PEGA$_{40}$)-TTC and P(AA$_{40}$)-TTC before the determination of the CMC of each MR agent. In these adsorption studies concentrations of MR agent from 0 to 1mM were used, which are concentrations much higher than the CMC value. The amount of MR agent adsorbed onto Au NPs was followed by UV-Vis spectroscopy, since MR agents have an absorption peak around 300-310 nm due to the trithio moiety of the RAFT agent. However, the reproducibility of the results was poor, at least in this range of concentrations. Just for the record, these preliminary adsorption results as well as the UV-Vis spectra of the colloids obtained using P(PEGA$_{40}$)-TTC and P(AA$_{40}$)-TTC are display in ***Annex E***. In view of this, MR agents P(PEGA$_{40}$)-TTC, P(AA$_{40}$)-TTC and P(AA$_{20}$-*co*-PEGA$_{20}$)-TTC were adsorbed onto Au NPs using a concentration below and above the CMC value, as will be presented and discuss in the next *sub-sections.*

Preparation of the Au nanocomposites after CMC determination

After the CMC determination of each MR, the adsorption of the MR was performed below and above the critical micelle concentration. The concentration below to CMC leads to free and random MR chains in solution that, in theory, can easily interact and adsorb onto the surface of Au NPs. On the other hand, above CMC the organized micellar structures can limit the interaction and adsorption of the MR with the NP surface. The MR agent P(PEGA$_{40}$)-TTC, P(AA$_{40}$)-TTC or P(AA$_{20}$-*co*-PEGA$_{20}$)-TTC was added dropwise to a dispersion of Au NPs and the corresponding mixtures stirred overnight. After that, the colloids were centrifuged to remove excess of MR that did not adsorb onto NPs surface, yielding the colloids named *gf*-PEGATTC@Au NPs, *gf*-AATTC@Au NPs and *gf*-AAPEGATTC@Au NPs, respectively. Table 3.12 shows the experimental conditions used for the MR adsorption onto Au NPs. The ratio of initial concentration of MR agent per Au NPs concentration ($C_{initial}/C_{NPs}$) was kept the same for the three MR agents, using MR agent concentrations below and above the CMC. The colloids obtained were characterized by UV-Vis spectroscopy and electron microscopy.

Table 3.12. Experimental conditions for the adsorption of MR onto Au NPs, below and above CMC.

colloid		**$C_{initial}$ (mM)**	**C_{NPs} (mol NPs/L)**	**$C_{initial}/C_{NPs}$ (mmol MR/mol NPs)**
***gf*-PEGATTC@Au NPs**	**< *CMC***	0.056	6.0E-10	9.4E+07
	> *CMC*	1.4	1.3E-09	1.0E+09
***gf*-AATTC@Au NPs**	**< *CMC***	0.050	6.0E-10	8.2E+07
	> *CMC*	0.5	5.0E-10	9.4E+08
***gf*-AAPEGATTC@Au NPs**	**< *CMC***	0.068	6.0E-10	1.1E+08
	> *CMC*	1.2	1.2E-09	9.7E+08

In general UV-Vis spectra, in Figure 3.29, do not show any sign of aggregation and the λ_{LSPR} red-shifted, as expected, due to the presence of the MR agent around the NPs. This shift is higher for the colloids prepared using a concentration of MR agent above the CMC. In addition, the presence of the MR in the colloid was proven by the presence of the band around 300 nm, which is more noticeable for the colloids prepared using the higher concentration of MR agent. This can be due to a higher amount of free MR agent, i.e. MR agent that is not covering the NPs, and that was not totally removed by centrifugation. Indeed, in SEM images (Figure 3.30) a higher amount of MR agent that is spread on the copper grid can be observed. The MR around the NPs is not clearly observed, but in the case of the colloids containing the monomer PEGA is possible to observe a slight grey background around the NPs. In the specific case of the use of P(PEGA$_{40}$)-TTC above CMC (Figure 3.30-A2) aggregates of MR agent are observed.

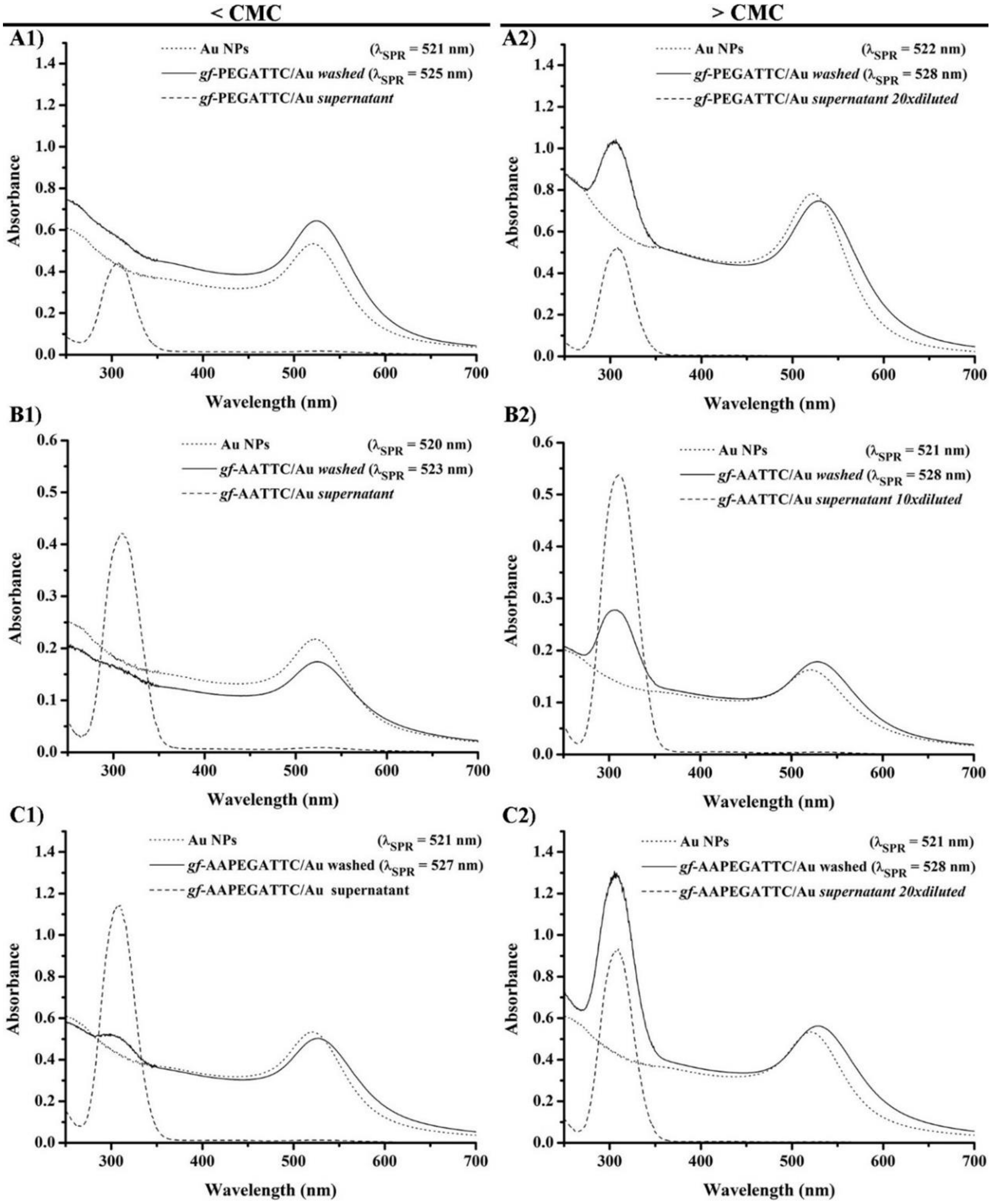

Figure 3.29. UV-Vis spectra of (A) *gf*-PEGATTC@Au, (B) *gf*-AATTC@Au and (C) *gf*-AAPEGATTC@Au nanocomposites prepared (A1, B1, C1) below the CMC and (A2, B2, C2) above the CMC.

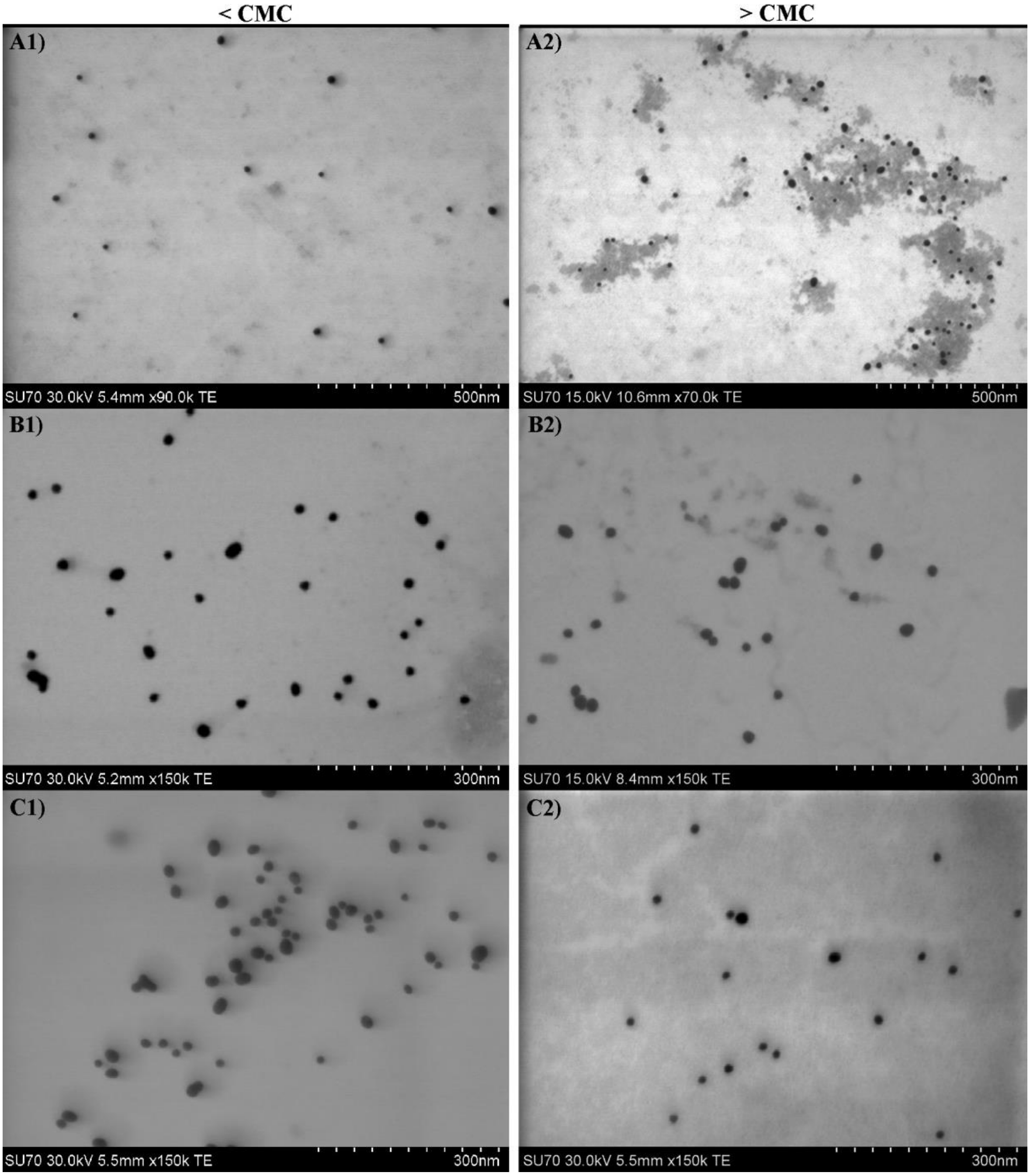
< CMC
> CMC
A1)
A2)
B1)
B2)
C1)
C2)
SU70 30.0kV 5.4mm x90.0k TE 500nm
SU70 15.0kV 10.6mm x70.0k TE 500nm
SU70 30.0kV 5.2mm x150k TE 300nm
SU70 15.0kV 8.4mm x150k TE 300nm
SU70 30.0kV 5.5mm x150k TE 300nm
SU70 30.0kV 5.5mm x150k TE 300nm

Figure 3.30. SEM images, in transmission mode, of (A) *gf*-PEGATTC@Au, (B) *gf*-AATTC@Au and (C) *gf*-AAPEGATTC@Au nanocomposites prepared (A1, B1, C1) below the CMC and (A2, B2, C2) above the CMC.

3.4.3.3.2. Copolymerization from macroRAFT@Au nanostructures

The adsorption of MR agent on the surface of Au NPs is important to have control over the copolymerization in the second step. In other words, to have control of the molecular weight and kinetics during RAFT polymerization it is important to have control over the ratio of monomer (M) and initiator (ACPA) in relation to the RAFT agent (in this case MR agent), i.e. *[M]/[MR]* and *[MR]/[ACPA]*. As explained in the introduction (**1.4.2.**), *[MR]/[ACPA]* should be higher than one, but not too high, in order to ensure a higher number of dormant chains than active chains. Moreover, the amount of monomer added in the reaction vessel (*[M]/[MR])* will determine the size of the hydrophobic chain, and consequently the width of the polymeric shell. Furthermore, this second step occurs in emulsion so it is necessary to guarantee the stability of the system. Stenzel has actually reported the importance of a balance between the free MR in solution and the MR adsorbed on the NPs surface during the polymerization from NPs surface [202]. An additional advantage of this strategy is that the MR agent acts as surfactant due to its amphiphilic character.

Optimization of the copolymerization was first performed using P(PEGA$_{40}$)-TTC@Au NPs prepared above the CMC. The mixture of hydrophobic monomers (10MMA:1BA w/w) was copolymerized from freshly prepared MR@Au colloid and the mixture of hydrophobic monomers was added to the reaction vessel via two ways. In the first case, it was added in one shot before purging the mixture (MR@Au NPs and initiator) with N_2; in the second experiment it was added in a controlled way during the copolymerization.

Both experiments above led to colloidal stable Au colloids whose UV-Vis spectra are depicted in Figure 3.31, showing a red-shift for the λ_{LSPR} as expected due to the presence of the polymer shells. Moreover, a high absorbance is observed between 200 and 250 nm for the colloid prepared by adding the mixture of monomers in one shot, which corresponds to the formation of the copolymer. Noteworthy, the DLS measurements (Table 3.13) show that the hydrodynamic average diameter of the particulates increased only for the case where the monomer was added in a controlled way. In fact, SEM images of the Au colloids obtained after one-shot addition of the monomers show fiber-like copolymer particles (Figure 3.32-A1) as well as polymer coated Au NPs (Figure 3.32-A2). This type of polymer nanostructures can be formed in emulsion under specific reaction conditions as already reported by Charleux *et al.* [203]. On the other hand, when the mixture of hydrophobic monomers was added drop-wise only well-defined copolymer@Au nanostructures have been observed (Figure 3.32-B).

Table 3.13. $d_{average}$ from DLS measurements of *gf*-copPEGATTC@Au NPs.

	One shot of *M*	**Controlled addition of *M***
MR@AuNPs	33.2 (PdI=0.328)	34.5 nm (PdI= 0.256)
copolymer@AuNPs	33.2 (PdI=0.317)	40.1 nm (PdI= 0.262)

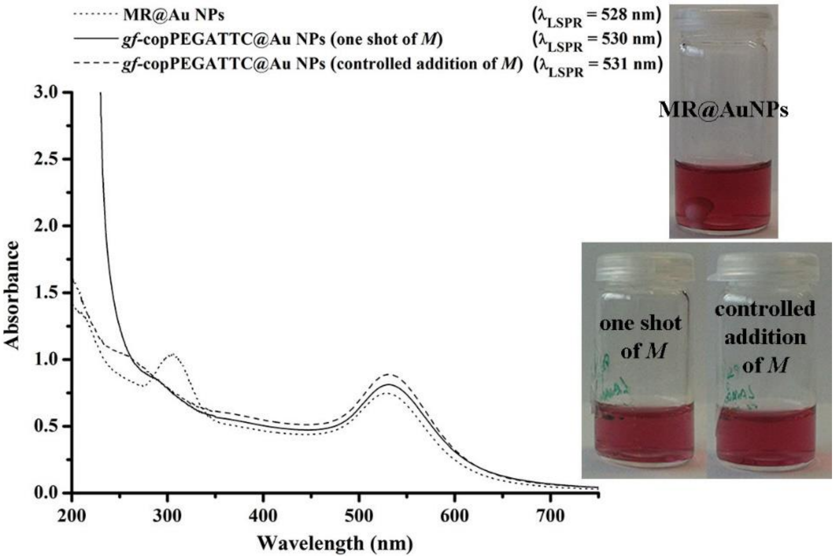

Figure 3.31. UV-Vis spectra of *gf*-copPEGATTC@Au NPs prepared by adding the mixture of monomers (*M*) in one shot at the beginning and in a controlled way during the polymerization.

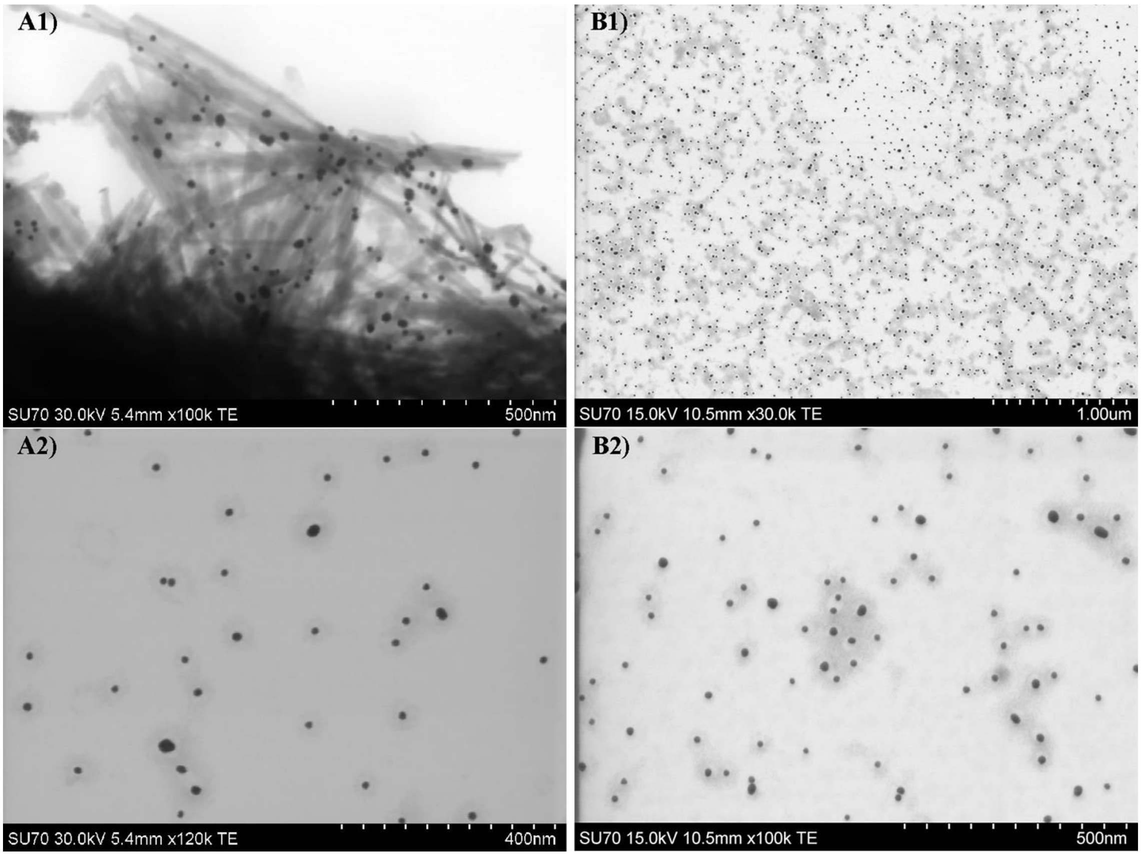
A1)
SU70 30.0kV 5.4mm x100k TE
500nm
B1)
SU70 15.0kV 10.5mm x30.0k TE
1.00um
A2)
SU70 30.0kV 5.4mm x120k TE
400nm
B2)
SU70 15.0kV 10.5mm x100k TE
500nm

Figure 3.32. SEM images, in transmission mode, of *gf*-copPEGATTC@Au NPs prepared by adding the mixture of monomers (A) in one shot at the beginning and (B) in a controlled way during the polymerization.

These results highlight the relevance of the addition step of hydrophobic monomers on the morphology of the final colloidal nanocomposites. Although, the monomer added in one step is stabilized by the amphiphilic free MR agent (monomer droplet), thus keeping the Au colloid stable, free polymer particles are also formed. In fact, similarly to conventional RAFT emulsion polymerization, the monomer diffuses from the monomer droplet to the growing polymer particle stabilized by the MR agent, thus leading to the formation of fiber-like polymer particles. Hence, by adding small amounts of the hydrophobic monomers during the polymerization, the growth from the MR agent occurs preferentially from MR@Au NPs, which results in morphological well-defined polymer coated Au NPs.

In the next experiments, the copolymerization was performed from MR@Au NPs prepared using the three MR agents, P(PEGA$_{40}$)-TTC, P(AA$_{40}$)-TTC and P(AA$_{20}$-*co*-PEGA$_{20}$)-TTC, in concentrations above and below the CMC, and the mixture of hydrophobic monomers was added to the polymerization vessels in a control way. Figure 3.33 shows the UV-Vis spectra of the colloids prepared with the three MR agents, before and after RAFT emulsion copolymerization of the mixture MMA:BA (10:1 w/w). In general, stable colloids were obtained after the copolymerization and a red-shift in the λ_{LSPR} was observed, as expected due to the increase to the shell thickness. DLS measurements also showed this increase in the hydrodynamic average diameter of the shell@core, as can be observed in Table 3.14.

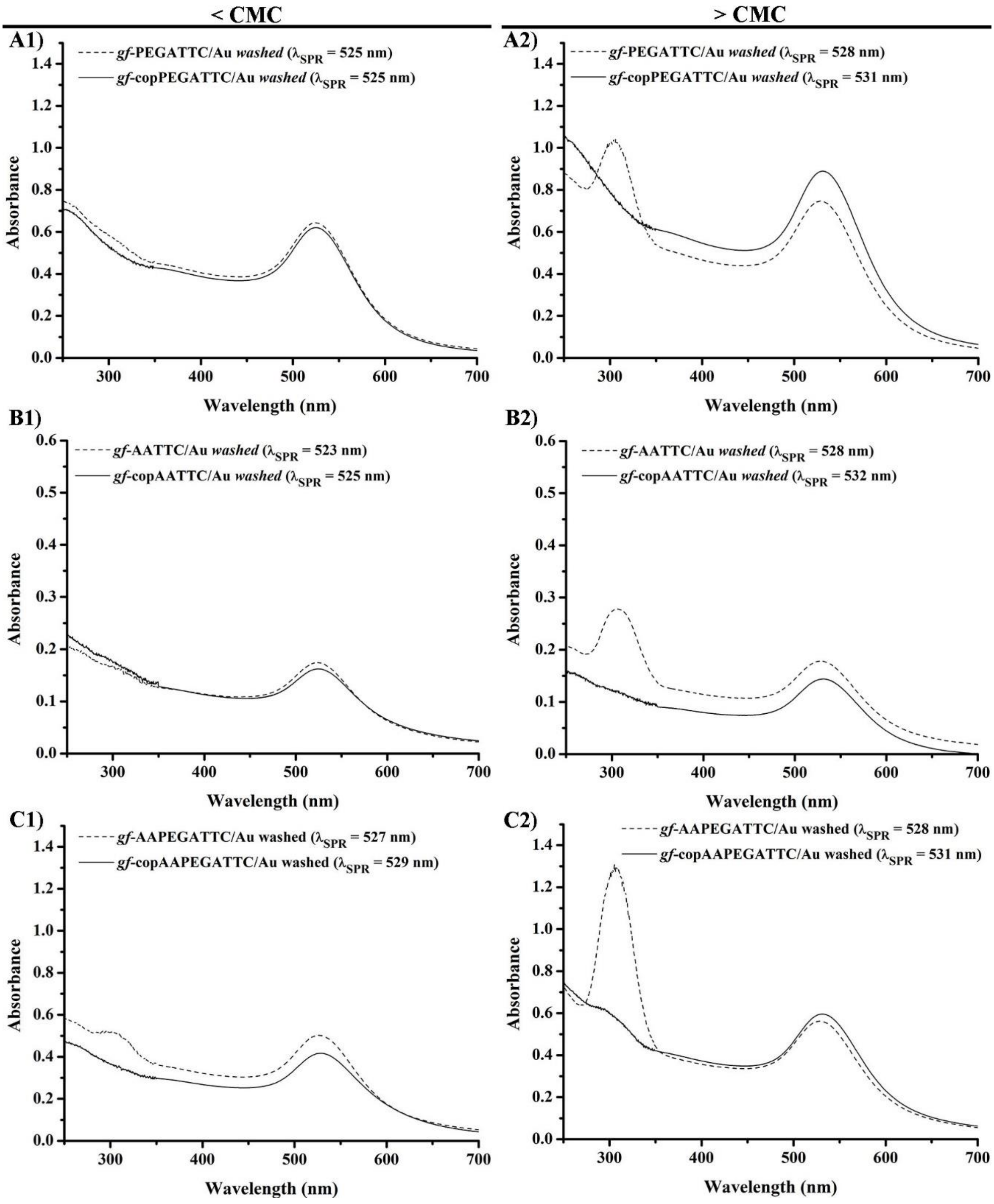

Figure 3.33. UV-Vis spectra of (A) *gf*-copPEGATTC@Au, (B) *gf*-copAATTC@Au and (C) *gf*-copAAPEGATTC@Au nanocomposites prepared (A1, B1, C1) below the CMC and (A2, B2, C2) above the CMC.

Table 3.14. $d_{average}$ **from DLS measurements before and after emulsion copolymerization.**

MR used		**< CMC**	**> CMC**
PEGATTC	**Before copolymerization**	35.5 nm (PdI= 0.246)	34.5 nm (PdI= 0.256)
	After copolymerization	36.2 nm (PdI= 0.277)	40.1 nm (PdI= 0.262)
AATTC	**Before copolymerization**	32.5 nm (PdI= 0.541)	36.9 nm (PdI= 0.442)
	After copolymerization	*	47.1 nm (PdI= 0.374)
AAPEGATTC	**Before copolymerization**	21.8 nm (PdI= 0.522)	30.6 nm (PdI= 0.351)
	After copolymerization	50.5 nm (PdI= 0.290)	36.4 nm (PdI= 0.326)

*limitations in the equipment did not allow to measure this colloid.

SEM images in transmission mode (Figure 3.34) show that for both situations, below and above the CMC, the presence of a slight grey background around the Au NPs indicating the presence of the polymeric shell. Moreover, unlike the SEM images of MR@Au NPs (Figure 3.30), no free polymer was observed for the colloids prepared above CMC.

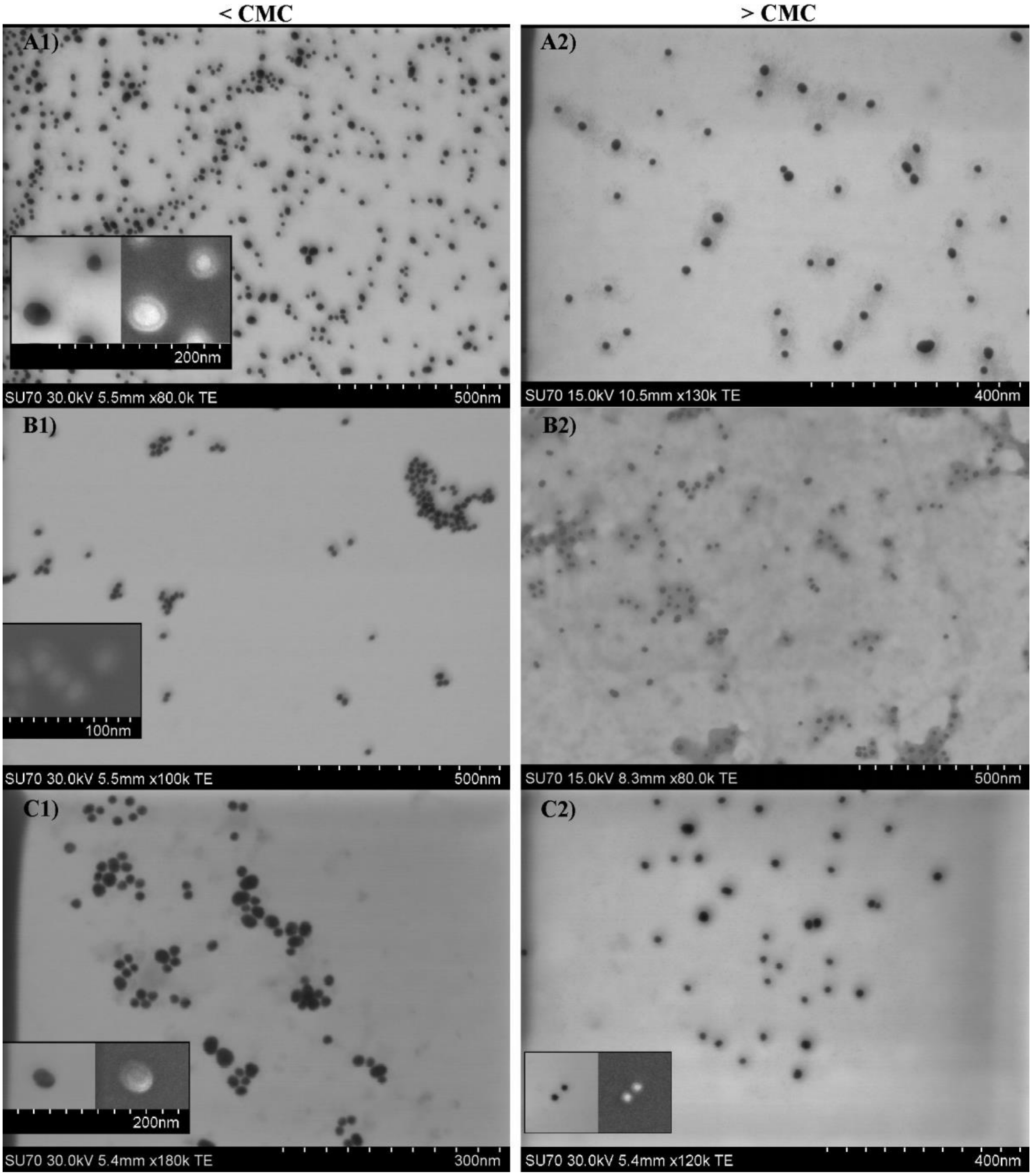
< CMC
> CMC
A1)
200nm
SU70 30.0kV 5.5mm x80.0k TE 500nm
A2)
SU70 15.0kV 10.5mm x130k TE 400nm
B1)
100nm
SU70 30.0kV 5.5mm x100k TE 500nm
B2)
SU70 15.0kV 8.3mm x80.0k TE 500nm
C1)
200nm
SU70 30.0kV 5.4mm x180k TE 300nm
C2)
SU70 30.0kV 5.4mm x120k TE 400nm

Figure 3.34. SEM images, in transmission mode, of (A) *gf*-copPEGATTC@Au, (B) *gf*-copAATTC@Au and (C) *gf*-copAAPEGATTC@Au nanocomposites prepared (A1, B1, C1) below the CMC and (A2, B2, C2) above the CMC. *Insets*: secondary electrons and/or transmission imaging showing in detail some core@shell nanoparticles.

3.4. Conclusions

Reversible addition-fragmentation chain transfer (RAFT) polymerization offers the possibility of full control over the composition and architecture of polymers. Moreover, RAFT agent contains sulfur atoms (trithio group) that have high affinity to Au surface, enabling a strong interaction between the RAFT agent and the Au NP. In this chapter, three distinct strategies to prepare Au nanocomposites were explored: *post-modification* strategy, *in situ* generation of Au NPs in previously prepared copolymer and *grafting from* strategy. In the first two strategies, a copolymer was prepared via RAFT emulsion polymerization using previously prepared macroRAFT agents P(PEGA$_{40}$)-TTC and P(AA$_{40}$)-TTC. The *post-modification* strategy, which seems the most straightforward strategy, consisting in mixing the copolymer with previously prepared Au NPs, however due to the well-defined micelle structures of diblock copolymer formed in water, the Au NPs are not able to migrate to the core of these polymer NPs. In the case of P(PEGA$_{40}$)-*b*-(MMA-*co*-BA)$_{140}$-TTC, it seems that Au NPs interact with the ether groups of PEGA in the hydrophilic shell of the polymeric NP. In contrast, using P(AA$_{40}$)-*b*-(MMA-*co*-BA)$_{160}$-TTC it seems that repulsive electrostatic interactions occur between the Au-Cit NPs and the carboxylic acid of AA in the hydrophilic shell of the polymeric NP. *In situ* generation of Au NPs in the previous prepared copolymer is very attractive since it occurs in one step synthesis. However, this strategy lead to the formation of Au NPs on the surface of the well-defined diblock polymeric NPs. Moreover, it was found that the generation of the NPs depends on the pH, the amount the copolymer, the *[HAuCl$_4$]/[copolymer]* ratio and also on the chemical nature of the repeating units, namely the acrylic acid and the poly(ethylene glycol) that compose the hydrophilic block. These two strategies did not lead to shell@core type-structures and do not seem promising to be used in biosensing applications.

The third strategy, *grafting from* strategy, required two main steps to yield stable and robust copolymer@AuNPs - shell@core type nanostructures. For the first step two pathways were followed for the preparation of MR@AuNPs: *in situ* generation of Au NPs in previously prepared macroRAFT agents, and adsorption of macroRAFT agents onto Au NPs. Again, *in situ* strategy is very attractive since it occurs in one step. However, the generation of Au NPs depends on the pH, the amount the MR, the ratio *[HAuCl$_4$]/[MR]* and also the chemical nature of repeating units. Therefore, it is not easy to control the size of the NPs and obtain a narrow particle size distribution. In general, it was observed that increasing the MR agent concentration the size of the NPs decreases, namely when a MR agent concentration above the CMC was used a brown colloid was generated and the LSPR band was not detected, indicating that only Au clusters ($d < 3$ nm) were formed. Regarding the generation of Au NPs using P(AA$_{40}$)-TTC the best results were obtained at pH 7. Alternatively, using the P(PEGA$_{40}$)-TTC at pH=3 led to colloids with well-defined LSPR band. Moreover, in these cases it was found that the evolution of the NPs continued over time and after copolymerization at 70ºC the size of the Au NPs changed. These results are very interesting and can be very promising in the synthesis of new polymer@Au nanocomposite. However, further studies should be done in order to correlate all the parameters and further understand the kinetics of nucleation and growth of the Au NPs.

Adsorption of the MR onto Au NPs allows to previously define the size and the shape of the Au NPs, although in this work only spherical Au NPs with ~15 nm were explored. It was found that UV-Vis spectroscopy is not the best technique to quantify the MR adsorbed since an adsorption profile was not possible to obtain, but this could be due to the concentration range considered (i.e. above the CMC). After determination of CMC, adsorption of the MR agent onto Au NPs was performed below and above CMC. Both situations led to Au NPs covered with MR agent but it seems that the ones carried out above CMC afforded more free MR chains. Concerning the second step, the copolymerization of the hydrophobic block was successfully performed below and above CMC, leading the polymer@Au shell@core-type nanostructures.

In summary, the preparation of Au nanocomposites following the *grafting from* strategy via macroRAFT adsorption onto previously prepared Au NPs seems to be the most interesting strategy to be explored for biosensing applications since well-defined shell@core nanostructures were produced. Therefore, in the next chapter (**Chapter 4** – ***Functionalization of gold nanostructures prepared via RAFT polymerization***) this strategy was applied. Moreover, the MR agent P(PEGA$_{40}$)-TTC was the MR agent chosen to be explored in the next chapter since it is known to be have high biocompability and no interaction with proteins which are important characteristics for bioapplications.

CHAPTER 4. Functionalization of gold nanostructures prepared via RAFT polymerization

4.1. Introduction

In this chapter, shell@core type nanostructures are be prepared following a *grafting from* strategy via macroRAFT agent adsorption onto previously prepared Au NPs. In fact this type of structure is important in biosensing, namely having a Au NP as core, in order that all the recognition moieties at the surface of the nanostructure are at the same distance from the Au core. Hence, the interaction between the biotarget and the bioreceptor (recognition moiety) at the nanostructure will lead to a uniform response, in this case an optical response. Therefore, the main objective in this chapter is the preparation of biofunctional copolymer@Au NPs that can be used as a biosensor. Based on the results obtained in ***Chapter 3***, the nanostructures will be prepared using the MR agent P(PEGA$_{40}$)-TTC since it is known that PEGA has little interaction with proteins.

As discussed, RAFT polymerization was selected not only because it allows control over the molecular weight of the polymer but also because it allows to introduce functional monomers that will be important for the biofunctionalization. The combination of RAFT polymerization with *click chemistry* is very attractive and has been largely explored in the literature, as reviewed in the introduction. For example, a monomer containing an azide can be polymerized and can be placed at a specific length from the core, in the polymer, that afterwards using the specific *click chemistry* reaction with an alkyne group will allow to design a (bio)functional polymer. However, *click chemistry* together with RAFT polymerization is not as easy and straightforward as reported in the literature which led us to face several drawbacks. Specifically, rigorous safety issues should be present, such as azides should not be handled at temperatures above 50ºC, due to explosive risk [167]. Still there are some works reporting polymerization of monomers containing the azide moiety at higher temperatures (65ºC-70ºC). [204–206]

In ***Chapter 3***, the synthesis of MR agents as well as the growth of the hydrophobic chain were carried out at 70ºC using ACPA as initiator (10h half-life ($t_{1/2}$) in water at 69ºC [207]) which for the polymerization of a monomer containing an azide moiety is too high. In turn, a monomer containing the alkyne moiety, instead of the azide moiety, could be polymerized but also several issues regarding side reactions are raised. In this sense, monomers containing alkyne moieties are usually protected before polymerization and after that these repeating units are deprotected yielding alkylated polymers. [208]. But the deprotection procedures could be aggressive for the final copolymer@Au nanostructure leading to unstable colloids and aggregation.

An alternative method could be the modification of the copolymer@Au NPs with an azide function after the preparation of the nanostructure. However, this strategy is not viable in this case since it would involve a reaction between the carboxylate ion at the surface of the nanostructure and the hydroxyl from the 3-azido-1-propanol in aqueous solution, using the intermediate *N*-(3-

dimethylaminopropyl)-*N'*-ethylcarbodiimide (EDC), as shown in Scheme 4.1. EDC is widely used to promote amide linkages as well as ester linkages in organic media, but in aqueous solutions the ensuing ester linkages are easily hydrolyzed. Consequently this strategy was not followed here.

Scheme 4.1 Schematic representation of the reaction between the carboxylate ion at the surface of copolymer@Au nanostructure and the hydroxyl group from the 3-azido-1-propanol using EDC as intermediate.

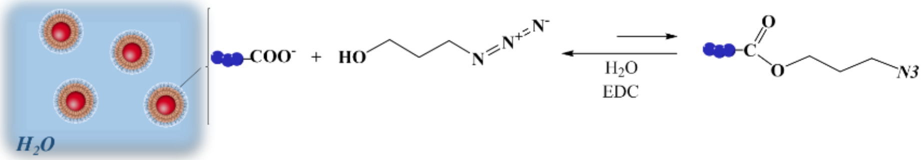

Therefore, a macroRAFT agent was first prepared via RAFT polymerization, at 70ºC, and then it was functionalized with the azide moiety (***sub-chapter 4.2.***). Next, the *azide*-MR agent was copolymerized with the mixture of MMA:BA (10:1 w/w) via RAFT emulsion polymerization at a lower temperature (44ºC), as is discussed in ***sub-chapter 4.3.***. Afterwards, these functional copolymer@Au nanostructures were explored towards biosensing applications, ***sub-chapter 4.4.***. In ***sub-chapter 4.5.***, complementary studies to better understand the interaction between the copolymer, biotin and avidin were performed using Langmuir monolayers of the copolymer at air/water interface. Finally, ***sub-chapter 4.6.*** describes an approach to prepare fluorescent copolymer@Au nanostructures.

4.2. Preparation and characterization of functionalized macroRAFT agent

The initial idea was to prepare a MR agent containing the azide moiety, i.e. to polymerize an azide-monomer. However, due to the temperature of polymerization (70ºC) of the MR agents studied in ***Chapter 3***, the azide moiety was covalently bonded to the MR agent after its synthesis. Thus, a MR agent based on PEGA was synthesized in solution via RAFT polymerization at 70ºC using the same initiator (ACPA). In this case, two units of AA were polymerized per chain before the polymerization of PEGA with the purpose to increase the number of carboxylic acids where the functionalization with the azide group occurs, obtaining the MR agent P(AA_2-*b*-$PEGA_{40}$)-TTC. In other words, the polymerization occurred in one batch: first AA was polymerized during 3 hours and then PEGA was added to the reaction vessel and the polymerization continued for further 4 hours, following the procedure used to prepare the MR agent P(PEGA$_{40}$)-TTC discussed in ***Chapter 3.***.

The monomer conversion (*%Conversion*) was monitor by ^{1}H-NMR spectroscopy of withdrawn aliquots using the 1,3,5-trioxane as internal standard. However, *%Conversion* of AA (Figure 4.1) was not easy to determine due to the low amount of monomer in the reaction vessel, i.e. internal standard was added in a molar ratio of $^1/_6$ related to PEGA. So the integration of the vinylic protons of the AA monomer did not show significant changes during the polymerization in comparison with the protons integration of the internal standard. After adding PEGA the polymerization continued during 4 hours, obtaining a PEGA conversion of 91.5% ($\overline{M}_{n\ (exp\_NMR)}$ = 18291 g/mol, DP_{PEGA}=37) determined by ^{1}H-NMR.

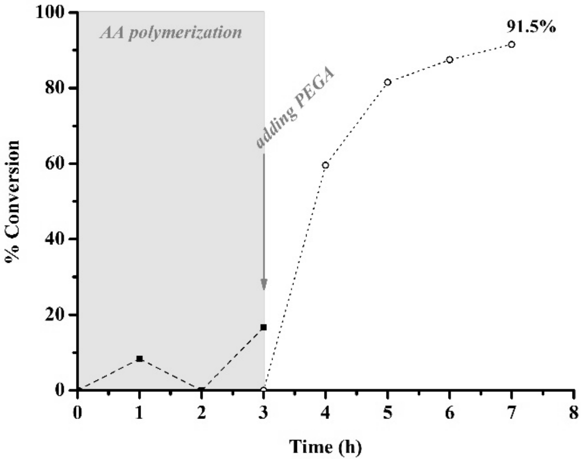

Figure 4.1. *%Conversion* of AA and PEGA during the synthesis of the MR agent P(AA$_2$-b-PEGA$_{40}$)-TTC.

Next, the macroRAFT agent P(AA$_2$-*b*-PEGA$_{40}$)-TTC was functionalized with an azide moiety, yielding the *N3*-MR agent. Although, the AA conversion was not conclusive, each MR agent chain has already one carboxylic acid group, that belongs to the *R*-group (hydrophilic moiety) of the RAFT agent, where the azide moiety can be linked. For this, the MR agent was dispersed in dichloromethane and EDC was added to activate the carboxylic acid, in the presence of 4-(dimethylamino)pyridine (DMAP). The 3-azido-1-propanol was added to the reaction vessel and stirred at room temperature over two days. Typical esterification reactions procedures, in organic media, are carried out during one day but to ensure that all the carboxyl groups from MR agents were modified and also following the procedure used in the preparation of the alkylated biotin [209] (described later), the esterification reaction occurred during two days. This esterification reaction is represented in Figure 4.2. Although the ester linkage can be formed between the hydroxyl group and the carboxylic acid from the *R*-

group of the RAFT agent, here only the chemical reaction with the carboxylic acid from AA repeating unit was represented.

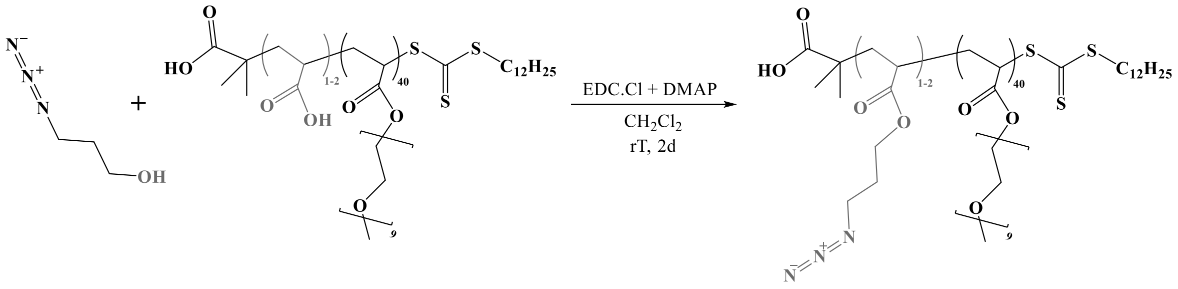

Figure 4.2. Preparation of *N3*-MR agent by esterification reaction between the carboxyl group from the MR agent and the hydroxyl from the 3-azido-1-propanol.

The *N3*-MR agent was characterized by ATR-FTIR and ^{1}H-NMR spectroscopies. The new ester bond was difficult to identify by ATR-FTIR spectroscopy since its vibration frequency (1730 cm^{-1}) overlaps with the ones from ester bonds of each repeating unit of the MR agent. Nevertheless, the vibrational mode characteristic of the azide at 2097 cm^{-1} was observed, as indicated in Figure 4.3. By ^{1}H-NMR spectroscopy (Figure 4.4), the chemical shifts corresponding to the protons from two carbons of 3-azido-1-propanol were also identified [161]. The integration of these signals, using CH_3 from *Z*-group as reference (marked in the spectrum with *, δ=0.8 ppm), indicates that there is one or two azide moieties per polymer chain (see ***Annexe F***).

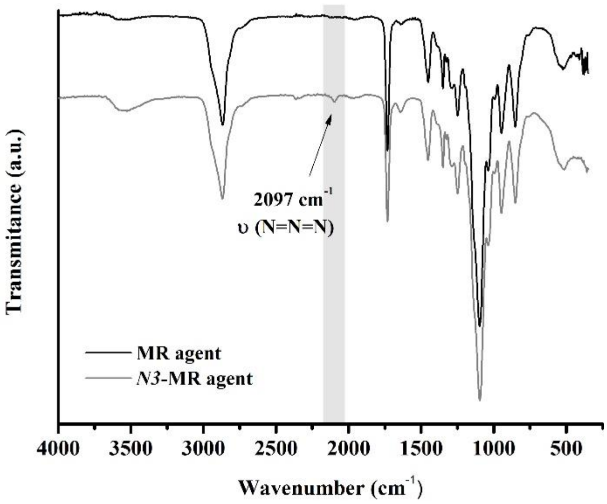

Figure 4.3. ATR-FTIR spectra of MR agent P(AA$_2$-*b*-PEGA$_{40}$)-TTC before and after functionalization with the azide moiety.

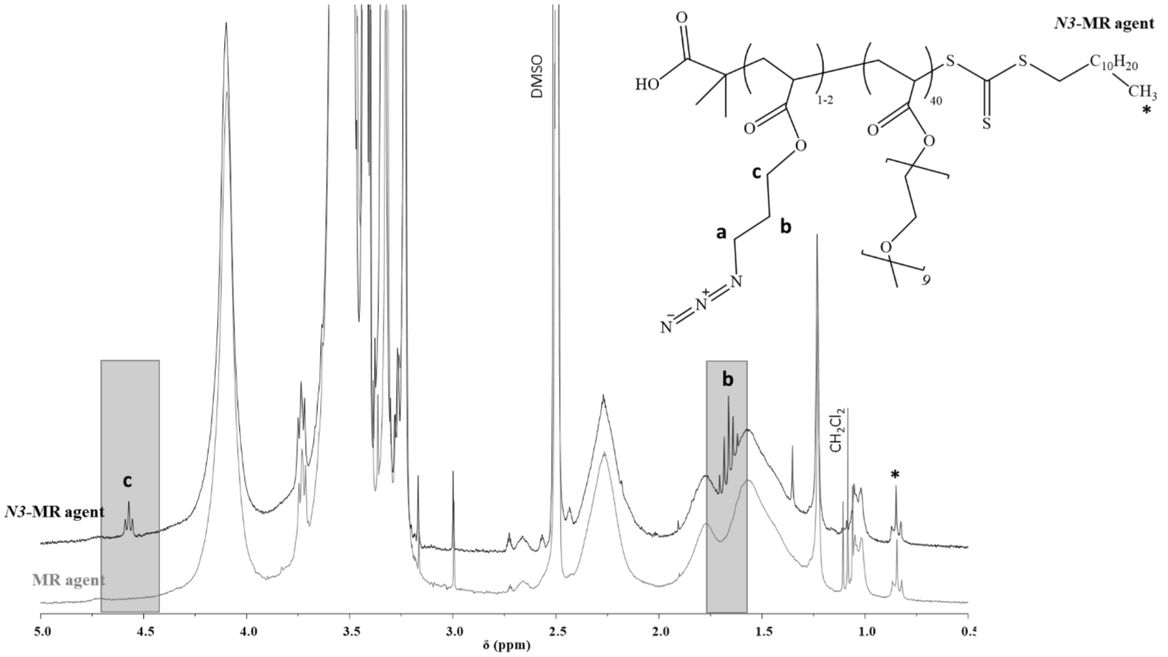

Figure 4.4. ^{1}H-NMR spectra of MR agent P(AA_2-*b*-$PEGA_{40}$)-TTC before and after functionalization with the azide moiety. (*inset*) Chemical structure of the *N3*-MR agent.

The functionalization of the MR agent P(AA_2-*b*-$PEGA_{40}$)-TTC with an azide group was successful achieved. Therefore, in the next sub-chapter the *N3*-MR agent will be used to prepare the functional azide-copolymer@Au NPs.

4.3. Preparation of functionalized gold nanocomposites via RAFT polymerization using the *grafting from* strategy

The preparation of copolymer@Au NPs involves first the adsorption of the MR agent at room temperature (MR@Au NPs) and then the growth of the hydrophobic chain using temperature. The macroRAFT agent (*N3*-MR agent) prepared in ***sub-chapter 4.2.*** has a similar *%Conversion* and $\overline{M}_{n(exp\_NMR)}$ in comparison to the P($PEGA_{40}$)-TTC described in ***Chapter 3***, hence even with the AA repeating units ($DP_{AA} \leq 2$), the adsorption behavior of these MR agents onto Au NPs should be similar. Moreover, in ***Chapter 3***, the second step was performed at 70ºC, but using the *N3*-MR agent lower temperatures should be used. For that reason an initiator with a half-time ($t_{1/2}$) at lower temperature was chosen - 2,2'-azobis[2-(2-imidazolin-2-yl)propane]dihydrochloride (VA-044, $t_{1/2}$ = 10h at 44ºC) [109]. Consequently, the polymerization conditions to growth the hydrophobic chain via RAFT emulsion polymerization were studied at 70ºC and 44ºC (without Au NPs). The copolymers were characterized by gravimetric analysis (to determine the monomer conversion), GPC-SEC analysis and DLS measurements (***4.3.1.***). After that the copolymerization from MR@Au NPs at 44ºC was carried out (***4.3.2.***).

4.3.1. Study of RAFT emulsion polymerization using VA-044 as initiator

The temperature of polymerization as well as the initiator were changed, which consequently influenced the polymerization rate of the copolymers. Therefore, a study was performed in order to adjust the polymerization conditions to obtain a copolymer with similar *%Conversion* and $\bar{M}_n$ in comparison to the copolymer prepared using ACPA at 70ºC.

P(PEGA$_{40}$)-TTC was first copolymerized with the hydrophobic monomers (10 MMA: 1 BA w/w) at 70ºC using VA-044, as initiator, and keeping the polymerization conditions used in the copolymerization where ACPA was used as initiator. Figure 4.5 shows a comparison of the monomer conversion (*%Conversion*) using the initiator ACPA and VA-044 at 70ºC. Using VA-044, after one hour of copolymerization the *%Conversion* is already close to the monomer conversion using the ACPA after 4 hours. Moreover after the 4 hours (using VA-044), 100% of monomer conversion was obtained, by gravimetric analysis. Differences in the rate of polymerization using ACPA and VA-044 at 70ºC were already reported by Perrier *et al.* [109, 210], since VA-044 has a higher decomposition rate coefficient (k_d) which allows to speed up the polymerization without affecting its livingness.

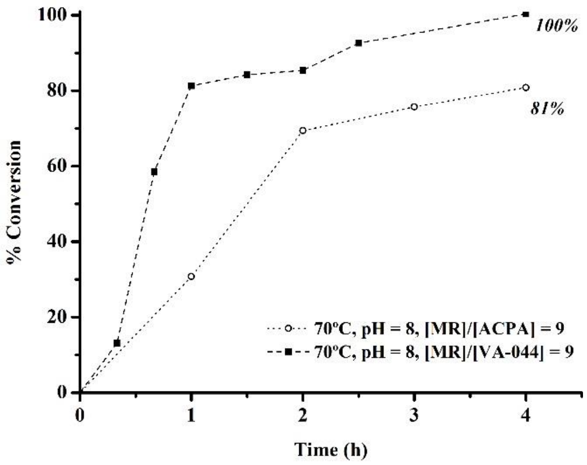

Figure 4.5. *%Conversion* during the copolymerization of MMA:BA (10:1 w/w) in the presence of P(PEGA$_{40}$)-TTC, using initiators ACPA and VA-044 at 70ºC.

In addition to the gravimetry results, GPC-SEC analysis were also performed, see Table 4.1. The GPC-SEC chromatograms (Figure 4.6) show that using both initiators at 70ºC, polymers with two molecular average weights were synthesized. This result suggests that besides controlled RAFT polymerization ($\bar{M}_{n\ (exp\_gpc)}$ of 11 485 and 12 135 g/mol, by using ACPA and VA-044 respectively) conventional free radical polymerization also occurred, which corresponds to the highest molecular weights identified. Furthermore, the dispersity (Đ) is in agreement with what was discussed, i.e. Đ values close to 1 correspond to the peaks of controlled polymerization and Đ > 1.3 corresponds to the conventional free radical polymerization. However, the $\bar{M}_n$ determined by GPC-SEC ($\bar{M}_{n\ (exp\_gpc)}$ of 11 485 and 12 135 g/mol) is much lower than the molecular weight determined for the MR agent P(PEGA$_{40}$)-TTC by ^{1}H-NMR spectroscopy, which was 20104 g/mol. Yet, previous experience in the group revealed that with the conditions used for GPC-SEC analysis (THF as mobile phase) of polymers based on PEGA, the $\bar{M}_{n\ (exp\_gpc)}$ has been much lower than the value expected. In turn, DLS measurements (Table 4.1) show a low PdI value using both initiators and just one peak in the hydrodynamic diameter in intensity ($d_{intensity}$) and number (d_{number}) distribution.

Table 4.1. Theoretical and experimental data of gravimetry and GPC-SEC analysis of block copolymers P(PEGA$_{40}$)-*b*-(MMA-*co*-BA)$_n$-TTC prepared with ACPA or VA-044 at 70ºC.

	Experimental conditions	**70ºC, pH=8, 4h, *[MR]/[ACPA]*=9**	**70ºC, pH=8, 4h, *[MR]/[VA-044]*=9**
	$\bar{M}_{n\ (theoretical)}$ g/mol	35 332	34 457
	DP $_{(theoretical)}$	173	168
Gravimetry	***%Conversion***	81	100
	$\bar{M}_{n\ (exp\_grav)}$ g/mol*	31 971	34 457
	DP*	140	168
GPC-SEC	**$\bar{M}_w$ g/mol** *(peak 1; peak 2)*	467 293 ; 13 530	244 930 ; 13 370
	$\bar{M}_{n\ (exp\_gpc)}$ g/mol *(peak 1; peak 2)*	341 660 ; 11 485	171 616 ; 12 135
	Đ *(peak 1; peak 2)*	1.37 ; 1.18	1.43 ; 1.01
DLS	**$d_{average}$ (nm)**	98.8	74.1
	$d_{intensity}$ / d_{number} (nm)	106.5 / 74.7	77.5 / 62.2
	PdI	0.057	0.057

***** $\bar{M}_n$ and DP estimated using the *%Conversion* determined by gravimetric analyzes.

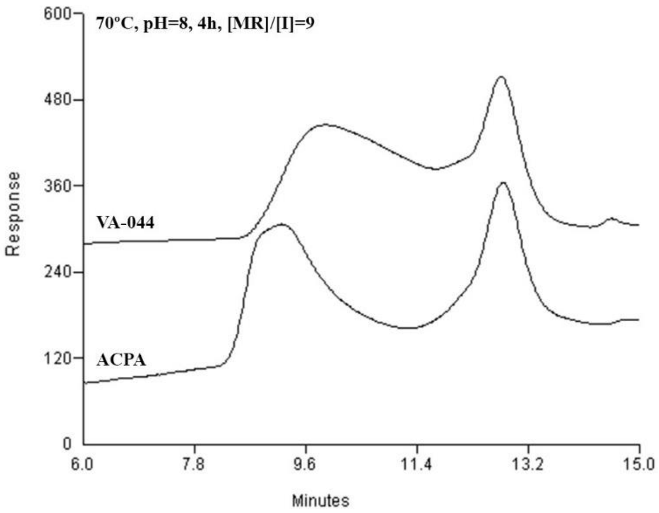

Figure 4.6. GPC-SEC chromatograms of P(PEGA$_{40}$)-*b*-(MMA-*co*-BA)$_n$-TTC copolymers prepared with ACPA or VA-044 at 70ºC.

The identification of two molecular weights, using ACPA and VA-044 at 70ºC, was not expected and the GPC-SEC analysis was only possible to perform after the preparation of the copolymer@Au nanostructures. Furthermore, this result confirms the need of RAFT emulsion polymerization be carried out in starved conditions, i.e. controlled addition of monomer, that should be taken into consideration for future work.

Then, VA-044 was used as initiator in the copolymerization of the mixture of hydrophobic monomers (10 MMA: 1 BA w/w) in the presence of the MR agent P(PEGA$_{40}$)-TTC at 44ºC. Parameters such as pH, the *[MR]/[initiator]* ratio and the polymerization time were studied in order to optimize the RAFT emulsion polymerization at 44ºC. Figure 4.7 shows the monomer conversion determined by gravimetric analysis as a function of time, varying those parameters. At first, the copolymerization of the MR agent was carried out using the same polymerization conditions, i.e. pH=8 and *[MR]/[I]*=9, but at a lower temperature (44ºC). After 22h of polymerization only 33% of monomer conversion was obtained. In the literature, the initiator VA-044 is usually used at a pH around 6, therefore the copolymerization was also performed at this pH. However, the polymerization was only carried out during 7h and a monomer conversion of 15% was obtained. This *%Conversion* is similar to the monomer conversion (16%) in the polymerization conditions mentioned before, after the 7 hours of reaction (see the *inset* in Figure 4.7). Hence, pH was maintained at 8. Then the *[MR]/[I]* ratio was reduced to 5 because it was expected that the decrease of the *[MR]/[I]* ratio would allow to have more active chains, so the polymerization should occur faster, even in a control way

(*[MR]/[I]>1)*. Although, after 23h of polymerization only 21% of monomer conversion was obtained, which is less than in the last polymerization conditions used at pH=8. Nevertheless, as justified in ***4.3.2.,*** these were the polymerization conditions (pH = 8, 24h) selected for the preparation of copolymer@Au nanostructures. Later, aiming further optimization, the copolymerization was repeated with the initial experimental conditions (pH=8 and *[MR]/[I]* = 9) but the polymerization was carried out over a longer period of time. After 53 hours, 51% of monomer conversion was achieved.

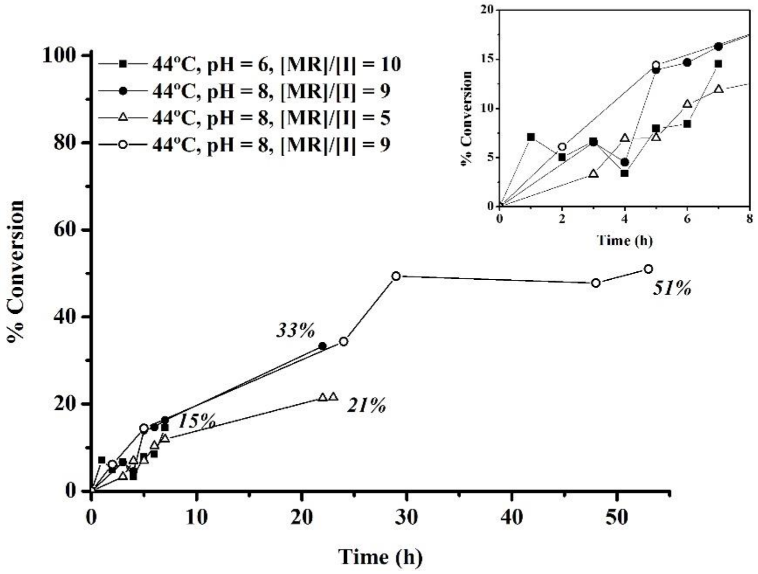

Figure 4.7. ***%Conversion*** **during the copolymerization of MMA:BA (10:1 w/w) in the presence of P(PEGA$_{40}$)-TTC using the initiator VA-044 at 44ºC, varying the pH, [MR]/[initiator] ratio and polymerization time.** ***Inset*** **shows an amplification of the first 8h of polymerization.**

GPC-SEC analysis (Table 4.2) and chromatograms (Figure 4.8) of the copolymers prepared at 44ºC revealed that the copolymers have one molecular weight, indicating that at this temperature just the controlled polymerization (RAFT polymerization) took place. As mentioned above, the molecular weight of the copolymers determined by GPC-SEC analysis is lower than the molecular weight of the MR agent ($\overline{M}_{n\ (exp\_NMR)}$ = 20104 g/mol). Even so the comparison between the results from GPC-SEC is possible since all the copolymers were prepared using the same MR agent. In general, the $\overline{M}_w$ and $\overline{M}_n$ (Table 4.2) are very close for all the copolymers and reasonably Đ values were obtained, except for the copolymer prepared during 53h. This suggests that although low monomer conversion was achieved the copolymerization occurred in a controlled way. In addition, with the 53h of polymerization a higher $\overline{M}_n$ was obtained in comparison with the $\overline{M}_n$ values of the other copolymers, which is in agreement with the monomer conversion (51%). However, the peak in the chromatogram presented a shoulder contributing to a higher $\overline{M}_w$ value and hence higher Đ (1.63).

Table 4.2. Theoretical and experimental data of gravimetry and GPC-SEC analysis of block copolymers P(PEGA$_{40}$)-*b*-(MMA-*co*-BA)$_n$-TTC prepared with VA-044 at 44ºC.

	Experimental conditions	**pH=6** ***[MR]/[I]*=10** **7h**	**pH=8** ***[MR]/[I]*=9** **22h**	**pH=8** ***[MR]/[I]*=5** **23h**	**pH=8** ***[MR]/[I]*=9** **53h**
	$\bar{M}_{n\ (theoretical)}$ g/mol	33 936	34 906	34 782	34 714
	DP $_{(theoretical)}$	163	172	171	170
Gravimetry	***%Conversion***	15	33	21	51
	$\bar{M}_{n\ (exp\_grav)}$ g/mol*	19 641	23 119	20 982	26 187
	DP*	23	56	36	86
GPC-SEC	**$\bar{M}_w$ g/mol**	15 522	15 522	15 101	21 836
	$\bar{M}_{n\ (exp\_gpc)}$ g/mol	12 670	12 216	12 064	13 395
	Đ	1.23	1.27	1.25	1.63

***** $\bar{M}_n$ and DP estimated using the *%Conversion* determined by gravimetric analyzes.

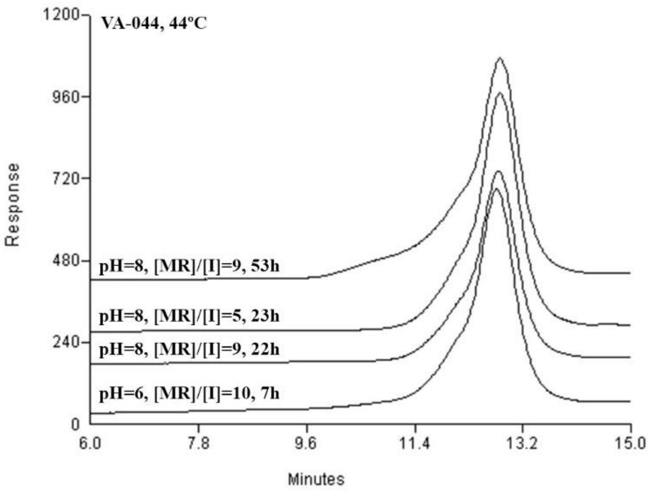

Figure 4.8. GPC-SEC chromatograms of P(PEGA$_{40}$)-*b*-(MMA-*co*-BA)$_n$-TTC copolymers prepared with the initiator VA-044 at 44ºC, varying the pH, [MR]/[initiator] ratio, and polymerization time.

The macroRAFT P(AA$_2$-*b*-PEGA$_{40}$)-TTC ($\bar{M}_{n\ (exp\_NMR)}$ = 18291 g/mol), that was synthesized to be functionalized with the azide moiety (***sub-chapter 4.2.***), was also copolymerized with the hydrophobic monomers (10 MMA: 1 BA w/w). In this case, the polymerization conditions of pH=8 and *[MR]/[I]=9* were used at 70ºC and 44ºC using ACPA and VA-044 as initiators, respectively. Likewise, *%Conversion* by gravimetric analysis as well as the GPC-SEC results are in agreement with what was observed and discussed for the macroRAFT P(PEGA$_{40}$)-TTC, see Figure 4.9 and Table 4.3. High monomer conversion was obtained after 4h and 2 peaks were found in GPC-SEC chromatogram, using ACPA as initiator at 70ºC. Concerning, the use of VA-044 at 44ºC, a lower monomer conversion (20%) was achieved after 23h, and also one peak was found (Đ=1.21) by GPC-SEC analysis. Indeed higher monomer conversion, around 30%, was expected as observed for the copolymerization of the P(PEGA$_{40}$)-TTC under the same conditions. This result can be explained by the presence of the AA repeating units which in fact can influence the number and size of formed micelles that stabilizes the growing polymer, and subsequently change the rate of polymerization.

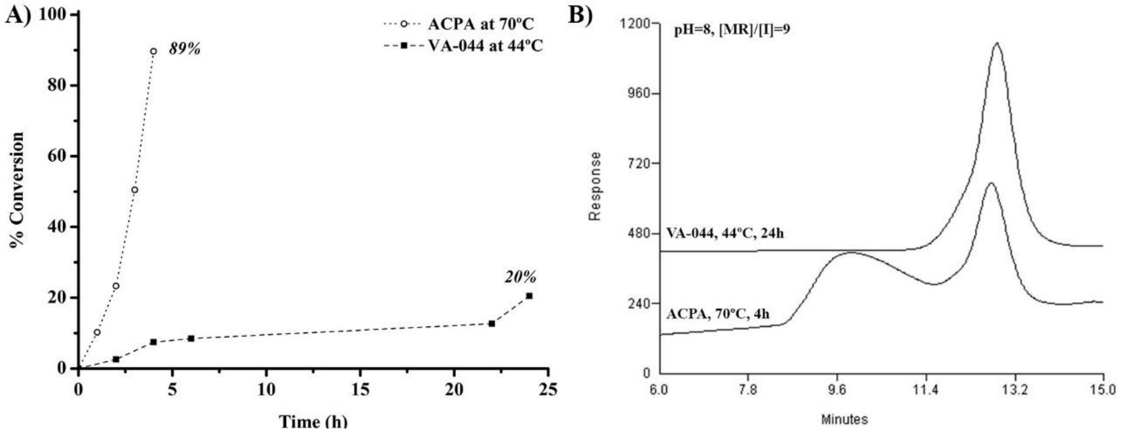

Figure 4.9. (A*) %Conversion* and (B) GPC-SEC chromatograms of the copolymerization of MMA:BA (10:1 w/w) in the presence of P(AA$_2$-*b*-PEGA$_{40}$)-TTC using the initiator ACPA at 70ºC and VA-044 at 44ºC. At pH= 8 and *[MR]/[initiator]*=9.

Table 4.3. Theoretical and experimental data of gravimetry and GPC-SEC analysis. Copolymers were prepared with P(AA$_2$-*b*-PEGA$_{40}$)-TTC using ACPA at 70ºC and VA-044 at 44ºC.

	Experimental conditions	**70ºC, 4h, pH=8, *[MR]/[ACPA]*=9**	**44ºC, 24h, pH=8, *[MR]/[VA-044]*=9**
	$\bar{M}_{n\ (\mathrm{theoretical})}$ g/mol	35 840	35 820
	DP $_{(\mathrm{theoretical})}$	175	174
Gravimetry	***%Conversion***	89	20
	$\bar{M}_{n\ (\mathrm{exp\_grav})}$ g/mol*	34 055	21 557
	DP*	156	35
GPC-SEC	**$\bar{M}_w$ g/mol** *(peak 1; peak 2)*	269 044 ; 13 684	13 740
	$\bar{M}_{n\ (\mathrm{exp\_gpc})}$ g/mol *(peak 1; peak 2)*	184 498 ; 12 388	11 337
	Đ *(peak 1; peak 2)*	1.46 ; 1.10	1.21

***** $\bar{M}_n$ and DP estimated using the *%Conversion* determined by gravimetric analyzes.

The optimization of the RAFT emulsion polymerization conditions at 44ºC using the VA-044 as initiator was performed for the free MR agent, i.e. without the presence of Au NPs. In other words, in spite of the optimization of the polymerization conditions for the MR agent, the polymerization from MR@Au NPs could not strictly follow the same behavior and the same monomer conversions. Also the copolymerization carried out during 53h (high monomer conversion obtained, 51%) was performed after and/or in parallel with the preparation of the Au nanostructures, where polymerization from the MR@Au NPs was performed during 24h. Moreover, in ***Chapter 3*** it was demonstrated the importance of adding the mixture of hydrophobic monomers in a controlled way during the preparation of copolymer@Au NPs, at 70ºC. Here, the GPC-SEC analysis, for the copolymers prepared at 70ºC, also reinforced the influence of the controlled addition of the monomers during the RAFT emulsion polymerization.

Therefore, the next *sub-chapter* presents and discusses the copolymerization of MMA:BA (10:1 w/w), added in a controlled way, from MR@Au NPs at 44ºC, during 24h, using the VA-044 as initiator, without further optimization to achieve higher monomer conversions.

4.3.2. Preparation and characterization of biofunctional copolymer@Au nanostructures

The preparation of the biofunctional copolymer@Au nanostructures was performed following the *grafting from* strategy via adsorption of the MR agent. In the first step the MR was adsorbed at the Au NPs surface using a concentration below the CMC. Then, in the second step, hydrophobic monomers were polymerized from the surface of MR@Au NPs at 44ºC during 24h, the mixture of monomers (10 MMA : 1 BA w/w) was added in a controlled way in the first 5h of emulsion polymerization. Here, two Au nanostructures were prepared: one using the MR agent P(PEGA$_{40}$)-TTC, yielding the copolymer@Au NPs, and the other one prepared using a mixture of this MR agent with the MR agent modified with the azide group (2 MR : 1 *N3*-MR), yielding *N3*-copolymer@Au NPs. This [2MR:1*N3*-MR] molar ratio was chosen in order to add the azide functionality to the nanostructure without significant perturbation of the emulsion copolymerization (i.e. polymerization conditions were just studied for the MR agent P(PEGA$_{40}$)-TTC). The Au nanostructures were characterized by UV-Vis spectroscopy, DLS and zeta potential measurements and electron microscopy.

UV-Vis spectra, in Figure 4.10, show that in both cases the λ_{LSPR} shifted to higher wavelengths ($\Delta\lambda$ ~3nm, see Table 4.4) as had been observed in the copolymerization from MR@Au NPs at 70ºC, using ACPA as initiator. Moreover, the increase of the absorbance around 200-250 nm indicates the presence of the copolymer as observed before.

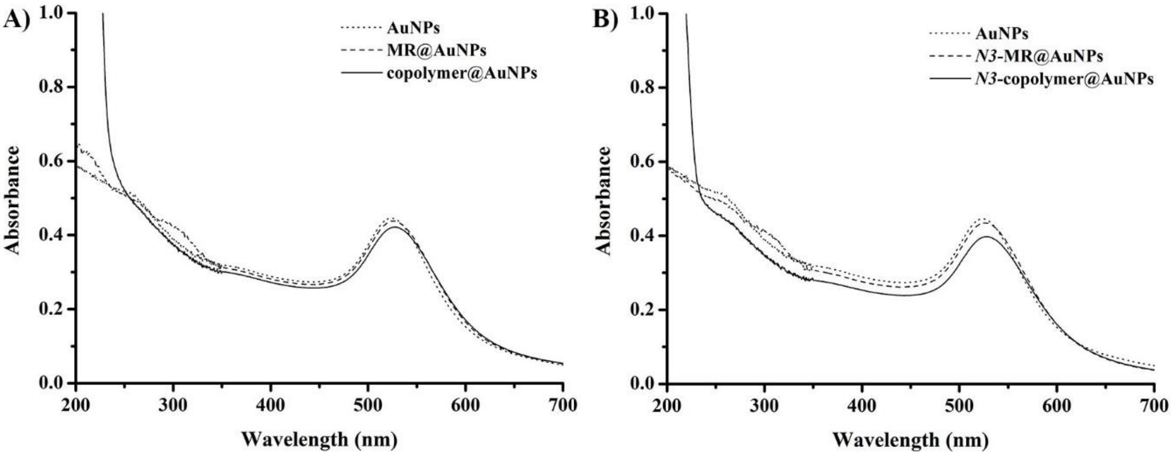

Figure 4.10. UV-Vis spectra of Au nanostructures before and after emulsion copolymerization at 44ºC. Au nanostructure (A) without and (B) with azide function.

Table 4.4. λ_{LSPR} and $d_{average}$ Au nanostructures, without and with azide function, before and after emulsion copolymerization at 44ºC.

MR used		**λ_{LSPR} (nm)**	**$d_{average}$**	**PdI**
MR agent	**Before copolymerization**	525	25.8	0.586
	After copolymerization	528	27.3	0.546
***N3*-MR agent**	**Before copolymerization**	526	26.6	0.561
	After copolymerization	529	27.9	0.531

Note: Au NPs: λ_{LSPR} (nm) = 523 nm, $d_{average}$ = 16.3 nm (PdI=0.573).

Table 4.4 shows DLS results in which the hydrodynamic average diameter increased around 2 nm. This small increase of the $d_{average}$ was also observed in the previous case when the copolymerization from MR@Au NPs was performed at 70ºC. Electron microscopy images (Figure 4.11) show that after the copolymerization the polymer shell is well-defined, namely in the case of *N3*-copolymer@Au NPs (Figure 4.11-B2). In the case of copolymer@Au NPs (Figure 4.11-A2), a slight grey background around the Au NPs was observed, as also observed in the samples obtained by copolymerization at 70ºC (see Figure 3.34-A1).

Concerning the surface charge of these nanostructures, zeta potential measurements were performed using a batch of nanostructures prepared following the same procedure. The results showed that after adsorption of the MR agent and the mixture [2 MR : 1 *N3*-MR] of MR agents onto Au NPs the zeta potential decreased from -49.3 ± 19.0 mV (Au NPs, pH 5.6) to -25.7 ± 12.6 mV and -25.1 ± 14.1 mV, at pH=6.9, respectively. After the copolymerization the zeta potential slightly increased to $\zeta_{\text{copolymer@Au NPs}}$ = -31.8 ± 12.5 mV (pH = 5.6) and $\zeta_{N3\text{-copolymer@Au NPs}}$ = -26.4 ± 10.2 mV (pH = 5.7).

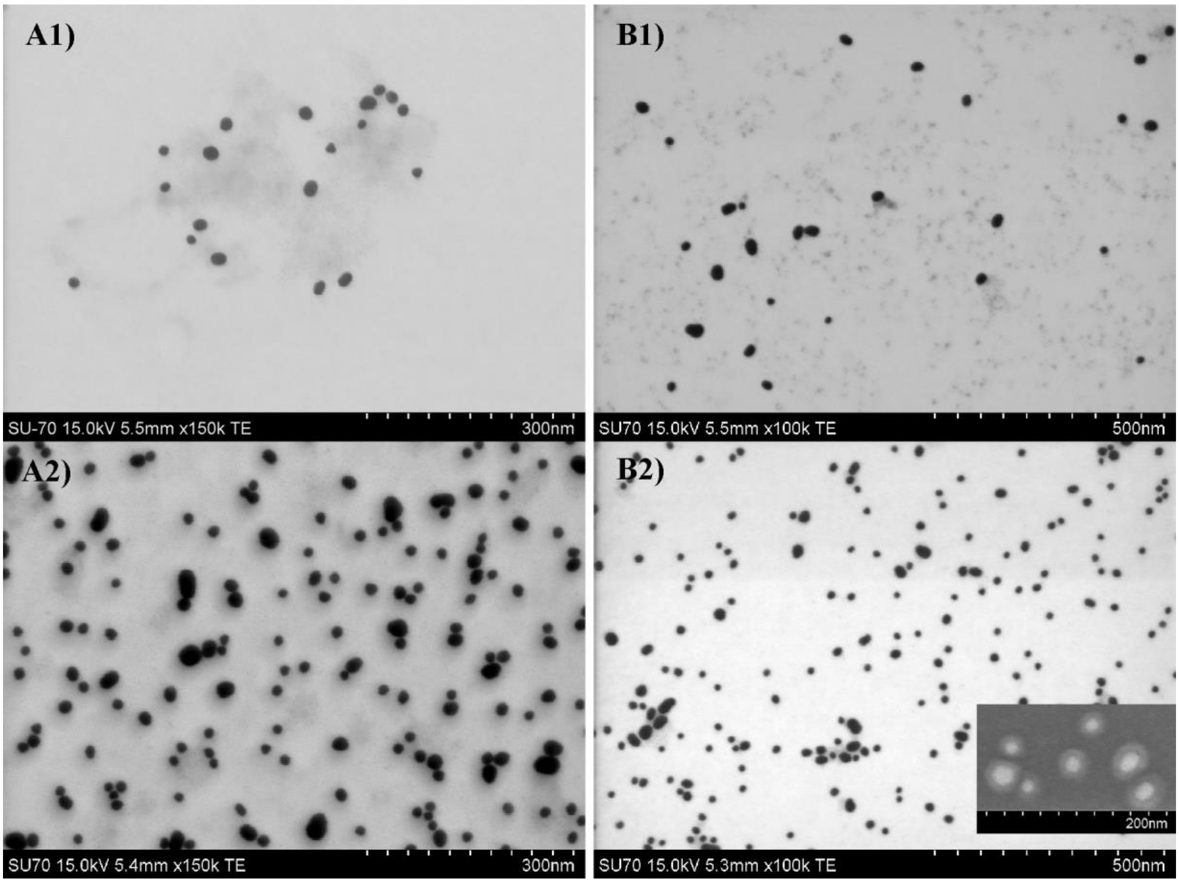
A1)
B1)
A2)
B2)
SU-70 15.0kV 5.5mm x150k TE
300nm
SU70 15.0kV 5.5mm x100k TE
500nm
SU70 15.0kV 5.4mm x150k TE
300nm
SU70 15.0kV 5.3mm x100k TE
500nm
200nm

Figure 4.11. SEM images (transmission mode) of Au nanostructures prepared with (A) MR agent and with (B) the mixture 2MR:1 *N3*-MR agents. (A1 and B1) before and (A2 and B2) after emulsion copolymerization. (B2-*inset*) secondary electron imaging showing in detail the shell@core nanostructure.

The copolymerization from MR@Au NPs was successfully performed at 44ºC using the initiator VA-044, just as the copolymerization at 70ºC using ACPA as initiator. However, at 44ºC, 24 hours are required for the copolymerization instead of the 4 hours at 70ºC. Moreover, the results obtained demonstrate that the presence of the azide modified repeating units does not affect (at least significantly) the formation of Au nanostructures. Although, the determination of the amount of azide moiety per NP was not possible, even by elemental analysis, during the adsorption step the solution of *N3*-MR agent was added dropwise to the Au NPs colloid and stirred 2h prior the solution of MR agent (without azide) be added to ensure functionalized MR was adsorbed.

4.4. Response of the gold nanostructures towards avidin

In order to evaluate the use of the copolymer@Au NPs in biosensing applications, the well-known model biotin-avidin (bioreceptor-biotarget) was used. The *N3*-copolymer@Au nanostructures prepared as described above (***4.3.2.***) were first biotinylated using the specific *click chemistry* reaction. Then, the optical response of the biotinylated and non-biotinylated copolymer@Au NPs was assessed by adding avidin to the colloidal nanostructures, which is a protein that has high affinity towards biotin. BSA was used as control, which is a protein that does not have affinity to biotin.

Regarding the biotinylation step, the alkylated biotin (*biotin-CCH*) was prepared following the procedure described in [209]. An esterification reaction was promoted in DMF, using EDC and DMAP, between the carboxylic acid group from biotin and the hydroxyl group from 3-butyn-1-ol (Figure 4.12). The alkylated biotin was characterized by ^{1}H-NMR, see Figure G.11 (***Annex G***).

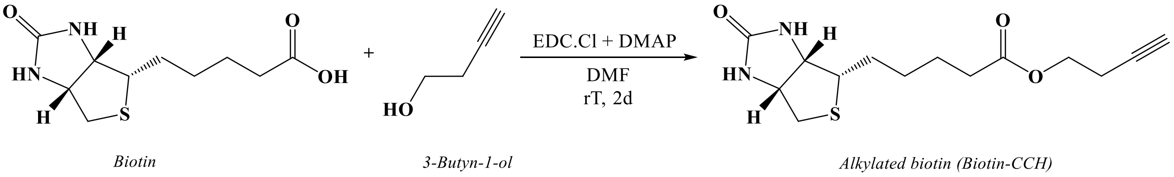

Figure 4.12. Preparation of alkylated biotin.

Afterwards, *biotin-CCH* was covalently bound to the *N3*-copolymer@Au nanostructures in the presence of $CuSO_4$ and sodium ascorbate thus forming a covalent 1,2,3-triazole linkage via *click chemistry* thus yielding *biotin*-copolymer@Au NPs (Figure 4.13). The role of sodium ascorbate is to reduce Cu(II) to Cu(I) which in turn catalyzes this reaction. After biotinylation, the UV-Vis spectrum showed a small shift in the λ_{LSPR} ($\Delta\lambda \sim +1$ nm) and no sign of aggregation, but the formation of the 1,2,3-triazole linkage was not confirmed by any further characterization technique. By FTIR spectroscopy, due to the small amount of azide/triazole group (consumption of azide and subsequently formation of triazole during the *click* reaction) in the copolymer@Au nanostructure is not possible to visualize the characteristic vibrational frequency of the azide neither the triazole in the spectrum. However, CuAAC is known to be a very specific and highly efficient reaction [154], therefore it is believed that the reaction occurred yielding stable *biotin*-copolymer@Au NPs obtained via *click chemistry*.

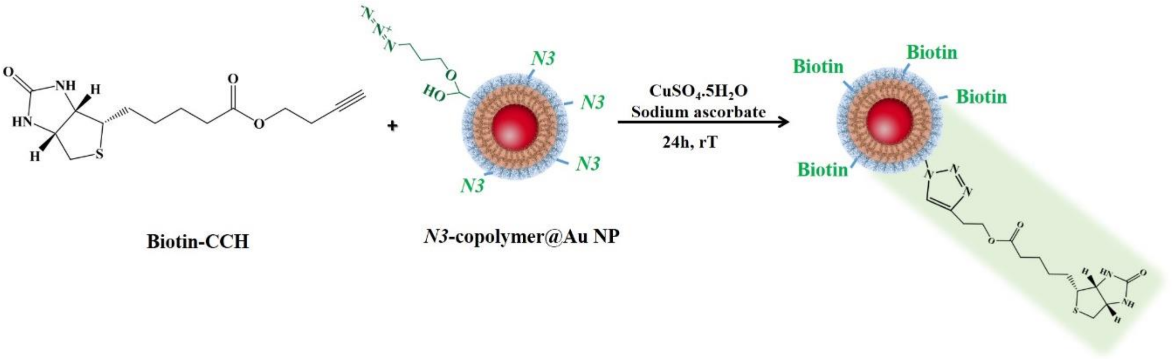

Figure 4.13. Schematic representation of biotinylation of *N3*-copolymer@Au NPs via *click chemistry* reaction.

Concerning the response of the biotinylated gold nanostructures towards avidin, the neat copolymer@Au nanostructures were used in order to evaluate the interaction of avidin with the Au nanostructures but without biotin. Hence, in a first experiment, a solution of avidin and BSA in phosphate buffer saline (PBS) were added to copolymer@Au NPs or *biotin*-copolymer@Au NPs. As a control of the dilution, PBS was also added to both types of Au nanostructures. After 10 minutes the colloids were characterized by UV-Vis spectroscopy. Figure 4.14 shows the UV-Vis spectra of the interaction between the Au nanostructures and the proteins, indeed non-specific interactions could also occurred, as shown in Figure 4.14-A where a small decrease of the absorbance and a small shift in the λ_{LSPR} ($\Delta\lambda$ = + 1 nm) were observed, especially in the presence of avidin. These non-specific interactions can be assigned to a variety of interactions (electrostatic, H bonding, van der Waals, etc.) between the nanostructures and the proteins [211, 212]. As regards specific interactions, one of the most frequently referred are electrostatic interactions. In fact, at this pH (around 7) BSA presents a negative surface charge (pI = 4.7) while avidin is positively charged (pI=10), hence the stronger response. Concerning the *biotin*-copolymer@Au NPs (Figure 4.14-B), a strong decrease of absorbance, a broadening and a shift of the LSPR band ($\Delta\lambda$ = + 7 nm) revealed aggregation of the nanostructures resulting from the strong interaction between avidin and the biotinylated nanostructure. These results make these Au nanostructures very promising to be used in biosensing.

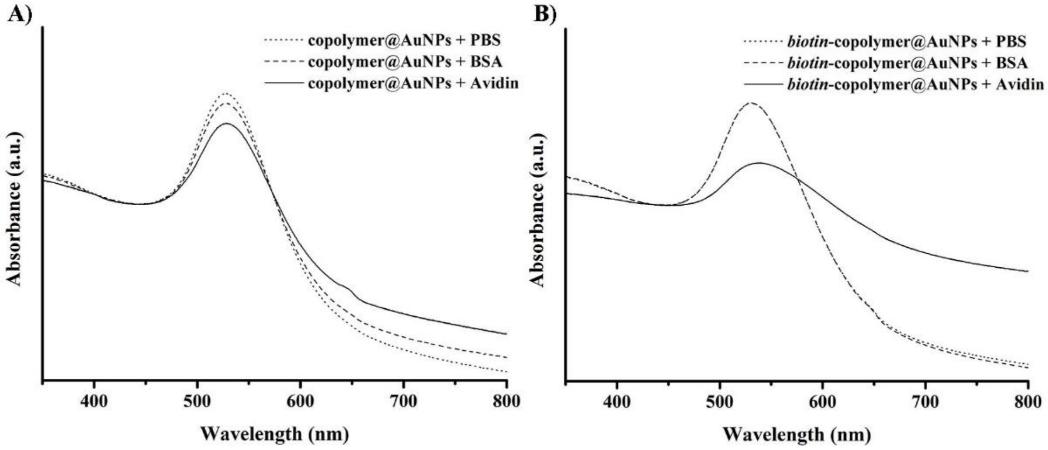

Figure 4.14. Visible spectra of copolymer@Au NPs and *biotin*-copolymer@Au NPs in the presence of Avidin and BSA. The spectra were normalized at 450nm.

In view of the limited evidence that the click reaction had actually taken place, a second experiment was carried out to assess the role of the covalently bound biotin towards the presence of avidin. For that purpose, the reagents of the "click" reaction (alkylated biotin, $CuSO_4$ and the sodium ascorbate) were added to copolymer@Au NPs (without azide function) and stirred overnight. In parallel, in order to allow a direct comparison the same procedure was followed using *N3*-copolymer@Au NPs. Additionally, BSA was mixed with the nanostructures during 30 min before adding avidin to evaluate the possibility of minimizing non-specific interactions, as already reported by others [23].

After 10 min in the presence of the proteins, the optical properties of the Au nanostructures were evaluated by visible spectroscopy (Figure 4.15). The UV-Vis spectroscopy showed that the presence of BSA did not shoed influence in the LSPR band. Even for a high amount of BSA (60 µL) used, the LSPR band just suffered a small decrease in the absorbance. Instead, avidin in the presence of both nanostructures caused a decrease, broadening and shift ($\Delta\lambda\sim$ +5nm) in the LSPR band, indicating that aggregation occurred. This result was not expected for the nanostructures without azide because the colloid had been rinsed to remove unreacted species (Figure 4.15-A). This indicates that alkylated biotin was not only covalently linked to the nanostructure by the specific *click chemistry* reaction with the azide but also it was adsorbed and/or trapped in the polymer shell contributing to the aggregation in the presence of avidin. When BSA was added to the nanostructures before adding the avidin (Figure 4.15 and Table 4.5), there was no broadening of the LSPR band, suggesting a different aggregation profile. In other words, BSA interacted with the Au nanostructures, via non-specific interactions without inducing aggregation, and stayed at the surface of the nanostructures. Hence when avidin was added, aggregation was induced due to specific interaction with biotin. However, due to the presence of BSA (dimensions: 4 x 4 x 14 nm [213]) at the surface of the nanostructures, the gold cores in the aggregates were more apart from each other so the λ_{LSPR} did not shift neither suffered a broadening, as was observed in the colloids without BSA, even so some aggregation occurred.

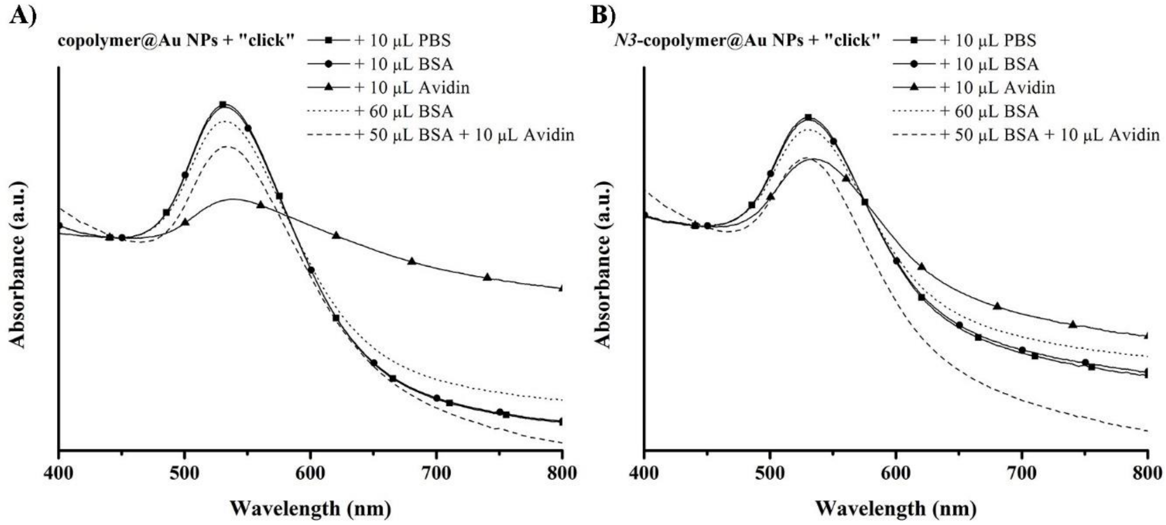

Figure 4.15. Visible spectra of copolymer@Au NPs and *N3*-copolymer@Au NPs after "*click*" reaction with alkylated biotin, $CuSO_4$ and sodium ascorbate, in the presence of BSA and/or Avidin. The spectra were normalized at 450nm.

Table 4.5. λ_{LSPR} values of copolymer@Au NPs and *N3*-copolymer@Au NPs after "*click*" reaction in the presence of BSA and/or avidin.

	λ_{LSPR} (nm)	
	copolymer@Au NPs + "click"	***N3*-copolymer@Au NPs + "click**
+ 10 µL PBS	532.0	530.5
+ 10 µL BSA	531.0	530.0
+ 10 µL Avidin	536.5	535.0
+ 60 µL BSA	531.0	530.0
+ 50 µL BSA + 10 µL Avidin	535.0	530.0

Concerning the fact that biotin could be adsorbed and/or trapped in the polymer shell, experiments were performed in order to remove the biotin that was not covalently linked to the nanostructure. In fact, the low solubility of biotin in water (0.2 mg/mL) can prevent non-linked biotin to be removed by centrifugation, thus remaining with the nanostructure that was precipitated and not in the supernatant. Note that for the *click chemistry* reaction, in order to increase the solubility of biotin in solution, alkylated biotin was dissolved in aqueous solution containing 10% of DMSO (solubility of biotin in DMSO is 50mg/mL). So, copolymer@Au NPs were mixed with alkylated biotin, $CuSO_4$

and sodium ascorbate and stirred overnight, then the mixture was centrifuged and the precipitate redispersed with ultra-pure water or an aqueous solution containing DMSO (1DMSO:10 H_2O v/v). The procedure was repeated twice and in the last centrifugation step all the colloids were redispersed with ultra-pure water (see the Scheme 6.1). Afterwards, BSA and avidin were added to these Au nanostructures and their optical response was followed by UV-Vis spectroscopy, as shown in Figure 4.16, in order to assess if biotin had been removed. However, in spite of all the washing steps performed, all the Au nanostructures aggregated in the presence of avidin indicating that biotin was not removed by centrifugation steps, even by increasing the solubility of biotin in the supernatant with an aqueous solution containing DMSO (1DMSO:10 H_2O v/v).

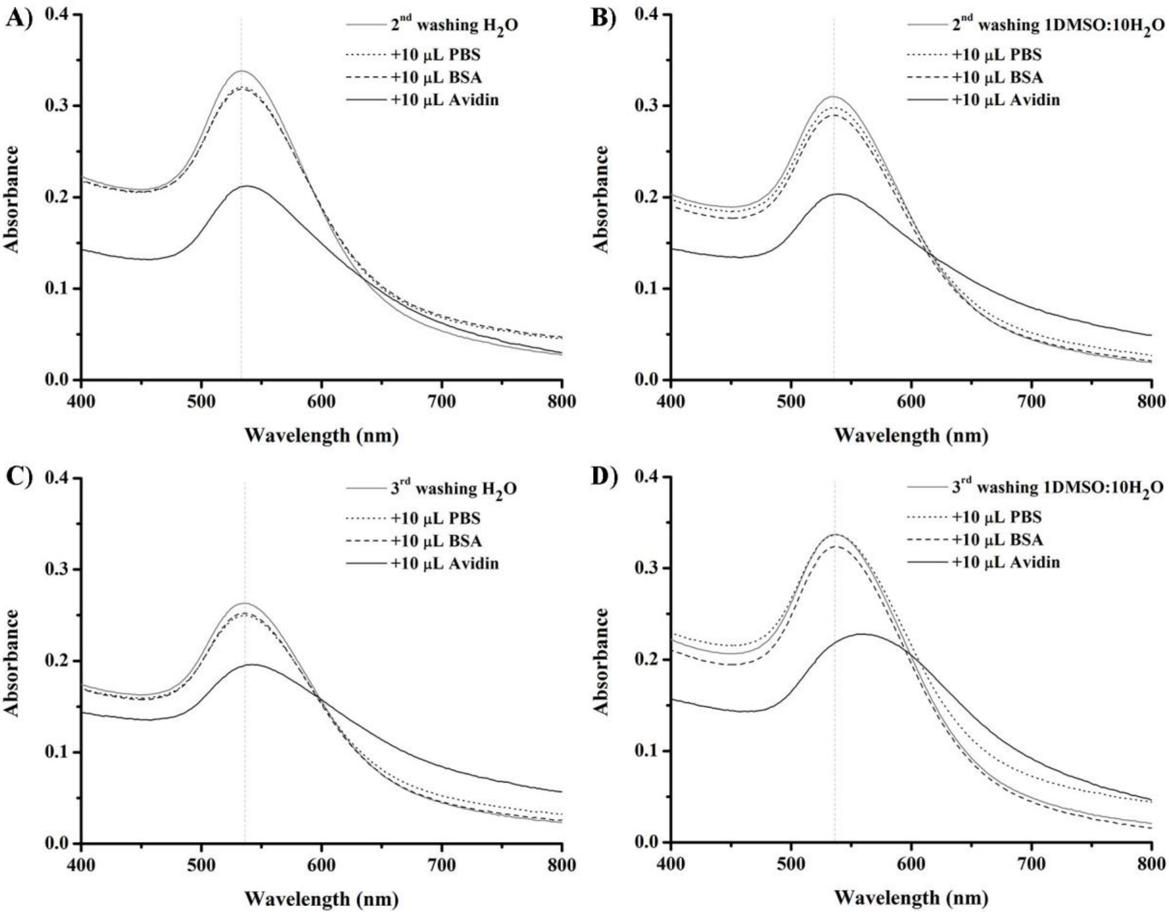

Figure 4.16. Visible spectra of copolymer@Au NPs submitted to the *click chemistry* reaction, and with several washing steps performed by centrifugation, in the presence of BSA or Avidin.

In order to understand if any reaction occurred between the alkyne group and the polymer shell, the same procedure was followed as described above, but using biotin (without the alkyne function). So, copolymer@Au NPs were mixed with biotin and stirred overnight, then washing steps were also performed by centrifugation and after that BSA and avidin were added to the colloids. The optical response of the Au nanostructures to the proteins was also followed by UV-Vis spectroscopy and similar results were found, i.e. all the nanostructures had aggregated in the presence of avidin. This result confirms that no reaction occurred between the alkyne and the polymer but most probably the biotin was adsorbed or trapped in the polymer shell.

As a final remark, the biofunctionalization of polymer@Au nanostructures via *click chemistry* is a very interesting strategy to be explored using a panoply of (bio)receptors. However, for the specific case of bioreceptor-biotarget (biotin-avidin) model followed here, the low solubility of biotin in water revealed some drawbacks. On the other hand, these results have shown that copolymer@Au NPs, i.e. without using *click chemistry* reaction, can be used to recognize biotin and have potential to be applied to other (bio)molecules with low solubility in water. Moreover, other applications for these copolymer@Au nanostructures could be explored, e.g. for drug carrier/delivery systems since PEG is also known to have thermoresponsiveness. Nevertheless, and as future work, strategies to minimize the adsorption of biotin in the polymer shell should be studied. For instance, by performing the *click chemistry* reaction at lower temperatures (4ºC) biotin adsorption in the polymer shell could be avoided. Alternatively the use of bioreceptors with higher solubility in water should be considered for the functionalization of *N3*-copolymer@Au nanostructures via click chemistry in order to ensure complete removal of unbound material.

4.5. Langmuir monolayers of copolymers at air/water interface

The copolymers prepared in this work have an amphiphilic character. Resulting from the presence of the repeating units of PEGA and the hydrophobic character given by the C12 chain of the RAFT agent together with the hydrophobic repeating units of MMA and BA (Figure 4.17). Therefore, Langmuir monolayers of these copolymers at the air/water interface could be prepared in order to get a better understanding of the interaction between the copolymer, biotin and avidin.

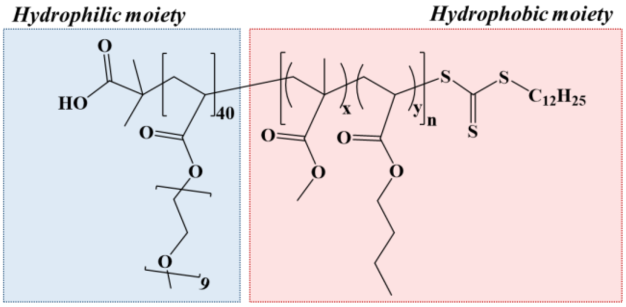

Figure 4.17. Chemical structure of the copolymer P(PEGA$_{40}$)-*b*-(MMA-*co*-BA)$_n$-TTC.

As discussed in ***sub-chapter 4.3.1.***, the RAFT emulsion polymerization conditions used to prepare copolymer P(PEGA$_{40}$)-*b*-(MMA-*co*-BA)$_n$-TTC at 44ºC using VA-044 initiator were studied. Here, the behavior at the air/water interface of the copolymers prepared at 70ºC using ACPA and VA-044, as well as of the copolymers obtained with higher monomer conversions prepared at 44ºC using VA-044 were studied (***4.5.1.***). Then the monolayer of the selected copolymer was used to assess copolymer-biotin-avidin interactions (***4.5.2.***).

4.5.1. Langmuir monolayers of copolymers prepared via RAFT emulsion polymerization using VA-044 as initiator

First, a comparison of the copolymers prepared at 70ºC was performed. A solution of these copolymers was prepared in ethanol:chloroform (1:10) and spread (50 µL) on the water surface. After 15 min of solvent evaporation the Langmuir monolayers were prepared by compressing the barriers at 15 cm^2/min. Figure 4.18 shows that both copolymers presented a similar profile at the air/water interface with three well-defined regions (*i*, *ii* and *iii* indicated in the figure). First, note that both presented a high surface pressure after spreading the copolymer solution (around 11 mN/m) at the water surface. This is because, using this amount of copolymer, there is already proximity and interactions between copolymer chains, which suggested that a liquid-expanded/gaseous phase is already present (region *i*) before the compression of the barriers starts. Then a second phase (region *ii*) was observed which correspond to a liquid-expanded phase, where hydrophilic and hydrophobic chains started to self-organize. Finally, a liquid-condensed phase (region *iii*) was observed which corresponds to an organized monolayer of the copolymer, however the way that these monolayers are organized at the air/water interface was not studied. The extrapolation of the linear portion (region *iii*) of the isotherm at zero surface pressure allowed to determine the mean molecular area at zero surface pressure (MMA$_0$) which was 1655 Å^2/molecule and 1688 Å^2/molecule for the copolymers prepared using ACPA and VA-044, respectively. This small difference can be attributed to differences in monomer conversion. In fact, when VA-044 was used the conversion was higher, therefore the hydrophobic chain has a higher DP: DP$_{\text{ACPA, 70ºC}}$= 140 and DP$_{\text{VA-044, 70ºC}}$= 168, see Table 4.1 in ***sub-chapter 4.3.1.***.

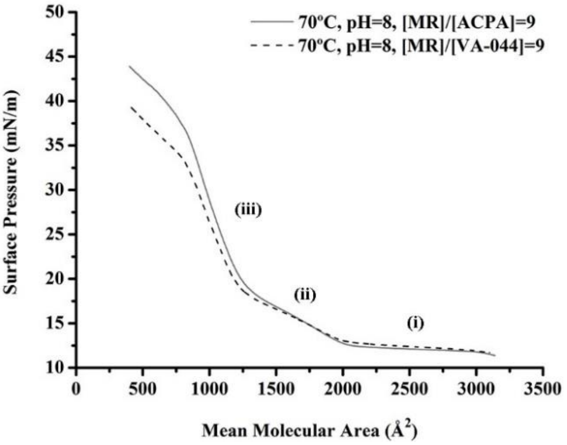

Figure 4.18. Langmuir surface pressure-area isotherms of the copolymers after RAFT emulsion copolymerization of MMA:BA (10:1 w/w) in the presence of P(PEGA$_{40}$)-TTC at 70ºC, using ACPA and VA-044.

A comparison between the copolymers prepared during 22h and 53h by using VA-044 at 44ºC, was performed (Figure 4.19). For comparative purposes the isotherm obtained with the copolymer prepared at 70ºC using VA-044 (50 µL) is also presented. Notice that in this case 200 µL of solution were necessary to obtain a monolayer whilst in the previous case 50 µL of copolymer solution sufficed. Unlike the isotherms of the copolymers prepared at 70ºC, the isotherms of the copolymers prepared at 44ºC did not present well-defined regions. For the copolymer prepared at 44ºC during 22h (*%Conversion* = 33% and DP = 56) during the compression of the barriers the surface pressure increased slightly suggesting that the copolymer started to have some organization but also migrated to the water subphase and the liquid-condensed phase was not formed. Probably the length of the hydrophobic chain in this copolymer is not long enough to stabilize the hydrophilic chain at the air/water interface. Consequently, the copolymer migrates to the water subphase driven by the hydrophilic chain and copolymer micelles are formed in the subphase [214, 215]. Regarding the copolymer obtained after 53h (*%Conversion* = 51% and DP = 86) the longer hydrophobic chain resulted in a higher stability at the air/water interface as demonstrated by the Langmuir surface pressure-area isotherm in Figure 4.19 where a liquid-condensed phase was observed. Even so, the isotherm profile of this copolymer is quite different from the one prepared at 70ºC, which can be assigned to the large difference in the DP of the hydrophobic chain ($DP_{44ºC,\ 53h}$ = 86 and $DP_{70ºC,\ 4h}$ = 168), different length of the hydrophobic chain and consequently different air/water interface organization.

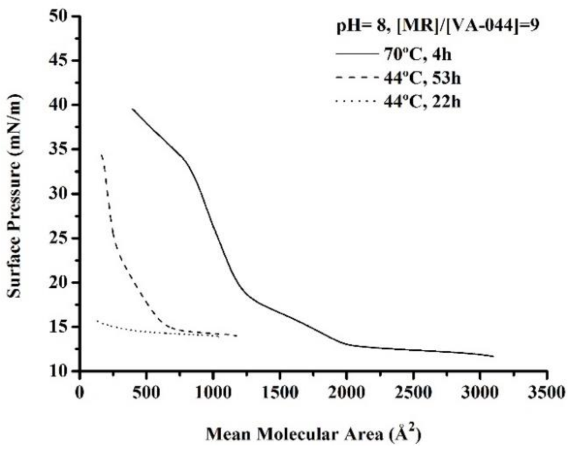

Figure 4.19. Langmuir surface pressure-area isotherms of the copolymers after RAFT emulsion copolymerization of MMA:BA (10:1 w/w) in the presence of P(PEGA$_{40}$)-TTC using VA-044 at 44ºC, during 22h and 53h, and at 70ºC during 4h.

Concerning the copolymer prepared using the macroRAFT agent P(AA$_2$-*b*-PEGA$_{40}$)-TTC, which was synthesized to be functionalized with the azide moiety, a comparison was made with the copolymer prepared using P(PEGA$_{40}$)-TTC, in the same conditions (70ºC using ACPA). These copolymers had a similar behavior at the air/water interface as shown in Figure 4.20. However, a lower MMA$_0$ value was obtained (1478 Å^2/molecule) for the copolymer derived from P(AA$_2$-*b*-PEGA$_{40}$)-TTC, even though the monomer conversion and DP of the hydrophobic chain is higher, in comparison with the copolymer derived from P(PEGA$_{40}$)-TTC (1655 Å^2/molecule). Therefore, these results highlight the fact that small differences in the composition of the macroRAFT agents hydrophilic chain, as well as in the chain length of the hydrophobic block affect their organization of the monolayer.

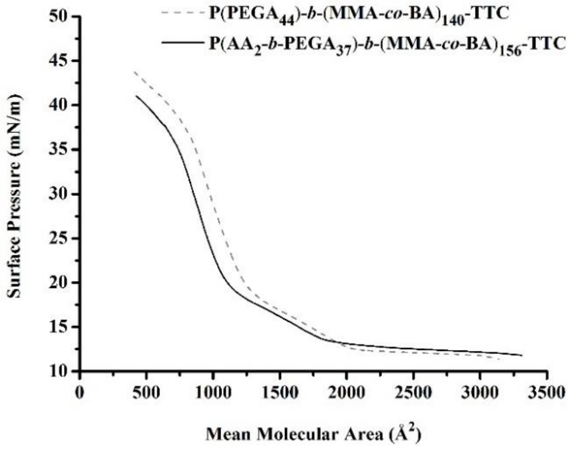

Figure 4.20. Comparison of Langmuir surface pressure-area isotherms of the copolymer derived from the MR agent P(AA$_2$-b-PEGA$_{40}$)-TTC and P(PEGA$_{40}$)-TTC prepared at 70ºC using ACPA.

As a final remark, the hydrophobic length of the copolymer has a high impact in the stability of the copolymer at the air/water surface. Hence, for the studies of the interaction of the copolymer with biotin and avidin, the copolymer chosen was that one showing the highest stability, i.e. a well-defined surface pressure-area isotherm, which is the copolymer prepared with P(PEGA$_{40}$)-TTC at 70ºC using VA-044. The stability of the monolayer was proven by five consecutive compression/expansion cycles as illustrated in Figure 4.21. Despite of the hysteresis upon 5 isocycles there was hardly any shift to smaller areas. The copolymer containing the acrylic acid units was not considered for this study as the objective was to assess the interactions between the PEGA block and biotin as discussed.

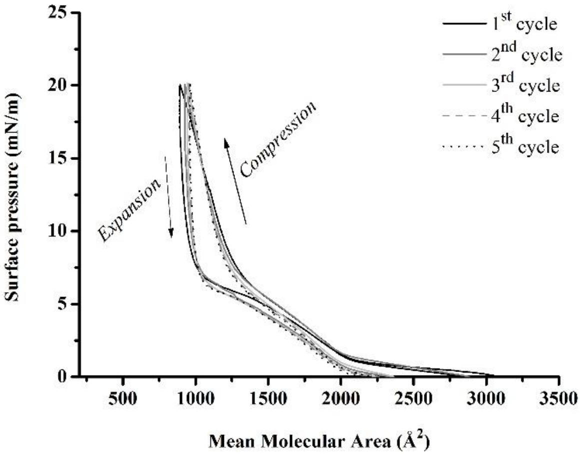

Figure 4.21. Compression/expansion cycles of the copolymer P(PEGA$_{40}$)-b-(MMA-co-BA)$_{168}$-TTC prepared using VA-044 at 70ºC during 4h.

4.5.2. Langmuir monolayers to study copolymer-biotin-avidin interactions

Having assessed the behavior of the copolymer at the air/water interface the next step was to evaluate the copolymer-biotin interactions, namely the biotin-copolymer interactions that were observed in the gold colloids. As discussed before in ***sub-chapter 4.4.***, biotin was adsorbed/trapped in the polymeric shell and was not remove even after several centrifugation steps. Here, biotin (without alkyne function) was mixed with the copolymer (without the azide moiety) before spreading it on the water surface in order to study its influence on the copolymer monolayer in air/water interface. Note that in the colloids, the monomer conversion and DP of the copolymerization of MMA:BA (10:1 w/w) from MR@Au NPs were not possible to determine. Therefore, the length of the hydrophobic chains in the nanostructure and the copolymer used for the preparation of the Langmuir monolayer could be different. The copolymer@Au NPs were prepared at 44ºC using the VA-044 during 24h and the copolymer used here was the one prepared at 70ºC using VA-044 during 4h.

A solution of copolymer (2.0 mg/mL) and a solution of copolymer (2mg/mL) containing 0.2 mM (1x10^{-6} mol) of biotin were prepared in ethanol:chloroform (1:10). 50 µL of copolymer solution or copolymer solution containing biotin were spread on the water surface and after 15 min of solvent evaporation the Langmuir monolayers were prepared by compressing the barriers at 15 cm^2/min. For the assay with avidin, instead of using ultra-pure water as subphase, a solution containing avidin (0.5 mg/L) was added to the Langmuir trough before spreading the copolymer solution containing biotin. The Langmuir surface pressure-area isotherm (Figure 4.22) of the copolymer mixed with biotin showed a similar isotherm profile in comparison with the copolymer (without biotin), however the liquid-condensed phase was formed at higher mean molecular areas, see Table 4.6. This result suggests that the biotin is at the air/water interface and not just interacting with the hydrophilic PEGA chains, thus occupying space between the copolymer chains which made the liquid-condensed phase to be formed at higher mean molecular areas. No significant changes have been observed using an avidin solution in the subphase in comparison with the same situation but using ultra-pure water in the subphase. This could indicate that biotin was not available to interact with avidin, i.e. avidin is not able to reach the biotin at the air/water interface. Therefore, avidin did not migrate to the air/water interface, interacting with biotin, neither biotin migrated to the subphase to interact with avidin.

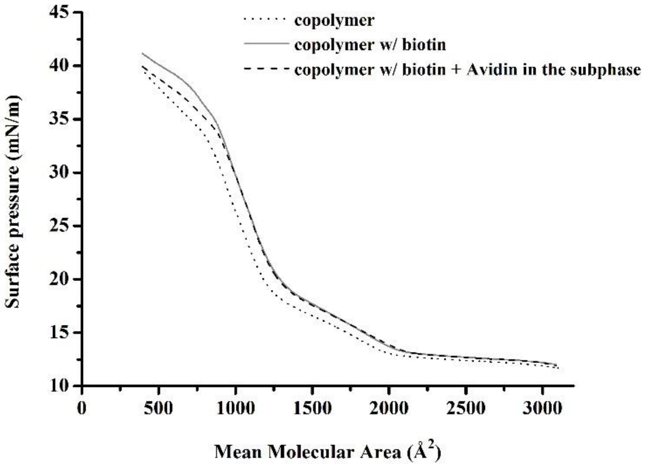

Figure 4.22. Langmuir surface pressure-area isotherms of the copolymer P(PEGA$_{40}$)-b-(MMA-co-BA)-TTC (VA-044 at 70ºC) mixed with biotin before spreading and using ultra-pure water as subphase or an avidin solution (0.5mg/L in ultra-pure water).

Table 4.6. Mean molecular area at surface pressure = 0 mN/m (MMA$_0$) for the copolymer P(PEGA$_{40}$)-b-(MMA-co-BA)-TTC (VA-044 at 70ºC) mixed with biotin before spreading and using ultra-pure water as subphase or an avidin solution.

Spreading solution	Copolymer	Copolymer with biotin	Copolymer with biotin
Subphase	Ultra-pure water	Ultra-pure water	Avidin (0.5 mg/L)
MMA$_0$ (Å^2)	1670	1752	1731

It was possible to perform further studies using a Langmuir trough with a different size equipped with a polarization modulation-infrared reflection-adsorption spectrometer (PM-IRRAS) which allows the identification of the functional groups involved in the interactions established at the interface, in a controlled environment (clean room). The adsorption of avidin was monitored as a function of time and the results are shown in Figure 4.23.

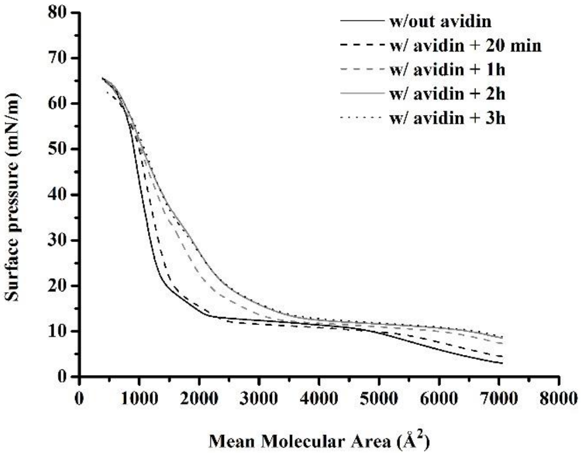

Figure 4.23. Langmuir surface pressure-area isotherm of P(PEGA$_{40}$)-b-(MMA-co-BA)-TTC (VA-044 at 70ºC, 4h) mixed with biotin, using avidin solution as subphase and varying the contact time before barriers compression starts.

Although only a small difference can be observed after 20 minutes of contact with the suphase, upon 1 hour the isotherms showed a distinct profile indicating that avidin is being adsorbed onto the monolayer causing its expansion, especially when the monolayer was compressed to values smaller than 3000 Å^2. Due to time constraints the identification of the type of interactions was not possible as the resolution of the IR obtained required further optimization studies.

4.6. Preparation of fluorescence gold nanocomposites via RAFT polymerization using the *grafting from* strategy

Au NPs can also be used as fluorescence quenchers and the quenching effect depends on the distance between the Au NP and the fluorophore. Hence, changes in that distance due to the presence of a specific biomolecule might allow its specific recognition by fluorescence spectroscopy, as revised in the introduction (see Figure 1.6 which illustrates the use of Au NPs as biosensor based on quenching fluorescence). With this principle in mind, a fluorescent copolymer@Au nanostructure was prepared in order to demonstrate that functional monomers can be used towards the preparation of multifunctional copolymer@Au nanostructures by using the *grafting from strategy*. Additionally, these nanostructures were assessed towards biosensing applications using the model biotin-avidin. The click chemistry reaction was not used in this study because as observed previously biotin became adsorbed/trapped in the polymer shell. Although, it is known that fluorescence quenching can occur when the excitation wavelength of the fluorophore overlaps with the absorbance band of RAFT agent [216], in this work the RAFT agent absorbs at λ_{max} ~ 310 nm and the fluorophore used (fluorescein isothiocyanate, FITC) has a λ_{exc} at 495 nm, which precludes such process.

Fluorescent copolymer@Au nanostructures were prepared following the *grafting from* strategy via adsorption of the MR agent P(PEGA$_{40}$)-TTC onto colloidal Au NPs. The fluorescent monomer was polymerized from MR@Au NPs before adding the mixture of hydrophobic monomers (1 MMA : 10 BA w/w) to the reaction vessel. The fluorescent monomer was prepared using the monomer 2-aminoethyl methacrylate hydrochloride (AEM) and the fluorophore fluorescein isothiocyanate (FITC), adapting the procedure described in [217]. A thiourea linkage was formed via the reaction between the amine group from the AEM and the isothiocyanate group from FITC, in the presence of triethylamine at room temperature, as shown in Figure 4.24. AEM-FITC was characterized by ^{1}H-NMR (Figure H.12, ***Annex H***) and also by UV-Vis and photoluminescence (PL) spectroscopy, as shown in Figure 4.25. The modified monomer (AEM-FITC) presented the absorbance and fluorescence band of the FITC moiety.

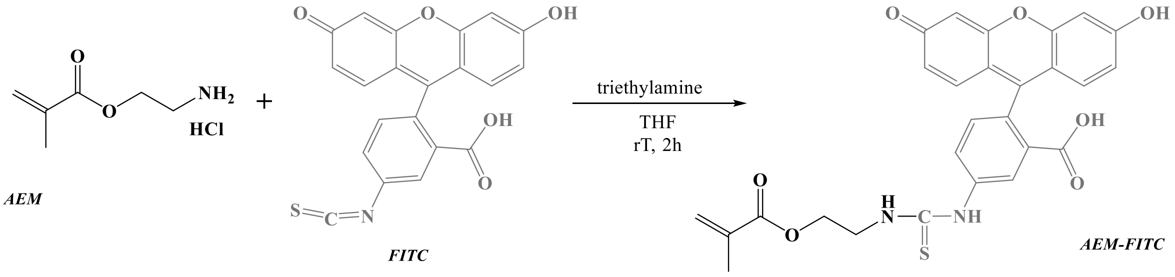

Figure 4.24. Preparation of fluorescent monomer (AEM-FITC).

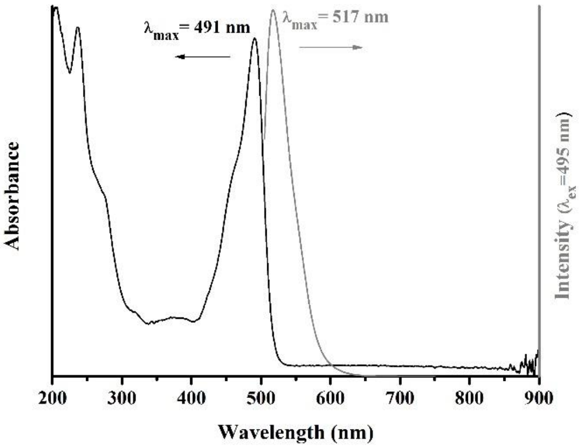

Figure 4.25. UV-Vis and PL spectra of AEM-FITC.

In a first attempt, an aqueous solution of AEM-FTIC was added to the MR@Au colloid (t_0) and the polymerization was carried out at 70ºC using the VA-044 as initiator, during 2h (t_1). As observed in **4.3.1**, this initiator was able to polymerize the hydrophobic monomers more rapidly at 70ºC (1h, ~80%) then ACPA (1h, ~30%). In addition Perrier *et al.* 2015 [218] have also reported a ultrafast and one batch RAFT polymerization of a multiblock copolymer using VA-044 at 100ºC during few minutes per monomer (3 min, DP per monomer = 10). Therefore, here the polymerization was performed at 70ºC, since the azide moiety was not present which allowed reducing the time of polymerization. Afterwards, the MMA:BA (10:1 w/w) mixture was added to the reaction vessel and polymerized for 4h (t_2), then more MMA:BA mixture was added and the polymerization continued for further 2h (t_3). Aliquots were withdrawn during the polymerization at the times mentioned above. Once the polymerization was stopped, the aliquots and the final colloid were centrifuged and redispersed twice in ultra-pure water. The ensuing colloids were characterized by DLS and zeta potential measurements, UV-Vis and PL spectroscopy and electron microscopy.

As expected the DLS measurements (Table 4.7), showed an increase of the hydrodynamic average diameter (d_{average}) of the nanostructures during the copolymerization corresponding to the growth of the hydrophobic chain. However, a small decrease of d_{average} was observed from t_0 to t_1 which can be associated with some MR agent reorganization due to the incorporation of the AEM-FITC and/or miscibility of the functionalized repeating units in the MR agent. As regards the zeta potential measurements, all the nanostructures presented a negative surface charge and this value increased slightly, in module, for longer reaction times suggesting some increase in colloidal stability.

Table 4.7. DLS and zeta potential measurements of the aliquots withdrawn during the preparation of the fluorescent copolymer@Au NPs.

aliquot	d_{SEM} Au NPs (nm)*	$d_{average}$ (nm)	PdI	ζ (mV)	pH
Au NPs	16.2 ± 4.4	17.3	0.597	-39.6 ± 19.9	5.7
MR@Au NPs	16.8 ± 3.3	26.5	0.573	-25.9 ± 13.4	6.6
t_0	16.1 ± 3.4	26.9	0.546	-29.1 ± 16.0	6.3
t_1	16.2 ± 3.5	24.9	0.554	-29.5 ± 13.1	6.0
t_2	16.9 ± 3.6	39.9	0.476	-32.3 ± 13.3	5.7
t_3	16.3 ± 3.2	42.3	0.447	-35.5 ± 13.8	5.6

* The diameter of Au core nanostructures was measured in the SEM images using the software ImageJ.

The visible spectra in Figure 4.26-A show that all the colloids presented the LSPR characteristic band of the Au NPs. Yet, its intensity, shape and absorption maximum changed for samples collected during the polymerization. For the aliquot taken at t_0 a small λ_{LSPR} shift ($\Delta\lambda$=2 nm) was registered which can be assigned to changes in the surrounding environment, specifically the reaction mixture, i.e. the presence of the initiator solution and the AEM-FITC solution. During the polymerization the λ_{LSPR} shifted to higher wavelengths due to the growth of the new chain and a broadening of the LSPR band at t_2 and t_3 was observed.

As regards the PL measurements (Figure 4.26-B), all the aliquots withdrawn presented the fluorescence peak characteristic of the FITC. However, the direct comparison of the fluorescence intensity of aliquots proved to be very difficult because FITC is a pH sensitive fluorophore and the pH was not constant during the course of the polymerization (Table 4.7). Indeed, the pH-sensitivity of fluorescein and fluorescein derivatives (e.g. FITC) is well documented [219]. The fluorescence intensity increases with increasing pH values due to the different ionized species that fluorescein can originate at all pH range. Figure H.13 (Annex H) illustrates the pH-dependent fluorescein structures and corresponding UV-Vis and PL spectra. Moreover, notice should be made that the aliquot taken at t_0 (mixture of MR@Au NPs with AEM-FITC before starting the copolymerization), exhibits the fluorescence of FITC which indicates that the fluorescent monomer stayed adsorbed on the polymer shell despite of the two centrifugation-redispersion cycles using water. Therefore, the fluorescence intensity of each aliquot can be the contribution not only of the copolymerized AEM-FITC but also of the AEM-FITC that stayed adsorbed. Yet, considering that pH values of the aliquots taken at t_2 and t_3 are almost the same, it is interesting to observe that the PL intensity increased as a result of the chain growth and subsequent increase of the distance between the Au core and the fluorophore.

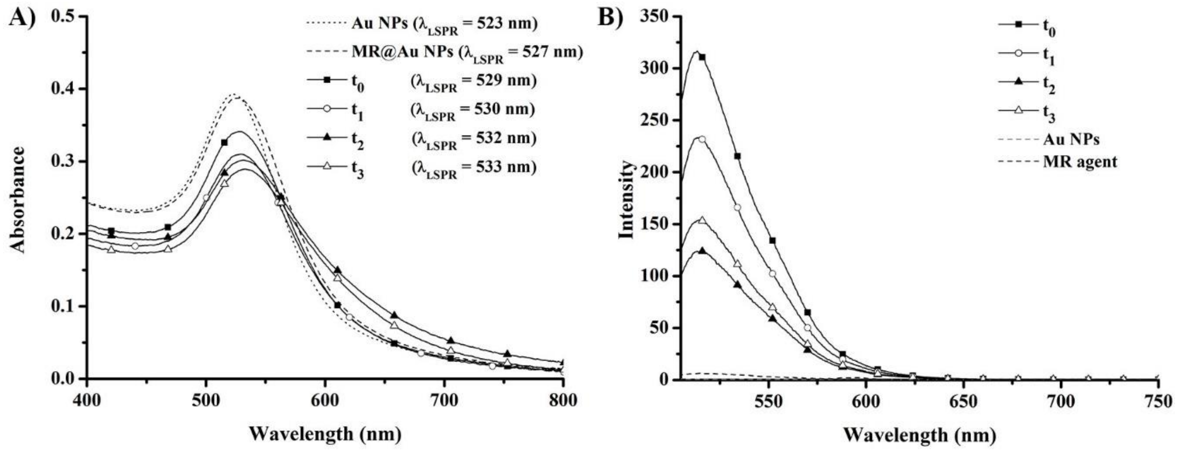

Figure 4.26. Visible and PL spectra (λ_{ex}=495 nm) of the aliquots withdrawn during the copolymerization of AEM-FITC after 2h (t_1) and of MMA:BA (10:1 w/w) (after 4h - t_2 and further 2h - t_3) from MR@Au NPs. t_0 corresponds to the mixture of MR@Au NPs with FITC-AEM before placing the reaction vessel at 70ºC.

Nevertheless, taking into account the pH sensitivity of FITC tagged nanostructures all the aliquots were diluted 1:1 (v/v) with PBS (1M, pH= 7.4) and the spectra collected are shown in Figure 4.27.

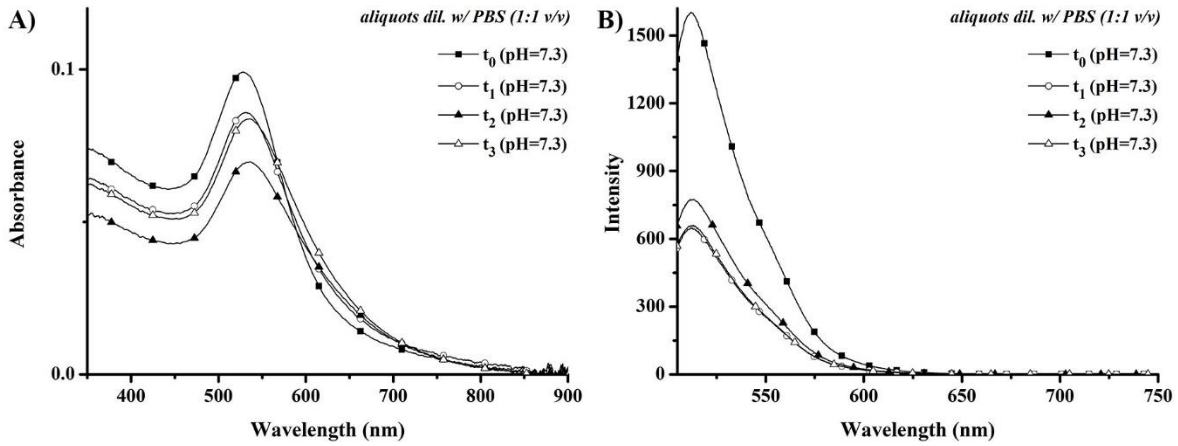

Figure 4.27. Visible and PL spectra (λ_{ex}=495 nm) of the aliquots withdrawn during the copolymerization of AEM-FITC and MMA:BA (10:1 w/w) (t_0, t_1, t_2 and t_3) diluted 1:1 (v/v) with PBS (1M, pH=7.4).

The PL spectra of the aliquots shown in Figure 4.27-B clearly highlight the pH sensitivity of FITC. Despite dilution in the buffer, the fluorescence intensity of the colloids diluted in PBS is stronger than that observed the as prepared colloids (Figure 4.26-B). For instance, the fluorescence intensity for the aliquot taken at t_0 increased from ~325 (at pH 6.3) to ~1500 (at pH 7.3). Regarding the variation of PL intensity during the copolymerization of AEM-FITC, the fluorescence intensity decreased for the sample taken at t_1, which can be assigned to AEM-FITC copolymerized. In this case, the fluorophore is closer to the Au core and consequently quenching of the fluorescence is observed. As for the other aliquots, an increase of fluorescence intensity was observed from t_1 to t_2, as expected, due to the increase of the polymer shell. Unexpectedly a decrease in the fluorescence intensity, from t_2 to t_3, was observed thought more hydrophobic monomers were added to increase the polymer shell. In fact, as discussed above, an intensity increase was observed for the colloids that were not diluted in the buffer, (Figure 4.26-B). Even though the use of a buffer can be very useful to overcome the pH sensitivity of FITC, the stability of colloids is also sensitive to the ionic strength. Interestingly, both UV-Visible and PL spectra show distinct intensities for the aliquot taken at t_2 whilst the spectra of aliquots taken at t_1 and t_3 are very similar. Besides the difficulties associated with the pH sensitivity of FITC, and the ionic strength sensitivity of colloidal nanostructures, there is still the possibility that the fluorescent monomer (AEM-FITC) may not be fully incorporated in the growing chain during the first couple of hours. In this case, it is reasonable to admit that unreacted fluorescent monomer had been incorporated later in the growing chain thus altering the expected variation of PL intensity. Additionally, it is also possible that some free polymer particles containing the fluorescent monomer may also be present and affect the results obtained. In view of all these variables, these PL results should be critically interpreted though indicate the potential usefulness of this strategy.

In SEM in transmission mode images (Figure 4.28) a slight grey background around the Au NPs indicates the presence of the polymeric shell in all the aliquots, yet the thickness of this polymeric shell is not possible to measure. Regarding the aliquot taken at t_3, further electron microscopy characterization was performed using a dedicated STEM instrument (Figure 4.29). This instrument allows the observation of the sample with a higher resolution (200 kV) and also the visualization in Z contrast (ZC) mode in which the contrast in the image is related with the atomic number. In Figure 4.29-A is observed that isolated Au NPs as well as small aggregates are present in the sample. Figure 4.29-B shows the sample in different imaging modes, in transmission (TE) a very thin layer around the NPs can be detected. However, in Z contrast (ZC) and secondary electrons (SE) imaging the polymer shell does not seem to be so thin. Although electron microscopy characterization was performed with a higher resolution, it is still difficult to observe a well-defined shell and to measure its thickness, because the polymer burned under the electron beam. Therefore, cryo-SEM/cryo-TEM imaging is suggested for future characterization. Nevertheless, it is important to remark that all the nanostructures contain Au cores.

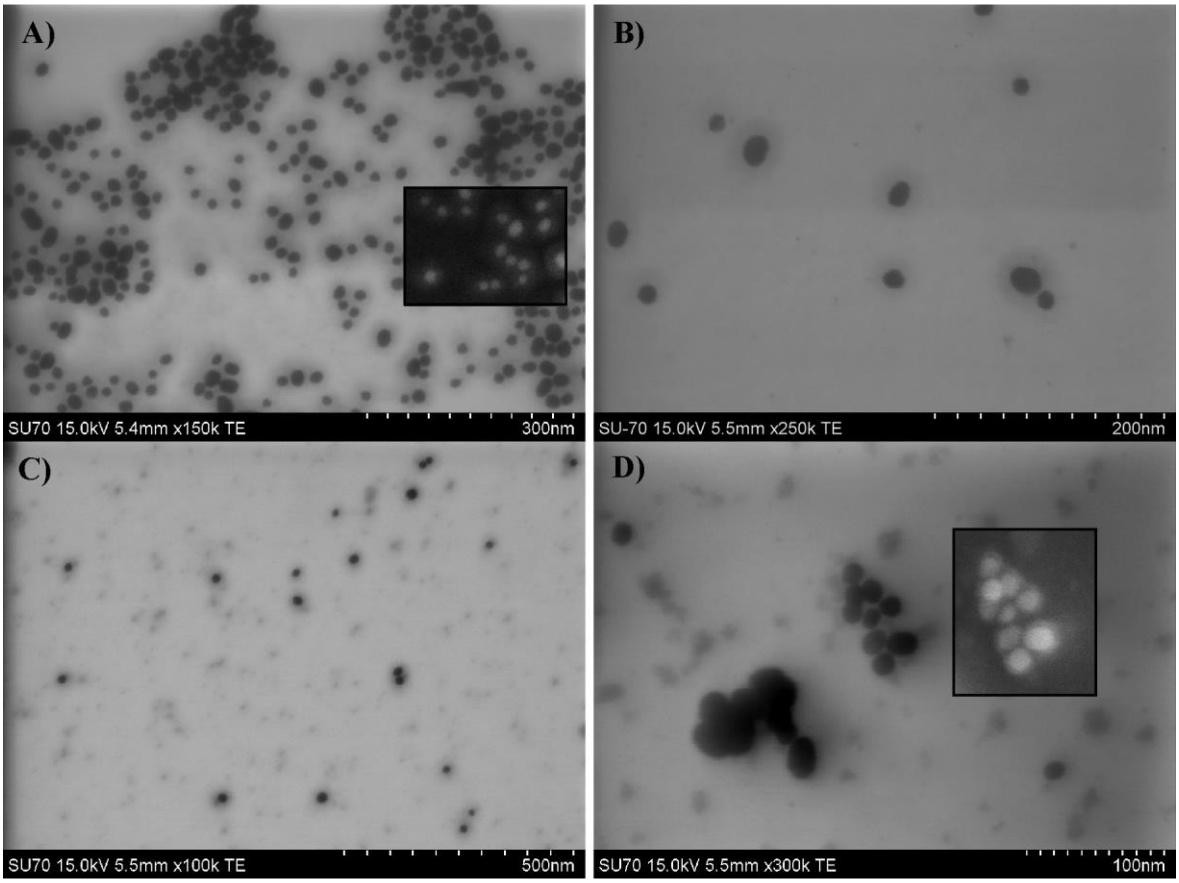
A)
SU70 15.0kV 5.4mm x150k TE
300nm
B)
SU-70 15.0kV 5.5mm x250k TE
200nm
C)
SU70 15.0kV 5.5mm x100k TE
500nm
D)
SU70 15.0kV 5.5mm x300k TE
100nm

Figure 4.28. SEM images, in transmission mode, of the aliquots withdrawn during the preparation of the fluorescent copolymer@Au NPs. A) t_0, B) t_1, C) t_2 and D) t_3. (*insets*) corresponding SEM images.

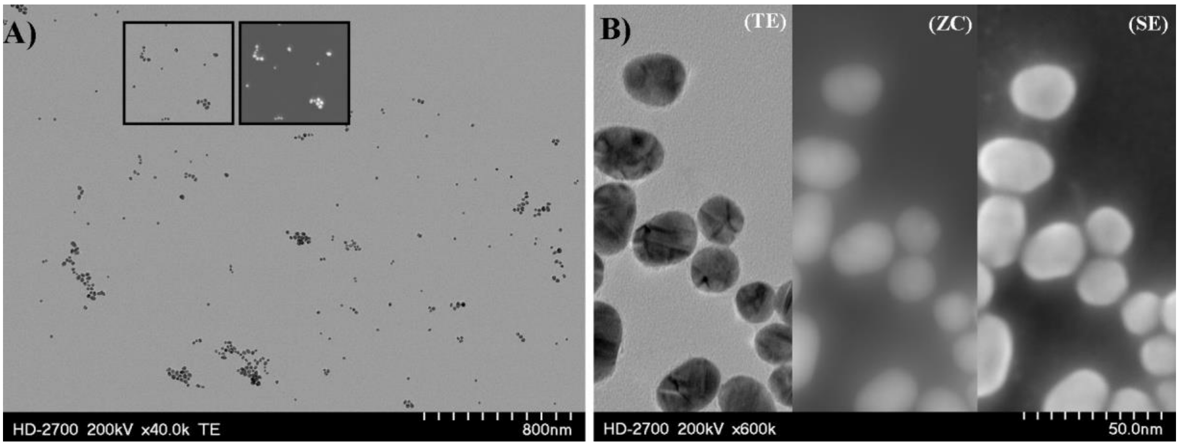
A)
HD-2700 200kV x40.0k TE
800nm
B)
(TE)
(ZC)
(SE)
HD-2700 200kV x600k
50.0nm

Figure 4.29. STEM images of aliquot t_3 of fluorescent copolymer@Au NPs (A) in transmission mode and *insets* in transmission and secondary electrons imaging; and (B) an amplification in transmission, Z contrast and secondary electrons imaging.

Pursing the objective of preparing multifunctional Au NPs, the possibility of preparing nanostructures containing the fluorescent monomer as well as an azide moiety for subsequent covalent grafting of biotin was evaluated. For that purpose AEM-FITC was copolymerized from MR@Au NPs at 70ºC using VA-044. The temperature was then reduced to 44ºC and the mixture of hydrophobic monomers (1 MMA : 10 BA w/w) was added to the reaction vessel in a controlled way. After 24h the emulsion copolymerization was quenched and the colloid was washed by applying two centrifugation-redispersion cycles using the same volume of ultra-pure water to yield the 1stCE-copolymer@Au NPs (CE – chain extension). Additionally, taking advantage of the living nature of the RAFT mechanism, the nanostructures were submitted to a second chain extension in order to increase the thickness of the polymeric shell. This second chain extension was carried out from the washed 1stCE-copolymer@Au NPs at 44ºC, using VA-044 and the MMA:BA mixture was added in a controlled way. The reaction was stopped after 24h and the colloid washed twice by centrifugation-resdispersion, affording the 2ndCE-copolymer@Au NPs. In view of the effect that consecutive centrifugation-redispersion cycles can have on the composition, pH and ionic strength of colloids, for a better comparison the 1stCE-copolymer@Au NPs were further submitted to two more cycles of centrifugation-redispersion and were named 1stCE-copolymer@Au NPs(2w). The nanostructures were characterized by DLS and zeta potential measurements UV-Vis and PL spectroscopy, and electron microscopy.

Despite of the high PdI values, the DLS measurements provide hydrodynamic average diameter (d_{average}) that gives a good approximation about the average size of the nanostructures. However for the results set that is presented below DLS results should be discussed by taking into consideration the hydrodynamic diameter in intensity and number distribution ($d_{\text{intensity}}$ and d_{number}). Hence, here the DLS measurements (Table 4.8) are presented and discussed with the d_{average}, $d_{\text{intensity}}$ and d_{number} values. The colloid of Au NPs as prepared presents an average diameter of 11.9 ± 0.9 nm, measured in STEM images using the software *ImageJ*, and a d_{average} of 15.9 nm ($d_{\text{intensity}}$ 16.6 nm and d_{number} = 12.7 nm). However, colloidal Au NPs in the concentration used in these procedures present a d_{average} of 21.5 nm which is a higher value as well as a higher PdI value (PdI = 0.581). In addition, in number distribution a value of 1.3 nm (Table 4.8) was found but, this type of result was already reported as a false minor peak [220]. In spite of that, the d_{average} is a good approximation to compare the colloids average diameter. After the MR agent adsorption (MR@Au NPs) and copolymerization (first chain extension, 1stCE-copolymer@Au NPs) the d_{average} increased due to the increase of the polymeric shell, as already discussed in the preparation of similar copolymer@Au nanostructures in other batches. Moreover, a peak in intensity distribution that could correspond to the nanostructure diameter is measured, indeed this value increased from 34.7 nm to 39.1 nm after the first chain extension from MR@Au NPs, as the d_{average} had increased. However, the DLS measurements of the same nanostructure but with different number of washing steps (1stCE-copolymer@Au NPs and 1stCE-copolymer@Au NPs(2w)) showed different d_{average} values. The d_{average} of 1stCE-copolymer@Au NPs(2w) (46.2 nm) is much higher than the d_{average} of 1stCE-copolymer@Au NPs (29.0 nm), suggesting that some aggregation occurred after the washing steps. Even so the colloid with 2 extra washing steps, presented $d_{\mathrm{intensity}}$ of 31.1 nm and d_{number} of 21.1 nm. After the second chain extension 2ndCE-copolymer@Au NPs, both $d_{\mathrm{intensity}}$ and d_{number} increased from 31.1 nm to 43.7 nm and from 21.1 nm to 31.3 nm, respectively, even though the d_{average} is much higher (81.3 nm), but as discussed before aggregation was observed. As a general summary, DLS measurements indicate that the copolymerization from the MR@Au NPs increased the hydrodynamic diameter as a result of the hydrophobic chain extension, thus increasing the polymeric shell, yet the colloidal stability may have been compromised even though the charge density after the second chain extension is reasonably high. In fact, the zeta potential measurements (Table 4.8) showed that all the colloids present a negative surface charge in particularly after the second chain extension, the colloid presented a ζ = -35.4 mV. Furthermore, the disparity of the values obtained seems to suggest the presence of aggregates as well as the possibility of free polymer particles.

Table 4.8. DLS measurements of Au NPs after MR agent adsorption and emulsion copolymerization from MR@Au NPs.

	d_{average} (nm)	$d_{\mathrm{intensity}}$ (nm)	d_{number} (nm)	PdI	ζ (mV)	pH
Au NPs	**21.5**	51.6 (89.9%) 1.7(3.4%) 1.2 (6.7%)	1.3 (100%)	0.581	-41.6 ± 17.7	5.6
MR@AuNPs	**23.6**	**34.7** (86.3%) 2.5 (11.3%)	1.9 (100%)	0.475	-17.6 ± 11.4	6.5
1st-CE copolymer@AuNPs	**29.0**	**39.1** (93.9%) 2.2 (6.1%)	2.1 (100%)	0.344	-18.6 ± 12.9	6.3
1st-CE copolymer@AuNPs (2w)	46.2	90.3 (62.3%) **31.1** (35.8%)	**21.1** (67.3%) 10.1 (32.7%)	0.417	-29.7 ± 9.2	6.0
2nd-CE copolymer@AuNPs	81.3	129.4 (69.0%) **43.7** (30.6%) 14.0 (0.4%)	**31.3** (69.3%) 13.0 (30.7%)	0.380	-35.4 ± 10.1	6.2

For the electron microscopy characterization, a dedicated STEM instrument was used. In the STEM images in ZC mode (Figure 4.30), a slight grey background around the Au NPs suggests the presence of the polymer shell. However, the observation of these images does not allow concluding about the increase of the thickness after the second chain extension. The images obtained for 2ndCE-copolymer@Au NPs in secondary electron and Z contrast imaging mode are shown in Figure I.14

(***Annex I***). These results seem to suggest that the conversion of the hydrophobic monomers at 44ºC may be lower than expected despite of the 24h reaction time. Furthermore, the presence of free polymer particles does not seem to be evidenced.

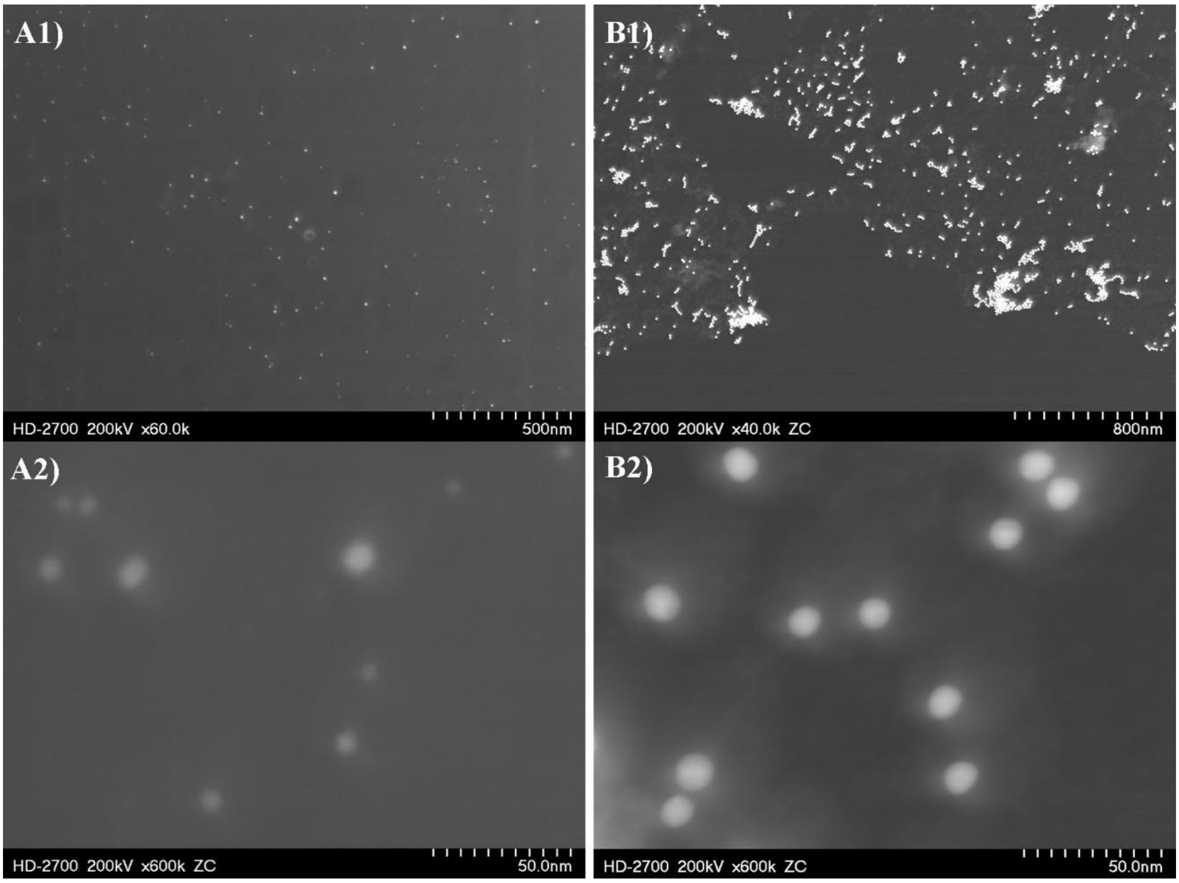
A1)
HD-2700 200kV x60.0k
500nm
B1)
HD-2700 200kV x40.0k ZC
800nm
A2)
HD-2700 200kV x600k ZC
50.0nm
B2)
HD-2700 200kV x600k ZC
50.0nm

Figure 4.30. SEM images in Z contrast mode of (A) 1stCE-copolymer@Au NPs and (B) 2ndCE-copolymer@Au NPs, at different magnifications.

The nanostructures prepared were then analyzed by visible and fluorescence spectroscopies. Figure 4.31-A shows that the visible spectra of the MR@Au NPs and the 1stCE-copolymer@Au NPs present the characteristic LSPR band of the Au NPs and, as expected, a red-shift in the λ_{LSPR} was detected due to the MR agent coating and subsequent chain extension from the MR@Au NPs. Moreover, the 1stCE-copolymer@Au NPs presented the fluorescence band of FITC, indicating that the nanostructure contained the AEM-FITC (Figure 4.31-B).

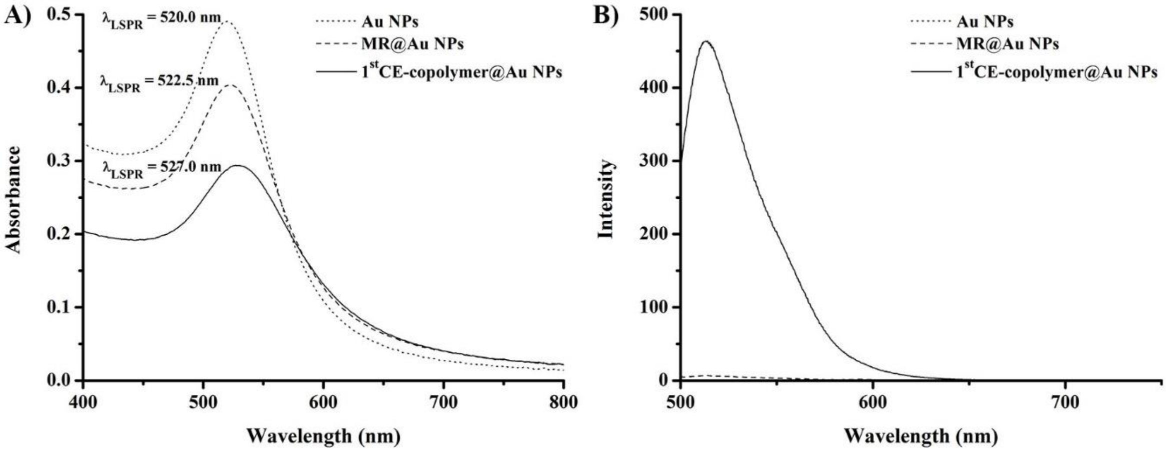

Figure 4.31. Visible spectra and PL spectra (λ_{ex}=495 nm) of Au NPs, MR@Au NPs and copolymer@Au NPs with one chain extension step (1stCE-copolymer@Au NPs).

As regards the second chain extension, the colloidal sample 2ndCE-copolymer@Au NPs was centrifuged and the resulting precipitate did not redisperse totally, forming also agglomerates. Therefore, the redispersible precipitate was placed in half of the volume of water. This could be an indication of loss of stability, which cannot be solely attributed to the centrifugation step since the 1stCE-copolymer@Au NPs was submitted to the same procedure (1stCE-copolymer@Au NPs(2w)) and irreversible agglomeration did not occur. In fact, the visible spectra (Figure 4.32-A) revealed that after the second chain extension the λ_{LSPR} shifted to higher wavelengths which could be the result of the polymer shell growth and eventually some aggregation resulting from loss of stability. Moreover, as shown in Figure 4.32-B the fluorescence intensity, after the second extension (2ndCE-copolymer@Au NPs), almost disappeared, and that of 1stCE-copolymer@Au NPs(2w) also decreased abruptly, indicating that probably the nanostructure still had unreacted AEM-FITC adsorbed in the polymer shell that was not removed by centrifugation after the first chain extension.

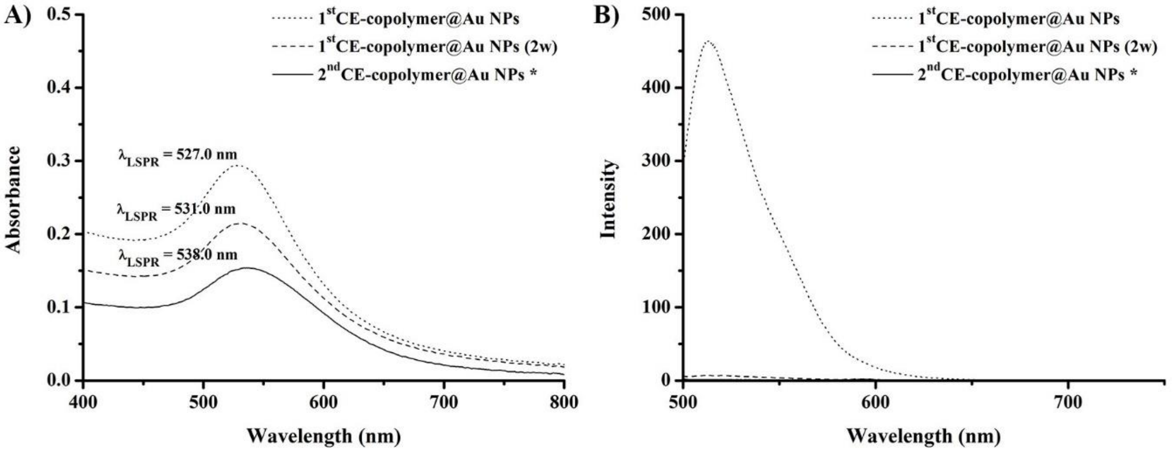

Figure 4.32. Visible spectra and PL spectra (λ_{ex}=495 nm) of copolymer@Au NPs with one and two chain extension steps. (* after the second chain extension the precipitate colloid was redispersed in half of the volume).

Because the washing procedures can affect the pH and consequently reduce the PL intensity, the colloids were diluted 1:1 with PBS (1M, pH=7.4) and the PL was measured (Figure 4.33). Conversely to the nanostructures prepared at 70 ºC, for the 1stCE-copolymer@Au NPs, the fluorescence intensity decreased despite the fact that, as discussed above, this colloid may still have unreacted AEM-FITC adsorbed in the polymer shell which can contribute to the fluorescence intensity hence, this result can not be explained. Regarding the other colloids, 1stCE-copolymer@Au NPs(2w) and 2ndCE-copolymer@Au NPs, after the dilution with PBS and consequent increase of pH, the fluorescence intensity increased slightly. Still the fluorescence intensity is extremely low which seems to indicate that the amount of fluorescent monomer incorporated in the chain is rather low and/or that hydrophobic chain did not actually grow which is in line with the results obtained from electron microscopy.

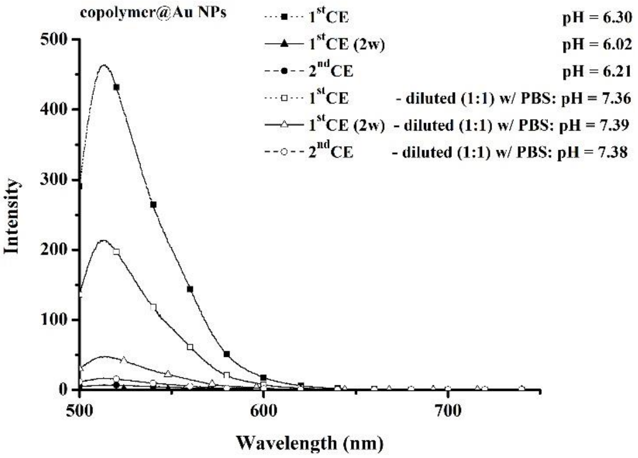

Figure 4.33. PL spectra (λ_{ex}=495 nm) of copolymer@Au NPs with one and two chain extension steps diluted (1:1 v/v) with PBS (1M, pH 7.4).

The results presented here regarding the preparation of the fluorescent copolymer@Au NPs showed several difficulties in the discussion and comparison of the colloids, namely in what regards the fluorescence spectroscopic data. Aspects such as the pH, the ionic strength, the amount of AEM-FITC adsorbed and/or copolymerized and also the distance between the fluorophore and the Au core play an important role. Therefore, it is recommended that in future, a fluorescent copolymer@Au NPs should be prepared following the same strategy – *grafting from* strategy, but by adsorption of a fluorescent macroRAFT agent, for instance P((PEGA$_{40}$)-*b*-(AEM-FITC$_{1\text{-}5}$))-TTC, before carrying out the copolymerization of the mixture of the hydrophobic monomers from this P((PEGA$_{40}$)-*b*-(AEM-FITC$_{1\text{-}5}$))-TTC@Au nanostructures. This would allow adequate removal of unreacted FITC functionalized monomer as well as minimization of the amount of free polymer containing FITC moieties which can significantly affect PL intensity. Moreover, the adsorption and copolymerization should be performed in a controlled pH medium using for example a buffer solution, such as PBS. In this case, the comparison of the fluorescence intensity of the several colloids should be easier because all are at the same pH and the majority of the FITC molecules present in the nanostructures should be covalently bonded, i.e. belonging to the macroRAFT agent and not adsorbed in the polymeric shell. In addition, in order to control the thickness of the polymer shell, the kinetics of this polymerization needs to be studied using blank copolymers (i.e. not adsorbed on to Au NPs).

Despite of all the difficulties encountered in the preparation and characterization of the fluorescence nanostructures, some preliminary biosensing assays, using the biotin-avidin model, were performed using the 1stCE-copolymer@Au NPs. The nanostructures were mixed with biotin and stirred overnight, then the mixture was washed twice by centrifugation and the precipitate redispersed in the same volume with ultra-pure water. 14.25 µL, 28.50 µL and 57.00 µL of avidin and BSA were added to 500 µL of *biotin*-copolymer@Au NPs. The same volume of PBS (10 mM) was also added to the Au nanostructures, as a “dilution” control. The optical response of the nanostructures to avidin was followed by visible and fluorescence spectroscopy (Figure 4.34).

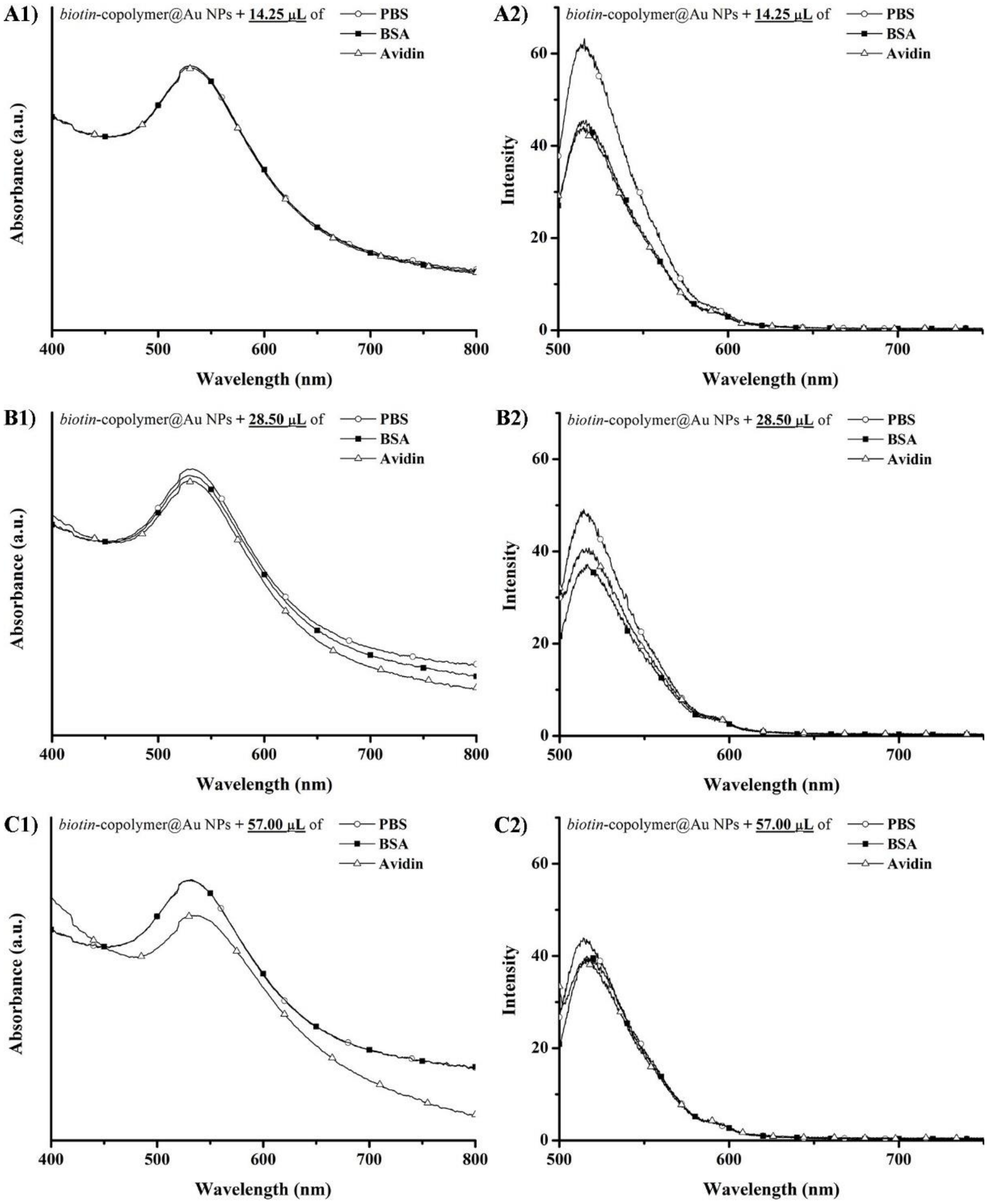

Figure 4.34. Visible and PL spectra (λ_{ex}=495 nm) of *biotin*-copolymer@Au NPs in the presence of avidin and BSA. The visible spectra were normalized at 450nm.

Visible spectroscopy (Figure 4.34-A1, B1 and C1) showed that aggregation of the nanostructures was induced in the presence of avidin, especially when a high amount of avidin was added. This type of optical response was already discusses in ***sub-chapter 4.4*** (nanostructures without fluorescence). Regarding the fluorescence spectroscopy (Figure 4.34-A2, B2 and C2), the fluorescence intensity decreased in the presence of both proteins (BSA and avidin), thus not inline with the visible spectroscopy results. Fluorescence spectroscopy is very sensitive to non-specific interactions resulting in the reduction of the fluorescence intensity observed. Moreover, the PL intensity registered for the control samples when compared to the values obtained in Figure 4.33 indicates that the centrifugation-redispersion steps carried out to remove excess biotin, have contributed to further remove unreacted fluorescent monomer. In addition, the fact that biotin was not covalently bonded to the nanostructures may also have affected the results obtained as the presence of avidin in the medium may act as a driving force for its migration to the aqueous medium without causing any aggregation of the colloids and thus not affecting significantly the PL intensity. In summary, the PL results were not conclusive but have helped to identify a number of issues that need to be taken into consideration for the preparation of fluorescent tagged nanostructures. Moreover, the importance of bonding the bioreceptor onto nanostructures was evidenced. Indeed, the fact that biotin could not be removed from the nanostructures due to its low solubility in water discussed in sub-chapter 4.4, does not mean that it is completely insoluble, and in the presence of avidin, it may be thermodynamically favorable for this bioreceptor to migrate to the aqueous medium altering the biosensing results. Hence, the relevance of covalently attaching the bioreceptor onto the nanostructures following, for example, the click chemistry path developed in this work is reinforced by the results obtained.

4.7. Conclusions

The study of distinct polymerization conditions of those used in the previous chapter was required since here the macroRAFT contains azide repeating units. In order to carry out the polymerization at 44ºC instead of at 70ºC, a new initiator (VA-044) had to be used and the effect of other reaction parameters such as pH, *[MR agent]/[initiator]*, reaction time have assessed. Stable *N3*-MR@Au NPs were then successfully prepared via RAFT emulsion copolymerization of a mixture of hydrophobic monomer (10 MMA : 1 BA w/w) from *N3*-MR@Au NPs, during 24h at 44ºC using VA-044 as initiator. Here the *[MR agent]/[initiator]* and the pH were maintained the same, in comparison to the conditions used at 70ºC with the ACPA (***Chapter 3***).

Biotin-copolymer@Au NPs were prepared via the specific *click chemistry* reaction between the azide moiety at the surface of the nanostructure (*N3*-copolymer@Au NPs) and an alkylated biotin. Optical biosensing tests revealed that aggregation of *biotin*-copolymer@Au NPs was induced in the presence of avidin, contrary to the nanostructures without biotin, showing that the nanostructures are specific for the biotarget (avidin). Also some non-specific interactions were observed between the copolymer@Au NPs (without biotin) and the avidin which can be assigned to electrostatic interactions. However, copolymer@Au NPs mixed with biotin (but not convalently bound) responded as well to the presence of avidin. This result suggests that biotin was adsorbed and/or trapped in the polymer shell, probably due to the low solubility of biotin in water, contributing to the aggregation in the presence of avidin. Therefore, the nanostructures prepared here can be used as platforms for the recognition of the biotarget avidin and in this specific case biotin can just be adsorbed to the nanostructure. In fact, preliminary studies at the air/water interface using Langmuir copolymer monolayers showed that the presence of biotin affects the surface pressure-area isotherm of the copolymer which suggests that biotin is interacting with the copolymer. Strategies to minimize the adsorption of the bioreceptor (biotin) in the polymer shell should be studied in order to promote the *click chemistry* reaction and allow the removal of unreacted bioreceptor. Since PEGA is thermoresponsive, the study of the influence of the temperature during the *click chemistry* reaction and adsorption should be considered. Moreover, copolymer@Au NPs covalently bonded to the bioreceptor avoid the risk of partial leakage of biotin to the aqueous medium containing the bioanalyte which would alter the signal. Additionally covalently bonded bioreceptors offer the possibility of reusing biosensors.

Attempts to prepare fluorescent copolymer@Au NPs have shown that the incorporation of fluorescent repeating units at different distances from the core is a promising strategy but needs further studies. Nevertheless, the results obtained allowed to identify a number of issues that need to be taken into consideration for the preparation of fluorescent tagged nanostructures. Moreover, the importance of bonding the bioreceptor onto nanostructures was evidenced.

CHAPTER 5. General Conclusions and future work

In this thesis, functional polymer@Au nanostructures, with shell@core type structure, were prepared to be used in biosensing applications. The Au core provide the characteristic optical properties due to the localized surface plasmon resonance (LSPR) while the polymer shell provides robustness and stability to the nanostructure. Additionally it allows the introduction of functional molecules such as biorecognition moieties (biotin) and fluorophores (FITC). Two main methodologies were explored in this work: one using the well-known the layer-by-layer (LbL) method based on electrostatic self-assembly of commercially available ionic polymers with opposite charges; the second one using the RAFT polymerization to encapsulate NPs.

In the first methodology, LbL method, multifunctional nanostructures were prepared using PAH and PSS as polyelectrolytes. Biotin and FITC were successfully attached to the PAH allowing to have a functional layer. This type of nanostructure proved to be promising for biorecognition of avidin using visible and fluorescence spectroscopies. However, all the studies were performed using ultra-pure water since these nanostructures easily destabilize and aggregate with changes in the ionic strength and pH of the medium. Therefore, other methodology was explored in order to prepare multifunctional Au nanostructures stable in physiological medium aiming the biosensing applications.

In the second methodology the use of RAFT polymerization was explored to encapsulate Au NPs. In the literature three main strategies have been reported, namely the *post-modification* strategy, the *in situ* strategy and the *grafting from* strategy, which were explored to encapsulate Au NPs with amphiphilic block copolymers which could be latter functionalized. These block copolymers were prepared via RAFT emulsion polymerization using a well-tailored macroRAFT agent prepared in solution also via RAFT polymerization using a trithiocarbonate RAFT agent.

In the *post-modification* strategy, the previously prepared block copolymer was mixed with Au NPs in aqueous solution but shell@core type nanostructure were not obtained. In fact, the amphiphilic block copolymer formed well-defined micelles in water and the Au NPs are not able to migrate to the core of these polymer NPs where the trithio-group is located.

Regarding the *in situ* strategy, Au NPs were generated in the presence of the previously prepared block copolymer also in aqueous solution. Also shell@core type nanostructure were not obtained. In this case, the gold precursor was also not able to migrate to the trithio group in the core of the well-defined diblock polymeric nanoassemblies. However, this strategy allowed to identify and conclude about several key parameters that influence the generation of Au NPs, such as the pH, the amount of the copolymer, the $[HAuCl_4]/[copolymer]$ ratio as well as the chemical nature of the repeating units, namely the acrylic acid and the poly(ethylene glycol) that compose the hydrophilic block.

In the third strategy, the *grafting from* strategy involves two main steps. Regarding the first step, associated with the preparation of MR@AuNPs, two pathways were followed: the *in situ* generation of Au NPs in previously prepared macroRAFT agents, and the adsorption of macroRAFT agents onto Au NPs. In the *in situ* pathway, it was concluded that the nucleation and growth of the Au NPs depends on the pH, the amount the MR agent, the ratio *[HAuCl₄]/[MR]* and also on the chemical nature of repeating units. For instance, by increasing the MR agent concentration the size of the NPs decreases, namely when a MR agent concentration above the CMC was used a brown colloid was generated and the LSPR band was not detected, indicating that only Au clusters ($d < 3$ nm) were formed. Although this one step synthesis is interesting to prepare spherical Au NPs, the control over the size is not easy and depends on many parameters. In the alternative pathway, adsorption of the MR agent onto Au NPs surface which were previously prepared with the desire size and shape can be used. In fact, in this work only spherical NPs with diameters around 15 nm were explored but Au NPs with bigger sizes (e.g. 50 and 100 nm) and different morphologies (e.g. nanorods and nanoprims) would be interesting to encapsulate and explore their optical properties. In this strategy, MR agent in concentrations above and below the CMC was adsorbed onto Au NPs surface and both situations afforded stable MR@Au NPs. Yet, when the concentration above CMC was used more free MR agent was observed by electron microscopy. In what concerns the adsorption of the MR agent onto Au NPs, it is important to perform further adsorption studies below the CMC in order to find the optimal concentration and *[MR]/[Au NPs]* ratio to use. In fact, our preliminary results regarding the adsorption studies of MR agent were not conclusive because they were carried out above the CMC.

As regards the growth of the hydrophobic chain from MR@Au NPs during the second step of the *grafting from* strategy, stable copolymer@AuNPs - shell@core type nanostructures were obtained using the colloids MR@Au NPs prepared above and below the CMC. The major breakthrough was the controlled addition of the hydrophobic monomers during the copolymerization from MR@Au NPs. Indeed, when the hydrophobic monomers were added in one shot at the beginning of the polymerization reaction, fiber-like nanostructures were also obtained. Following this *grafting from* strategy via RAFT mediated emulsion polymerization, by controlled addition of the hydrophobic monomers, it was demonstrated that it is possible to encapsulate Au NPs with amphiphilic block copolymer in aqueous media.

Functionalization of Au nanostructures, prepared by the *grafting from* strategy via RAFT mediated emulsion polymerization, was explored using the specific reaction of *click chemistry* between an azide and an alkyne. This functionalization strategy was a challenge, first because all the copolymer@Au NPs were prepared at 70ºC and the azide should not be handled at temperatures above 50ºC due to safety issues. Therefore, the copolymerization conditions had to be adjusted using a new initiator (VA-044) which has half-time ($t_{1/2}$) of 10h at 44ºC. Under these conditions it was possible to polymerize the mixture of hydrophobic monomers from *N3*-MR@Au NPs (MR@Au NPs containing the azide moiety) during 24h (at 44°C), yielding stable *N3*-copolymer@Au NPs. The *click chemistry* between the *N3*-copolymer@Au NPs and an alkylated biotin was carried out however the formation of the triazole could not confirmed beyond doubt due to the small amount of this specific group in comparison with the FTIR signal of the copolymer in the nanostructure.

Concerning the biosensing tests, the *biotin*-copolymer@Au NPs specifically respond to the presence of avidin inducing aggregation and subsequently changing the LSPR band. However, even the colloids where biotin was not covalently bonded via *click chemistry* aggregated in the presence of avidin. This result suggested that biotin was adsorbed/trapped in the polymer shell contributing to the aggregation in the presence of the analyte. In addition, *fluorescent*-copolymer@Au NPs were prepared however, further optimization of the preparation of these functional nanostructures is still required. The results obtained suggested that the fluorescent monomer was also adsorbed/trapped in the polymer shell.

Although the desired shell@core nanostructures were obtained, further studies sould be performed to get a better understanding about the copolymerization from the surface of the MR@Au NPs, in order to prepare stable nanostructures with thicker polymer shells and even to copolymerize other hydrophobic monomers. For instance, the use of a previously prepared fluorescent MR agent is recommended to study the effect of chain extension on the fluorescence quenching. Moreover, the functionalization strategy via click chemistry reaction should be optimized to ensure that the biorecognition moiety is covalently attached to the nanostructure allowing the preparation of specific and reproducible systems.

Despite of the difficulties encountered, the *grafting from* strategy via RAFT mediated emulsion polymerization proved to be the most promising to prepare multifunctional shell@core nanostructures. The ensuing nanostructures will have the properties of the stable core (e.g. different sizes and morphologies of Au NPs should be explored) and the polymer shell prepared via RAFT polymerization can be tailored and designed providing several functionalities, such as the incorporation of functional monomers at specific lengths from the core and/or the use of monomers that are responsive to pH or temperature. Hence this strategy opens the possibility to design a panoply of novel nanostructures aiming at specific applications.

CHAPTER 6. Experimental procedures

6.1. Chemicals

Chemicals used in *Chapter 2*

Hydrogen tetrachloroaurate (III) trihydrate, 99.9+% ($HAuCl_4.3H_2O$), sodium citrate tribasic dehydrate, ≥ 99% ($Na_3C_6H_5O_7.2H_2O$), biotin, ≥ 99%, avidin from egg white ≥ 98%, fluorescein isothiocyanate isomer I (FITC, suitable for protein labeling, ≥90% (HPLC)), N-(3-dimethylaminopropyl)-N'-ethyl-carbodiimide (EDC), poly(allylamine hydrochloride) MW 15,000 (PAH) and poly(styrenesulfonic acid sodium salt) MW 17,000 (PSS) were purchased from Sigma-Aldrich. Potassium hydroxide (pellets) was purchased from LabChem. Dimethyl sulfoxide (DMSO), >99.7%, was purchased from SdS Carlo Erba. Ultrapure water purified using a Station 8000/Station 9000 purification unit was used throughout C***hapter 2***

Chemical used in *Chapter 3* and *Chapter 4*

Poly(ethylene glycol) methyl ether acrylate (PEGA, Mn = 480 g/mol, Sigma-Aldrich), acrylic acid (AA, 99%, Fluka), 2-aminoethyl methacrylate hydrochloride (AEM, contains ~500 ppm phenothiazine as stabilizer, 90%, Sigma-Aldrich) RAFT agent 2-(dodecylthiocarbonothioylthio)-2-methylpropionic acid (TTC-A, 98%, HPLC, Sigma-Aldrich), initiator 4,4′-azobis(4-cyanovaleric acid) (ACPA, ≥98% Fluka), hydrogen tetrachloroaurate (III) trihydrate (HAuCl4.3H2O, 99.9+%, Sigma-Aldrich), sodium citrate tribasic dehydrate ($Na_3C_6H_5O_7$.2H2O, Sigma-Aldrich) and 1,3,5-trioxane (99.5+%, Acros) were used as received. Monomers *n*-butyl acrylate (BA, 99%, Acros) and methyl methacrylate (MMA, 99%, Acros) were passed through a column of neutral aluminum oxide (Carlo Erba, particle size 63-200 µm) prior to use to remove the inhibitor. Ethanol, diethyl ether, 1,4-dioxane BDH Prolabo, VWR. Dimethyl sulfoxide-d6 ($(CD_3)_2SO$, Merck) was used to dissolve the macroRAFT agent for ^{1}H-NMR. Ultrapure water was obtained from a MilliQ water purification system (Millipore, Billerica, MA) was used throughout ***Chapter 3*** and ***Chapter 4***

6.2. Instrumentation

The UV/VIS spectra of the colloids were recorded using quartz cells and a Jasco V-560 UV/VIS spectrometer or a UV/Visible GBC Cintra-303, using water as the reference. The fluorescence spectra of the colloids were recorded using quartz cells, a FluoroMax-3 Horiba Jobin Yvon spectrometer and a Jasco Spectrofluorometer FP-8300 were used in ***Chapter 2*** and ***Chapter 4***, respectively. Transmission electron microscopy (TEM) images were obtained using a Hitachi H-9000 microscope operated at 300 kV. Scanning Electron Microscopy (SEM) and SEM in transmission mode images were obtained using a Hitachi SU-70 operating at an accelerating voltage of 15 or 30 kV. Scanning transmission electron microscopy (STEM) images, with transmission, secondary electron and Z contrast detection, were obtained using a Hitachi HD2700C (dedicated STEM instrument) operating at 200 kV. The samples were prepared by placing a drop of diluted colloidal solutions on a copper grid coated with an amorphous carbon film and left to evaporate. The zeta potential and dynamic light scattering (DLS) measurements were carried out using a ZetaSizer Nano ZS Model Zen 3500 from Malvern. In ***Chapter 2***, for DLS measurements, one drop of the colloidal solution was diluted in circa 1 mL of water and for zeta potential measurements, the colloids were analysed as prepared (the pH of the colloids varied between 5.5 and 6.5, room temperature). In ***Chapter 3*** and ***Chapter 4***, for DLS and zeta potential measurements, the gold colloids were analysed as prepared and the latex were diluted circa 10-fold. Centrifugation was performed in a Force 1618 Microcentrifuge at room temperature. ^{1}H-NMR spectra were recorded on a Bruker Avance 300 spectrometer by diluting or dissolving the sample in the adequate deuterated solvent. GPC-SEC analysis were performed on a PL-110 GPC instrument equipped with a two PLMIXED 300x7.5 mm column and a refractive index (RI) detector. The columns, injector system and the detector were maintained at 50ºC during the analysis. Before sample analysis, the methylation of the carboxyl groups from the copolymers were performed using diazomethane ***(6.5.2).*** The methylated copolymers (5 mg) were dissolved in 0.4 mL of THF (CHROMASOLV® Plus, for HPLC > 99.9%, Aldrich) and 20 µL of toluene was added as internal standard. 100 µL of copolymer solutions were pumped at a flow rate of 0.9 mL/min. The columns were calibrated with with PS standards (Polymer Laboratories, UK) in a range of MW = 1700 - 66 000. Langmuir monolayers were prepared using a NIMA 611 Langmuir-Blodgett trough and the copolymer solutions were spread at the air/water interface using a microsyringe (Hamilton,100 µL).

6.3. Experimental of chapter 2

6.3.1. Synthesis of Au NPs via citrate method

10 mL of sodium citrate solution (38.8 mM) were added to 100 mL of $HAuCl_4.3H_2O$ solution (1mM) previously brought to 90 ºC and under vigorous stirring. After 1h, heating was switched off and stirring was kept overnight. The concentration of the gold nanoparticle stock solution obtained was estimated according to the method published by Decher *et al.* [192] to be around 12 nmol/L in particles. This solution was centrifuged in 1.5 mL Eppendorfs for 1.5 h at 14 000 rpm (15 996g) before use. The supernatant was removed from each tube and replaced by ultrapure water using a volume twice that of the initial.

6.3.2. Modification of poly(allylamine hydrochloride) with fluorescein

In order to prepare the poly(allylamine hydrochloride) polyelectrolyte modified with fluorescein (PAHF), PAH (208.6 mg) was dissolved in 20 mL of water and aqueous KOH solution (3M) was added dropwise to the stirred solution until pH 9.4. Next, fluorescein isothiocyanate (8.4 mg) was added, and the solution was stirred overnight under exclusion of light. Under the same conditions, the mixture was dialysed (Spectra/Por® Dialysis Membrane MWCO 6-8 kDa from SpectrumLabs.com) using DMSO in water (~0.1 %V/V) to remove unreacted fluorophore. During this process, the dialysate was monitored by optical spectroscopy.

6.3.3. Modification of PAH and PAHF with biotin

Biotinylated PAH (PAHB) and PAHF (PAHFB) polyelectrolytes were prepared by adding 2 mL of biotin solution (1mg/mL) and 2 mL of EDC solution (2mg/mL) to 20 mL of a PAH solution (5 mg/mL, pH=5.5) or PAHF (~5 mg/mL, pH=5.5). The solutions were mixed and stirred for 1h at room temperature. These solutions were not dialyzed and were used to modify Au NPs.

6.3.4. Preparation of Au/PE hybrid nanostructures

Au/PE hybrid nanostructures with a distinct number of layers (n = 0 or 2) have been prepared: Au_0PAH (with a single PE layer) and Au_2PAH (with one intermediary bi-layer of PAH/PSS and a third outermost layer of PE), as illustrated in Scheme 2.1.

Typically, 60 mL of the Au NPs colloid was added dropwise, under vigorous stirring, to 60 mL of a solution of PAH (5mg/mL) and stirred for 2h, at room temperature. The mixture was centrifuged for 60 minutes at 14 000 rpm (15 996g). The supernatant was removed and the precipitate re-dispersed in water. This step was repeated once again and the re-dispersed volume after the second centrifugation was adjusted in order to obtain a final volume of 60 mL to yield a NPs colloid designated as Au_0PAH. Then, these NPs were added dropwise, under vigorous stirring, to 60 mL of a solution of PSS (6.25mg/mL) and stirred for 2h at room temperature. The mixture was centrifuged for 60 minutes at 14 000 rpm (15 996g). The supernatant was removed and the precipitate re-dispersed in water. This centrifugation process was repeated once again and the re-dispersed volume after this second centrifugation was adjusted in order to obtain a final volume of 60 mL. At the end of this second surface modification, the hybrid nanostructures Au/PAH/PSS named as Au_2 NPs have been obtained (Scheme 2.1-B). Finally the outermost layer (Scheme 2.1-C) was deposited following the same procedure and using two biotinylation strategies.

Biotinylation - strategy 1

The biotinylation of the surface modified Au NPs was first explored following a procedure similar to the preparation of Au_0 and Au_2 NPs. The biotinylated polyelectrolytes - PAHB or PAHFB have been used in this strategy using 10 mL of colloid. The scheme illustrating this surface modification is shown in Scheme 2.1-C.

A posteriori biotinylation - strategy 2

A second strategy for the biotinylation of the Au NPs was also investigated following the path also illustrated in Scheme 2.1-C. In this procedure, 1 mL of biotin (1mg/mL) and 1 mL of EDC (2 mg/mL) were added to the colloids Au_nPAH or Au_nPAHF (10 mL). The mixtures were stirred for 1 hour and then centrifuged (60 min, 14 000 rpm - 15 996g) to remove the unreacted biotin. The supernatant was removed and replaced by water (final volume = 10 mL). The resulting nanostructures were named Au_nPAH+B and Au_nPAHF+B, respectively. The "+" means that biotinylation was carried out a posteriori, thus yielding samples distinct from those obtained in strategy 1.

6.3.5. Optical response of Au/PE assemblies to avidin

In order to evaluate the potential use of the biotinylated hybrid Au/PE nanostructures in optical biosensing, the optical behaviour of the respective colloids was studied in the presence of avidin. In this case, the samples Au_nPAH and Au_nPAHF were used as blanks regarding the response to avidin. 100 µL of an avidin solution (0.4 mg/mL) was added to 1 mL of the colloidal solution diluted twofold. One week later, optical measurements have also been performed in order to evaluate the stability of the colloids. Parallel to this, as it was thought that the amount of avidin added could be too small to trigger a specific response, the theoretical quantity of avidin to interact with all the biotin in the system was added to each colloid. The spectra were recorded immediately upon addition of the avidin and 2 h later. For adequate evaluation of the optical response of the colloids in the presence of avidin, data were compiled as described below.

The original colloidal Au NPs presented a LSPR band at around 525 nm. The intensity of this band decreased and light absorption between 600-750 nm became noticeable due to particle aggregation. In a first approximation, by assuming that these differences in terms of band intensity are mainly due to an aggregation process and by not taking into account band broadening, we have defined a semi-quantitative parameter indicative of aggregation extension due to the presence of avidin:

$$\Delta\mathrm{A}(avidin/colloid) = \frac{\mathrm{A_{LSPR}(colloid{+}avidin)} - \mathrm{A_{650}(colloid{+}avidin)}}{\mathrm{A_{LSPR}(colloid)} - \mathrm{A_{650}(colloid)}} \qquad (equation\,5)$$

Where A_{LSPR}*(colloid+avidin)*: absorbance at the LSPR wavelength for a colloid in the presence of avidin, A_{650}*(colloid+avidin)*: absorbance at 650 nm for a colloid in the presence of avidin, A_{LSPR}*(colloid)*: absorbance at the LSPR wavelength for the initial colloid and A_{650}*(colloid)*: absorbance at 650 nm for the initial colloid.

For the FITC functionalized Au colloids, attempts have been made to correlate fluorescence measurements with aggregation effects due to the presence of avidin. Hence, the ratio between the fluorescence intensity (at 517 nm) of the Au colloid in the presence of avidin and that of the initial Au colloid: I_{517}*(avidin)*/I_{517}*(colloid)*, was calculated for the experimental conditions indicated in the graphs.

6.4. Experimental of chapter 3

6.4.1. Synthesis of macroRAFT agents

The macroRAFT agents were synthesized in one-step solution polymerization. First, the RAFT agent TTC-A was dissolved in the appropriate solvent, then the chosen monomer was added followed by the initiator (ACPA) and 1,3,5-trioxane. The last one was used as internal standard for determination of monomer conversion by ^{1}H-NMR. It was used a ratio [*trioxane*]/[*monomer*]=6. The mixture was purged with nitrogen for 30 minutes in an ice bath under stirring. The reaction was carried out at 70 ºC or 80ºC for 4 hours. See Table 6.1 for experimental conditions. The final product was purified by precipitation in cold diethyl ether (3 times) and then dried under reduced pressure at room temperature. Aliquots were withdrawn and analyzed by ^{1}H-NMR for determination of monomer conversion.

Table 6.1. Experimental conditions for the synthesis of the macroRAFT agents.

Sample name	PEGATTC	PAATTC
macroRAFT agent	**P(PEGA$_{40}$)-TTC**	**P(AA$_{40}$)-TTC**
Monomer	PEGA	AA
$[TTC\text{-}A]$ (mol/L solvent)	0.086	0.077
$[\boldsymbol{Monomer}]/[\boldsymbol{TTC\text{-}A}]$	44	44
$[\boldsymbol{TTC\text{-}A}]/[\boldsymbol{ACPA}]$	15	10
Solvent	ethanol	dioxane
Time (hours)	4	4
Temperature (ºC)	70ºC	80ºC

6.4.2. Synthesis of copolymers via RAFT emulsion polymerization based on the MR agents

The diblock copolymers were prepared by RAFT emulsion polymerization. The macroRAFT agent was dispersed in water and pH adjusted to 7.5 with a solution of NaOH (0.5 M). Initiator ACPA solution (3.2 mM) was prepared in water adding two drops of NaOH 1M to help dissolution. A solution of initiator (2.8 mL, 3.2 mM) and 1.54 mL of monomer mixture of MMA:BA (10:1 w/w) were added to the system. After deoxygenation by bubbling with nitrogen for 30 min in an ice bath under stirring, the sealed vessel containing the reaction mixture was immersed in an oil bath at 70ºC during four hours. Samples were periodically withdrawn to monitor the monomer conversion by gravimetric analyses and the evolution of the average particle diameter by DLS measurements. See Table 6.2 for experimental conditions.

Table 6.2. Experimental conditions for the synthesis of the block copolymers.

Sample name	**copPEGATTC**	**copAATTC**
copolymer	**P(PEGA$_{40}$)-*b*-(MMA-*co*-BA)$_{140}$-TTC**	**P(AA$_{40}$)- *b*-(MMA-*co*-BA)$_{160}$-TTC**
macroRAFT	P(PEGA$_{40}$)-TTC	P(AA$_{40}$)-TTC
[MR] (mM)	8.2	8.1
$[\boldsymbol{MMA}:\boldsymbol{BA}]/[\boldsymbol{MR}]$	148	144
$[\boldsymbol{MR}]/[\boldsymbol{ACPA}]$	9	8
solvent	H_2O	H_2O
Time (hours)	4	4
Temperature (ºC)	70ºC	70ºC

6.4.3. Synthesis of Au NPs via citrate method

Au-Cit NPs used in this chapter were prepared following the same procedure as in the Chapter 3. 10 mL of sodium citrate solution (38.8 mM) were added to 100 mL of $HAuCl_4.3H_2O$ solution (1mM) previously brought to 90 ºC and under vigorous stirring. After 1h, heating was switched off and stirring was kept overnight. Prior to use, the colloidal solution was centrifuged for 30 minutes at 15600g. The supernatant was removed and replaced by the same volume with ultrapure water. Au NPs with a diameter of circa 15 nm were obtained and the concentration (mol NPs/L) was calculated by UV-Vis spectroscopy [221].

6.4.4. Synthesis of Au nanocomposites via *post-modification* strategy

Previously prepared Au-cit NPs (3 mL) were added dropwise to a diluted solution of copolymer (60 µL of latex was dispersed in 2.4 mL of water) and the mixture was stirred for 2h, at room temperature. After that, it was centrifuged (30 min, 15 600g) and redispersed in the same volume with ultra-pure water. For comparison, a same dilution of latex was also centrifuged and redispersed in the same conditions as the Au nanocomposite. P(PEGA$_{40}$)-*b*-(MMA-*co*-BA)x-TTC and P(AA$_{40}$)-*b*-(MMA-*co*-BA)x-TTC were used in this strategy.

6.4.5. Synthesis of Au nanocomposites via *in situ* generation of Au NPs in previously prepared copolymers

Generally, 250 µL of $HAuCl_4$ (0.01 M) were added to a diluted solution of copolymer (50 µL of latex was dispersed in 4.7 mL of water). After 20 min stirring, a shot of a freshly prepared $NaBH_4$ (25 µL, 0.1 M) was added and the mixture stirred overnight. After that, the colloid was centrifuged (30 min, 15 600g) and redispersed in the same volume with ultra-pure water. P(PEGA$_{40}$)-*b*-(MMA-*co*-BA)$_{140}$-TTC and P(AA$_{40}$)-*b*-(MMA-*co*-BA)$_{160}$-TTC were used in this strategy. For comparison, a same dilution of latex was also centrifuged and redispersed in the same conditions as the Au nanocomposite. The same procedure was employed with various concentrations of $HAuCl_4$ and copolymer and also other pH values, to evaluate the influence of these parameter as indicate in **3.4.2.**, see Table 6.3 and Table 6.4.

Table 6.3. Experimental conditions for the generation of Au NPs in the presence of P(PEGA$_{40}$)-*b*-(MMA-*co*-BA)$_{140}$-TTC.

$\frac{[HAuCl_4]}{[copPEGATTC]}$	Latex (µL)	$HAuCl_4$* (µL)	pH	$NaBH_4$* (µL)	Final Volume (mL)
2.4	50	100	4	10	5.0
4.8	25	100	4	10	5.0
6.0	50	250	4	25	5.0
6.0	50	250	8	25	5.0

* HAuCl4 0.01 M and NaBH4 0.1 M were used in all the experiments.

Table 6.4. Experimental conditions for the generation of Au NPs in the presence of P(AA$_{40}$)-*b*-(MMA-*co*-BA)$_{160}$-TTC.

$\frac{[HAuCl_4]}{[copAATTC]}$	Latex (µL)	$HAuCl_4$* (µL)	pH	$NaBH_4$* (µL)	Final Volume (mL)
30.0	10	250	4	25	5.0
12.0	25	250	4	25	5.0
6.0	50	250	4	25	5.0
4.0	75	250	4	25	5.0
6.0	50	250	8	25	5.0
6.0	50	250	6	25	5.0

* HAuCl4 0.01 M and NaBH4 0.1 M were used in all the experiments.

6.4.6. Determination of CMC

A set of solutions with concentrations between 1.8x10^{-3} mM and 1 mM were prepared for each MR agent, P(PEGA$_{40}$)-TTC, P(AA$_{40}$)-TTC and P(AA$_{20}$-*co*-PEGA$_{20}$)-TTC. Conductivity and DLS measurements were performed for MR agent solutions in ultra-pure water as prepared and also for MR agent solutions whose pH was raised to 7.5-8.0 using NaOH (1M or 0.1M).

6.4.7. Synthesis of Au nanocomposites following a *grafting from* strategy via *in situ* generation of Au NPs in previously prepared macroRAFT agents

Generally, 300 µL of $HAuCl_4$ (0.01 M) were added to a diluted solution of MR agent and stirred about 20 minutes before adding a shot of a freshly prepared $NaBH_4$ (300 µL, 0.01 M) and the mixture stirred overnight. In some cases the pH of the mixture $HAuCl_4$ with MR was increased to pH=7, using NaOH 0.1M and 0.01M. This procedure was employed for various concentrations of MR, without adjusting the pH (c.a. pH=3) and at pH 7 to evaluate the influence of these parameters in the generation of Au NPs. The MR agents used were P(AA$_{40}$)-TTC (see Table 6.5) , P(PEGA$_{40}$)-TTC (see Table 6.6) and , P(AA$_{20}$-*co*-PEGA$_{20}$)-TTC (see Table 6.7).

Table 6.5. Experimental conditions for the generation of Au NPs in the presence of P(AA$_{40}$)-TTC.

$\frac{[HAuCl_4]}{[MR]}$	V_{MR}(a) (mL)	[MR] (mM)	V_{HAuCl4} (mL)	[$HAuCl_4$] (mM)	pH	V_{NaBH4} (mL)	$NaBH_4$ (mM)	Final Volume (mL)
5.9	1.500	0.051	0.300	0.30	3.1	0.300	0.30	10.0
5.9	1.500	0.051	0.300	0.30	7.0	0.300	0.30	10.0
13.7	0.750	0.026	0.300	0.35	7.1	0.300	0.35	8.5
6.9	1.500	0.051	0.300	0.35	7.3	0.300	0.35	8.5
3.4	3.000	0.100	0.300	0.34	7.1	0.300	0.34	8.7

(a) stock concentration of P(AA$_{40}$)-TTC 0.34 mM.

Table 6.6. Experimental conditions for the generation of Au NPs in the presence of P(PEGA$_{40}$)-TTC.

$\frac{[HAuCl_4]}{[MR]}$	$V_{MR}$$^{(a)}$ (mL)	[MR] (mM)	V_{HAuCl4} (mL)	[HAuCl$_4$] (mM)	pH	V_{NaBH4} (mL)	NaBH$_4$ (mM)	Final Volume (mL)
13.9	0.750	0.022	0.300	0.30	3.0	0.300	0.30	10.0
6.9	1.500	0.043	0.300	0.30	2.9	0.300	0.30	10.0
13.9	0.375	0.022	0.150	0.30	7.3	0.150	0.30	5.0
6.9	0.750	0.043	0.150	0.30	8.1	0.150	0.30	5.0

$^{(a)}$ stock concentration of P(PEGA$_{40}$)-TTC 0.29 mM.

Table 6.7. Experimental conditions for the generation of Au NPs in the presence of P(AA$_{20}$-*co*-PEGA$_{20}$)-TTC.

$\frac{[HAuCl_4]}{[MR]}$	$V_{MR}$$^{(a)}$ (mL)	[MR] (mM)	V_{HAuCl4} (mL)	[HAuCl$_4$] (mM)	pH	V_{NaBH4} (mL)	NaBH$_4$ (mM)	Final Volume (mL)
13.8	0.375	0.022	0.150	0.30	3.0	0.150	0.30	5.0
6.9	0.750	0.043	0.150	0.30	3.0	0.150	0.30	5.0
13.8	0.375	0.022	0.150	0.30	7.4	0.150	0.30	5.0
6.9	0.750	0.043	0.150	0.30	7.4	0.150	0.30	5.0

$^{(a)}$ stock concentration of P(AA$_{20}$-*co*-PEGA$_{20}$)-TTC 0.29 mM.

For the systematic study of the effect of the molar ratio of gold precursor to P(PEGA$_{40}$)-TTC concentration at pH~3 a methodology as described above as followed using the experimental conditions summarized in Table 6.8.

Table 6.8. Experimental conditions for the generation of Au NPs in the presence of P(PEGA$_{40}$)-TTC.

$\frac{[HAuCl_4]}{[MR]}$	$V_{MR}$$^{(a)}$ (mL)	[MR] (mM)	V_{HAuCl4} (mL)	[HAuCl$_4$] (mM)	pH	V_{NaBH4} (mL)	NaBH$_4$ (mM)	Final Volume (mL)
18.5	0.560	0.011	0.300	0.20	3.7	0.300	0.20	15.00
9.2	1.125	0.022	0.300	0.20	3.3	0.300	0.20	15.00
6.1	1.700	0.033	0.300	0.20	3.4	0.300	0.20	15.00
4.6	2.250	0.043	0.300	0.20	3.4	0.300	0.20	15.00
3.7	2.800	0.054	0.300	0.20	3.3	0.300	0.20	15.00
1.4	7.440	0.143	0.300	0.20	3.2	0.300	0.20	15.00

$^{(a)}$ stock concentration of P(PEGA$_{40}$)-TTC 0.29 mM.

Copolymerization of MMA:BA from MR@Au NPs via RAFT emulsion polymerization

The growth of the hydrophobic block was carried out in emulsion for the colloids prepared using the $[HAuCl_4]/[[MR]$ ratios 9.2, 6.1 and 3.7.The pH of colloids was adjusted using NaOH (0.1 or 0.01 M). 1mL of a solution of initiator ACPA and 5µL of the mixture of hydrophobic monomers MMA:BA (10:1 w/w) were added to the reaction vessel containing the colloid. The mixture was purged with nitrogen for 30 minutes in an ice bath under stirring. The polymerization was carried out at 70 ºC during 4hours. Experimental details are presented in Table 6.9.

Table 6.9. Experimental condition for the copolymerization of MMA:BA (10:1 w/w) from MR@Au NPs.

$\frac{[HAuCl_4]}{[MR]}$	**9.2**	**6.1**	**3.7**
$V_{colloid}$ (mL)	5.0	4.4	5.0
pH	7.7	7.3	7.9
MR moles[(a)]	1.1E-07	1.4E-07	2.7E-07
Conc. ACPA (mM)[(b)]	0.01	0.02	0.03
V_{ACPA} (mL)	1.0	1.0	1.0
$V_{Monomer}$ (µL)	5.0	5.0	5.0

[(a)] moles of MR used for the generation of Au NPs. [(b)] Concentration of initiator in the volume added to the reaction vessel.

6.4.8. Synthesis of Au nanocomposites following a *grafting from* strategy via macroRAFT adsorption onto previously prepared Au NPs

Preparation of the MR@Au NPs below CMC

A solution of MR agent (18 mL) below the CMC was prepared and the pH increased to 7-8 using NaOH (0.1M and 0.01M). This solution was added dropwise under stirring, to a dispersion of Au NPs (2 mL, $6.0x10^{-9}$ mol NPs/L) and stirred overnight, at room temperature. The mixture was centrifuged 30 min at 15600g, the supernatant was collected and the precipitate was redispersed with ultra-pure water, see Table 6.10 . In the case of P(PEGA$_{40}$)-TTC and P(AA$_{22}$-co-PEGA$_{22}$)-TTC the precipitate was redispersed in half of the volume, and for P(AA$_{40}$)-TTC the precipitate was redispersed in the same volume.

Preparation of the MR@Au NPs above CMC

A solution of MR agent above the CMC was prepared and the pH increased to 7-8 using NaOH (0.1M and 0.01M). This solution was added dropwise, under stirring, to a dispersion of Au NPs and stirred overnight, at room temperature. Au NPs dispersion was diluted from a stock solution: in the case of P(PEGA$_{40}$)-TTC and P(AA$_{20}$-co-PEGA$_{20}$)-TTC, 1mL of Au NPs (6.0x10^{-9} mol NPs/L) was diluted with 2 mL of ultra-pure water; in the case of P(AA$_{40}$)-TTC, 2 mL of Au NPs (5.0x10^{-9} mol NPs/L) were diluted with 2 mL of ultra-pure water. The mixture was centrifuged 30 min at 15600g, the supernatant was collected and the precipitate redispersed, in the same volume, with ultra-pure water. See Table 6.10.

Table 6.10. Experimental conditions the preparation of *gf*-MR/Au NPs colloids, below and above CMC.

colloid		$V_{\text{Au NPs}}$ (mL)	$C_{\text{MR agent}}$ (mM)	$V_{\text{MR agent}}$ (mL)	pH	$V_{\text{Adsorption}}^{(a)}$ (mL)
***gf*-PEGATTC@Au NPs**	< ***CMC***	2.0	6.3E-02	18.0	7.6	20.0
	> ***CMC***	1.0	4.0	1.6	8.0	4.6
***gf*-AATTC@Au NPs**	< ***CMC***	2.0	5.5E-02	18.0	7.0	20.0
	> ***CMC***	2.0	0.68	15.7	7.6	19.7
***gf*-AAPEGATTC@Au NPs**	< ***CMC***	2.0	7.6E-02	18.0	7.2	20.0
	> ***CMC***	1.0	2.8	1.51	7.1	5.1

Copolymerization of MMA:BA from gf-PEGATTC@Au NPs via RAFT emulsion polymerization by one-shot addition of the monomers mixture

The growth of the hydrophobic block was carried out in emulsion. The pH of freshly prepared PEGATTC@Au NPs (4 mL) was adjusted to 9 using NaOH (0.1 or 0.01 M). The solution of initiator ACPA (0.2 mL, 3.2 mM) and 110 µL of MMA:BA (10:1 w/w) were added the reaction vessel containing the colloid. The mixture was purged with nitrogen for 30 minutes in an ice bath under stirring and the polymerization started by placing the reaction vessel at 70 ºC. After 4h the reaction vessel was placed in an ice bath in contact with oxygen to stop the polymerization. The resulting colloids was centrifuged 30 min at 15600g, the supernatant was collected and the precipitate redispersed, in the same volume, with ultra-pure water.

Copolymerization of MMA:BA from MR@Au NPs via RAFT emulsion polymerization by controlled addition of the monomers mixture

The pH of freshly prepared MR@Au NPs was adjusted using NaOH (0.1 or 0.01 M) and the solution of initiator ACPA was added the reaction vessel containing the colloid. The mixture was purged with nitrogen for 30 minutes in an ice bath under stirring and the polymerization started by placing the reaction vessel at 70 ºC. The mixture of monomers (10 MMA : 1 BA w/w) was added in a control way: in the case of *gf*-PEGATTC@Au NPs and *gf*-AAPEGATTC@Au NPs, below CMC, 5 µL of the mixture of monomers was added before the copolymerization started and then 5 µL were added each hour during 2 hours; in the case of *gf*-PEGATTC@Au NPs and *gf*-AAPEGATTC@Au NPs above CMC, 10 µL of the mixture of monomer was added before the copolymerization started and then 20 µL were added each hour during 4 hours; concerning *gf*-AATTC@Au NPs, 5 µL of the mixture of monomers was added before the copolymerization started and for the colloid prepared using MR concentration above CMC, more 10 µL were added each hour during 3 hours. Afterwards the copolymerization continued for two more hours and then the reaction vessel was placed in an ice bath in contact with oxygen to stop the polymerization. Experimental details are presented in Table 6.11. The resulting colloids were centrifuged 30 min at 15600g, the supernatant was collected and the precipitate redispersed, in the same volume, with ultra-pure water.

Table 6.11. Experimental conditions for the copolymerization of MMA:BA (10:1 w/w) from MR@Au NPs.

MR used		**< CMC**	**> CMC**
PEGATTC	**$V_{colloid}$ (mL)**	8.0	4.0
	pH	8.0	8.8
	MR moles$^{(a)}$	1.0E-06	5.6E-06
	Conc. ACPA (mM)$^{(b)}$	0.124	3.2
	V_{ACPA} (mL)	1.0	0.2
	$V_{Monomer}$ (µL)	20	110
AATTC	**$V_{colloid}$ (mL)**	18.0	18.0
	pH	7.1	8.2
	MR moles$^{(a)}$	8.9E-07	9.6E-06
	Conc. ACPA (mM)$^{(b)}$	0.66	0.028
	V_{ACPA} (mL)	2.0	2.0
	$V_{Monomer}$ (µL)	5	50
AAPEGATTC	**$V_{colloid}$ (mL)**	9.0	4.3
	pH	8.8	7.4
	MR moles$^{(a)}$	1.2E-06	3.6E-06
	Conc. ACPA (mM)$^{(b)}$	0.124	3.2
	V_{ACPA} (mL)	1.0	0.2
	$V_{Monomer}$ (µL)	20	110

(a) moles of MR used for the adsorption. (b) Concentration of initiator in the volume added to the reaction mixture.

6.5. Experimental of chapter 4

6.5.1. Synthesis of the macroRAFT agent containing the azide function: P(azAA$_2$-*b*-PEGA$_{40}$)-TTC (*N3*-MR agent)

Synthesis of the macroRAFT agent P(AA$_2$-b-PEGA$_{40}$)-TTC

The macroRAFT agent was synthesized in one-step solution polymerization. First, the RAFT agent TTC-A (0.1836 g) was dissolved in ethanol (10 mL), then 0.068mL of AA was added followed by the initiator ACPA (0.0145 g) and 1,3,5-trioxane (0.3050 g). The latter was used as internal standard for the determination of monomer conversion by ^{1}H-NMR. Using a ratio [*trioxane*]/[*monomer*]=6. The mixture was purged with nitrogen for 30 minutes in an ice bath under stirring. The reaction was carried out at 70 ºC for 3 hours. Then 9.25 mL of PEGA was added and the polymerization continued for 4 more hours. The final product was purified by precipitation in cold diethyl ether (3 times) and then dried under reduced pressure at room temperature. Aliquots were withdrawn and analyzed by ^{1}H-NMR for determination of monomer conversion. See Table 6.12 for experimental conditions.

Table 6.12. Experimental conditions for the synthesis of the P(AA$_2$-b-PEGA$_{40}$)-TTC

	AA	PEGA
$[TTC\text{-}A]$ (mol/L solvent)	0.050	
$[TTC\text{-}A]/[ACPA]$	9.7	
$[Monomer]/[TTC\text{-}A]$	2	41
Time (hours)	3	4
solvent	ethanol	
Temperature (ºC)	70ºC	

Functionalization of P(AA$_2$-b-PEGA$_{40}$)-TTC with an azide group

The previously prepared P(AA$_2$-b-PEGA$_{40}$)-TTC (1.5 g) was dissolved in dichloromethane (15 mL) and then 0.020 g of EDC and 0.003 g of DMAP were added in ice bath under stirring. 0.0153 mL of 3-azido-1-propanol was added and the reaction was carried out for 2 hours and after this period of time it was allowed to thaw room temperature and was stirred for 2 days. The azide-functionalized MR agent (*N3*-MR agent) was purified by dialyses (Spectra/Por® Dialysis Membrane MWCO 6-8 kDa from SpectrumLabs.com) using dichloromethane, during one day.

6.5.2. Synthesis of the copolymers via RAFT emulsion polymerization using VA-044 as initiator

Synthesis of the copolymers via RAFT emulsion polymerization using P(PEGA$_{40}$)-TTC

P(PEGA$_{40}$)-*b*-(MMA-*co*-BA)$_n$-TTC copolymers were prepared by RAFT emulsion polymerization, following the procedure described above (**6.4.2.**) but using VA-044 as initiator and varying pH, [MR agent]/[initiator] ratio and polymerization time. Table 6.13 summarizes the experimental conditions used for the preparation of each block copolymer.

Table 6.13. Experimental conditions for the copolymerization of MMA:BA (10:1 w/w) from P(PEGA$_{40}$)-TTC using VA-044 as initiator.

MR agent used	**P(PEGA$_{40}$)-TTC**				
$[macroRAFT]$ **(mM)**	8.5	8.8	8.2	8.2	8.4
$[MMA{:}BA]/[macroRAFT]$	168	163	172	171	170
$[macroRAFT]/[VA-044]$	9	10	9	5	9
pH	8	6	8	8	8
Time (hours)	4	7	22	23	53
Temperature (ºC)	70ºC	44ºC	44ºC	44ºC	44ºC

Synthesis of the copolymers via RAFT emulsion polymerization using P(AA$_2$-b-PEGA$_{40}$)-TTC

P(AA$_2$-*b*-PEGA$_{40}$)-*b*-(MMA-*co*-BA)$_n$-TTC copolymers were prepared by RAFT emulsion polymerization, following the procedure described above (**6.4.2.**) but using ACPA or VA-044 as initiators at 70ºC and 44ºC, respectively. Table 6.14 summarizes the experimental conditions used for the preparation of each block copolymer.

Table 6.14. Experimental conditions for the copolymerization of MMA:BA (10:1 w/w) from P(AA$_2$-*b*-PEGA$_{40}$)-TTC using ACPA or VA-044 as initiators.

MR agent used	P(AA$_2$-*b*-PEGA$_{40}$)-TTC	
$[\boldsymbol{macroRAFT}]$ **(mM)**	8.2	8.2
$[\boldsymbol{MMA:BA}] / [\boldsymbol{macroRAFT}]$	175	174
$[\boldsymbol{macroRAFT}] / [\boldsymbol{initiator}]$	9	9
initiator	ACPA	VA-044
pH	8	8
Time (hours)	4	24
Temperature (ºC)	70ºC	44ºC

Preparation of copolymer sample for GPC-SEC analysis: Methylation process

The methylation of the carboxyl groups from the copolymers was performed using diazomethane, note that care should be taken since this reaction is highly explosive. Three reaction vessels with N_2 inlet and outlet were used and circa of 20 mL of diethyl ether were added to each vessel. In a fourth vessel, an aqueous solution of acetic acid (50%) was used to neutralize the unused diazomethane. In the first vessel 2 g of diazomethane precursor (Diazald® 99%, Aldrich) was dissolved in the diethyl ether and a KOH solution in ethanol (0.5g/10 mL) was added. The diazomethane generated was allowed to pass through the entire system by the N_2 flow. The third vessel was used as control and 1mL of the diazomethane of the second vessel was used for the methylation of the copolymers (5 mg). After ~3h the diethyl ether was evaporated under nitrogen flow and the samples were dissolved in 0.4 mL of THF for GPC-SEC analyses.

6.5.3. Preparation of Au nanocomposites following a *grafting from* strategy via macroRAFT adsorption onto previously prepared Au NPs (at 44ºC)

Preparation of copolymer@Au NPs (without azide function)

Copolymer@Au NPs were prepared using P(PEGA$_{40}$)-TTC and the adsorption step was performed using a concentration below the CMC. To prepare the MR@Au NPs, a solution of MR agent (20 mL, 0.05 mM) was prepared and the pH increased to 7-8 using NaOH (0.1M and 0.01M). This solution was added dropwise under stirring, to a dispersion of Au NPs (2 mL, 6.0×10^{-9} mol NPs/L) and stirred overnight, at room temperature. The mixture was centrifuged 30 min at 15600g, the supernatant was collected and the precipitate redispersed in 10 mL with ultra-pure water. In the second step, the growth of the hydrophobic block in emulsion, the pH of the freshly prepared MR@Au NPs (9mL) was adjusted to pH=8 using NaOH (0.1 or 0.01 M). Then a solution of initiator VA-044 (1mL, 0.25 mM) and 5 µL of the mixture of hydrophobic monomers MMA:BA (10:1 w/w) were added to the reaction vessel containing the colloid. The mixture was purged with nitrogen for 30 minutes in an ice bath under stirring. The polymerization started by placing the reaction vessel at 44ºC. 20 µL more of MMA:BA (10:1 w/w) was added in the first 5 hours (5µL, each hour, added using a microsyringe) and the polymerization continued until a total of 24 hours. The polymerization was stopped by placing the relation vessel in an ice bath in contact with oxygen. The resulting colloid was centrifuged 30 min at 15600g, the supernatant was collected and the precipitate redispersed, in the same volume, with ultra-pure water.

Preparation of N3-copolymer@Au NPs

N3-copolymer@Au NPs were prepared using a mixture of P(PEGA$_{40}$)-TTC with MR agent modified with the azide group (2 MR : 1 *N3*-MR), and the adsorption step was performed using a concentration below the CMC. To prepare the *N3*-MR@Au NPs, a solution of *N3*-MR agent (0.05 mM) and a solution of MR agent (0.05 mM) were prepared and the pH increased to 7-8 using NaOH (0.1M and 0.01M). First, 6.7 mL of *N3*-MR agent solution was added dropwise to a dispersion of Au NPs (2 mL, 6.0x10^{-9} mol NPs/L) and stirred during 2hours. Then, 13.3 mL of MR agent solution was also added dropwise and the mixture stirred overnight, at room temperature. The mixture was centrifuged 30 min at 15600g, the supernatant was collected and the precipitate redispersed in 10 mL with ultra-pure water. In the second step, the growth of the hydrophobic block in emulsion, the procedure described above for the preparation of copolymer@Au NPs was followed.

6.5.4. Functionalization of biotin with an alkyne group

Biotin was functionalized with an alkyne group following the work of Matyjaszewski *et al* [209]. The DMF used in this synthesis was dried using molecular sieves and purged with nitrogen. 0.7 g of biotin, 1.1 g of EDC and 0.035 g of DMAP were added to a 100 mL round bottom flask. The contents were vacuum dried and 49 mL of DMF was added. The flask was placed in an ice bath. 0.4 g of 3-butyn-1-ol was dissolved in 4.7 mL of DMF. This solution was added slowly to the reaction vessel using a syringe pump over a period of 2h. The mixture was allowed to thaw room temperature and was stirred under nitrogen for 2 days. After this period of time, the DMF was removed using a rotary evaporator, and the contents were dissolved into 80 mL of dichloromethane. This solution was washed once with 50 mL of an aqueous solution of NaOH (1M) and four times with 50 mL of distilled water. Dichloromethane was removed using a rotary evaporator. The resulting white-brownish solid was dissolved in THF, precipitated twice into an excess of hexane and the precipitate was filtered under reduced pressure. The alkylated biotin was dissolved in DMSO-d_6 and characterized by ^{1}H-NMR (***Annex G***).

6.5.5. Azide alkyne 1,3-cycloaddition catalyzed by Cu(I) - Click chemistry reaction

250 µL of alkylated biotin (1.67 mM, aqueous solution with 10% of DMSO to a better solubilization of biotin) was added to 10 mL of *N3*-copolymer@Au nanostructures, under stirring. Then 42 µL of $CuSO_4.5H_2O$ (2.5 mM) and 42 µL of sodium ascorbate (5 mM) were added and the mixture was stirred 24h. The determination of azide moieties in the nanostructure was not possible therefore it was admitted $8x10^{-7}$ moles (moles of *N3*-MR agent used in the adsorption), the ratios used were: 1 [azide] : 0.5 [alkyne] : 0.125 [$CuSO_4$] : 0.25 [sodium ascorbate]. After 24h, the colloidal mixture was centrifuged 30 min at 15600g, the supernatant was collected and the precipitate redispersed in 10 mL with ultra-pure water. Regarding the blank nanostructures, this procedure was carried out using biotin (without alkyne) and copolymer@Au nanostructures (without azide function), which is better explained in the discussion in the ***sub-chapter 4.4***.

6.5.6. Optical response of copolymer@Au nanostructures to Avidin

A solution of avidin and BSA (0.5mg/mL) was prepared with phosphate saline buffer (PBS, pH 7.4, 10 mM). 10 µL of BSA and avidin solution were added to 350 µL of copolymer@Au NPs or *biotin*-copolymer@Au NPs and after 10 min the visible spectra were recorded. As a control of the dilution, PBS was also added to both types of Au nanostructures.

In order to remove biotin that was adsorbed/trapped in the polymer shell, the copolymer@Au NPs (without azide moiety) mixed with alkylated biotin, $CuSO_4$ and sodium ascorbate were submitted to several washing steps by centrifugation (precipitation and redispersion), as shown in Scheme 6.1.

Scheme 6.1. Washing steps of copolymer@Au NPs mixed with alkylated biotin by centrifugation aiming non-linked biotin removal.

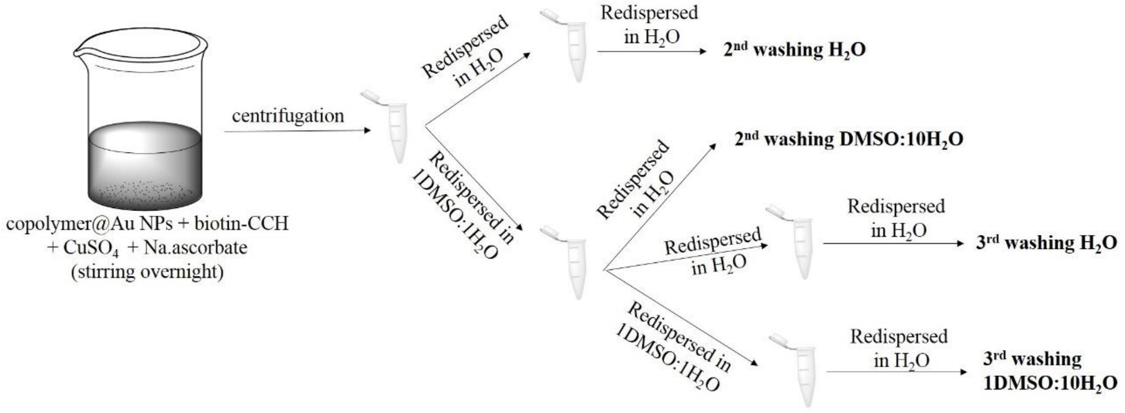
copolymer@Au NPs + biotin-CCH
+ CuSO4 + Na.ascorbate
(stirring overnight)
centrifugation
Redispersed in H2O
Redispersed in 1DMSO:1H2O
Redispersed in H2O
2nd washing H2O
Redispersed in H2O
2nd washing DMSO:10H2O
Redispersed in H2O
Redispersed in H2O
3rd washing H2O
Redispersed in 1DMSO:1H2O
Redispersed in H2O
3rd washing 1DMSO:10H2O

6.5.7. Preparation of Langmuir monolayers of copolymers

The surface pressure – area isotherms were performed at room temperature and using a teflon trough equipped with a Wilhelmy plate balance. Typically a volume of a copolymer solution prepared with ethanol:chloroform (1:10) solution was spread at the air/water interface and allowed to reach equilibrium (solvent evaporation) for 15 min before compression. Langmuir monolayers were prepared compressing the barriers at 15 cm^2/min. See Table 6.15 for experimental details.

Table 6.15. Experimental detail to prepare Langmuir monolayers of copolymers derived of P(PEGA$_{40}$)-TTC and P(AA$_2$-b-PEGA$_{40}$)-TTC.

	Experimental conditions	$\bar{M}_n$ (exp_grav) g/mol	Conc. (mg/mL)	Spreading volume (µL)
P(PEGA$_{40}$)-*b*-(MMA-*co*-BA)$_n$-TTC	**pH=8, 70ºC, 4h *[MR]/[ACPA]*=9**	31971	1.7	50
	pH=8, 70ºC, 4h *[MR]/[VA-044]*=9	34457	2.0	50
	pH=8, 44ºC, 53h *[MR]/[VA-044]*=9	26187	2.0	200
	pH=8, 44ºC, 22h *[MR]/[VA-044]*=9	23119	2.0	200
P(AA$_2$-*b*-PEGA$_{40}$)-*b*-(MMA-*co*-BA)$_{35}$-TTC pH=8, 70ºC, 4h, *[MR]/[ACPA]*=9		34055	2.0	50

6.5.8. Preparation of Langmuir monolayers to study copolymer-biotin-avidin interactions

600 µL of a biotin solution (0.4 mg/mL) was added to 34 µL of latex and stirred overnight. The mixture was dried under an air flow and then dissolved with ethanol:chloroform (1:10) solution. 50 µL of this solution (2 mg/mL of copolymer containing biotin) was spread on the air/water interface using ultra-pure water or an avidin solution as subphase. The avidin solution for subphase was prepared by diluting 500 µL of an avidin solution (0.5 mg/mL) in 500 mL of ultra-pure water. Before barriers compression started, the copolymer-biotin mixture was allowed to reach equilibrium (solvent evaporation) for 15 min. Langmuir monolayers were prepared compressing the barriers at 15 cm^2/min.

The study of copolymer-biotin-avidin interactions performed in collaboration with Oliveira's group in Brazil (University of São Paulo in São Carlos) was performed using a KSV-Nima Small KN2001. 10 µL of copolymer solution containing biotin, as described above, were spread on the air/water interface using an avidin solution (0.5mg/mL) as subphase. Before barriers compression started, the copolymer-biotin mixture was allowed to reach equilibrium (solvent evaporation) for 15 min plus a time contact of 20 min, 1h, 2h or 3h. Langmuir monolayers were prepared compressing the barriers at 10 mm^2/min.

6.5.9. Preparation of fluorescent copolymer@Au NPs following a *grafting from* strategy via macroRAFT adsorption onto previously prepared Au NPs

Preparation of a fluorescent monomer (FITC-AEM)

The fluorescent monomer (FITC-AEM) was prepared by adapting the procedure of [217]. The fluorescein isothiocyanate (FITC, 100 mg, 0.26 mmol), 2-aminoethyl methacrylate hydrochloride (AEM, 128 mg, 0.77 mmol) and trimethylamine (0.105 mL) were stirred in 12.2 mL of dry THF for 2h. HCl (1M) was added and the product was extracted with CH_2Cl_2. The organic layer was dried over anhydrous Na_2SO_4 and concentrated under reduced pressure. The product was purified by preparative thin laver chromatography using as stationary phase silica (with GF-50 as indicator), and as eluent a mixture of CH_3OH: CH_2Cl_2 (1:9). The final orange product (FITC-AEM) was dissolved in DMSO-d_6 and characterized by ^{1}H-NMR.

Preparation of fluorescent copolymer@Au NPs – 1st experiment

The fluorescent copolymer@Au NPs were prepared following a similar procedure as described in **6.5.3.**. A solution of MR agent P($PEGA_{40}$)-TTC (80 mL, 0.05 mM, pH=7.9) was added dropwise under stirring, to a dispersion of Au NPs (8 mL, 6.0x10^{-9} mol NPs/L) and stirred overnight, at room temperature. The mixture was centrifuged 30 min at 15600g and the precipitate was redispersed in half of the volume with ultra-pure water. Regarding the growth of the hydrophobic chain, the pH of the freshly prepared MR@Au colloid was adjusted to pH= 8 using NaOH (0.1 or 0.01 M). Then a solution of initiator VA-044 (1mL, 0.5 mM) and 1 mL of aqueous solution of FITC-AEM (0.2 mg/mL) were added to the reaction vessel containing 38 mL of MR@Au NPs. The mixture was purged with nitrogen for 30 minutes in an ice bath under stirring. The polymerization started by placing the reaction vessel at 70ºC and an aliquot (2 mL) was withdrawn (t_0). After 2 hours another aliquot (4 mL, t_1) was withdrawn and 64 µL of MMA:BA (10:1 w/w) was added dropwise. The polymerization continued for further 4 hours at which tome a third aliquot (16 mL, t_2) was withdrawn and 32 µL more of MMA:BA (10:1 w/w) was added dropwise. After 2 more hours, the polymerization was stopped (t_3) by placing the relation vessel in an ice bath in contact with oxygen. The final colloid and the aliquots were centrifuged twice 30 min at 15600g, the supernatant was collected and the precipitate redispersed, in the same volume, with ultra-pure water.

Preparation of fluorescent copolymer@Au NPs – 2nd experiment

MR@Au NPs were prepared as described above in the 1st experiment. Then a solution of initiator VA-044 (1mL, 0.5 mM) and 1 mL of aqueous solution of FITC-AEM (0.2 mg/mL) were added to the reaction vessel containing 38 mL of MR@Au NPs. The mixture was purged with nitrogen for 30 minutes in an ice bath under stirring. The polymerization started by placing the reaction vessel at 70ºC. After one hour the temperature was dropped until reach 44ºC. After two hours of the beginning of polymerization the mixture of hydrophobic monomers MMA:BA (10:1 w/w) were added to the reaction vessel in a controlled way. 10 µL were added each hour during 6 hours, after 7 hours 20 µL were added and the polymerization continued for 13 more hours (a total of 24 hour of polymerization). The polymerization was stopped by placing the reaction vessel in an ice bath in contact with oxygen. The ensuring colloid was centrifuged 30 min at 15600g, the supernatant was collected and the precipitate redispersed, in the same volume, with ultra-pure water, yielding the 1stCE-copolymer@Au NPs. Further chain extension was carried out. The pH of 1stCE-copolymer@Au NPs was adjusted to 8 using NaOH (0.1 or 0.01 M), 0.5 mL of initiator VA-044 (0.5 mM) and 5 µL of MMA:BA (10:1 w/w) were added. The mixture was purged with nitrogen for 30 minutes in an ice bath under stirring. The polymerization started by placing the reaction vessel at 44ºC. 5 µL of MMA:BA (10:1 w/w) were added each hour during 4 hours, after 5 hours 10 µL were added and the polymerization continued until a total of 24 hour of polymerization. The polymerization was stopped by placing the relation vessel in an ice bath in contact with oxygen. The resulting colloid was centrifuged 30 min at 15600g, the supernatant was collected and the precipitate redispersed, in the same volume, with ultra-pure water, yielding the 2ndCE-copolymer@Au NPs.

Optical response of non-linked biotin 1stCE-copolymer@Au nanostructures to Avidin

A solution of biotin (0.3 mL, 1.67 mM) was added to 12 mL of 1stCE-copolymer@Au nanostructures and stirred overnight. The colloid was centrifuged twice at 15600g 30 min and redispersed in 12 mL with ultra-pure water. A solution of avidin and BSA (0.5mg/mL) was prepared with phosphate saline buffer (PBS) pH 7.4 (10 mM). 14.25 µL, 28.5 µL or 57 µL of PBS, BSA or avidin solution were added to 500 µL of colloidal solution of *non-linked biotin* 1stCE-copolymer@Au nanostructures and after 10 min the visible spectra were recorded.

REFERENCES

1. M.A. Martins, S.O. Pereira, and T. Trindade (2015) Inorganic Nanoparticles in New Upcoming Biomedical Applications, In: van Herk, A., Forcada, J., and Pastorin, G. (eds.) Controlled Release Systems: Advances in Nanobottles and Active Nanoparticles, pp. 197–228 Pan Stanford, Boca Raton.
2. A.M. Dennis, J.B. Delehanty, and I.L. Medintz (2016) Emerging Physicochemical Phenomena along with New Opportunities at the Biomolecular-Nanoparticle Interface., The journal of physical chemistry letters. 2139–2150.
3. E.C. Dreaden, A.M. Alkilany, X. Huang, C.J. Murphy, and M. a El-Sayed (2012) The golden age: gold nanoparticles for biomedicine, Chem. Soc. Rev. 41, 2740–2779.
4. V. Biju (2014) Chemical modifications and bioconjugate reactions of nanomaterials for sensing, imaging, drug delivery and therapy, Chem. Soc. Rev. 43, 744–764.
5. K. Saha, S.S. Agasti, C. Kim, X. Li, and V.M. Rotello (2012) Gold Nanoparticles in Chemical and Biological Sensing, Chemical Reviews. 112, 2739–2779.
6. K.E. Sapsford, W.R. Algar, L. Berti, K.B. Gemmill, B.J. Casey, E. Oh, M.H. Stewart, and I.L. Medintz (2013) Functionalizing nanoparticles with biological molecules: Developing chemistries that facilitate nanotechnology, Chemical Reviews. 113, 1904–2074.
7. L.M. Liz-Marzán (2004) Nanometals: Formation and color, Materials Today. 7, 26–31.
8. Y.-C. Yeh, B. Creran, and V.M. Rotello (2012) Gold nanoparticles: preparation, properties, and applications in bionanotechnology, Nanoscale. 4, 1871–1880.
9. T.L. Doane and C. Burda (2012) The unique role of nanoparticles in nanomedicine: imaging, drug delivery and therapy, Chemical Society Reviews. 41, 2885.
10. X. Huang, S. Neretina, and M. a. El-Sayed (2009) Gold Nanorods: From Synthesis and Properties to Biological and Biomedical Applications, Advanced Materials. 21, 4880–4910.
11. P.N. Njoki, I.-I.S. Lim, D. Mott, H.-Y. Park, B. Khan, S. Mishra, R. Sujakumar, J. Luo, and C.-J. Zhong (2007) Size Correlation of Optical and Spectroscopic Properties for Gold Nanoparticles, Journal of Physical Chemistry C. 111, 14664–14669.
12. J. Pérez-Juste, I. Pastoriza-Santos, L.M. Liz-Marzán, and P. Mulvaney (2005) Gold nanorods: Synthesis, characterization and applications, Coordination Chemistry Reviews. 249, 1870–1901.
13. E. Dulkeith, A.C. Morteani, T. Niedereichholz, T.A. Klar, J. Feldmann, S.A. Levi, F.C.J.M. van Veggel, D.N. Reinhoudt, M. Möller, and D.I. Gittins (2002) Fluorescence Quenching of Dye Molecules near Gold Nanoparticles: Radiative and Nonradiative Effects, Physical Review Letters. 89, 203002.
14. Z. Gueroui and A. Libchaber (2004) Single-Molecule Measurements of Gold-Quenched Quantum Dots, Physical Review Letters. 93, 166108.
15. T.L. Jennings, M.P. Singh, and G.F. Strouse (2006) Fluorescent Lifetime Quenching near d = 1.5 nm Gold Nanoparticles: Probing NSET Validity, Journal of the American Chemical Society. 128, 5462–5467.
16. K.E. Sapsford, L. Berti, and I.L. Medintz (2006) Materials for Fluorescence Resonance Energy Transfer Analysis: Beyond Traditional Donor–Acceptor Combinations, Angewandte Chemie International Edition. 45, 4562–4589.
17. C.S. Yun, A. Javier, T. Jennings, M. Fisher, S. Hira, S. Peterson, B. Hopkins, N.O. Reich, and G.F. Strouse (2005) Nanometal Surface Energy Transfer in Optical Rulers, Breaking the FRET Barrier, Journal of the American Chemical Society. 127, 3115–3119.

18. B. Valeur (2001) Molecular Fluorescence, Wiley-VCH Verlag GmbH, Weinheim, FRG.

19. P.C. Ray, G.K. Darbha, A. Ray, J. Walker, and W. Hardy (2007) Gold Nanoparticle Based FRET for DNA Detection, Plasmonics. 2, 173–183.

20. E. Boisselier and D. Astruc (2009) Gold nanoparticles in nanomedicine: preparations, imaging, diagnostics, therapies and toxicity, Chemical Society Reviews. 38, 1759.

21. G. Doria, J. Conde, B. Veigas, L. Giestas, C. Almeida, M. Assunção, J. Rosa, and P. V Baptista (2012) Noble Metal Nanoparticles for Biosensing Applications, Sensors. 12, 1657–1687.

22. K. Aslan and V.H. Pérez-Luna (2006) Nonradiative Interactions between Biotin-Functionalized Gold Nanoparticles and Fluorophore-Labeled Antibiotin, Plasmonics. 1, 111–119.

23. N. Kato and F. Caruso (2005) Homogeneous, competitive fluorescence quenching immunoassay based on gold nanoparticle/polyelectrolyte coated latex particles, Journal of Physical Chemistry B. 109, 19604–19612.

24. B. Dubertret, M. Calame, and a J. Libchaber (2001) Single-mismatch detection using gold-quenched fluorescent oligonucleotides., Nature biotechnology. 19, 365–70.

25. J.M. Obliosca, P.-C. Wang, and F.-G. Tseng (2012) Probing quenched dye fluorescence of Cy3-DNA-Au-nanoparticle hybrid conjugates using solution and array platforms., Journal of colloid and interface science. 371, 34–41.

26. M.-C. Daniel and D. Astruc (2004) Gold nanoparticles: assembly, supramolecular chemistry, quantum-size-related properties, and applications toward biology, catalysis, and nanotechnology., Chemical reviews. 104, 293–346.

27. F. Dumur, A. Guerlin, E. Dumas, D. Bertin, D. Gigmes, and C.R. Mayer (2011) Controlled spontaneous generation of gold nanoparticles assisted by dual reducing and capping agents, Gold Bulletin. 44, 119–137.

28. A. Jimenez-Ruiz, P. Perez-Tejeda, E. Grueso, P.M. Castillo, and R. Prado-Gotor (2015) Nonfunctionalized Gold Nanoparticles: Synthetic Routes and Synthesis Condition Dependence, Chemistry - A European Journal. 21, 9596–9609.

29. J. Turkevich, P.C. Stevenson, and J. Hillier (1951) A study of the nucleation and growth processes in the synthesis of colloidal gold, Discussions of the Faraday Society. 11, 55–57.

30. B. V. Enustun and J. Turkevich (1963) Coagulation of Colloidal Gold, Journal of the American Chemical Society. 85, 3317–3328.

31. J.W. Park and J.S. Shumaker-Parry (2014) Structural study of citrate layers on gold nanoparticles: Role of intermolecular interactions in stabilizing nanoparticles, Journal of the American Chemical Society. 136, 1907–1921.

32. N.G. Bastús, J. Comenge, and V. Puntes (2011) Kinetically Controlled Seeded Growth Synthesis of Citrate-Stabilized Gold Nanoparticles of up to 200 nm: Size Focusing versus Ostwald Ripening, Langmuir. 27, 11098–11105.

33. C. Ziegler and A. Eychmüller (2011) Seeded Growth Synthesis of Uniform Gold Nanoparticles with Diameters of 15−300 nm, The Journal of Physical Chemistry C. 115, 4502–4506.

34. M. Brust, M. Walker, D. Bethell, D.J. Schiffrin, and R. Whyman (1994) Synthesis of thiol-derivatised gold nanoparticles in a two-phase Liquid?Liquid system, Journal of the Chemical Society, Chemical Communications. 801.

35. S.R.K. Perala and S. Kumar (2013) On the Mechanism of Metal Nanoparticle Synthesis in the Brust–Schiffrin Method, Langmuir. 29, 9863–9873.

36. D.I. Gittins and F. Caruso (2001) Spontaneous phase transfer of nanoparticulate metals from organic to aqueous media, Angewandte Chemie - International Edition. 40, 3001–3004.

37. V.J. Gandubert and R.B. Lennox (2005) Assessment of 4-(dimethylamino)pyridine as a capping agent for gold nanoparticles, Langmuir. 21, 6532–6539.

38. I. Hussain, S. Graham, Z. Wang, B. Tan, D.C. Sherrington, S.P. Rannard, A.I. Cooper, and M. Brust (2005) Size-Controlled Synthesis of Near-Monodisperse Gold Nanoparticles in the 1−4 nm Range Using Polymeric Stabilizers, Journal of the American Chemical Society. 127, 16398–16399.

39. S.E. Lohse, J. a Dahl, and J.E. Hutchison (2010) Direct Synthesis of Large Water-Soluble Functionalized Gold Nanoparticles Using Bunte Salts as Ligand Precursors, Langmuir. 26, 7504–7511.

40. N.R. Jana, L. Gearheart, and C.J. Murphy (2001) Seeding Growth for Size Control of 5−40 nm Diameter Gold Nanoparticles, Langmuir. 17, 6782–6786.

41. S. Sistach, K. Rahme, N. Pérignon, J.-D. Marty, N.L. Viguerie, F. Gauffre, and C. Mingotaud (2008) Bolaamphiphile Surfactants as Nanoparticle Stabilizers: Application to Reversible Aggregation of Gold Nanoparticles, Chemistry of Materials. 20, 1221–1223.

42. J. Keilitz, M.R. Radowski, J. Marty, R. Haag, F. Gauffre, and C. Mingotaud (2008) Dendritic Polymers with a Core−Multishell Architecture: A Versatile Tool for the Stabilization of Nanoparticles, Chemistry of Materials. 20, 2423–2425.

43. S. Wang, K. Qian, X. Bi, and W. Huang (2009) Influence of Speciation of Aqueous HAuCl 4 on the Synthesis, Structure, and Property of Au Colloids, The Journal of Physical Chemistry C. 113, 6505–6510.

44. X. Ji, X. Song, J. Li, Y. Bai, W. Yang, and X. Peng (2007) Size control of gold nanocrystals in citrate reduction: the third role of citrate., Journal of the American Chemical Society. 129, 13939–48.

45. L. Zhao, D. Jiang, Y. Cai, X. Ji, R. Xie, and W. Yang (2012) Tuning the size of gold nanoparticles in the citrate reduction by chloride ions, Nanoscale. 4, 5071.

46. S.E. Lohse, N.D. Burrows, L. Scarabelli, L.M. Liz-Marzán, and C.J. Murphy (2014) Anisotropic noble metal nanocrystal growth: The role of halides, Chemistry of Materials. 26, 34–43.

47. N. Li, P. Zhao, and D. Astruc (2014) Anisotropic Gold Nanoparticles: Synthesis, Properties, Applications, and Toxicity, Angewandte Chemie International Edition. 53, 1756–1789.

48. N.R. Jana, L. Gearheart, and C.J. Murphy (2001) Seed-Mediated Growth Approach for Shape-Controlled Synthesis of Spheroidal and Rod-like Gold Nanoparticles Using a Surfactant Template, Advanced Materials. 13, 1389–1393.

49. N.R. Jana, L. Gearheart, and C.J. Murphy (2001) Wet Chemical Synthesis of High Aspect Ratio Cylindrical Gold Nanorods, The Journal of Physical Chemistry B. 105, 4065–4067.

50. J. Gao, C.M. Bender, and C.J. Murphy (2003) Dependence of the Gold Nanorod Aspect Ratio on the Nature of the Directing Surfactant in Aqueous Solution, Langmuir. 19, 9065–9070.

51. B. Nikoobakht and M.A. El-Sayed (2003) Preparation and Growth Mechanism of Gold Nanorods (NRs) Using Seed-Mediated Growth Method, Chemistry of Materials. 15, 1957–1962.

52. A. Gole and C.J. Murphy (2004) Seed-Mediated Synthesis of Gold Nanorods: Role of the Size and Nature of the Seed, Chemistry of Materials. 16, 3633–3640.

53. C.J. Murphy, L.B. Thompson, D.J. Chernak, J.A. Yang, S.T. Sivapalan, S.P. Boulos, J. Huang, A.M. Alkilany, and P.N. Sisco (2011) Gold nanorod crystal growth: From seed-mediated synthesis to nanoscale sculpting, Current Opinion in Colloid & Interface Science. 16, 128–134.

54. X. Ye, Y. Gao, J. Chen, D.C. Reifsnyder, C. Zheng, and C.B. Murray (2013) Seeded growth of monodisperse gold nanorods using bromide-free surfactant mixtures, Nano Letters. 13, 2163–2171.

55. S. Zeng, K.-T. Yong, I. Roy, X.-Q. Dinh, X. Yu, and F. Luan (2011) A Review on Functionalized Gold Nanoparticles for Biosensing Applications, Plasmonics. 6, 491–506.

56. G. Wang, Y. Wang, L. Chen, and J. Choo (2010) Nanomaterial-assisted aptamers for optical sensing, Biosensors and Bioelectronics. 25, 1859–1868.

57. R. Wilson (2008) The use of gold nanoparticles in diagnostics and detection., Chemical Society reviews. 37, 2028–2045.

58. Z. Yuan, C.-C. Hu, H.-T. Chang, and C. Lu (2016) Gold nanoparticles as sensitive optical probes, The Analyst. 141, 1611–1626.

59. K. Sato, K. Hosokawa, and M. Maeda (2003) Rapid aggregation of gold nanoparticles induced by non-cross-linking DNA hybridization, Journal of the American Chemical Society. 125, 8102–8103.

60. J.J. Storhoff, A.A. Lazarides, R.C. Mucic, C.A. Mirkin, R.L. Letsinger, and G.C. Schatz (2000) What Controls the Optical Properties of DNA-Linked Gold Nanoparticle Assemblies?, Journal of the American Chemical Society. 122, 4640–4650.

61. A. Kohut, A. Voronov, and W. Peukert (2005) Organization of Functionalized Gold Nanoparticles by Controlled Protein Interactions, Particle & Particle Systems Characterization. 22, 329–335.

62. K. Aslan, C.C. Luhrs, and V.H. Pérez-Luna (2004) Controlled and Reversible Aggregation of Biotinylated Gold Nanoparticles with Streptavidin, The Journal of Physical Chemistry B. 108, 15631–15639.

63. K. Aslan and V.H. Pérez-Luna (2004) Quenched Emission of Fluorescence by Ligand Functionalized Gold Nanoparticles, Journal of Fluorescence. 14, 401–405.

64. N.T.K. Thanh and L. a. W. Green (2010) Functionalisation of nanoparticles for biomedical applications, Nano Today. 5, 213–230.

65. J. Cho and F. Caruso (2005) Investigation of the Interactions between Ligand-Stabilized Gold Nanoparticles and Polyelectrolyte Multilayer Films, Chemistry of Materials. 17, 4547–4553.

66. D.I. Gittins and F. Caruso (2001) Tailoring the Polyelectrolyte Coating of Metal Nanoparticles, The Journal of Physical Chemistry B. 105, 6846–6852.

67. G. Schneider and G. Decher (2004) From Functional Core/Shell Nanoparticles Prepared via Layer-by-Layer Deposition to Empty Nanospheres, Nano Letters. 4, 1833–1839.

68. G. Schneider and G. Decher (2008) Functional core/shell nanoparticles via layer-by-layer assembly. Investigation of the experimental parameters for controlling particle aggregation and for enhancing dispersion stability, Langmuir. 24, 1778–1789.

69. N. Higashi, T. Takagi, and T. Koga (2010) Layer-by-layer fabrication of well-packed gold nanoparticle assemblies guided by a β-sheet peptide network, Polymer Journal. 42, 95–99.

70. M. Beija, J.-D. Marty, and M. Destarac (2011) Thermoresponsive poly(N-vinyl caprolactam)-coated gold nanoparticles: sharp reversible response and easy tunability, Chemical Communications. 47, 2826.

71. J. Shan and H. Tenhu (2007) Recent advances in polymer protected gold nanoparticles: synthesis, properties and applications., Chemical communications (Cambridge, England). 4580–4598.

72. L.M. Zanoli, R. D'Agata, and G. Spoto (2012) Functionalized gold nanoparticles for ultrasensitive DNA detection, Analytical and Bioanalytical Chemistry. 402, 1759–1771.

73. D. Li, Q. He, and J. Li (2009) Smart core/shell nanocomposites: Intelligent polymers modified gold nanoparticles, Advances in Colloid and Interface Science. 149, 28–38.

74. P.K. Deshmukh, K.P. Ramani, S.S. Singh, A.R. Tekade, V.K. Chatap, G.B. Patil, and S.B. Bari (2013) Stimuli-sensitive layer-by-layer (LbL) self-assembly systems: Targeting and biosensory applications, Journal of Controlled Release. 166, 294–306.

75. F. Caruso (1998) Nanoengineering of Inorganic and Hybrid Hollow Spheres by Colloidal Templating, Science. 282, 1111–1114.

76. S.O. Pereira, A. Barros-Timmons, and T. Trindade (2014) Biofunctionalisation of colloidal gold nanoparticles via polyelectrolytes assemblies, Colloid and Polymer Science. 292, 33–50.

77. K.S. Mayya, B. Schoeler, and F. Caruso (2003) Preparation and Organization of Nanoscale Polyelectrolyte-Coated Gold Nanoparticles, Advanced Functional Materials. 13, 183–188.

78. K. Ariga, J.P. Hill, and Q. Ji (2007) Layer-by-layer assembly as a versatile bottom-up nanofabrication technique for exploratory research and realistic application, Physical Chemistry Chemical Physics. 9, 2319.

79. M. Schönhoff (2003) Self-assembled polyelectrolyte multilayers, Current Opinion in Colloid & Interface Science. 8, 86–95.

80. J.J. Richardson, M. Bjornmalm, and F. Caruso (2015) Technology-driven layer-by-layer assembly of nanofilms, Science. 348, aaa2491–aaa2491.

81. G. Decher and J.-D. Hong (1991) Buildup of ultrathin multilayer films by a self-assembly process, 1 consecutive adsorption of anionic and cationic bipolar amphiphiles on charged surfaces, Makromolekulare Chemie. Macromolecular Symposia. 46, 321–327.

82. G. Decher and J.D. Hong (1991) Buildup of Ultrathin Multilayer Films by a Self-Assembly Process: II. Consecutive Adsorption of Anionic and Cationic Bipolar Amphiphiles and Polyelectrolytes on Charged Surfaces, Berichte der Bunsengesellschaft für physikalische Chemie. 95, 1430–1434.

83. J.R. Siqueira, L. Caseli, F.N. Crespilho, V. Zucolotto, and O.N. Oliveira (2010) Immobilization of biomolecules on nanostructured films for biosensing, Biosensors and Bioelectronics. 25, 1254–1263.

84. K. Ariga, Y. Yamauchi, G. Rydzek, Q. Ji, Y. Yonamine, K.C.-W. Wu, and J.P. Hill (2014) Layer-by-layer Nanoarchitectonics: Invention, Innovation, and Evolution, Chemistry Letters. 43, 36–68.

85. P. Gentile, I. Carmagnola, T. Nardo, and V. Chiono (2015) Layer-by-layer assembly for biomedical applications in the last decade, Nanotechnology. 26, 422001.

86. M. Ferreira, P. a Fiorito, O.N. Oliveira, and S.I. Córdoba de Torresi (2004) Enzyme-mediated amperometric biosensors prepared with the Layer-by-Layer (LbL) adsorption technique, Biosensors and Bioelectronics. 19, 1611–1615.

87. L. Caseli, D.S. dos Santos, R.F. Aroca, and O.N. Oliveira (2009) Controlled fabrication of gold nanoparticles biomediated by glucose oxidase immobilized on chitosan layer-by-layer films, Materials Science and Engineering: C. 29, 1687–1690.

88. J.M.G. Cowie and V. Arrighi (2007) Polymers: chemistry and physics of modern materials, CRC Press.

89. C. Barner-Kowollik (2008) Handbook of RAFT polymerization, Wiley-VCH.

90. H. Warson (2001) Fundamentals of Polymer Chemistry, In: Warson, H. and Finch, C.A. (eds.) Applications of Synthetic Resin Latices , Volume 1, Fundamental Chemistry of Latices & Applications in Adhesives, John Wiley and Sons.

91. N. Karak (2009) Fundamentals of polymers: raw materials to finish products, PHI Learning Pvt. Ltd.

92. P.A. Lovell and M.S. El-Aasser (1997) Emulsion polymerization and emulsion polymers, Wiley.

93. S.C. Thickett and R.G. Gilbert (2007) Emulsion polymerization: State of the art in kinetics and mechanisms, Polymer. 48, 6965–6991.

94. A.D. Jenkins, R.G. Jones, and G. Moad (2009) Terminology for reversible-deactivation radical polymerization previously called “controlled” radical or “living” radical polymerization (IUPAC Recommendations 2010), Pure and Applied Chemistry. 82, 483–491.

95. W. a. Braunecker and K. Matyjaszewski (2007) Controlled/living radical polymerization: Features, developments, and perspectives, Progress in Polymer Science. 32, 93–146.

96. G. Moad, E. Rizzardo, and S.H. Thang (2005) Living Radical Polymerization by the RAFT Process, Australian Journal of Chemistry. 58, 379.

97. G. Moad, E. Rizzardo, and S.H. Thang (2006) Living Radical Polymerization by the RAFT Process—A First Update, Australian Journal of Chemistry. 59, 669.

98. A. York, S. Kirkland, and C. McCormick (2008) Advances in the synthesis of amphiphilic block copolymers via RAFT polymerization: Stimuli-responsive drug and gene delivery☆, Advanced Drug Delivery Reviews. 60, 1018–1036.

99. M. Beija, J.-D. Marty, and M. Destarac (2011) RAFT/MADIX polymers for the preparation of polymer/inorganic nanohybrids, Progress in Polymer Science. 36, 845–886.

100. J. Chiefari, Y.K. (Bill) Chong, F. Ercole, J. Krstina, J. Jeffery, T.P.T. Le, R.T.A. Mayadunne, G.F. Meijs, C.L. Moad, G. Moad, E. Rizzardo, and S.H. Thang (1998) Living Free-Radical Polymerization by Reversible Addition−Fragmentation Chain Transfer: The RAFT Process, Macromolecules. 31, 5559–5562.

101. P. Le Tam, G. Moad, E. Rizzardo, S. Thang, T.P. Le, S.H. Thang, T. Le, J.P. Le, L.T. Phuong, M. Graeme, R. Ezio, and T.S. Hoa (1998), Synthesis of di:thioester group containing polymer with controlled structure - by addition polymerisation using di:thioester chain transfer agent, vinyl monomers and free radical source.

102. P. Corpart, D. Charmot, T. Biadatti, S. Zard, and D. Michelet (1998), Block polymer synthesis - by controlled radical polymerisation, PCT Int. Pat. Appl. WO 9858974.

103. G. Moad, J. Chiefari, (Bill) Y. K. Chong, J. Krstina, R.T.A. Mayadunne, A. Postma, E.

Rizzardo, and S.H. Thang (2000) Living free radical polymerization with reversible addition–fragmentation chain transfer (the life of RAFT), Polymer International. 49, 993–1001.

104. A.B. Lowe and C.L. McCormick (2007) Reversible addition–fragmentation chain transfer (RAFT) radical polymerization and the synthesis of water-soluble (co)polymers under homogeneous conditions in organic and aqueous media, Progress in Polymer Science. 32, 283–351.

105. A. Favier and M.-T. Charreyre (2006) Experimental Requirements for an Efficient Control of Free-Radical Polymerizations via the Reversible Addition-Fragmentation Chain Transfer (RAFT) Process, Macromolecular Rapid Communications. 27, 653–692.

106. S. Sistach, M. Beija, V. Rahal, A. Brûlet, J.-D. Marty, M. Destarac, and C. Mingotaud (2010) Thermoresponsive Amphiphilic Diblock Copolymers Synthesized by MADIX/RAFT: Properties in Aqueous Solutions and Use for the Preparation and Stabilization of Gold Nanoparticles, Chemistry of Materials. 22, 3712–3724.

107. Y. Mitsukami, M.S. Donovan, A.B. Lowe, and C.L. McCormick (2001) Water-Soluble Polymers. 81. Direct Synthesis of Hydrophilic Styrenic-Based Homopolymers and Block Copolymers in Aqueous Solution via RAFT, Macromolecules. 34, 2248–2256.

108. C.L. McCormick and A.B. Lowe (2004) Aqueous RAFT Polymerization: Recent Developments in Synthesis of Functional Water-Soluble (Co)polymers with Controlled Structures †, Accounts of Chemical Research. 37, 312–325.

109. G. Gody, T. Maschmeyer, P.B. Zetterlund, and S. Perrier (2014) Pushing the Limit of the RAFT Process: Multiblock Copolymers by One-Pot Rapid Multiple Chain Extensions at Full Monomer Conversion, Macromolecules. 47, 3451–3460.

110. C.J. Ferguson, R.J. Hughes, B.T.T. Pham, B.S. Hawkett, R.G. Gilbert, A.K. Serelis, and C.H. Such (2002) Effective ab Initio Emulsion Polymerization under RAFT Control, Macromolecules. 35, 9243–9245.

111. P.B. Zetterlund, Y. Kagawa, and M. Okubo (2008) Controlled/Living Radical Polymerization in Dispersed Systems, Chemical Reviews. 108, 3747–3794.

112. J. Rieger, G. Osterwinter, C. Bui, F. Stoffelbach, and B. Charleux (2009) Surfactant-Free Controlled/Living Radical Emulsion (Co)polymerization of n -Butyl Acrylate and Methyl Methacrylate via RAFT Using Amphiphilic Poly(ethylene oxide)-Based Trithiocarbonate Chain Transfer Agents, Macromolecules. 42, 5518–5525.

113. X. Zhang, S. Boissé, W. Zhang, P. Beaunier, F. D’Agosto, J. Rieger, and B. Charleux (2011) Well-Defined Amphiphilic Block Copolymers and Nano-objects Formed in Situ via RAFT-Mediated Aqueous Emulsion Polymerization, Macromolecules. 44, 4149–4158.

114. W. Zhang, F. D’Agosto, P.-Y. Dugas, J. Rieger, and B. Charleux (2013) RAFT-mediated one-pot aqueous emulsion polymerization of methyl methacrylate in presence of poly(methacrylic acid-co-poly(ethylene oxide) methacrylate) trithiocarbonate macromolecular chain transfer agent, Polymer. 54, 2011–2019.

115. B.S. Sumerlin, A.B. Lowe, P. a. Stroud, P. Zhang, M.W. Urban, and C.L. McCormick (2003) Modification of Gold Surfaces with Water-Soluble (Co)polymers Prepared via Aqueous Reversible Addition−Fragmentation Chain Transfer (RAFT) Polymerization †, Langmuir. 19, 5559–5562.

116. A.-S. Duwez, P. Guillet, C. Colard, J.-F. Gohy, and C.-A. Fustin (2006) Dithioesters and Trithiocarbonates as Anchoring Groups for the “Grafting-To” Approach, Macromolecules. 39, 2729–2731.

117. K. Kusolkamabot, P. Sae-Ung, N. Niamnont, K. Wongravee, M. Sukwattanasinitt, and V.P. Hoven (2013) Poly(N -isopropylacrylamide)-stabilized gold nanoparticles in combination with tricationic branched phenylene-ethynylene fluorophore for protein identification, Langmuir. 29, 12317–12327.

118. Z. Zhang, S. Maji, A.B.D.F. Antunes, R. De Rycke, Q. Zhang, R. Hoogenboom, and B.G. De Geest (2013) Salt Plays a Pivotal Role in the Temperature-Responsive Aggregation and Layer-by-Layer Assembly of Polymer-Decorated Gold Nanoparticles, Chemistry of Materials. 25, 4297–4303.

119. C. Durand-Gasselin, R. Koerin, J. Rieger, N. Lequeux, and N. Sanson (2014) Colloidal stability of zwitterionic polymer-grafted gold nanoparticles in water, Journal of Colloid and Interface Science. 434, 188–194.

120. M. Takara, M. Toyoshima, H. Seto, Y. Hoshino, and Y. Miura (2014) Polymer-modified gold nanoparticles via RAFT polymerization: a detailed study for a biosensing application, Polym. Chem. 5, 931–939.

121. N. Chen, X. Xiang, and P. a Heiden (2013) Tuning thermoresponsive behavior of diblock copolymers and their gold core hybrids. Part 2. How properties change depending on block attachment to gold nanoparticles, Journal of Colloid and Interface Science. 396, 39–46.

122. C. Boyer, M.R. Whittaker, K. Chuah, J. Liu, and T.P. Davis (2010) Modulation of the Surface Charge on Polymer-Stabilized Gold Nanoparticles by the Application of an External Stimulus, Langmuir. 26, 2721–2730.

123. M. Beija, E. Palleau, S. Sistach, X. Zhao, L. Ressier, C. Mingotaud, M. Destarac, and J.-D. Marty (2010) Control of the catalytic properties and directed assembly on surfaces of MADIX/RAFT polymer-coated gold nanoparticles by tuning polymeric shell charge, Journal of Materials Chemistry. 20, 9433.

124. M.I. Gibson, D. Paripovic, and H.-A. Klok (2010) Size-Dependent LCST Transitions of Polymer-Coated Gold Nanoparticles: Cooperative Aggregation and Surface Assembly, Advanced Materials. 22, 4721–4725.

125. M.I. Gibson, M. Danial, and H.-A. Klok (2011) Sequentially Modified, Polymer-Stabilized Gold Nanoparticle Libraries: Convergent Synthesis and Aggregation Behavior, ACS Combinatorial Science. 13, 286–297.

126. J.W. Hotchkiss, A.B. Lowe, and S.G. Boyes (2007) Surface Modification of Gold Nanorods with Polymers Synthesized by Reversible Addition−Fragmentation Chain Transfer Polymerization, Chemistry of Materials. 19, 6–13.

127. C. Boyer, M.R. Whittaker, C. Nouvel, and T.P. Davis (2010) Synthesis of Hollow Polymer Nanocapsules Exploiting Gold Nanoparticles as Sacrificial Templates, Macromolecules. 43, 1792–1799.

128. Y. Liu and X. Wang (2011) Recent advances in block copolymer-assisted synthesis of supramolecular inorganic/organic hybrid colloids, Polymer Chemistry. 2, 2741.

129. M. Grzelczak, A. Sánchez-Iglesias, and L.M. Liz-Marzán (2014) A general approach toward polymer-coated plasmonic nanostructures, CrystEngComm. 16, 9425–9429.

130. A.B. Lowe, B.S. Sumerlin, M.S. Donovan, and C.L. McCormick (2002) Facile Preparation of Transition Metal Nanoparticles Stabilized by Well-Defined (Co)polymers Synthesized via Aqueous Reversible Addition-Fragmentation Chain Transfer Polymerization, Journal of the American Chemical Society. 124, 11562–11563.

131. H.J. Jeon, D.H. Go, S. Choi, K.M. Kim, J.Y. Lee, D.J. Choo, H.-O. Yoo, J.M. Kim, and J.

Kim (2008) Synthesis of poly(ethylene oxide)-based thermoresponsive block copolymers by RAFT radical polymerization and their uses for preparation of gold nanoparticles, Colloids and Surfaces A: Physicochemical and Engineering Aspects. 317, 496–503.

132. Z.L. Wang, J.T. Xu, B.Y. Du, and Z.Q. Fan (2011) Facile fabrication of amphiphilic gold nanoparticles with V-shaped brushes from block copolymers with a trithiocarbonate group as the junction, Journal of Colloid and Interface Science. 360, 350–354.

133. A. Glaria, M. Beija, R. Bordes, M. Destarac, and J.-D. Marty (2013) Understanding the Role of ω-End Groups and Molecular Weight in the Interaction of PNIPAM with Gold Surfaces, Chemistry of Materials. 25, 1868–1876.

134. L. Wu, U. Glebe, and A. Böker (2015) Surface-initiated controlled radical polymerizations from silica nanoparticles, gold nanocrystals, and bionanoparticles, Polym. Chem. 6, 5143–5184.

135. J. Raula, J. Shan, M. Nuopponen, A. Niskanen, H. Jiang, E.I. Kauppinen, and H. Tenhu (2003) Synthesis of Gold Nanoparticles Grafted with a Thermoresponsive Polymer by Surface-Induced Reversible-Addition-Fragmentation Chain-Transfer Polymerization, Langmuir. 19, 3499–3504.

136. D. Nguyen, H.S. Zondanos, J.M. Farrugia, A.K. Serelis, C.H. Such, and B.S. Hawkett (2008) Pigment Encapsulation by Emulsion Polymerization Using Macro-RAFT Copolymers, Langmuir. 24, 2140–2150.

137. S.I. Ali, J.P.A. Heuts, B.S. Hawkett, and A.M. van Herk (2009) Polymer Encapsulated Gibbsite Nanoparticles: Efficient Preparation of Anisotropic Composite Latex Particles by RAFT-Based Starved Feed Emulsion Polymerization, Langmuir. 25, 10523–10533.

138. M.A. Mballa Mballa, S.I. Ali, J.P. Heuts, and A.M. van Herk (2012) Control of the anisotropic morphology of latex nanocomposites containing single montmorillonite clay particles prepared by conventional and reversible addition-fragmentation chain transfer based emulsion polymerization, Polymer International. 61, 861–865.

139. W. Zhong, J.N. Zeuna, and J.P. Claverie (2012) A versatile encapsulation method of noncovalently modified carbon nanotubes by RAFT polymerization, Journal of Polymer Science Part A: Polymer Chemistry. 50, 4403–4407.

140. D. Nguyen, C.H. Such, and B.S. Hawkett (2013) Polymer coating of carboxylic acid functionalized multiwalled carbon nanotubes via reversible addition-fragmentation chain transfer mediated emulsion polymerization, Journal of Polymer Science Part A: Polymer Chemistry. 51, 250–257.

141. V.T. Huynh, D. Nguyen, C.H. Such, and B.S. Hawkett (2015) Polymer coating of graphene oxide via reversible addition-fragmentation chain transfer mediated emulsion polymerization, Journal of Polymer Science Part A: Polymer Chemistry. 53, 1413–1421.

142. J. Garnier, J. Warnant, P. Lacroix-Desmazes, P.-E. Dufils, J. Vinas, Y. Vanderveken, and A.M. van Herk (2012) An Emulsifier-Free RAFT-Mediated Process for the Efficient Synthesis of Cerium Oxide/Polymer Hybrid Latexes, Macromolecular Rapid Communications. 33, 1388–1392.

143. N. Zgheib, J.-L. Putaux, A. Thill, E. Bourgeat-Lami, F. D’Agosto, and M. Lansalot (2013) Cerium oxide encapsulation by emulsion polymerization using hydrophilic macroRAFT agents, Polym. Chem. 4, 607–614.

144. J. Garnier, J. Warnant, P. Lacroix-Desmazes, P.-E. Dufils, J. Vinas, and A. van Herk (2013) Sulfonated macro-RAFT agents for the surfactant-free synthesis of cerium oxide-based

hybrid latexes, Journal of Colloid and Interface Science. 407, 273–281.

145. P. Das, W. Zhong, and J.P. Claverie (2011) Copolymer nanosphere encapsulated CdS quantum dots prepared by RAFT copolymerization: synthesis, characterization and mechanism of formation, Colloid and Polymer Science. 289, 1519–1533.

146. P. Das and J.P. Claverie (2012) Synthesis of single-core and multiple-core core-shell nanoparticles by RAFT emulsion polymerization: Lead sulfide-copolymer nanocomposites, Journal of Polymer Science Part A: Polymer Chemistry. 50, 2802–2808.

147. J. Warnant, J. Garnier, A. van Herk, P.-E. Dufils, J. Vinas, and P. Lacroix-Desmazes (2013) A CeO2/PVDC hybrid latex mediated by a phosphonated macro-RAFT agent, Polymer Chemistry. 4, 5656.

148. W.H. Binder and R. Sachsenhofer (2007) “Click” Chemistry in Polymer and Materials Science, Macromolecular Rapid Communications. 28, 15–54.

149. W.H. Binder and R. Sachsenhofer (2008) “Click” Chemistry in Polymer and Material Science: An Update, Macromolecular Rapid Communications. 29, 952–981.

150. P.L. Golas and K. Matyjaszewski (2010) Marrying click chemistry with polymerization: expanding the scope of polymeric materials., Chemical Society reviews. 39, 1338–1354.

151. J. a Opsteen and J.C.M. van Hest (2005) Modular synthesis of block copolymers via cycloaddition of terminal azide and alkyne functionalized polymers, Chemical Communications. 57.

152. D. Quémener, T.P. Davis, C. Barner-Kowollik, and M.H. Stenzel (2006) RAFT and click chemistry: A versatile approach to well-defined block copolymers, Chem. Commun. 5051–5053.

153. H.C. Kolb, M.G. Finn, and K.B. Sharpless (2001) Click Chemistry: Diverse Chemical Function from a Few Good Reactions, Angewandte Chemie International Edition. 40, 2004–2021.

154. V. V Rostovtsev, L.G. Green, V. V Fokin, and K.B. Sharpless (2002) A Stepwise Huisgen Cycloaddition Process: Copper(I)-Catalyzed Regioselective “Ligation” of Azides and Terminal Alkynes, Angewandte Chemie International Edition. 41, 2596–2599.

155. C.W. Tornøe, C. Christensen, and M. Meldal (2002) Peptidotriazoles on Solid Phase: [1,2,3]-Triazoles by Regiospecific Copper(I)-Catalyzed 1,3-Dipolar Cycloadditions of Terminal Alkynes to Azides, The Journal of Organic Chemistry. 67, 3057–3064.

156. U. Mansfeld, C. Pietsch, R. Hoogenboom, C.R. Becer, and U.S. Schubert (2010) Clickable initiators, monomers and polymers in controlled radical polymerizations – a prospective combination in polymer science, Polymer Chemistry. 1, 1560.

157. J.F. Lutz (2008) Copper-free azide-alkyne cycloadditions: New insights and perspectives, Angewandte Chemie - International Edition. 47, 2182–2184.

158. A.B. Lowe (2010) Thiol-ene “click” reactions and recent applications in polymer and materials synthesis, Polym. Chem. 1, 17–36.

159. R. Ranjan and W.J. Brittain (2008) Synthesis of High Density Polymer Brushes on Nanoparticles by Combined RAFT Polymerization and Click Chemistry, Macromolecular Rapid Communications. 29, 1104–1110.

160. R. Ranjan and W.J. Brittain (2007) Combination of Living Radical Polymerization and Click Chemistry for Surface Modification, Macromolecules. 40, 6217–6223.

161. S.R. Gondi, A.P. Vogt, and B.S. Sumerlin (2007) Versatile Pathway to Functional Telechelics via RAFT Polymerization and Click Chemistry, Macromolecules. 40, 474–481.

162. J. Zhu, X. Zhu, E.T. Kang, and K.G. Neoh (2007) Design and synthesis of star polymers with hetero-arms by the combination of controlled radical polymerizations and click chemistry, Polymer. 48, 6992–6999.

163. F. Chen, Z. Cheng, J. Zhu, W. Zhang, and X. Zhu (2008) Synthesis of poly(vinyl acetate) with fluorescence via a combination of RAFT/MADIX and “click” chemistry, European Polymer Journal. 44, 1789–1795.

164. C. Boyer, J. Liu, V. Bulmus, T.P. Davis, C. Barner-Kowollik, and M.H. Stenzel (2008) Direct Synthesis of Well-Defined Heterotelechelic Polymers for Bioconjugations, Macromolecules. 41, 5641–5650.

165. D. Quémener, M. Le Hellaye, C. Bissett, T.P. Davis, C. Barner-Kowollik, and M.H. Stenzel (2008) Graft block copolymers of propargyl methacrylate and vinyl acetate via a combination of RAFT/MADIX and click chemistry: Reaction analysis, Journal of Polymer Science Part A: Polymer Chemistry. 46, 155–173.

166. R.K. O&apos;Reilly, M.J. Joralemon, C.J. Hawker, and K.L. Wooley (2006) Fluorogenic 1,3-dipolar cycloaddition within the hydrophobic core of a shell cross-linked nanoparticle, Chemistry - A European Journal. 12, 6776–6786.

167. Y. Li, J. Yang, and B.C. Benicewicz (2007) Well-controlled polymerization of 2-azidoethyl methacrylate at near room temperature and click functionalization, Journal of Polymer Science Part A: Polymer Chemistry. 45, 4300–4308.

168. C. Le Droumaguet, C. Wang, and Q. Wang (2010) Fluorogenic click reaction., Chemical Society reviews. 39, 1233–1239.

169. M.J. Joralemon, R.K. O’Reilly, C.J. Hawker, and K.L. Wooley (2005) Shell Click-crosslinked (SCC) nanoparticles: A new methodology for synthesis and orthogonal functionalization, Journal of the American Chemical Society. 127, 16892–16899.

170. H.R. Rengifo, L. Chen, C. Grigoras, J. Ju, and J.T. Koberstein (2008) “Click-functional” block copolymers provide precise surface functionality via spin coating, Langmuir. 24, 7450–7456.

171. K. Ouadahi, K. Sbargoud, E. Allard, and C. Larpent (2012) FRET-mediated pH-responsive dual fluorescent nanoparticles prepared via click chemistry, Nanoscale. 4, 727–732.

172. K. Ouadahi, E. Allard, B. Oberleitner, and C. Larpent (2012) Synthesis of azide-functionalized nanoparticles by microemulsion polymerization and surface modification by click chemistry in aqueous medium, Journal of Polymer Science Part A: Polymer Chemistry. 50, 314–328.

173. X. Wang, L. Liu, Y. Luo, and H. Zhao (2009) Bioconjugation of Biotin to the Interfaces of Polymeric Micelles via In Situ Click Chemistry, Langmuir. 25, 744–750.

174. J. Jin, D. Wu, P. Sun, L. Liu, and H. Zhao (2011) Amphiphilic Triblock Copolymer Bioconjugates with Biotin Groups at the Junction Points: Synthesis, Self-Assembly, and Bioactivity, Macromolecules. 44, 2016–2024.

175. J.L. Brennan, N.S. Hatzakis, T.R. Tshikhudo, V. Razumas, S. Patkar, J. Vind, A. Svendsen, R.J.M. Nolte, A.E. Rowan, and M. Brust (2006) Bionanoconjugation via Click Chemistry: The Creation of Functional Hybrids of Lipases and Gold Nanoparticles, Bioconjugate Chemistry. 17, 1373–1375.

176. A.K. Oyelere, P.C. Chen, X. Huang, I.H. El-Sayed, and M. a El-Sayed (2007) Peptide-conjugated gold nanorods for nuclear targeting, Bioconjugate Chemistry. 18, 1490–1497.

177. A. V. Ustinov, V. V. Dubnyakova, and V. a. Korshun (2008) A convenient “click chemistry” approach to perylene diimide–oligonucleotide conjugates, Tetrahedron. 64, 1467–1473.

178. A.H. El-Sagheer and T. Brown (2012) Click Nucleic Acid Ligation: Applications in Biology and Nanotechnology, Accounts of Chemical Research. 45, 1258–1267.

179. L. Polito, D. Monti, E. Caneva, E. Delnevo, G. Russo, and D. Prosperi (2008) One-step bioengineering of magnetic nanoparticles via a surface diazo transfer/azide-alkyne click reaction sequence., Chemical communications (Cambridge, England). 621–623.

180. N. Xu, R. Wang, F. Du, and Z. Li (2009) Synthesis of amphiphilic biodegradable glycocopolymers based on poly(ε-caprolactone) by ring-opening polymerization and click chemistry, Journal of Polymer Science Part A: Polymer Chemistry. 47, 3583–3594.

181. K. Ariga, J.P. Hill, and H. Endo (2007) Developments in Molecular Recognition and Sensing at Interfaces, International Journal of Molecular Sciences. 8, 864–883.

182. R.M. Leblanc (2006) Molecular recognition at Langmuir monolayers, Current Opinion in Chemical Biology. 10, 529–536.

183. D.K. Schwartz (1997) Langmuir-Blodgett film structure, Surface Science Reports. 27, 245–334.

184. D.K. Schwartz (2001) Langmuir–Blodgett Films, Formation and Structure of, Encyclopedia of Materials: Science and Technology, pp. 4392–4399 Elsevier.

185. O.N. Oliveira Jr (1992) Langmuir-Blodgett films - properties and possible applications, Brazilian Journal of Physics. 22,.

186. S.A.H. Hussain (2010) Langmuir-Blodgett Films, GRIN Publishing GmbH.

187. T.M. Nobre, F.J. Pavinatto, L. Caseli, A. Barros-Timmons, P. Dynarowicz-Łątka, and O.N. Oliveira (2015) Interactions of bioactive molecules & nanomaterials with Langmuir monolayers as cell membrane models, Thin Solid Films. 593, 158–188.

188. A. Pavinatto, F.J. Pavinatto, A. Barros-Timmons, and O.N. Oliveira (2010) Electrostatic interactions are not sufficient to account for chitosan bioactivity, ACS Applied Materials and Interfaces. 2, 246–251.

189. A.A. Torrano, Â.S. Pereira, O.N. Oliveira, and A. Barros-Timmons (2013) Probing the interaction of oppositely charged gold nanoparticles with DPPG and DPPC Langmuir monolayers as cell membrane models, Colloids and Surfaces B: Biointerfaces. 108, 120–126.

190. C. Wang, J. Zheng, O.N. Oliveira, and R.M. Leblanc (2007) Nature of the Interaction between a Peptidolipid Langmuir Monolayer and Paraoxon in the Subphase, Journal of Physical Chemistry C. 111, 7826–7833.

191. M. Ferreira, W. Caetano, Itri, Rosangela, M. Tabak, and O.N. de Oliveira Jr. (2005) Técnicas de caracterização para investigar interações no nível molecular em filmes de Lagmuir e Lagmuir-Blodegett, Química Nova. 28, 502–510.

192. G. Schneider, G. Decher, N. Nerambourg, R. Praho, M.H. V Werts, and M. Blanchard-Desce (2006) Distance-dependent fluorescence quenching on gold nanoparticles ensheathed with layer-by-layer assembled polyelectrolytes, Nano Letters. 6, 530–536.

193. X. Li, L. Jiang, Q. Zhan, J. Qian, and S. He (2009) Localized surface plasmon resonance (LSPR) of polyelectrolyte-functionalized gold-nanoparticles for bio-sensing, Colloids and

Surfaces A: Physicochemical and Engineering Aspects. 332, 172–179.

194. L.M. Feller, S. Cerritelli, M. Textor, J. a. Hubbell, and S.G.P. Tosatti (2005) Influence of Poly(propylene sulfide- block -ethylene glycol) Di- and Triblock Copolymer Architecture on the Formation of Molecular Adlayers on Gold Surfaces and Their Effect on Protein Resistance: A Candidate for Surface Modification in Biosensor Research, Macromolecules. 38, 10503–10510.

195. H. Vaisocherová, E. Brynda, and J. Homola (2015) Functionalizable low-fouling coatings for label-free biosensing in complex biological media: advances and applications, Analytical and Bioanalytical Chemistry. 407, 3927–3953.

196. S. Lowe, N.M. O'Brien-Simpson, and L.A. Connal (2015) Antibiofouling polymer interfaces: poly(ethylene glycol) and other promising candidates, Polym. Chem. 6, 198–212.

197. T.J.V. Prazeres, M. Beija, F. V. Fernandes, P.G.A. Marcelino, J.P.S. Farinha, and J.M.G. Martinho (2012) Determination of the critical micelle concentration of surfactants and amphiphilic block copolymers using coumarin 153, Inorganica Chimica Acta. 381, 181–187.

198. Y. Shi, H.Q. Luo, and N.B. Li (2011) Determination of the critical premicelle concentration, first critical micelle concentration and second critical micelle concentration of surfactants by resonance Rayleigh scattering method without any probe, Spectrochimica Acta Part A: Molecular and Biomolecular Spectroscopy. 78, 1403–1407.

199. Malvern Instruments Ltd (2006) Surfactant micelle characterization using dynamic light scattering, Zetasizer Nano application note, pp. 1–5.

200. T. Sakai and P. Alexandridis (2005) Mechanism of gold metal ion reduction, nanoparticle growth and size control in aqueous amphiphilic block copolymer solutions at ambient conditions, Journal of Physical Chemistry B. 109, 7766–7777.

201. P. Sahu and B.L. V Prasad (2014) Time and Temperature Effects on the Digestive Ripening of Gold Nanoparticles: Is There a Crossover from Digestive Ripening to Ostwald Ripening?, Langmuir. 30, 10143–10150.

202. M.H. Stenzel (2009) Hairy Core-Shell Nanoparticles via RAFT: Where are the Opportunities and Where are the Problems and Challenges?, Macromolecular Rapid Communications. 30, 1603–1624.

203. S. Boissé, J. Rieger, K. Belal, A. Di-Cicco, P. Beaunier, M.-H. Li, and B. Charleux (2010) Amphiphilic block copolymer nano-fibers via RAFT-mediated polymerization in aqueous dispersed system, Chemical Communications. 46, 1950.

204. X. Jiang, J. Zhang, Y. Zhou, J. Xu, and S. Liu (2008) Facile preparation of core-crosslinked micelles from azide-containing thermoresponsive double hydrophilic diblock copolymer via click chemistry, Journal of Polymer Science Part A: Polymer Chemistry. 46, 860–871.

205. A.R. De Luzuriaga, N. Ormategui, H.J. Grande, I. Odriozola, and A. José (2008) Intramolecular Click Cycloaddition : An Efficient Route towards Bioconjugable Polymeric Nanoparticles at Room Temperature, 2–6.

206. L. a. Canalle, S.S. van Berkel, L.T. de Haan, and J.C.M. van Hest (2009) Copper-Free Clickable Coatings, Advanced Functional Materials. 19, 3464–3470.

207. Sigma-Aldrich Thermal Initiators: Decomposition Rate and Half-Life, http://www.sigmaaldrich.com/content/dam/sigma-aldrich/docs/Aldrich/General_Information/thermal_initiators.pdf.

208. V. Ladmiral, G. Mantovani, G.J. Clarkson, S. Cauet, J.L. Irwin, and D.M. Haddleton (2006)

Synthesis of neoglycopolymers by a combination of “click chemistry” and living radical polymerization, Journal of the American Chemical Society. 128, 4823–4830.

209. D.J. Siegwart, J.K. Oh, H. Gao, S. a. Bencherif, F. Perineau, A.K. Bohaty, J.O. Hollinger, and K. Matyjaszewski (2008) Biotin-, Pyrene-, and GRGDS-Functionalized Polymers and Nanogels via ATRP and End Group Modification, Macromolecular Chemistry and Physics. 209, 2179–2193.

210. G. Gody, T. Maschmeyer, P.B. Zetterlund, and S. Perrier (2014) Exploitation of the degenerative transfer mechanism in RAFT polymerization for synthesis of polymer of high livingness at full monomer conversion, Macromolecules. 47, 639–649.

211. A. Patra, T. Ding, G. Engudar, Y. Wang, M.M. Dykas, B. Liedberg, J.C.Y. Kah, T. Venkatesan, and C.L. Drum (2016) Component-Specific Analysis of Plasma Protein Corona Formation on Gold Nanoparticles Using Multiplexed Surface Plasmon Resonance, Small. 12, 1174–1182.

212. M. Cui, R. Liu, Z. Deng, G. Ge, Y. Liu, and L. Xie (2014) Quantitative study of protein coronas on gold nanoparticles with different surface modifications, Nano Research. 7, 345–352.

213. S.J. McClellan and E.I. Franses (2003) Effect of concentration and denaturation on adsorption and surface tension of bovine serum albumin, Colloids and Surfaces B: Biointerfaces. 28, 63–75.

214. T.J. Joncheray, S.A. Bernard, R. Matmour, B. Lepoittevin, R.J. El-Khouri, D. Taton, Y. Gnanou, and R.S. Duran (2007) Polystyrene-b-poly(tert-butyl acrylate) and polystyrene-b-poly(acrylic acid) dendrimer-like copolymers: Two-dimensional self-assembly at the air-water interface, Langmuir. 23, 2531–2538.

215. P.C.D.S. Claro, M.E. Coustet, C. Diaz, E. Maza, M.S. Cortizo, F.G. Requejo, L.I. Pietrasanta, M. Ceolín, and O. Azzaroni (2013) Self-assembly of PBzMA-b-PDMAEMA diblock copolymer films at the air–water interface and deposition on solid substrates via Langmuir–Blodgett transfer, Soft Matter. 9, 10899.

216. J.P.S. Farinha, P. Relógio, M.-T. Charreyre, T.J. V Prazeres, and J.M.G. Martinho (2007) Understanding Fluorescence Quenching in Polymers Obtained by RAFT, Macromolecules. 40, 4680–4690.

217. C.J. Stephenson and K.D. Shimizu (2006) Colormetric imprinted polymers as sensors, Polymer Preprints, p. 7.

218. G. Gody, R. Barbey, M. Danial, and S. Perrier (2015) Ultrafast RAFT polymerization: multiblock copolymers within minutes, Polym. Chem. 6, 1502–1511.

219. I. Johnson and M.T.Z. Spence, Eds, (2010) Chapter 20 - pH Indicators, Molecular Probes® Handbook—A Guide to Fluorescent Probes and Labeling Technologies, Invitrogen.

220. B.N. Khlebtsov and N.G. Khlebtsov (2011) On the measurement of gold nanoparticle sizes by the dynamic light scattering method, Colloid Journal. 73, 118–127.

221. W. Haiss, N.T.K. Thanh, J. Aveyard, and D.G. Fernig (2007) Determination of Size and Concentration of Gold Nanoparticles from UV−Vis Spectra, Analytical Chemistry. 79, 4215–4221.

ANNEXES

Annexe A.

Determination of monomer conversion by ^{1}H-NMR of MR agent.

The monomer conversion (*%Conversion*) was calculated using the equation below. The peaks assigned to the vinylic protons were integrated using the signal of 1,3,5-trioxane as internal standard, as shown in Figure A.1. *%Conversion* profile for the MR agents are shown in Figure A.2.

$$\%Conversion_{tx} = \frac{\left(\frac{a_{t0} + b_{t0} + c_{t0}}{3}\right) - \left(\frac{a_{tx} + b_{tx} + c_{tx}}{3}\right)}{\left(\frac{a_{t0} + b_{t0} + c_{t0}}{3}\right)} \times 100$$

a_{t0}, b_{t0}, c_{t0} – integral of the peaks ***a***, ***b*** and ***c*** before polymerization starts.
a_{tx}, b_{tx}, c_{tx} – integral of the peaks ***a***, ***b*** and ***c*** after ***x*** time of polymerization.

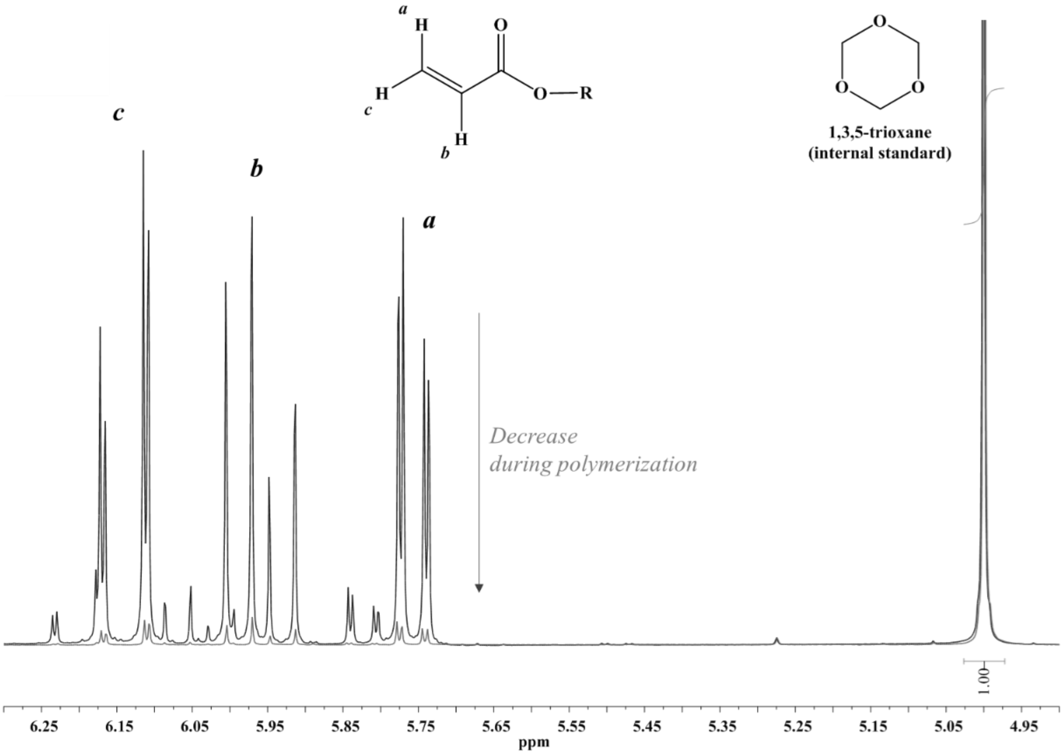

Figure A.1. Example of ^{1}H-NMR spectra showing the assignments for the vinylic protons of the monomer and the assignment for 1,3,5-trioxane, used as internal standard. The spectra of the aliquot t_0 and the aliquot withdrawn after 4h of polymerization are presented.

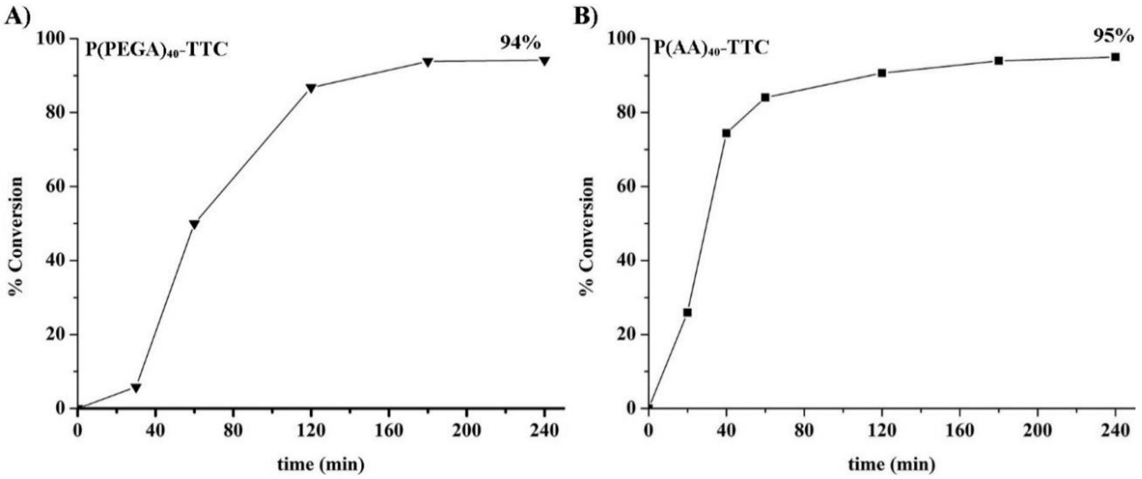

Figure A.2. %Conversion profile of (A) P(PEGA$_{40}$)-TTC and (B) P(AA$_{40}$)-TTC determined by H^1-NMR.

Annexe B.

How to calculate the monomer conversion by gravimetric analysis?

To calculate the monomer conversion (*%Conversion*) by gravimetric analysis, first the initial formulation for the polymerization should be known to calculate the fraction (*f*) of each reagent. The example showed here is for the copolymerization of P(AA_{40})-TTC (Table B.1)

Table B.1. Experimental formulation for the copolymerization of P(AA_{40})-TTC.

	water	MMA:BA	ACPA	MR agent	Total
Mass (g)	8.298	1.435	0.003	0.284	10.021
Fraction (*f*) in the initial formulation	0.828	0.143	0.0003	0.0283	1

Second, *dry polymer* and the *%Conversion* were calculated using withdrawn aliquots during polymerization. For that, the aliquots were put in an aluminum dish, then they stayed overnight in the fume hood and in the next day were dried in an oven with ventilation at 90ºC for 6h. Table B.2 shows the calculation of the dry latex in each aliquot.

Table B.2. Calculation of the dry latex in each aliquot.

Time (h)	Aluminium dish (g)	Dish + latex (g)	latex (g)	Dish + dry latex (g)	dry latex (g)
0	1.1692	1.7217	0.5525	1.1829	0.0137
1	1.1676	1.6768	0.5092	1.2449	0.0773
2	1.1646	1.7135	0.5489	1.2517	0.0871
3	1.1801	1.6499	0.4698	1.2558	0.0757
4	1.1648	1.6461	0.4813	1.2440	0.0792

After that, the *dry polymer* and the *%Conversion* were calculated based on the following equations, the values are showed in Table B.3.

$$Dry\ Polymer = Dry\ latex - latex \times (f_{ACPA} + f_{MR\ agent})$$

$$\%Conversion = \frac{Dry\ Polymer}{latex \times f_{MMA:BA}} \times 100$$

Table B.3. Calculation of the *dry polymer* and *%conversion*.

Time (h)	Dry polymer	%Conversion
0	0.000	00.00
1	0.063	86.00
2	0.071	90.80
3	0.062	92.51
4	0.065	94.90

%Conversion of monomer and DLS measurements during copolymerization of MR agents.

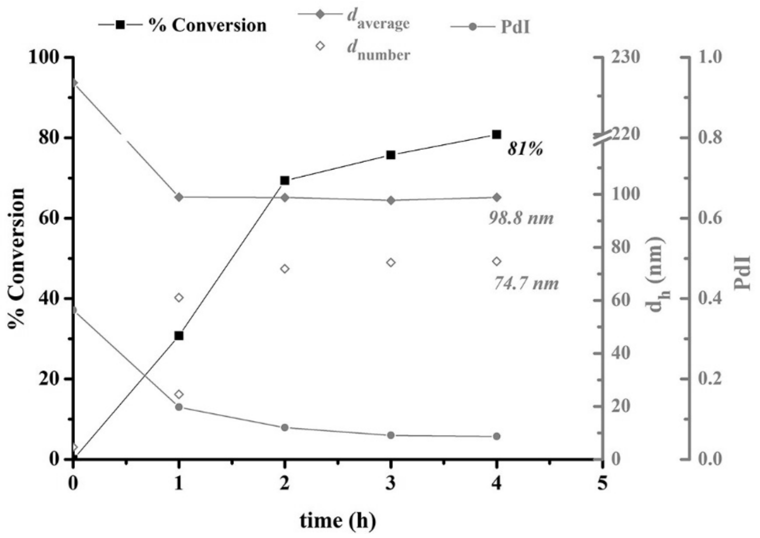

Figure B.3. Evolution the copolymerization of $P(PEGA_{40})$-TTC followed by determination of *%Conversion* by gravimetric analysis and DLS measurements.

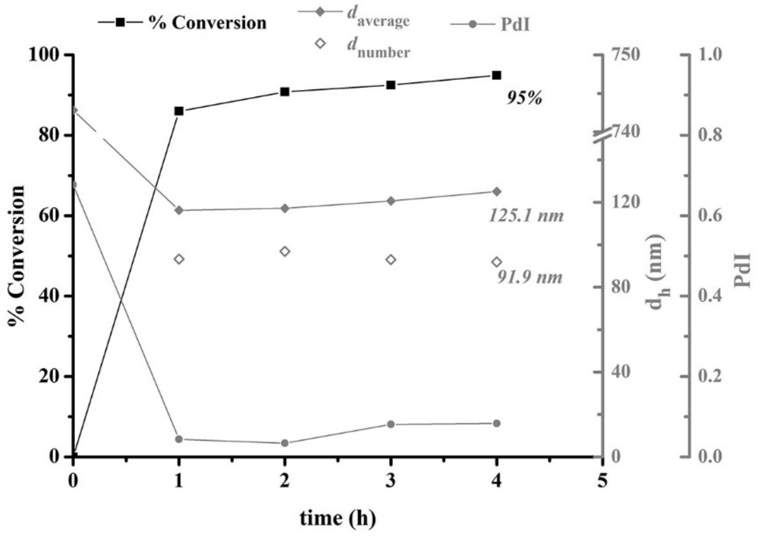

Figure B.4. Evolution the copolymerization of $P(AA_{40})$-TTC followed by determination of *%Conversion* by gravimetric analysis and DLS measurements.

Annexe C.

Determination of MR agents CMC at pH between 7.5 and 8

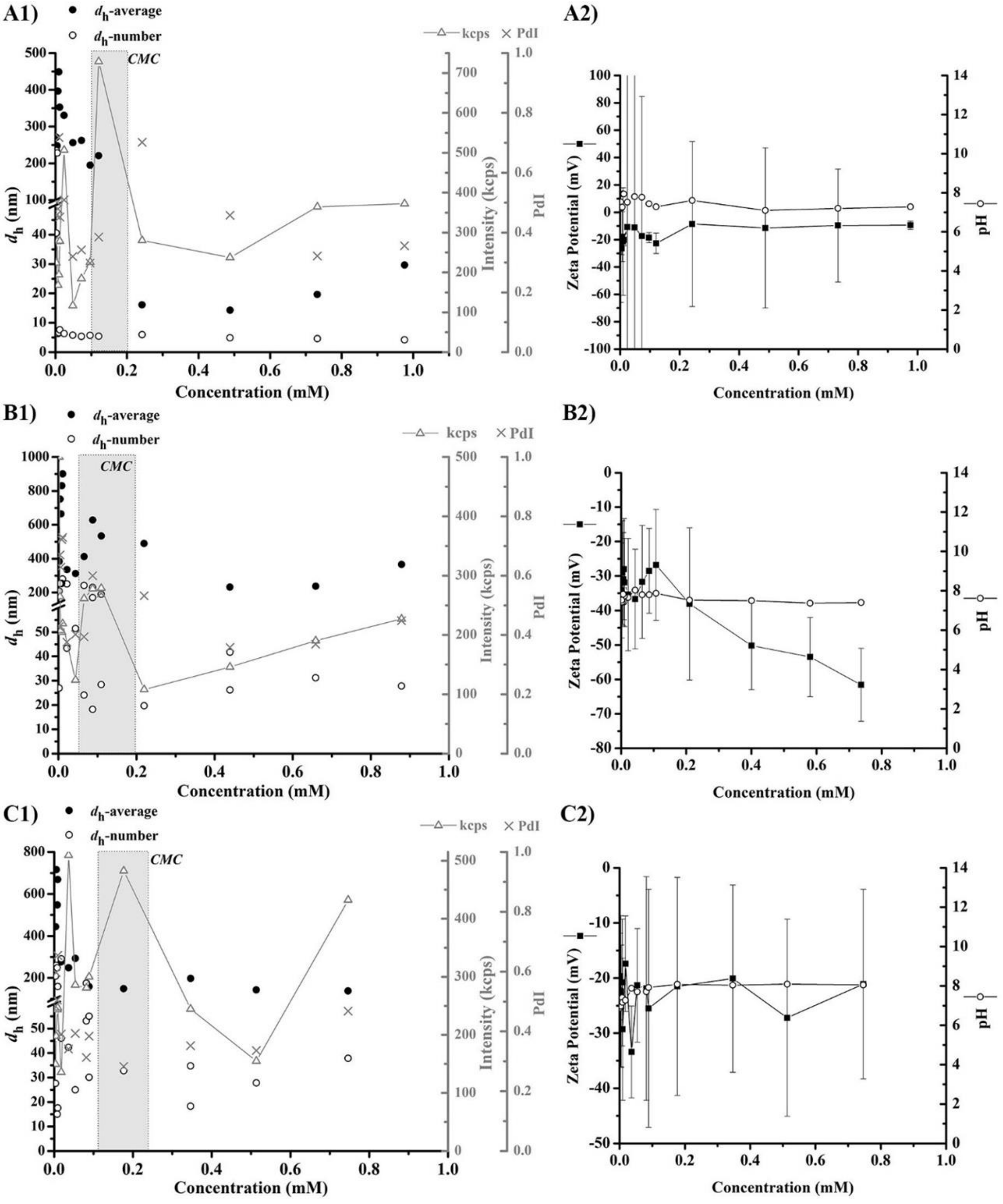

Figure C.5. (A1, B1, C1) DLS and (A2, B2, C2) zeta potential and pH measurements in function of concentration of (A) P(PEGA$_{40}$)-TTC, (B) P(AA$_{40}$)-TTC and (C) P(AA$_{20}$-co-PEGA$_{20}$)-TTC, at pH between 7.5 and 8.0.

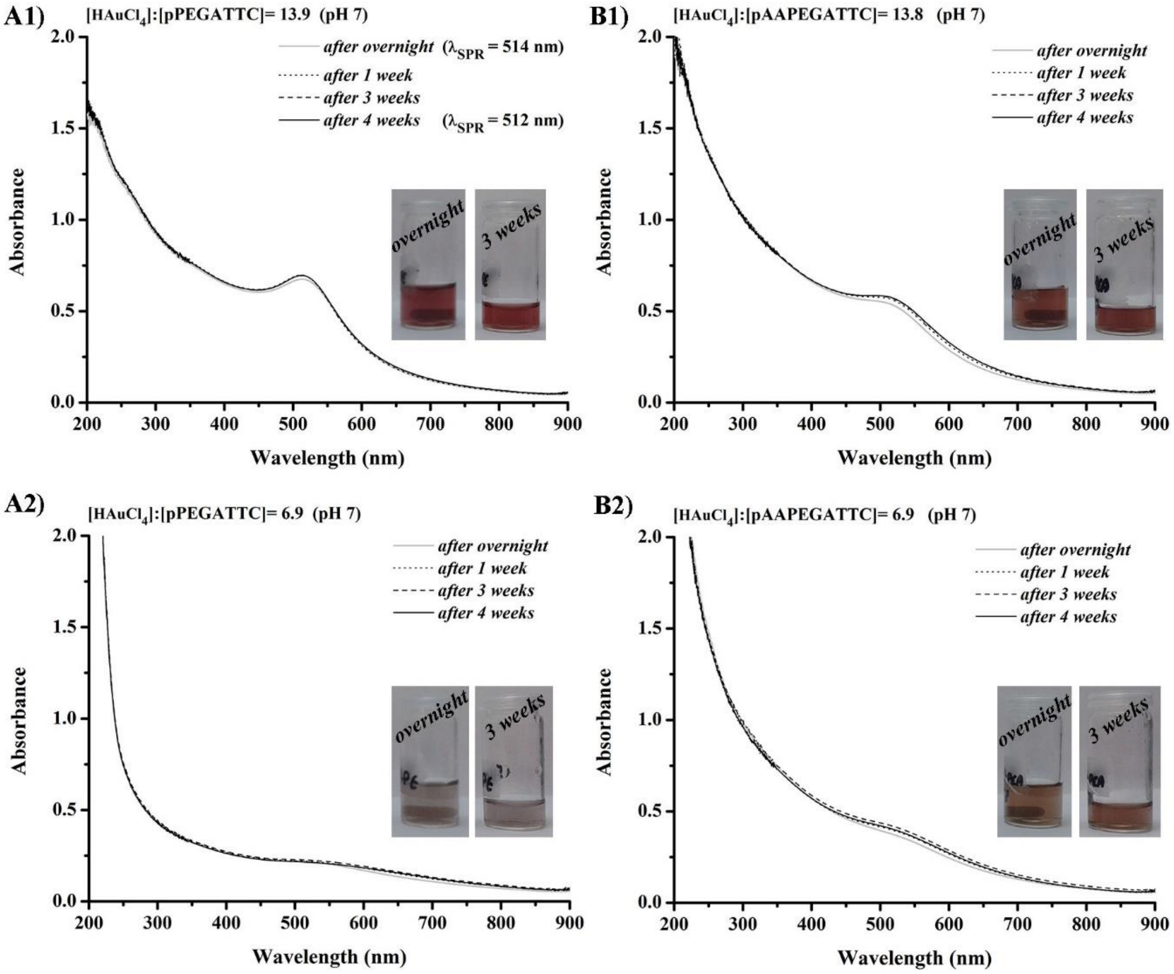

Figure D.6. UV-Vis spectra and (*inset*) photographs of colloids prepared at pH=7 using (A) P(PEGA$_{40}$)-TTC and (B) P(AA$_{20}$-*co*-PEGA$_{20}$)-TTC over 4 weeks.

Annexe E.

Preliminary adsorption studies of MR agent onto Au NPs: How to determine the MR agent adsorbed?

MR agents have an absorption peak around 300-310 nm due to the trithio moiety of the RAFT agent, thus the MR adsorption onto Au NPs were followed by UV-Vis spectroscopy. For that, a solution of MR, with different concentrations, was added drop by drop to a colloidal solution of Au NPs and stirred overnight. Afterwards the colloidal mixture was centrifuged (15 400 g, 30 min), the supernatant was collected and the precipitate was redispersed with ultra-pure water. UV-Vis measurements of the collected supernatants were performed in order to determinate the concentration of MR that does not adsorb on NPs surface. UV-Vis measurements of the precipitate redispersed were also performed in order to assess to the optical properties of the resulting MR/Au colloid. concentration of *non-adsorbed MR* (MR that did not adsorb on NPs surface).

Preliminary adsorption studies using P(PEGA$_{40}$)-TTC

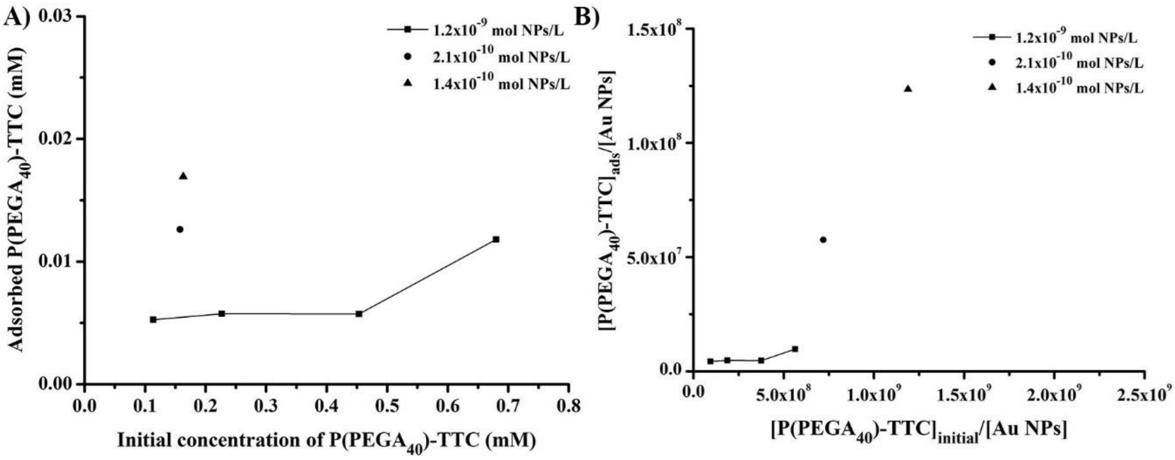

Figure E.7. Adsorption studies of P(PEGA40)-TTC onto Au NPs. (square) samples prepared with the same concentration of Au NPs (1.2x10-9 mol NPs/L) increasing MR concentration and, (circle and triagle) two samples with the same MR concentration (0.16mM) varying Au NPs concentration: 2.1x10-10 mol NPs/L and 1.4x10-10 mol NPs/L, respectively.

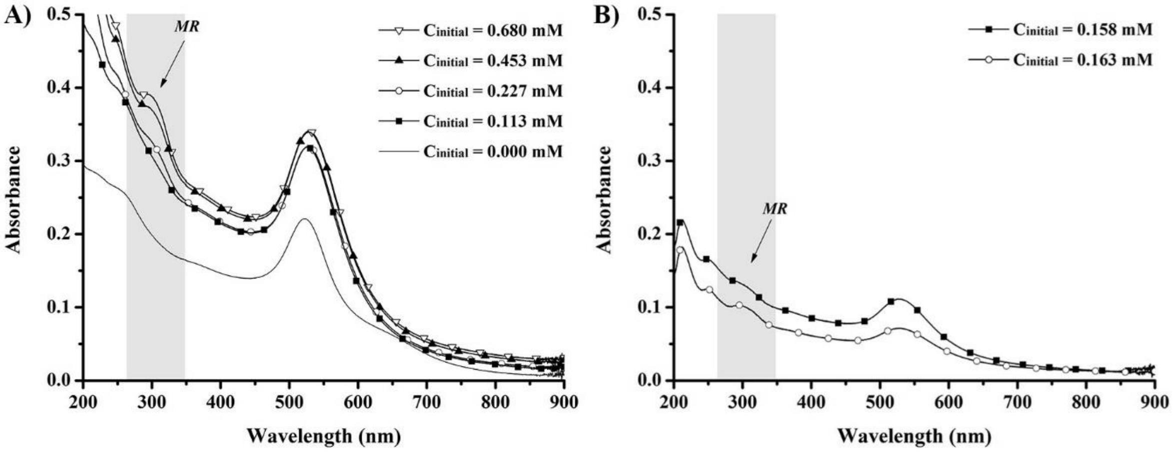

Figure E.8. UV-Vis spectra of redispersed precipitates prepared for the adsorption studies of P(PEGA40)-TTC onto Au NPs. (A) samples prepared with the same concentration of Au NPs (1.2x10-9 mol NPs/L) increasing MR concentration and, (B)) two samples with the same MR concentration (0.16mM) varying Au NPs concentration: 2.1x10-10 mol NPs/L and 1.4x10-10 mol NPs/L, respectively.

Preliminary adsorption studies using P(AA$_{40}$)-TTC

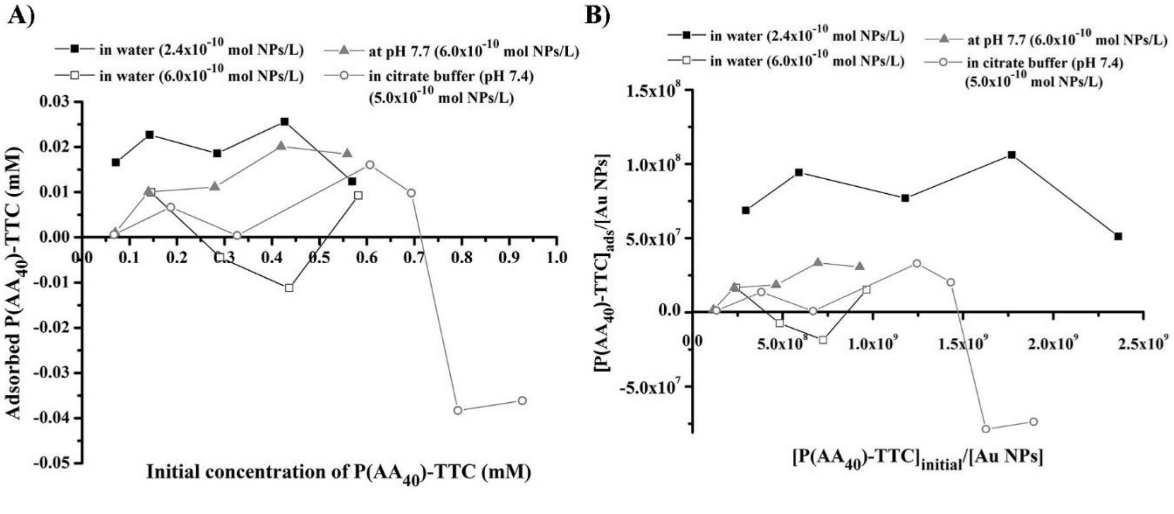

Figure E.9. Adsorption studies of P(AA$_{40}$)-TTC onto Au NPs, dispersed in water (pH~4), at pH 7.7 and MR dispersed in citrate buffer (pH 7.4).

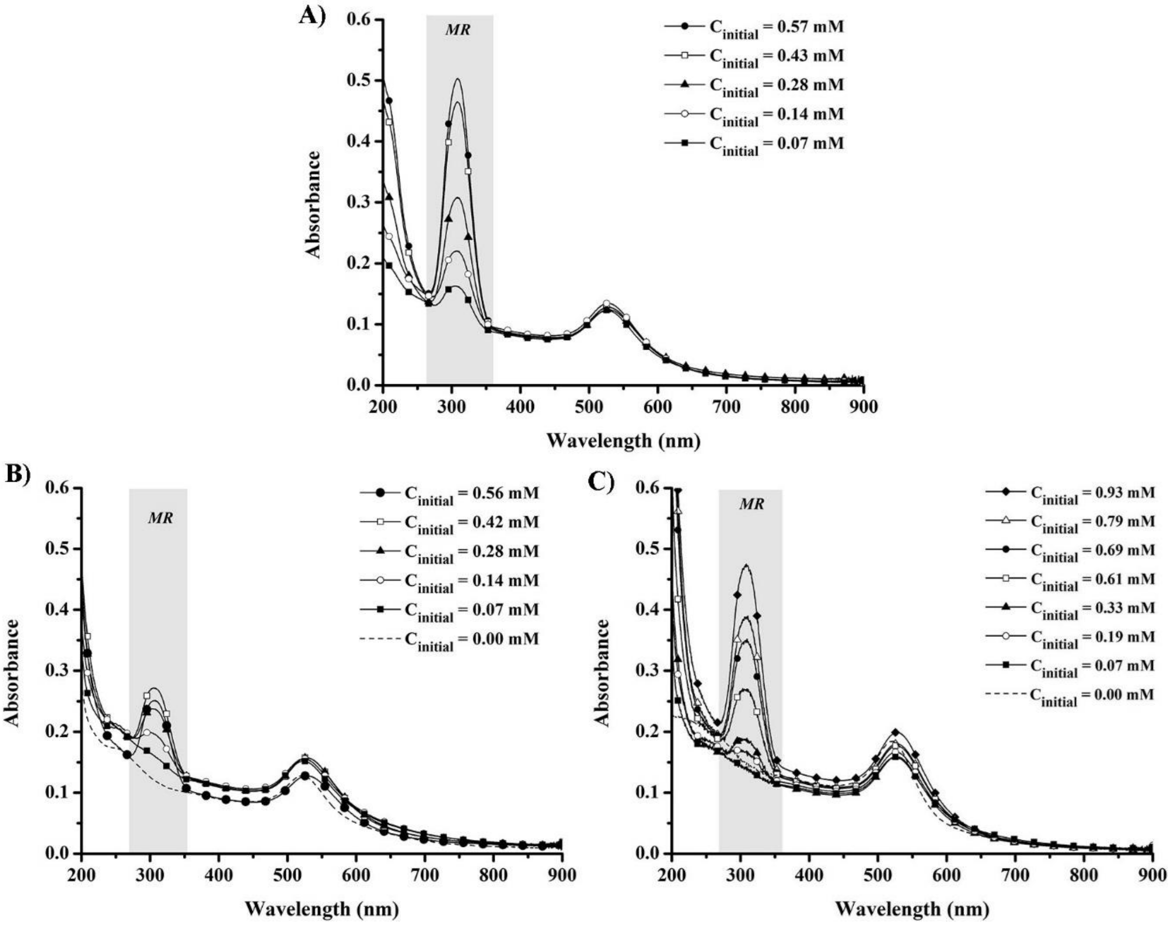

Figure E.10. UV-Vis spectra of redispersed precipitates prepared for the adsorption studies of P(AA$_{40}$)-TTC onto Au NPs. (A) MR dispersed in water (pH~4), (B) at pH 7.7 and (C) MR dispersed in citrate buffer (pH 7.4).

Annexe F.

Determination of azide moities per MR agent

The determination of the number of azide moieties per MR agent chain was estimated by the integration of the chemical shift of the protons from the 3-azido-1-propanol, using as reference the protons of –CH_3 from *Z*-group of the MR agent. The next equation was used:

$$n_{H^c} = \frac{n_{H^{ref}} \times I_{H^c}}{I_{H^{ref}}}$$

n_{H^c}- number of protons that corresponds to the chemical shift of ***c***
$n_{H^{ref}}$- number of protons that corresponds to the chemical shift of the ***reference***
I_{H^c}- integration of chemical shift of ***c***
$I_{H^{ref}}$- integration of chemical shift of the ***reference***

The software MestReNova© was used to analyze the ^{1}H-NMR spectra. The chemical shift of the protons of reference (marked in the spectrum with *, δ=0.84 ppm, in Figure 4.4) were integrated to 1 ($I_{H^{ref}} = 1$). This signal corresponds to 3 protons ($n_{H^{ref}} = 3$). The integration of the protons of ***c*** at the chemical shift 4.57 ppm was equal to 1.09 (I_{H^c}=1.09). Subsequently $n_{H^c} = 3.27$. But this chemical shift corresponds to a –CH_2-, which means that there is 1 or 2 azide moieties per chain. (If $n_{H^c} = 2$ would correspond to one azide per chain, if $n_{H^c} = 4$ would correspond to two azides per chain).

Annexe G.

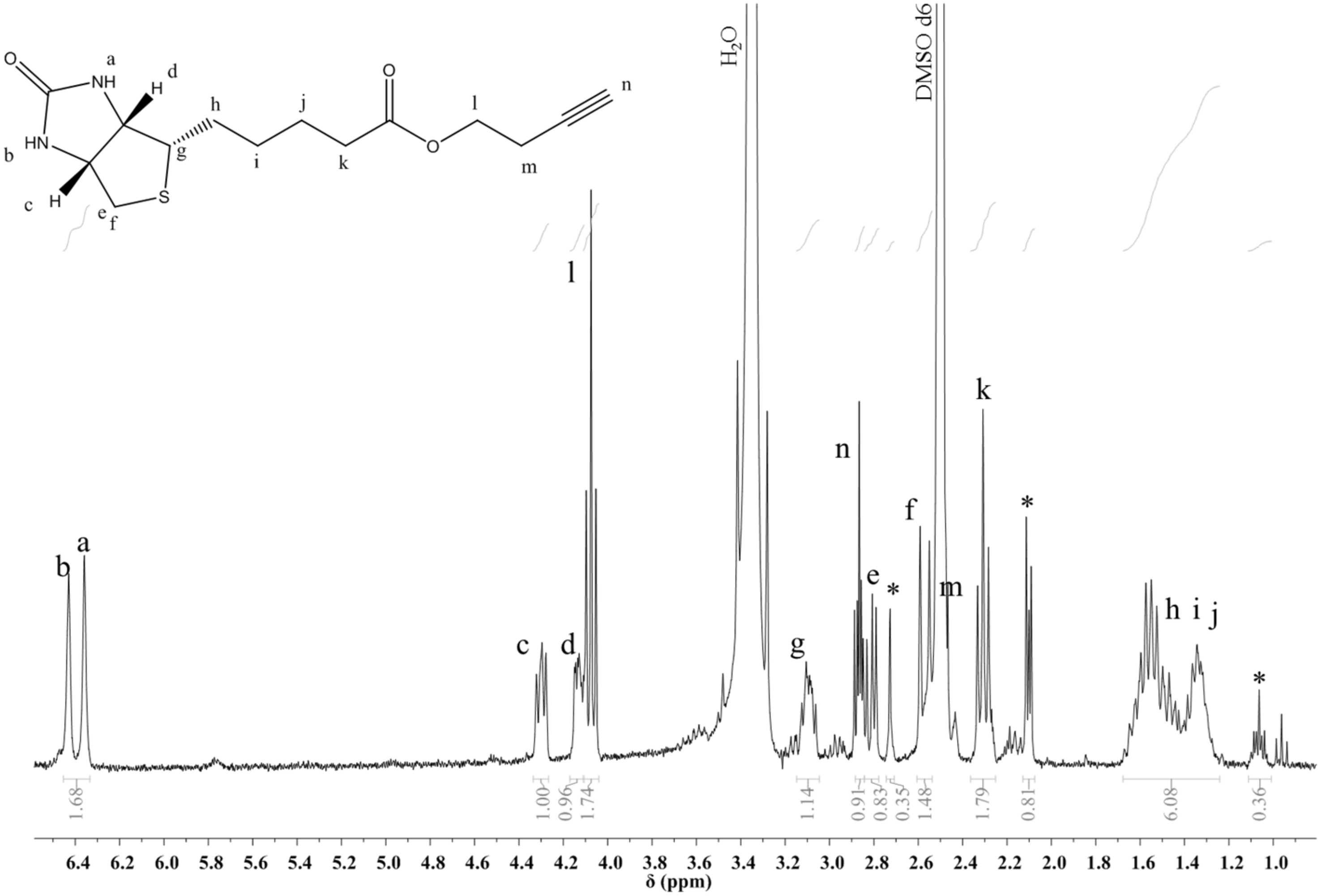

Figure G.11. ^{1}H-NMR of alkylated biotin in DMSO-d$_6$. (* EDC residues).

Annexe H.

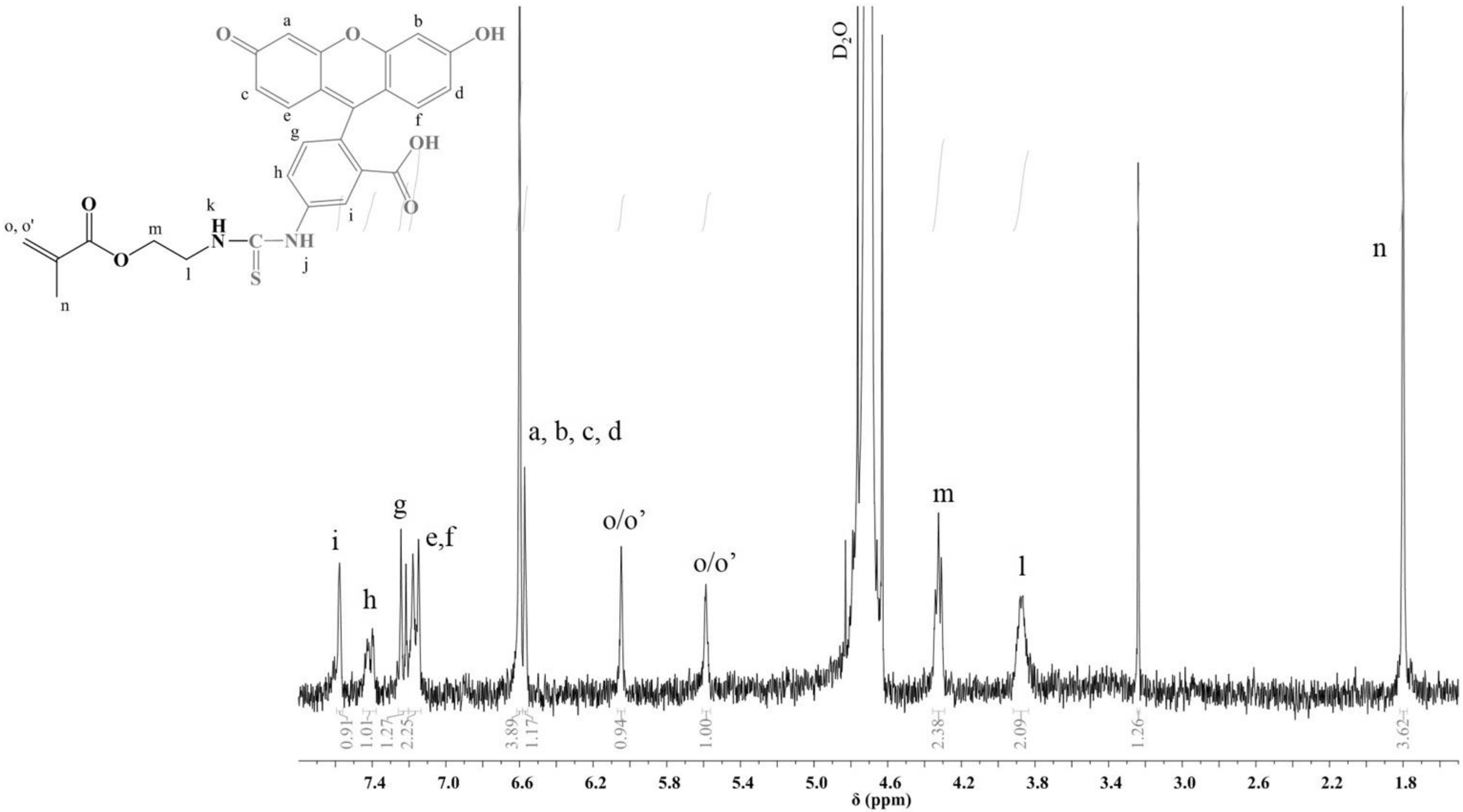

Figure H.12. ^{1}H-NMR of AEM-FITC in D$_2$O.

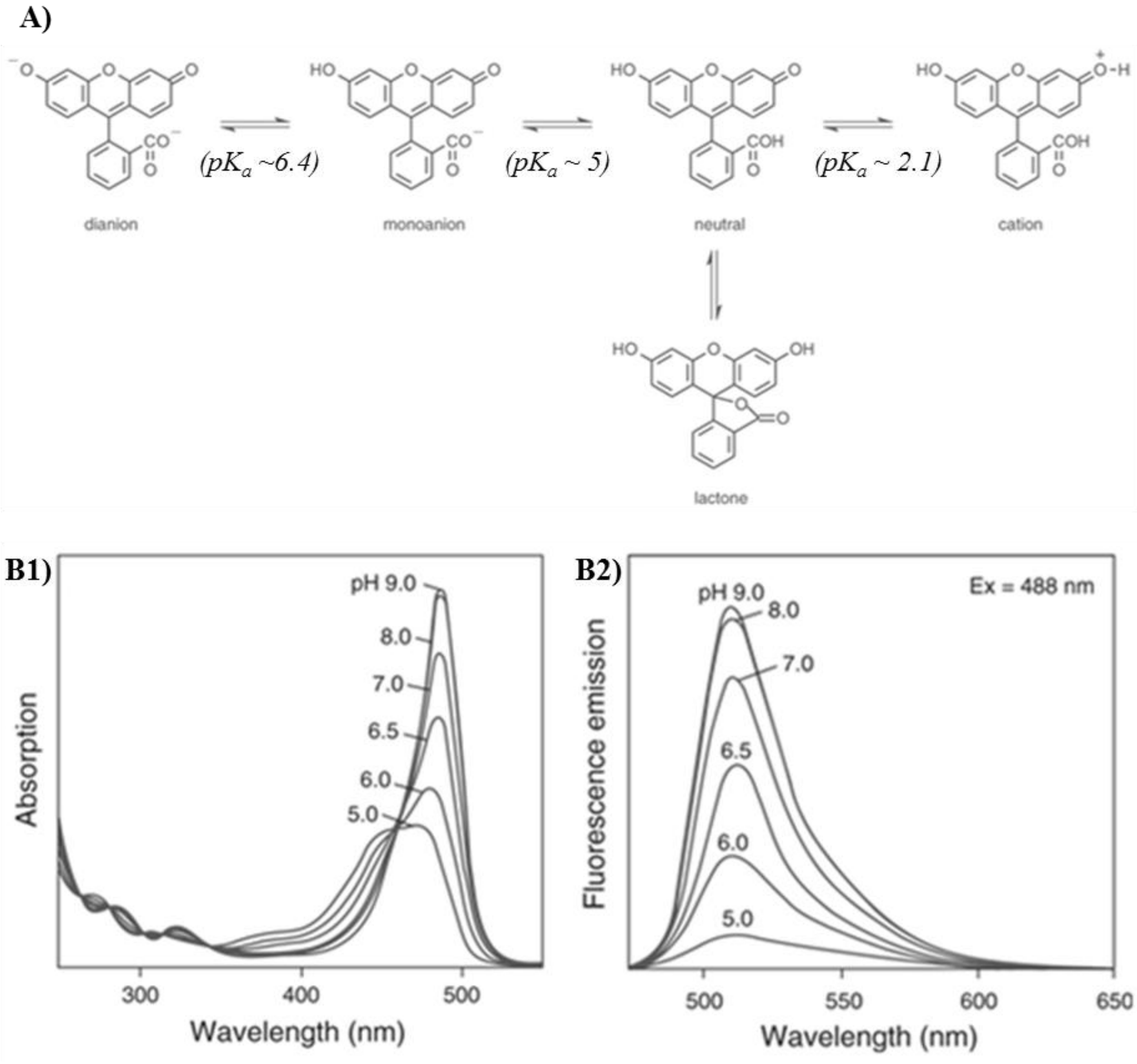

Figure H.13. (A) Ionization equilibria of fluorescein and the pH-dependent spectra of fluorescein: B1) absorption spectra, B2) emission spectra. Adapted from [219]**.**

Annexe I.

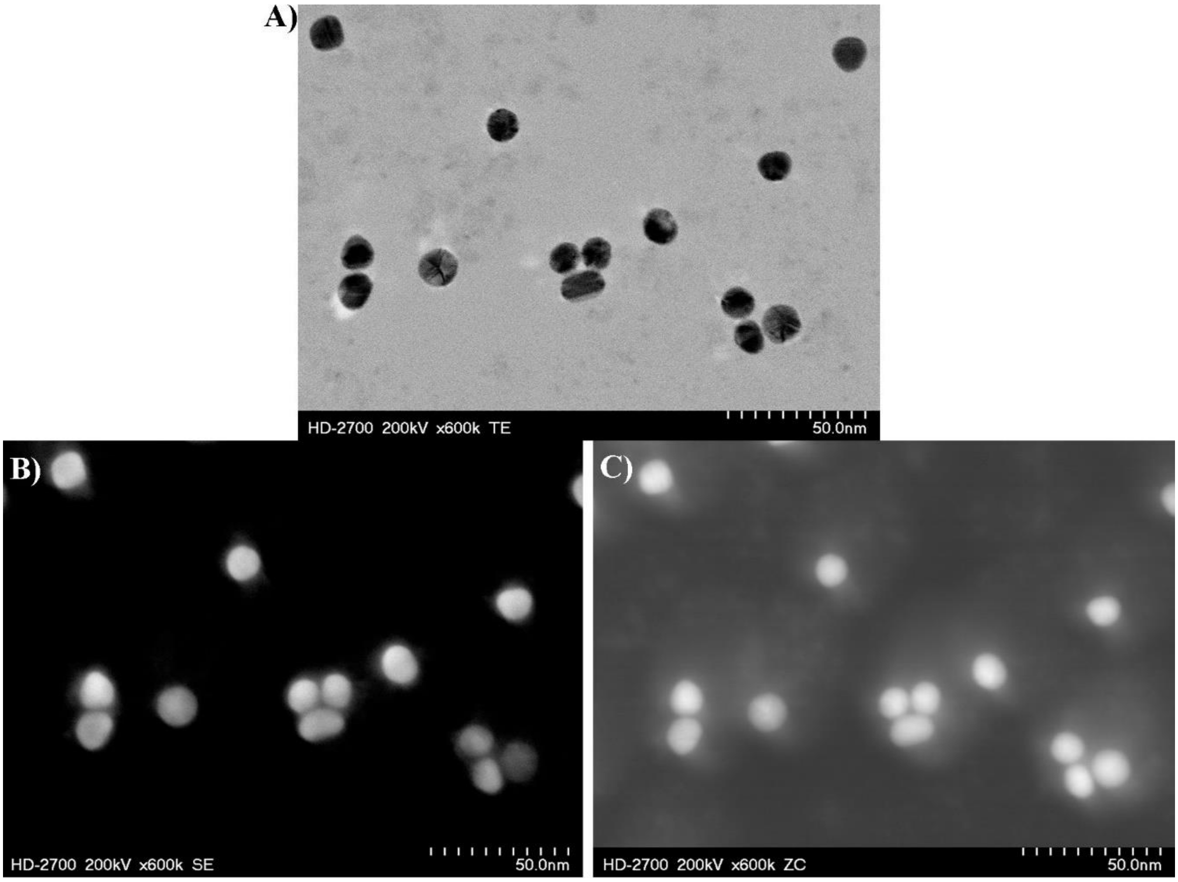
A)
HD-2700 200kV x600k TE
50.0nm
B)
HD-2700 200kV x600k SE
50.0nm
C)
HD-2700 200kV x600k ZC
50.0nm

Figure I.14. STEM images of 2ndCE-copolymer@Au NPs in (A) transmission, (B) secondary electron and (C) Z contrast mode detection.